A multidisciplinary approach to star-formation: observations and modelling of molecular emission in a pre-stellar core and laboratory spectroscopy of molecules of astrophysical interest.

Judit Ferrer Asensio

München 2024

A multidisciplinary approach to star-formation: observations and modelling of molecular emission in a pre-stellar core and laboratory spectroscopy of molecules of astrophysical interest.

Judit Ferrer Asensio

Dissertation
an der Fakultät für Physik
der Ludwig–Maximilians–Universität
München

vorgelegt von
Judit Ferrer Asensio
aus Barcelona, Spain

München, den 11. Januar 2024

Erstgutachter: Prof. Dr. Paola Caselli
Zweitgutachter: Prof. Dr. Til Birnstiel
Tag der mündlichen Prüfung: 23. Februar 2024

"Shadows are flickering in the cadence of thoughts."

... to Necromancy
Darkened Nocturn Slaughtercult

Contents

Zusammenfassung xxiv

Abstract xxvii

1 Introduction 1
- 1.1 Astrochemistry . . . 2
  - 1.1.1 Astrochemical processes . . . 4
- 1.2 Low-mass star formation . . . 10
  - 1.2.1 L1544 . . . 14
  - 1.2.2 IRAS 16293-2422 . . . 16
- 1.3 Observations . . . 18
  - 1.3.1 Level population . . . 18
  - 1.3.2 Radiative transfer . . . 22
  - 1.3.3 Spectral Line Broadening . . . 24
  - 1.3.4 Radio astronomy . . . 25
- 1.4 Modelling . . . 29
- 1.5 Laboratory . . . 32
  - 1.5.1 Rotational Spectroscopy . . . 32
  - 1.5.2 Laboratory Molecular Spectra Measurements . . . 42
- 1.6 This Thesis . . . 45

2 Tracing the contraction of the pre-stellar core L1544 with $HC^{17}O^+$ $J = 1$ - 0 emission.[1] 47
- 2.1 Introduction . . . 49
- 2.2 Observations . . . 51
- 2.3 Radiative transfer . . . 52
  - 2.3.1 Hyperfine collisional rate coefficient calculations . . . 53
  - 2.3.2 The LOC radiative transfer code . . . 54
  - 2.3.3 Chemical code . . . 55
- 2.4 Results . . . 56
  - 2.4.1 $HC^{17}O^+$ . . . 56
  - 2.4.2 $C^{17}O$ . . . 59

2.5 Discussion . . . 61
2.6 Conclusions . . . 63

3 Millimetre and sub-millimetre spectroscopy of doubly deuterated acetaldehyde (CHD_2CHO) and first detection towards IRAS 16293-2422 65
3.1 Introduction . . . 67
3.2 Spectroscopic investigation of CHD_2CHO . . . 69
3.2.1 Experimental . . . 69
3.2.2 Theory . . . 70
3.2.3 Line assignment and line analysis . . . 73
3.2.4 Spectroscopic catalogue . . . 75
3.3 Astrophysical observations . . . 76
3.4 Discussion of astronomical observational results . . . 77
3.5 Conclusions . . . 78

4 High sensitivity and spectral resolution molecular line observations towards the L1544 pre-stellar core: challenges to current models [2] 81
4.1 Introduction . . . 83
4.2 Observations . . . 85
4.3 Radiative transfer . . . 87
4.3.1 The LOC radiative transfer code + MCMC . . . 87
4.3.2 Models and Parameter Space . . . 89
4.4 Results . . . 92
4.4.1 Optically Thin Transitions . . . 92
4.4.2 Optically Thick Transitions . . . 99
4.4.3 SO . . . 103
4.5 Discussion . . . 106
4.6 Conclusions . . . 109

5 Conclusions and future work 111
5.1 Summary . . . 112
5.2 Future work . . . 113

A Tracing the contraction of the pre-stellar core L1544 with $HC^{17}O^+$ $J = 1$ - 0 emission. 117
A.1 Results of the considered scenarios . . . 118
A.1.1 Depletion . . . 118
A.1.2 Self-absorption . . . 118
A.2 Comparison with constant T_{ex} (CT_{ex}) approximation . . . 119
A.3 $HC^{17}O^+$ hyperfine collisional rate coefficients . . . 122
A.4 $C^{17}O$ hyperfine collisional rate coefficients . . . 134

B Millimetre and sub-millimetre spectroscopy of doubly deuterated acetaldehyde (CHD_2CHO) and first detection towards IRAS 16293-2422 **159**
B.1 Detected CHD_2CHO transitions . . . 160

C High sensitivity and spectral resolution molecular line observations towards the L1544 pre-stellar core: challenges to current models **165**
C.1 CS + $C^{34}S$ Modelling . . . 166
C.2 SO + ^{34}SO Modelling . . . 169
C.3 HCO^+ . . . 171
C.3.1 HCO^+ Redaelli et al. 2022 reproduction. . . . 173
C.3.2 HCO^+ + $HC^{17}O^+$ modelling . . . 174
C.4 H_2CO . . . 177
C.5 c-C_3H_2 . . . 179

Danksagung **192**

List of Figures

1.1 Graphic of the techniques used for the research in the field of Astrochemistry and some of their contributions. . . . 3

1.2 Scheme of the Langmuir-Hinshelwood Mechanism. A species in dark blue (left) adsorbs into an interstellar dust grain covered in ice. This species then diffuses to meet another species present in the ice (light blue) to react and desorb (right). . . . 7

1.3 Temperature-density diagram of the ISM phases. The dashed blue line corresponds to constant pressure. Taken from Yamamoto (2016). . . . 11

1.4 Artistic impression of star formation cycle. A diffuse cloud (top left) condensates, resulting in a dense cloud (top right). Upon contraction of the core, a protostar is formed. The gas and dust start accreting into the central protostar, generating feedback such as outflows (middle right, Class 0). The accretion onto the central protostar continues, and the outflows become less collimated (bottom right, Class I). At some point, the envelope clears out, revealing the disk (bottom left, Class II). In the next stage, the disk clears out, revealing the planets in the solar system (middle left, Class III). Finally, the star dies, resulting in a supernova explosion, which scatters the material back into the ISM, where it will be available for new star formation. . . . 13

1.5 *Herschel* four-colour image of the Taurus Molecular Cloud (160 μm, blue; 250 μm, green, 350 μm, green + red and 500 μm, red). The pre-stellar L1544 is seen as the orange spot inside the white circle on the top left of this image. Credit: ESA/Herschel/NASA/JPL-Caltech, R. Hurt. . . . 14

1.6 Three-color ALMA image of the IRAS 16293-2422 protostellar system. The red, green and blue colours indicate the continuum emission at 3.0 mm, 1.3 mm and 0.87 mm. The A1 and A2 protostars are located in the southeast (labelled with "A" as they are unresolved in this image), and the B protostar is marked with the "B" label in the northwest of this image. This Figure is taken from Jørgensen et al. (2016). . . . 17

1.7 Scheme of the radiative spontaneous deexcitation, stimulated deexcitation and excitation (from left to right, respectively) for a two-level system characterised by a lower level with energy E_l and an upper level with energy E_u. Wavy arrows represent photons. . . . 19

1.8 Schematics of the beam pattern. The main lobe is found in the horizontal plane in dark blue, and the side lobes are drawn around the main lobe in light blue shades. . 25
1.9 Picture of the IRAM 30m Telescope antenna. 27
1.10 Superconducting mixer (SIS) diagram. The superconducting layers are denoted with "S", while the insulating layer is denoted with "I". The blue segments represent the filled bands. 2Δ indicates the gap between the filled and empty bands. 27
1.11 Picutre of the ALMA Interferometer. Credit: ESO/C.Malin. 28
1.12 Pre-stellar core physical model profiles used in Chapter 2 and 4. The BES molecular hydrogen density profile is shown with a solid black line. The velocity profile is shown with a dash-dotted orange line. The temperature profile is plotted with a dashed blue line. The profiles have been rescaled so they fit in the same plot. . . . 30
1.13 Molecular fractional abundance profiles at $\sim 5{\times}10^5$ years computed with the pseudo-time dependent gas grain chemical model in (Sipilä et al. 2015) used in Chapter 4. The abundance profiles for CS, SO, HCO^+, c-C_3H_2 and H_2CO are plotted in blue, orange, green, red and purple, respectively. 30
1.14 Prolate (left) and Oblate (right) symmetries. The molecular axes are shown with dotted arrows. For the prolate case $I_b = I_c < I_a$. For the oblate case $I_a = I_b < I_c$. 36
1.15 Non-hyperfine (left) and hyperfine (right) levels and transitions of the J= 1 - 0 $HC^{17}O^+$ line. On the non-hyperfine split case (left), there is a single transition between the lower J= 0 and the upper $J^{'} = 1$ levels. On the hyperfine case (right), we can see three transitions happening between the lower level $F = 5/2$ and three upper levels $F^{'} = 3/2$, 5/2 and 7/2. 38
1.16 The hyperfine structure of the J= 1 - 0 $HC^{17}O^+$ transition observed towards the pre-stellar core L1544. From higher (left) to lower (right) frequencies, we have the $5/2 \rightarrow 5/2$, $7/2 \rightarrow 5/2$ and $3/2 \rightarrow 5/2$ transitions. The double-peaked hyperfine components are not due to quantum but physical reasons and are discussed in Chapter 2. 38
1.17 Torsional sub-level behaviour as a function of the potential barrier height (V_3) for a system with $N = 3$ equal configurations. On the left-hand axis, there are the Free Rotor levels quantised with the quantum number m. On the right-hand axis, there are the Harmonic Oscillator levels quantised with v. The lines connecting the $V_3 = 0$ and $V_3 = \infty$ represent the torsional sub-levels in the intermediate case. The labels of the intermediate states are found just below each of the curves. This scheme has been inspired by Figure 12.4 in Gordy & Cook (1970). 40
1.18 Doubly-deuterated acetaldehyde (CHD_2CHO) symmetric (left) and asymmetric (middle and right) conformers. The blue area depicts the plane defined by the aldehyde ($-CHO$) group. The symmetric conformer has the hydrogen on the blue plane and, therefore, is symmetric. The asymmetric conformers have one of the deuteriums on the blue plane, and there is no longer a symmetry plane. 41
1.19 Portion of a spectrum (80 to 100 GHz) taken with the CP-FTS of a mixture of acetaldehyde (CH_3CHO) and its deuterated isotopologues. 43

1.20 The liquid-He-cooled InSb Hot Electron Bolometer (HEB) detector used for the measurements with the CASAC setup. The black circular components on the bottom of the detector are where the radiation gets in and out of the bolometer. The blue funnel corresponds to the liquid N_2 inlet. 44
1.21 Scan of the $J_{K_a,K_c,v} \leftarrow J'_{K'_a,K'_c,v'}$ $13_{9,5,0} \leftarrow 12_{9,4,0}$ and $13_{9,4,0} \leftarrow 12_{9,3,0}$ (merged) transitions of CHD_2CHO taken with the CASAC experiment. This is an example of a second-derivative line profile due to the $2f$ modulation. 44

2.1 Spectrum of $HC^{17}O^+$(1-0) at the dust peak of L1544. The hyperfine structure is shown by vertical solid lines with heights proportional to their relative intensities (see Table 2.1). The vertical dotted line represents the LSR velocity of L1544 (7.2 km s^{-1}). 51
2.2 The radial profiles of the Keto et al. (2015) model physical parameters are plotted. The black solid line represents the number density of molecular hydrogen, the blue dashed line the gas temperature, and the orange dash-dotted line the velocity profile of the Keto et al. (2015) physical model. In order to display the various parameters in a single plot, the base 10 logarithm of the number density of molecular hydrogen, the temperature divided by 3, and the velocity scaled by -40 are shown. 55
2.3 The results of the $HC^{17}O^+$ observed spectrum modelling with LOC are displayed. *Left.* Observed spectrum of the $HC^{17}O^+$(1-0) (black), the result of a simulation using the original $HC^{17}O^+$ fractional abundance profile at 5×10^5 yrs and the original pre-stellar core model (OM; dotted red) and the result of a simulation using the $HC^{17}O^+$ fractional abundance profile at 5×10^5 yrs upscaled by a factor of 4 times that of the original pre-stellar core model (AM 1; solid red). Residuals are computed with the adopted model and are shown in the lower panel. The dashed lines represent the 3σ levels. *Right.* Observed spectrum of the $HC^{17}O^+$(1-0) (black) and the result of a simulation using the $HC^{17}O^+$ fractional abundance profile at 5×10^5 yrs upscaled by a factor of 3 and an upscaled velocity profile by 30% (AM 2; solid red). Residuals are computed with the adopted model and are shown in the lower panel. The dashed lines represent the 3σ levels. 57
2.4 Comparison between the $HC^{17}O^+$ and $C^{17}O$ radial abundance profiles. The dotted curve shows the $C^{17}O$ fractional abundance (abundance with respect to H_2) as a function of radius. The solid curve shows the fractional abundance of $HC^{17}O^+$, scaled by 10^4 computed with the chemical code from Sipilä et al. (2015, 2019) by scaling the CO and HCO^+ fractional abundance profiles by the isotope ratio $[^{16}O/^{17}O] = 2044$ (Penzias 1981; Wilson & Rood 1994). 58
2.5 Excitation temperature profile of the three $HC^{17}O^+$(1-0) and $C^{17}O$(1-0) hyperfine transitions across the core. The $HC^{17}O^+$(1-0) $5/2 \rightarrow 3/2$, $5/2 \rightarrow 7/2$, and $5/2 \rightarrow 5/2$ transitions are plotted as a black solid line, a black dash-dotted line, and a black dotted line, respectively. The profiles for $HC^{17}O^+$ are superimposed. The $C^{17}O$(1-0) $5/2 \rightarrow 3/2$, $5/2 \rightarrow 7/2$, and $5/2 \rightarrow 5/2$ transitions are plotted as a blue solid line, a blue dash-dotted line, and a blue dotted line, respectively. The inset presents a zoom-in of the radial T_{ex} profile from 0 to 0.1 pc. 58

2.6 The results of the $C^{17}O$ observed spectrum modelling with LOC are displayed. *Left.* Observed spectrum of the $C^{17}O$ (1-0) (black). This spectrum is the result of a simulation using the original $C^{17}O$ fractional abundance profile at 5×10^5 yrs and the original pre-stellar core model (OM; dotted red) and the result of a simulation using the $C^{17}O$ fractional abundance profile at 5×10^5 yrs upscaled by a factor of 3 and the original pre-stellar core model (AM 1; solid red). The residuals are computed with the adopted model and are shown in the lower panel. The dashed lines represent the 3σ levels. *Right.* Observed spectrum of the $C^{17}O$ (1-0) (black) and the result of a simulation using the $C^{17}O$ fractional abundance profile at 5×10^5 yrs increased by a factor of 3 and a scaled-up velocity profile by 30% (AM 2; solid red). Residuals are computed with the adopted model and are shown in the lower panel. The dashed lines represent the 3σ levels. 60

3.1 $\upsilon = 0$ and 1 tunnelling components, arising from the two isoenergetic Out configurations of several a-type transitions. The upper panel shows the $\upsilon = 1$ component of the unresolved K-type doublet $17_9 \leftarrow 16_9$. The lower panel depicts the $\upsilon = 0$ and 1 tunnelling components of the $19_{1,19} \leftarrow 18_{1,18}$ transition. 70

3.2 $\upsilon = 0$ and 1 tunnelling components of the a-type $17K_a \leftarrow 16K_a$ transitions, displaying no resolved asymmetry splitting, with $6 \leq K_a \leq 9$. The line at 295 312 MHz in the second panel is unidentified. 70

3.3 Two energetically equivalent out configurations and the higher energy In configuration are identified by their configuration number n = 1, 2, and 3. The two deuterium atoms are labelled 2 and 3. Furthermore, $\alpha_{eq}^{(n)}$ is the equilibrium value of the torsional angle $\alpha = \angle$HCCO. Configuration 3, displaying a symmetry plane and therefore having C_s symmetry, is approximately 14.487 cm^{-1} above Configurations 1 and 2 with C_1 symmetry. 72

3.4 $J = 0$ tunnelling pattern of CH_2DCHO and CHD_2CHO as retrieved by Margulès et al. (2009). The tunnelling parameter h_2 and the energy differences E_d and E'_d are defined in Section 3.2.2. The tunnelling sub-levels for CHD_2CHO are also labelled with the quantum number υ such that $\upsilon = 0$ and 1 correspond to the + and - tunnelling sub-levels, respectively, and $\upsilon = 2$ to the In conformation level. 72

3.5 Example of the CHD_2CHO fits in a selected frequency range. The synthetic spectra fitted to CHD_2CHO is shown in red and all other species identified in PILS are in blue. 78

4.1 Spectrum of the transitions taken towards the dust peak of L1544. $HC^{17}O^+$ is included from previous works (Ferrer Asensio et al. 2022). The vertical dotted grey line represents the LSR velocity of L1544 (7.2 km s^{-1}). 86

4.2 The 1D pre-stellar core physical model profiles used for the radiative transfer modelling are presented. The pre-stellar core physical model described in Keto et al. (2015) is plotted between 0 to 0.32 pc. The vertical dotted black line marks the radius at 0.32 pc. The physical profiles between 0.32 and 1 pc correspond to an "external layer" used for some of the transition modelling. The physical parameters in this external layer are constant profiles with values equal to the value at the edge (0.32 pc) of the pre-stellar core model in Keto et al. (2015). The physical parameters have been scaled to be presented in the same plot. The molecular hydrogen column density, n_{H_2}, is plotted logarithmically (black solid line). The gas temperature, T, is divided by a factor of 3 (blue dashed line). The velocity profile has been multiplied by a factor of -40 (orange dash-dotted line). 89
4.3 Schematics of the abundance profiles used for the radiative transfer modelling. The vertical axis represents the abundance, and the horizontal axis the radius in units of parsec. From the centre of the core (left) to the parameter r, we have the inner fractional abundance a_{in} and from r to 0.32 pc, there is the outer fractional abundance a_{out} regime. This constitutes the spatial extent of the "non-extended" model, as indicated by the red stripe at the bottom of the plot. From 0.32 to 1 pc, we have the shaded blue area representing the external layer characterised by an external fractional abundance a_{ext}, which we set to the molecular fractional abundance found towards diffuse clouds. Thus, the "extended" model (from the centre to 1 pc) is indicated by the blue stripe at the bottom of the plot. The parameters framed in a box (a_{in}, a_{out} and r) are those explored by the MCMC. . . 90
4.4 $C^{34}S$ (2 - 1) observations in black and modelling results in red towards the L1544 dust peak. The corner plot of the parameter exploration corresponding to these results is shown in Figure 4.5. 93
4.5 Corner plot of the parameters used for the model displayed in Figure 4.4. The top left subplot corresponds to the inner abundance values explored in the modelling. The second column is the outer abundance. The third corresponds to the radius separating the abundance regions. The fourth shows the velocity profile scaling, and the fifth the turbulent velocity. The rest of the panels show the correlation between the different variables. 93
4.6 $C^{34}S$ step fractional abundance profile obtained from the LOC + MCMC modelling of the observed line profile is plotted in a solid red over the fractional abundance profile obtained from the pyRate chemical model (Sipilä et al. 2015) in a grey dashed-dotted line. 94
4.7 Comparison of the $C^{34}S$ spectra computed with different models. The spectrum computed with our LOC + MCMC approach (Figure 4.4) is plotted in a red solid line. The $C^{34}S$ spectrum computed with the original pyRate chemical model fractional abundance profile (Sipilä et al. 2015) and the original pre-stellar core physical model velocity profile and $v_{turb} = 0.075$ km/s, is plotted in a grey dashed line. The spectrum computed with the original fractional abundance profile and the best f_v and v_{turb} values found with our LOC + MCMC approach is plotted with a dotted grey line. Finally, the observations are plotted with a black solid line. 94

4.8 ^{34}SO (2,3 - 1,2) observations in black and modelling results in red towards the L1544 dust peak. The corner plot of the parameter exploration corresponding to these results is shown in Figure 4.9. 95

4.9 Corner plot of the parameters used for the model displayed in Figure 4.8. 95

4.10 ^{34}SO step fractional abundance profile obtained from the LOC + MCMC modelling of the observed line profile is plotted in logarithmic scale in a red solid line over the fractional abundance profile obtained from the pyRate chemical model in (Sipilä et al. 2015) in a grey dashed-dotted line. 96

4.11 Comparison of the ^{34}SO spectra computed with different models. The spectrum computed with our LOC + MCMC approach (Figure 4.8) is plotted in a red solid line. The ^{34}SO spectrum computed with the original pyRate chemical model fractional abundance profile (Sipilä et al. 2015) and the original velocity profile and v_{turb} = 0.075 km/s is plotted in a grey dashed line. The spectrum computed with the original fractional abundance profile and the f_v and v_{turb} values found with our LOC + MCMC approach is plotted with a dotted grey line. Finally, the observations are plotted with a black solid line. 96

4.12 $HC^{17}O^+$ (1 - 0) observations in black and modelling results in red towards the L1544 dust peak. The corner plot of the parameter exploration corresponding to these results is shown in Figure 4.12. 97

4.13 Corner plot of the parameters used for the model displayed in Figure 4.12. 97

4.14 $HC^{17}O^+$ step fractional abundance profile obtained from the LOC + MCMC modelling of the observed line profile is plotted in logarithmic scale in a solid red line over the fractional abundance profile obtained from the pyRate chemical model in Sipilä et al. (2015) in a grey dashed-dotted line. 98

4.15 Comparison of the $HC^{17}O^+$ spectra computed with different models. Our LOC + MCMC approach (Figure 4.12) is plotted in a red solid line. The $HC^{17}O^+$ spectrum computed with the original pyRate chemical model fractional abundance profile (Sipilä et al. 2015) and the original velocity profile and v_{turb} = 0.075 km/s, is plotted in a grey dashed line. The spectrum computed with the original fractional abundance profile and the f_v and v_{turb} values found with our LOC + MCMC approach is plotted with a dotted grey line. Finally, the observations are plotted with a black solid line. 98

4.16 CS (2 -1) observations towards the L1544 dust peak in black. The "non-extended" model is plotted in the solid red spectra, and the "extended" model is plotted in the dash-dotted blue spectra. The corner plot of the parameter exploration corresponding to these results is shown in Figure 4.17. 100

4.17 Corner plot of the parameters used for the "non-extended" model displayed in a solid red line in Figure 4.16. 100

4.18 Corner plot of the parameters used for the "extended" model displayed in a dash-dotted blue line in Figure 4.16. 100

4.19 CS step fractional abundance profile obtained from the "non-extended" LOC + MCMC modelling of the observed line profile is plotted in logarithmic scale in a solid red line over the fractional abundance profile obtained from the pyRate chemical model in Sipilä et al. (2015) plotted with a dashed-dotted grey line. 101

4.20 CS step fractional abundance profile obtained from the "extended" LOC + MCMC modelling of the observed line profile is plotted in logarithmic scale in a solid blue line over the fractional abundance profile obtained from the pyRate chemical model in Sipilä et al. (2015) with a dashed-dotted grey line. 101

4.21 Comparison of the CS spectra computed with different models. Our "non-extended" LOC + MCMC approach (red spectrum in Figure 4.16) is plotted in a red solid line. The CS spectrum computed with the original pyRate chemical model fractional abundance profile (Sipilä et al. 2015) and the original velocity profile and v_{turb} = 0.075 km/s, is plotted in a grey dashed line. The spectrum computed with the original fractional abundance profile and the f_v and v_{turb} values found with our LOC + MCMC approach is plotted with a dotted grey line. Finally, the observations are plotted with a black solid line. 102

4.22 Comparison of the CS spectra computed with different models. Our "extended" LOC + MCMC approach (blue spectrum in Figure 4.16) is plotted in a blue solid line. The CS spectrum computed with the original pyRate chemical model fractional abundance profile (Sipilä et al. 2015) and the original velocity profile and v_{turb} = 0.075 km/s, is plotted in a grey dashed line. The spectrum computed with the original fractional abundance profile and the f_v and v_{turb} values found with our LOC + MCMC approach is plotted with a dotted grey line. Finally, the observations are plotted with a black solid line. 102

4.23 SO (2,3 - 1,2) observations in black and modelling results in red towards the L1544 dust peak. The corner plot of the parameter exploration corresponding to these results is shown in Figure 4.24. 103

4.24 Corner plot of the parameters used for the "non-extended" model displayed in Figure 4.23. 103

4.25 SO step fractional abundance profile obtained from the "non-extended" LOC + MCMC modelling of the observed line profile is plotted in logarithm scale in a solid red line over the fractional abundance profile obtained from the pyRate chemical model in Sipilä et al. (2015) in a dashed grey line. 104

4.26 Comparison of the SO spectra computed with different models. Our LOC + MCMC approach (Figure 4.23) is plotted in a red solid line. The SO spectrum computed with the original pyRate chemical model fractional abundance profile (Sipilä et al. 2015) and the original velocity profile and v_{turb} = 0.075 km/s is plotted in a grey dashed line. The spectrum computed with the original fractional abundance profile and the f_v and v_{turb} values found with our LOC + MCMC approach is plotted with a dotted grey line. Finally, the observations are plotted with a black solid line. . . . 104

5.1 Overlaid spectra of ortho-H_2O (1_{10} - 1_{01}) upscaled by a factor of 5 taken with Herschel in red (Caselli et al 2012) and HCO^+ (1-0) taken with the IRAM 30m telescope in black (Ferrer Asensio et al. 2024 in prep.) towards the dust peak of L1544. . . . 114

A.1 Spectrum of the $HC^{17}O^+$ (1 - 0) observation (black) and product of model with the upscaled by a factor of 16 fractional abundance profile at 5×10^5 yrs and modified to have 0 fractional abundance from 0 to 7000 au (red). . . . 119
A.2 Spectrum of the $HC^{17}O^+$ (1 - 0) observation (black) and product of model with an upscaled by a factor of 3 extended fractional abundance profile with A_v=4 at 5×10^5 yrs. . . . 119
A.3 Spectrum of the $HC^{17}O^+$ $J = 1$ - 0 at the dust peak of L1544 (black). The HFS fit was done with CLASS (blue). . . . 120

B.1 68 transitions of CHD_2CHO predicted to be the brightest, assuming a rotational temperature of 125 K. The red line indicates the predicted line intensities obtained by fitting the lines with the synthetic spectra, thereby constraining the column density. In each panel, the numbers on the upper left corner indicate the excitation temperature T_{ex} of the fitted transitions. An asterisk next to this number indicates situations where two lines from Table B.1 with similar values for E_u fall within 10 MHz of each other and are shown together in one panel. . . . 160
B.1 continued. . . . 161
B.1 continued. . . . 162

C.1 Corner plot for the CS + $C^{34}S$ "non-extended" model. . . . 167
C.2 CS (2-1) observations towards the L1544 dust peak in black and modelling results in red. . . . 167
C.3 $C^{34}S$ (2-1) observations towards the L1544 dust peak in black and modelling results in red. . . . 167
C.4 Corner plot for the CS + $C^{34}S$ "extended" model. . . . 168
C.5 CS (2-1) observations towards the L1544 dust peak in black and modelling results in a dash-dotted blue line. . . . 168
C.6 $C^{34}S$ (2-1) observations towards the L1544 dust peak in black and modelling results in a dash-dotted blue line. . . . 168
C.7 Corner plot of the parameters used for the SO + ^{34}SO "non-extended" model. . . . 169
C.8 SO (2,3 - 1,2) observations towards the L1544 dust peak in black and combined modelling results in red. . . . 170
C.9 ^{34}SO (2,3 - 1,2) observations towards the L1544 dust peak in black and combined modelling results in red. . . . 170
C.10 HCO^+ (1 - 0) observations towards the L1544 dust peak in black and "extended" modelling results in dash-dotted blue. . . . 172
C.11 Corner plot for the results displayed in Figure C.10. . . . 172

C.12 HCO^+ (1 - 0) observations towards the L1544 dust peak without the blue extended feature in black and "extended" modelling results in dash-dotted blue. 172
C.13 Corner plot for the results displayed in Figure C.12. 172
C.14 The model using the approach on Redaelli et al. (2022) is shown in a dash-dotted blue line. Observations towards the L1544 dust peak are shown in black. 173
C.15 Corner plot of the parameters used for the HCO^+ + $HC^{17}O^+$ "extended" model. . . 174
C.16 HCO^+ (1 - 0) observations towards the L1544 dust peak in black and combined modelling results in a dash-dotted blue line. 175
C.17 $HC^{17}O^+$ (1 - 0) observations towards the L1544 dust peak in black and combined modelling results in a dash-dotted blue line. 175
C.18 Corner plot of the parameters used for the HCO^+ + $HC^{17}O^+$ "extended" without the blue excess feature model. 176
C.19 HCO^+ (1 - 0) observations towards the L1544 dust peak in black and combined modelling results in a dash-dotted blue line. 176
C.20 $HC^{17}O^+$ (1 - 0) observations towards the L1544 dust peak in black and combined modelling results in a dash-dotted blue line. 176
C.21 H_2CO ($2_{1,2}$ - $1_{1,1}$) observations towards the L1544 dust peak are plotted in black, the "non-extended" modelling result is plotted in a solid red line, and the "extended" modelling result is plotted with a dash-dotted blue line. 178
C.22 Corner plot for the "non-extended" results displayed in Figure C.21. 178
C.23 Corner plot for the "extended" results displayed in Figure C.21. 178
C.24 The results of the c-C_3H_2 ($2_{1,2}$ - $1_{0,1}$) "non-extended" model are plotted with a solid red line, the "extended" model results are plotted with a blue dash-dotted line, and the observations towards the L1544 dust peak are plotted in black. 180
C.25 Corner plot for the "non-extended" model results displayed in Figure C.24. 180
C.26 Corner plot for the "extended" model results displayed in Figure C.24. 180

List of Tables

1.1 Types of rotors . . . 34
1.2 K_a and K_c selection rules . . . 36

2.1 Hyperfine transition frequencies measured in the laboratory (Dore et al. 2001a), upper energies of $HC^{17}O^+$(1-0) and relative intensities. . . . 52

3.1 Calculated molecular parameters . . . 73
3.2 Assigned transitions . . . 74
3.4 Spectroscopic parameters . . . 75
3.5 Partition functions ($Q_{\rm rot}$) of CHD_2CHO . . . 75

4.1 Observed Molecular Transitions . . . 85
4.2 $C^{34}S$ (2 - 1) best model parameters . . . 92
4.3 ^{34}SO (2,3-1,2) best model parameters . . . 95
4.4 $HC^{17}O^+$ (1-0) best model parameters . . . 97
4.5 CS (2 - 1) best "non-extended" model parameters . . . 99
4.6 CS (2 - 1) best "extended" model parameters . . . 99
4.7 SO (2,3 - 1,2) best model parameters . . . 103

A.1 Results of the CLASS HFS fit of the observed $HC^{17}O^+$(1 - 0) rotational transition towards L1544, treating the two peaks of each hyperfine line as separate velocity components. . . . 120
A.2 Derived column densities from HFS fitting. . . . 121
A.3 $HC^{17}O^+$ hyperfine collisional rate coefficients given in units of cm^3 s^{-1} for 10, 20, 30, 40, and 50 K. Transitions are labelled with the J, $F \rightarrow J^{'}$,$F^{'}$ quantum numbers, where the $J^{'}$ and $F^{'}$ quantum numbers refer to the final energy levels and J and F indicate initial energy levels. . . . 122
A.3 continued. . . . 123
A.3 continued. . . . 124
A.3 continued. . . . 125
A.3 continued. . . . 126
A.3 continued. . . . 127
A.3 continued. . . . 128

A.3 continued. . . . 129
A.3 continued. . . . 130
A.3 continued. . . . 131
A.3 continued. . . . 132
A.3 continued. . . . 133
A.4 $C^{17}O$ hyperfine collisonal rate coefficients given in units of cm^3 s^{-1} for 2, 5, 10, 20, 30, 40, and 50 K. Transitions are labelled with the J, $F \rightarrow J^{'}$,$F^{'}$ quantum numbers, where the $J^{'}$ and $F^{'}$ quantum numbers refer to the final energy levels and J and F indicate the initial energy levels. . . . 134
A.4 continued. . . . 135
A.4 continued. . . . 136
A.4 continued. . . . 137
A.4 continued. . . . 138
A.4 continued. . . . 139
A.4 continued. . . . 140
A.4 continued. . . . 141
A.4 continued. . . . 142
A.4 continued. . . . 143
A.4 continued. . . . 144
A.4 continued. . . . 145
A.4 continued. . . . 146
A.4 continued. . . . 147
A.4 continued. . . . 148
A.4 continued. . . . 149
A.4 continued. . . . 150
A.4 continued. . . . 151
A.4 continued. . . . 152
A.4 continued. . . . 153
A.4 continued. . . . 154
A.4 continued. . . . 155
A.4 continued. . . . 156
A.4 continued. . . . 157

B.1 Detected CHD_2CHO transitions towards IRAS 16293-2422. . . . 163

C.1 CS + $C^{34}S$ (2 - 1) best "non-extended" model parameters . . . 167
C.2 CS + $C^{34}S$ (2 - 1) best "extended" model parameters . . . 168
C.3 SO + ^{34}SO (2,3 - 1,2) combined "non-extended" model parameters. . . . 169
C.4 HCO^+ (1 - 0) "extended" model parameters. . . . 171
C.5 HCO^+ (1 - 0) without blue excess "extended" model parameters. . . . 171
C.6 HCO^+ + $HC^{17}O^+$ (1 - 0) best "extended" model parameters. . . . 174
C.7 HCO^+ + $HC^{17}O^+$ (1 - 0) best "extended" without the blue excess feature model parameters. . . . 176

C.8 H_2CO ($2_{1,2}$ - $1_{1,1}$) best "non-extended" model parameters 177
C.9 H_2CO ($2_{1,2}$ - $1_{1,1}$) best "extended" model parameters 177
C.10 c-C_3H_2 ($2_{1,2}$ - $1_{0,1}$) best "non-extended" model parameters 179
C.11 c-C_3H_2 ($2_{1,2}$ - $1_{0,1}$) best "extended" model parameters 179

Zusammenfassung

Diese Dissertation präsentiert Forschung zu den anfänglichen physikochemischen Bedingungen der Sternentstehung und dem Transfer von molekularer Komplexität. Diese Studien werden mit einem einzigartigen Ansatz durchgeführt, der Beobachtungs-, Modellierungs- und Laborverfahren kombiniert. Die Charakterisierung des frühesten Stadiums des Sternbildungsprozesses erfolgt durch Beobachtungen eines prästellaren Kerns und nutz eine Kombination aus Beobachtungen und der Modellierung des Strahlungstransfers. Darüber hinaus werden spektroskopische Messungen eines astrophysikalisch relevanten Moleküls im Labor durchgeführt, was die Erstellung eines genauen spektroskopischen Katalogs ermöglicht, der für die erste Detektion der molekularen Spezies im interstellaren Medium (ISM) verwendet wird.

Das erste in dieser Dissertation vorgestellte Projekt konzentriert sich auf molekulare Linienprofile, um die physikalische, chemische und kinematische Struktur des prästellaren Kerns L1544 zu verstehen. Um die beobachteten J = 1 - 0 Spektren des Moleküls $HC^{17}O^+$ mit hoher spektraler Auflösung und Sensitivität zu reproduzieren, wird eine Modellierung des Strahlungstransfers unter Berücksichtigung eines nicht-lokalen thermodynamischen Gleichgewichts (non-LTE) durchgeführt. Durch das Hochskalieren des Geschwindigkeitsprofils eines kontrahierenden Kernmodells konnte diese Spektrallinie mithilfe eines chemischen Modells reproduziert werden. Aufgrund der Kombination der kritischen Dichte des J = 1 - 0 Übergangs und der räumlichen Verteilung des Moleküls folgt der $HC^{17}O^+$ J = 1 - 0 Übergangs dem inneren Teil des Kerns, in dem die kontrahierende Geschwindigkeit höher ist als an den Rändern des Kerns. Andererseits folgt $C^{17}O$, eine optisch dünne Spektrallinie ohne Doppelpeakprofil, hauptsächlich den äußeren Teilen des Kerns, in denen das Gas sich langsamer bewegt. Die Tatsache, dass eine höhere Geschwindigkeit in Richtung des Zentrums des Kerns im Vergleich zur Geschwindigkeit des verwendeten physikalischen Modells erforderlich ist, um die Beobachtungen zu reproduzieren, könnte darauf hinweisen, dass L1544 weiter entwickelt ist als bisher angenommen.

Im zweiten Projekt habe ich die Rotationsspektren der doppelt deuterierten Form des astrophysikalisch relevanten Moleküls Acetaldehyd gemessen. Die Messungen wurden mit dem Chirped-Pulse Fourier Transform Spectrometer (CP-FTS) und einem hochauflösenden Absorptionsspektrometer durchgeführt. Die aufgezeichneten Spektrallinien wurden mit einem modifizierten Internal Axis Method (IAM)-Ansatz angepasst, der die Kopplung der internen Rotation mit der Gesamtrotation berücksichtigt. Aus diesen Ergebnissen habe ich einen genauen spektroskopischen Katalog für CHD_2CHO erstellt, den ich in der Cologne Database for Molecular Spectroscopy (CDMS) verfügbar gemacht habe. Mithilfe dieses Katalogs habe ich erstmals doppelt deuteriertes

Acetaldehyd im interstellaren Medium im Protosternsystem IRAS 16293-2422 in den Daten des ALMA Protostellar Interferometric Line Survey (PILS) nachgewiesen. Aus diesen Beobachtungen wurde ein Verhältnis der Säulendichte von doppelt zu einfach deuteriertem Acetaldehyd von 20% abgeleitet. Die Ähnlichkeit der D_2/D-Verhältnisse von Acetaldehyd und anderen komplexen organischen Molekülen (COMs) deutet auf eine gemeinsame Bildung dieser Moleküle hin, bei der die Deuteriumfraktionierung verstärkt ist, möglicherweise in der prästellaren Kernphase.

Schließlich werden im letzten Projekt molekulare Spektrallinien des prästellare Kerns L1544 mit hoher Sensibilität und spektraler Auflösung mit einer eindimensionalen non-LTE Strahlungstransfermodellierung analysiert, um die physikalische, chemische und kinematische Struktur des Kerns weiter zu präzisieren. Dabei ist die eindimensionale non-LTE Strahlungstransfermodellierung mit der Markov-Chain-Monte-Carlo (MCMC)-Methode gekoppelt, um die physikalischen und chemischen Parameter zu ermitteln, die die beobachteten Spektrallinien von HCO^+, CS, $C^{34}S$, H_2CO, $c-C_3H_2$, SO und ^{34}SO am besten reproduzieren. Dieser Ansatz führt bei optisch dünnen Übergängen zu besser bestimmten Parametern als bei optisch dicken Übergängen. Alle beobachteten Übergänge folgen unterschiedlichen Teilen des Kerns und unterstreichen die nicht-homogene Struktur von L1544. Diese Ergebnisse weisen auf die Notwendigkeit von dreidimensionaler Modellierung hin, um Beobachtungen molekulare Spektrallinien besser interpretieren zu können. Darüber hinaus werden die relativen Häufigkeitsprofile der untersuchten Moleküle, berechnet mit chemischen Modellen, mit den einfachen Stufenprofilen verglichen, die in dieser Arbeit hergeleitet werden. Dies wird verwendet, um die relativen Häufigkeitsprofile der untersuchten Moleküle in Richtung L1544 zu präzisieren.

Abstract

This thesis presents the research carried out on the initial physicochemical conditions of star formation and the journey of Complex Organic Molecules (COMs). These studies are tackled with a unique approach by combining observational, modelling and laboratory techniques. The characterisation of the earliest stage of the star formation process, via observations of a prestellar core, is done using a combination of observations and radiative transfer modelling. In addition, spectroscopic measurements of an astrophysically relevant molecule in the laboratory are carried out, allowing for the production of an accurate spectroscopic catalogue used for the first detection of the molecular species towards the Interstellar Medium (ISM).

The first project presented in this thesis focuses on molecular line profiles to understand the physical, chemical and kinematic structure of the prestellar core L1544. Non-Local Thermodynamic Equilibrium (non-LTE) radiative transfer modelling is performed to reproduce the $HC^{17}O^+$ J = 1 - 0 spectra observed with high spectral resolution and high sensitivity. This line is well-fitted with a contracting core model alongside a chemical model by upscaling the velocity profile. Due to a combination of the critical density of the transition and the spatial distribution of the molecule the $HC^{17}O^+$ J = 1 - 0 transition traces the inner part of the core where the contracting velocity is higher than on the edges of the core. On the other hand, $C^{17}O$, an optically thin transition that does not present the double-peak line profile, traces mostly the outer parts of the core where the gas moves slower. The fact that a higher velocity towards the centre of the core, compared to the velocity of the physical model used, is needed to reproduce the observations may indicate that L1544 is more evolved than previously thought.

In the second project, I measure the rotational spectra of the doubly-deuterated form of the astrophysically relevant molecule acetaldehyde. The measurements are carried out with the Chirped-Pulse Fourier Transform Spectrometer (CP-FTS) alongside the CAS Absorption Cell (CASAC) Experiment. The recorded transitions are fitted with a modified Internal Axis Method (IAM) approach which takes into account the coupling of the internal rotation with the overall rotation of the molecule. From these results, I build an accurate spectroscopic catalogue for CHD_2CHO that I make available in The Cologne Database for Molecular Spectroscopy (CDMS). With this catalogue, I detect doubly deuterated acetaldehyde for the first time in the ISM towards the protostellar system IRAS 16293-2422 in the ALMA Protostellar Interferometric Line Survey (PILS) data. From these observations, a doubly- over singly-deuterated column density ratio of 20% for acetaldehyde is retrieved. The similarity of the D_2/D ratios of acetaldehyde and other COMs indicates a common formation for these molecules where deuterium fractionation is enhanced, possibly the prestellar core stage.

Finally, in the last project, high-sensitivity and high-spectral resolution molecular line observations towards the pre-stellar core L1544 are analysed to constrain further the physical, chemical and kinematic structure of the core. The 1D non-LTE radiative transfer modelling software is coupled to the Markov Chain Monte Carlo (MCMC) method to explore the physical and chemical parameters that result in the best fit of the HCO^+, CS, $C^{34}S$, H_2CO, c$-C_3H_2$, SO, and ^{34}SO observed transitions. This fitting approach results in better-constrained parameters for the modelling of optically thin transitions w.r.t. optically thick transitions. All of the observed transitions trace different parts of the core, highlighting the non-homogeneous structure of L1544. These results point to the need for 3D radiative transfer modeling, to better interpret molecular line observations. Moreover, with the objective of constraining molecular fractional abundance profiles towards L1544, the molecular fractional abundance profiles computed with chemical models are compared to the simple step fractional abundance profiles obtained in this project.

1

Introduction

Astrochemistry enables us to unravel the intricacies of the Universe across past, present and future through molecules, ultimately bridging the micro and macroscopic realms.

1.1 Astrochemistry

The content of this Section is mostly based on the book "Introduction to Astrochemistry" (Yamamoto 2016).

Before the onset of radioastronomy the Interstellar Medium (ISM) was considered rather empty. The first molecular observations towards the ISM changed this perspective. The first molecule observed in space was CN (McKellar 1940), then observations of CH and CH^+ (Douglas & Herzberg 1941) followed. Diatomic molecules were thought to be the largest species present in space due to the relatively low density and temperature conditions of the ISM compared to Earth, but then detections of NH_3 (Cheung et al. 1968) and H_2O (Cheung et al. 1969) challenged this limit. In the present day, around 300 molecules [1] have been detected towards the interstellar medium with sizes up to 70 atoms (C_{70}; Cami et al. 2010).

Molecules play a key role in the Universe, from shaping its structure to the emergence of life. The elements from which molecules are built up have different origins depending on their atomic mass. Hydrogen (H), Helium (He), and Lithium (Li) were formed during the Big Bang. Atoms heavier than Lithium up to Iron (Fe) are formed by nucleosynthesis in the interior of stars. Finally, elements heavier than Fe are synthesized in the explosion of supernovas. In the early Universe, right after the recombination era, where the nuclei and electrons recombined to give neutral atoms, the first molecules H_2, HD and LiH were formed. The appearance of these molecules allowed for the cooling of the gas required for structure formation in the ISM (Galli & Palla 1998). In the current Universe, interstellar Complex Organic Molecules (COMs), molecules with six or more atoms with at least one carbon, are ubiquitous in the ISM. Even amino acids, the building blocks of life, have been detected towards small Solar System bodies (Altwegg et al. 2019; Naraoka et al. 2023), suggesting the emergence of life on Earth could have been aided by the exogenic delivery of organic material by comets.

There is a great variety of molecules arising from a unique chemistry driven by the gradient of conditions in the ISM. Temperatures in the ISM can range from 10 to 10^5 K and volume densities can range from 10^{-3} to 10^7 cm^{-3}. In broad terms, reactivity in the ISM is separated into gas-phase and surface processes. From observed molecular abundances, the consensus is that considering both gas-phase and surface processes is necessary to explain the formation of molecules on the ISM. The relevance of gas-phase and surface formation processes depends on the nature of the molecule as well as on the physical conditions of the environment. COMs formation is thought to start in the icy mantles (mainly composed of H_2O, CO, CO_2 and NH_3) of dust grains where simple molecules are subject to H and O addition reactions. Some of these newly formed molecules can desorb into the gas phase by thermal or non-thermal processes, where they further react through gas-phase reactions to give higher complexity COMs. Moreover, molecules in the grains can be photo-dissociated by cosmic-ray-induced UV photons, creating radicals. When temperatures increase to values of 20-30 K, these radicals can then diffuse on the surface and react with each other.

Astrochemistry is the discipline that studies the chemical composition and reactivity in the ISM and uses molecules to study the physical, kinematic and chemical structure and evolution of the Universe. Detecting molecules in space and deriving their abundances is possible thanks to

[1] https://cdms.astro.uni-koeln.de/classic/molecules

the combined efforts of different fields of study and techniques. Figure 1.1 schematically presents these techniques and some of their contributions. The unambiguous detection of a molecule in the ISM relies on the knowledge of the rest frequencies and relative intensities of its transitions. This information, enclosed in spectroscopic catalogues, is obtained from measurements in the laboratory. Then, these molecules can be detected by comparing spectroscopic catalogues with observations taken with a telescope. Finally, the coupling of modelling techniques with theory can help interpret observations and make predictions (Figure 1.1).

In this Thesis, I use Observational (Section 1.3), Modelling (Section 1.4) and Laboratory (Section 1.5) techniques to deepen the knowledge of the initial conditions of the star formation process.

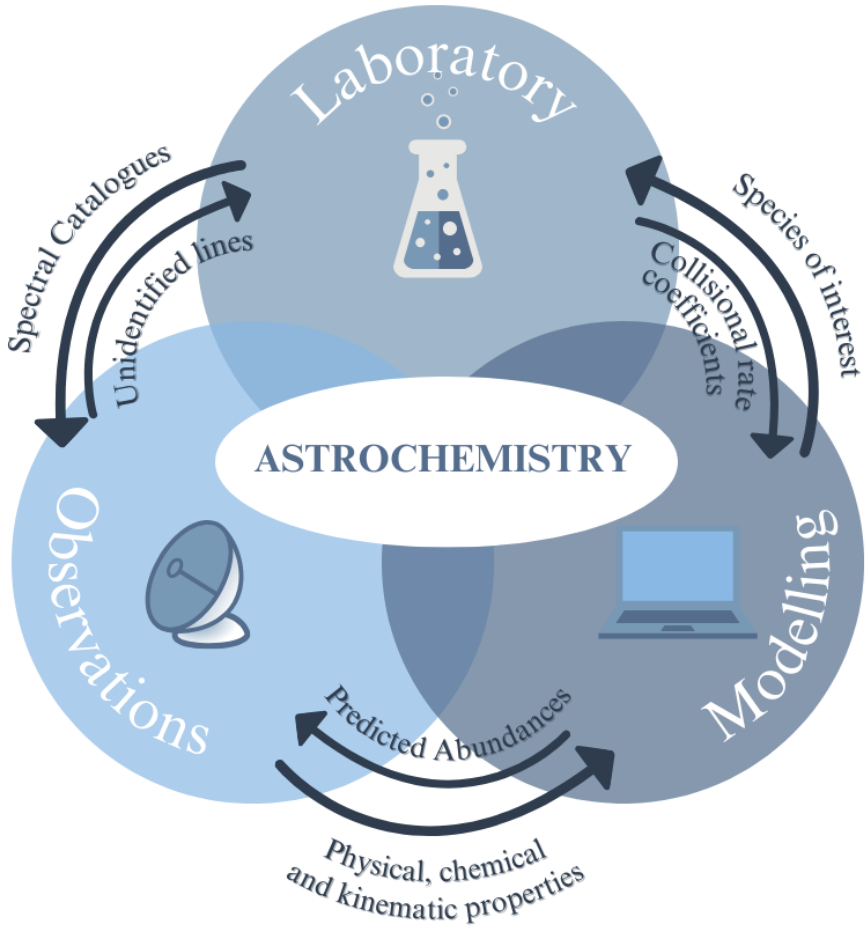

Figure 1.1: Graphic of the techniques used for the research in the field of Astrochemistry and some of their contributions.

1.1.1 Astrochemical processes

The content of this Section is mostly based on the book "Introduction to Astrochemistry" (Yamamoto 2016).

The presence of molecules and their abundance depend on the physical conditions of the environment. For the purpose of this Thesis, I introduce in this Subsection the chemistry relevant to molecular clouds. Molecular clouds are dense interstellar clouds constituted mostly of molecular hydrogen H_2, and are the birthplaces of stars (see Section 1.2). As introduced in Section 1.1, both gas-phase and solid-state reactions contribute to the molecular inventory observed towards molecular clouds.

Gas-phase reactions

Due to the relatively low densities in interstellar clouds, binary reactions represent the majority of reactions. Due to the lack of a third body to discard the excess reaction energy, reactions need to stabilize the products through different mechanisms. For example, the A + B → C + D type of reactions allow for the excess reaction energy to be dissipated in the form of kinetic energy of the products moving in opposite directions. Reactions resulting in a single product can occur by emitting a photon, providing stabilization. Additionally, due to the cold temperatures ($\sim$ 10 K) in these clouds, reactions requiring input energy do not take place. Even exothermic reactions may not occur if they have a higher activation energy barrier than the thermal energy of the reactants.

Relevant gas-phase chemical reactions in molecular clouds include ion-molecule reactions, neutral-neutral reactions, radiative association, dissociative electron recombination, photodissociation and photoionization.

Ion-molecule reactions

Ions are prevalent in the ISM due to the presence of the Interstellar Radiation Field (ISRF) as well as Cosmic Rays (CR), which ionize molecules. Upon the meeting of an ion and a neutral molecule, the electric field of the ion polarizes the molecule, resulting in an induced dipole moment in the latter. Because of this, an electrostatic attractive force appears, making the ion and molecule overcome possible activation energy barriers due to the long-range attractive force and react. Ion-molecule reactions can proceed even faster if the neutral molecule has a permanent dipole moment.

Some examples of exothermic ion-molecule reactions include the formation of two key species for ISM reactivity (H_3^+ and CH_2^+):

$$H_2^+ + H_2 \rightarrow H_3^+ + H \tag{1.1}$$

$$CH^+ + H_2 \rightarrow CH_2^+ + H. \tag{1.2}$$

Neutral-Neutral reactions

Interactions between neutral species can also occur. Neutral-neutral reactions are classified into dipole-dipole interactions, dipole-induced dipole interactions and dispersion-forces interactions. If the two molecules involved in the reaction have permanent dipole moments, they interact via dipole-dipole interactions. The interaction between a molecule that has a permanent dipole moment and a molecule that does not is regarded as dipole-induced dipole interaction. In this case, the permanent dipole moment of one of the molecules induces a dipole moment on the second one, causing the attraction of the two. Finally, neutral species can interact through the effects of dispersion forces, which arise due to temporary fluctuations in the electron distribution around molecules. This happens when an instantaneous dipole moment in a molecule is created when electrons move asymmetrically with respect to the nuclei, and then this instantaneous dipole moment induces a dipole moment on the other molecule.

Neutral-neutral reactions can present reaction barriers. As the interaction potential is weak and short-ranged, the energy contained in the two-species collision is small and may not be sufficient for the reaction to proceed. Radical-radical reactions, a sub-type of neutral-neutral reactions, do not have activation barriers as the unpaired electrons can directly form bonds.

An example of a neutral-neutral reaction is one of the formation reactions of the second-most abundant molecule in the ISM, CO:

$$CH + O \rightarrow CO + H. \tag{1.3}$$

Radiative association

The excess energy of a reaction needs to be dissipated in order for the products to survive. In reactions with an unimolecular product, the excess energy can be dissipated through the emission of a photon. Let us consider the following reaction mechanism:

$$A + B \rightleftharpoons AB^* \rightarrow AB + h\nu \tag{1.4}$$

where AB^* is an intermediate complex. The excess energy for the reaction is stored in the form of bond vibrational energy. When a molecule has no lower vibrational energy levels it can relax to, the bond breaks, resulting in the dissociation of the AB^* complex back into the reactants. For larger molecules, there are more available low-energy vibrational energy levels. Thus, some molecules can relax into a lower vibrational state, emitting a photon and preventing dissociation. An example of a radiative association reaction is:

$$CH_3^+ + HCN \rightarrow CH_3CNH^+ + h\nu. \tag{1.5}$$

Dissociative electron recombination

A molecular ion can recombine with an electron and dissociate into two or more products:

$$A^+ + e^- \rightarrow B + C. \tag{1.6}$$

The recombination of the ion and the electron first results in an excited neutral molecule. If the energy of the neutral molecule is not dissipated, it leads to fragmentation into products.

Photodissociation and Photoionization

The exposure of molecules to the UV radiation from the ISRF can cause them to dissociate and ionize. These processes are most effective in low column density environments and, therefore, will be significant on the outer layers of molecular clouds. Nevertheless, UV radiation can also be induced from cosmic ray ionization. Cosmic rays can penetrate into into the densest parts of molecular clouds where UV radiation is shielded. CR can ionize H_2, resulting in energetic electrons which can excite H_2 molecules, resulting in fluorescent UV radiation emission.

Surface reactions

It has been seen that solid-state chemistry on the surface of interstellar grains needs to be taken into consideration alongside gas-phase chemistry to explained observed molecular abundances. Many observed molecular abundances towards the ISM are larger that the predicted when just taking into account gas-phase reactions. Interstellar dust grains are comprised of a core of non-volatile silicate and carbonaceous compounds surrounded by an ice mantle, which can present a variety of compositions. The typical dust core size in molecular clouds is 0.1 μm. Because atoms and molecules can adsorb into dust grains, chemical species can meet, react and use the dust grain as a third body to release excess energy from reactions, preventing dissociation. Consequently, the presence of dust grains boosts chemical diversity in the ISM. For example, surface reactions are responsible for the formation of the most abundant molecule in the ISM, molecular hydrogen, H_2 (Hollenbach & Salpeter 1971), as well as some COMs (e.g. CH_3OH, Wirström et al. 2011).

Atoms and molecules adsorb onto the surface of grains through physisorption and chemisorption processes. Physisorption includes adsorption by van der Waals forces and electrostatic forces. On the other hand, chemisorption occurs when species form chemical bonds with the grain surface. As molecular bonds are involved, chemisorption binds molecules to grains in a stronger way compared to physisorption. Species in the ice mantles of dust grains can also desorb back into the gas phase by different processes such as thermal desorption, chemical desorption, shock heating, sputtering and cosmic-ray-induced desorption.

Grain-surface chemistry can be further categorised into diffusive and non-diffusive. The amount of diffusion an adsorbed chemical species can undergo depends on their nature as well as the nature of the surface. The species present in the grain surface are adsorbed in local potential minima called "sites". If a molecule is formed on the surface next to a reactive species, these can react as they do not need to overcome a diffusion energy barrier. On the other hand, if the reactants are spatially separated, they need to diffuse to meet and react. In Figure 1.2, I am presenting the so-called Langmuir-Hinshelwood mechanism where a reactant (left dark blue circle) lands on the surface of a grain, diffuses, meets with another reactant (light blue circle), reacts, and desorbs from the surface of the grain.

Diffusion energy is the energy required for molecules to diffuse through the surface or, in other words, to hop over potential barriers (Hasegawa et al. 1992). The mobility of these atoms

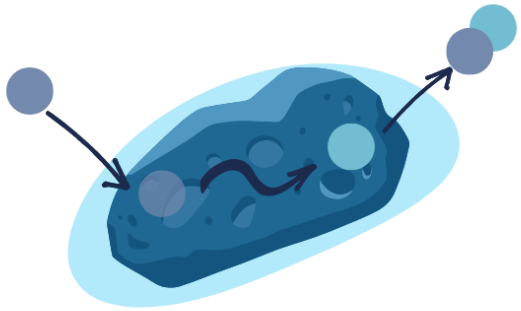

Figure 1.2: Scheme of the Langmuir-Hinshelwood Mechanism. A species in dark blue (left) adsorbs into an interstellar dust grain covered in ice. This species then diffuses to meet another species present in the ice (light blue) to react and desorb (right).

and molecules on the surface is key for reactivity. The higher the temperature, the easier it is to overcome diffusion barriers. For light species such as atomic hydrogen, quantum effects can be important, making these able to tunnel these barriers even at T $\sim$ 10 K. As a consequence, one of the most important surface reactions in the coldest regions within molecular clouds is hydrogenation.

Surface reactivity can be studied through the detection of molecules released into the gas phase with mm and sub-mm astronomy or by directly probing the vibrational modes of the molecules in the dust grains' ice mantles through mid-IR.

Deuterium Fractionation

The enrichment of interstellar molecules with deuterium, deuterium fractionation, is an important process happening in the densest and coldest substructures of molecular clouds, dense cores (see Ssection 1.2).

The hydrogen isotope deuterium, D, is mostly formed right after the Big Bang and consumed in the interiors of stars. The abundance of deuterium w.r.t. hydrogen is constant at fixed distances from the Galactic Centre ($D/H_{local\ ISM} \sim 10^{-5}$; Linsky 2003). Nevertheless, local enhancements of deuterium are observed in molecules. This is due to deuterium fractionation, which involves the enrichment of interstellar molecules with deuterium.

Deuterium fractionation is a consequence of multiple thermodynamic and kinetic factors. Heavier isotopes make stronger bonds due to their lower zero point energy (ZPE) compared to lighter isotopes.

Regarding kinetics, the reaction rates of isotopically substituted molecules are different from the rates of the main isotopologues. The magnitude of this effect can be assessed with the following

equation:

$$\frac{k_m}{k_i} = \sqrt{\frac{A_i}{A_m}} \tag{1.7}$$

where k_m and k_i correspond to reaction rates for a main isotopologue and the isotopically substituted species, respectively, and A_m and A_i correspond to the atomic masses of the main isotopologue and the rarer isotopologue. The larger the k_m/k_i ratio, the larger the kinetic isotope effect. By substituting the atomic masses of hydrogen and deuterium in Equation 1.7, a factor of 1.41 is obtained. If Equation 1.7 is applied to ^{32}S and ^{34}S, a value of 1.03 is obtained. The results for hydrogen and sulfur demonstrate that kinetic isotope effects are greater for a larger relative mass between isotopes.

In dense cores, the main gas-phase deuteration agent H_2D^+ is formed from the H_3^+ isotope exchange reaction with HD, as such:

$$H_3^+ + HD \rightleftharpoons H_2D^+ + H_2. \tag{1.8}$$

The backward reaction is endothermic with a value depending on the nuclear spin state of H_2. The H_2 ortho-to-para ratio (OPR) is important in the deuterium fractionation process. Ortho-H_2 has higher internal energy than para-H_2, which can help overcome the energy barrier of the backward reaction. Nevertheless, the OPR in dense cores has been observed to be below the statistical value of 3 (Kahane et al. 1984). Thus, in dense cores, the backward reaction does not occur, enhancing the H_2D^+/H_3^+ ratio. Moreover, this ratio is also enhanced due to the freeze-out of CO, the main destroyer of H_2D^+,

$$H_2D^+ + CO \rightarrow HCO^+ + H_2. \tag{1.9}$$

Thus, due to the depletion of CO, deuterium fractionation is further enhanced in the coldest, deepest regions of dense cores.

The H_2D^+ molecule transfers its deuterium atom to other molecules:

$$H_2D^+ + X \rightarrow DX^+ + H_2 \tag{1.10}$$

where X symbolises a molecule.

Besides H_2D^+, HD_2^+ and D_3^+ can also react with other molecules to transfer deuterium, resulting in a further enhancement of the molecular deuterium fractionation, including multi-deuterated species. The doubly- and triply-deuterated H_3^+ are formed by reactions with HD in extreme low-temperature conditions ($T \lesssim 10$ K).

A higher H_2D^+ abundance in the gas phase translates into a higher D/H atomic abundance on the surface of grains as deuterium atoms are released from the dissociative recombination of the deuterated forms of H_3^+. Therefore, H-D substitution reactions on the surface of grains have also been suggested as an effective deuteration mechanism in dense cores.

As a consequence of the evolution of some dense cores (see Section 1.2), the increasing material condensation in their centre causes the temperatures to decrease progressively, enhancing deuterium fractionation with time. At later stages, where most of the CO is frozen out, the

$[H_2D^+]/[H_3^+]$ ratio can even reach unity. Thus, deuterium fractionation can be used as an evolution tracer of molecular cores (Ceccarelli et al. 2014; van Gelder et al. 2022).

1.2 Low-mass star formation

The content of this Section is mostly based on the book "The Formation of Stars" (Stahler & Palla 2004).

Stars are a core constituent of the universe due to their key role in nucleosynthesis as well as feedback for the interstellar pressure. The characteristics and evolution of these objects are, for the most part, determined at the moment of their formation. Stars can be classified, amongst other characteristics, by their mass. Stars that are $\leq 2M_{\odot}$ ($M_{\odot} = 1.989 \times 10^{30}$ kg), like the Sun, are called low-mass stars. Stars that are between $2 < M_{\odot} < 8$ are intermediate-mass stars. Lastly, stars with $\geq 8M_{\odot}$ are called high-mass stars. The star formation process for low- and intermediate-mass stars differs from the process for high-mass stars. In this Thesis, I focus on the early stages of low-mass star formation.

Stars constitute 90% of the baryonic mass of the Milky Way. The 10% left accounts for the interstellar matter. Interstellar matter is present in the form of gas and dust. The mass ratio of gas to dust in the solar neighbourhood is ∼100. This interstellar matter is not uniformly distributed but organised in filamentary structures called clouds (André et al. 2014; Pineda et al. 2023). Depending on the physical and chemical properties of the gas, we differentiate between different ISM phases: Hot Ionized Medium (HIM), Warm Neutral Medium (WNM), Warm Ionized Medium (WIM), Cold Neutral Medium (CNM), also known as diffuse clouds, and Molecular Clouds (Figure 1.3). Due to the high densities of molecular clouds with respect to other ISM phases, most of the hydrogen is present in its molecular form H_2. Due to its high column densities, H_2 shields itself from the interstellar radiation field, preventing its dissociation on the inner parts of molecular clouds. Because of this shielding, other molecules can also survive photodissociation, making these clouds molecule-rich.

The ISM phases that lie on the constant-pressure blue dashed line in Figure 1.3 are in pressure equilibrium. The densest structures within Molecular Clouds are not in pressure equilibrium because they self-gravitate and, therefore, can collapse, leading to star formation. Figure 1.4 presents an artistic impression of the star formation cycle, which I will summarize in the next paragraphs.

Starless cores are highly compact structures within Molecular Clouds. They have typical sizes of around 10^4 au, they are centrally concentrated (Ward-Thompson et al. 1999), with volume densities larger than 10^5 cm^{-3} (Crapsi et al. 2005; Keto & Caselli 2008) and temperatures lower than 7 K (Crapsi et al. 2007) in the centre.

Highly centrally-concentrated ($n_{H_2} > 10^5$ cm^{-3}) starless cores that present contraction motions are called pre-stellar cores. Pre-stellar cores will eventually form a protostar. Due to their evolutionary state, pre-stellar cores are good sources to study the initial stages of star formation. However, because of their short lifetimes (of the order of $\sim 10^5$ yrs), these sources are rare, and consequently, their sample size is limited.

The gradient of physical properties within pre-stellar cores results in differentiated chemical layers in these objects. In the inner parts of the core, where the density is high ($n_{H_2} > 10^5$ cm^{-3}), and the temperatures are extremely low ($\sim$ 5 K), most atoms heavier than He are locked in molecules onto dust grains resulting in thick ice mantles. Due to the freeze-out of CO and the

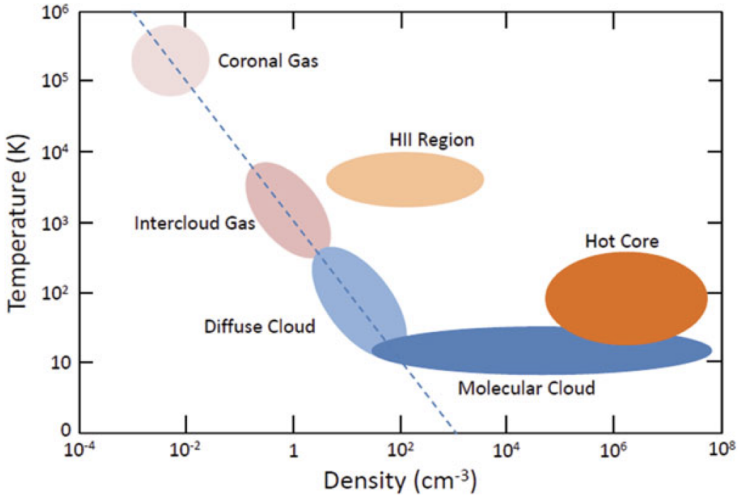

Figure 1.3: Temperature-density diagram of the ISM phases. The dashed blue line corresponds to constant pressure. Taken from Yamamoto (2016).

low temperatures in this region, deuteration is enhanced (see Section 1.2.1 for further details). The layer surrounding the centre is characterised by an increased number of molecular (including COMs) detections on the gas phase. The abundance and complexity of COMs detected have been related to the age of the core, being more evolved sources richer in COMs. Finally, the outermost layer in pre-stellar cores is less dense and rich in COMs, as many are being dissociated by the interstellar radiation field. In the outer parts of pre-stellar cores, UV radiation can penetrate, ionize and photodissociate. In contrast, in the centre, only cosmic rays can penetrate and ionize.

Core contraction occurs when the equilibrium between the gravitational force, the thermal pressure is disturbed. The physical requirements for collapse are determined through comparison with the Jean's mass (M_J). M_J is the minimum mass a core needs to have to collapse if it is kept in equilibrium by thermal energy only:

$$M_J = \left(\frac{3}{4\pi m}\right)^{\frac{1}{2}} \left(\frac{5k}{Gm}\right)^{\frac{3}{2}} T^{\frac{3}{2}} n^{-\frac{1}{2}} \tag{1.11}$$

where m is the mass of the gas that constitutes the cloud, G is the gravitational constant, T is the temperature of the core, and n is the volume density of the core. Taking into consideration the Jean's mass, two regimes for a pre-stellar core (with mass M_{psc}) can be set. In the supercritical regime $M_{psc} > M_J$, self-gravity overcomes pressure. On the other hand, in the subcritical $M_{psc} < M_J$ regime, gravitational collapse does not take place.

The observed star formation efficiency is lower than expected if the collapse of pre-stellar cores were solely thermally supported. This suggests that mechanisms other than thermal support regulate the collapse of pre-stellar cores. While turbulence has been observed to offer support on larger scales, it is not as important on the core scale. On these smaller scales, magnetic fields are seen to play a key role. Magnetic fields regulate the contraction of pre-stellar cores through ambipolar diffusion. The ions present in the gas phase couple with the magnetic field. The friction

between the frozen ions and neutrals in the gas slows the contraction. The collapse is thought to proceed in an inside-out fashion described in Shu (1977). The first stage is characterized by a release of the potential energy of the contraction due to efficient cooling mechanisms. One of these mechanisms involves dust grains absorbing and re-radiating the excess energy. Another cooling mechanism happens via molecular collisions and the subsequent decay from their excited states, releasing energy. As the density increases, the central clump gets dense enough to get opaque to its infrared cooling radiation, and as a consequence, the core starts to heat up. Alongside the temperature, the value of the Jean's mass also rises, halting the contraction and forming an equilibrium structure named the first core. The temperature continues to rise until it reaches the H_2 dissociation energy ($\sim 5\times10^4$ K). Molecular hydrogen adsorbs this thermal energy dissociating. Because of this the balance between thermal and gravitational forces is disrupted triggering the second collapse and the birth of the protostellar object (middle right in Figure 1.4).

The material surrounding the central protostar starts accreting onto it. Due to the non-spherical accretion, a flattened infalling envelope and a protostellar disk form around the protostar. The disk is crucial for delivering materials to the protostar. Simultaneously, an outflow is launched from the protostar, perpendicular to the protostellar disk. The outflow, consisting of an inner ionized jet and an outer molecular outflow, results from the interplay between magnetic fields and gas dynamics. This interplay is key in extracting angular momentum from the accreting material. Around the protostar, a high-density, compact ($\sim$ 100 au) and warm ($\sim$ 100 K) structure, named circumstellar disk, can arise. Objects that have accumulated less than half of their final mass and are still deeply embedded in their envelope are categorized as Class 0 sources. The Class 0 stage lasts approximately 10^5 yrs.

The later stages of the star formation process are summarized below to complete the picture of the star formation cycle. As the protostellar system continues to evolve, the dust in the disk starts to coagulate, igniting the formation of planets. On the Class I stage (bottom right in Figure 1.4), the material accretion onto the central protostar continues, and the outflows are less collimated than for Class 0. In the Class II stage (bottom left in Figure 1.4), the envelope has cleared out, and the protostar starts to burn deuterium in its interior. In Class III (middle left in Figure 1.4), the disk clears out, revealing planets and leftover material such as meteorites and asteroids. In this stage, the star, named T Tauri star, contracts, making its way to the Main Sequence stage, where it will burn hydrogen and remain for most of its life.

This Thesis focuses on the initial conditions of the star formation process, including the pre-stellar core and Class 0 stages. The two astronomical sources I have focused on in this Thesis, the pre-stellar core L1544 and the Class 0 protostellar object IRAS 16293 -2422, are presented in Sections 1.2.1 and 1.2.2, respectively.

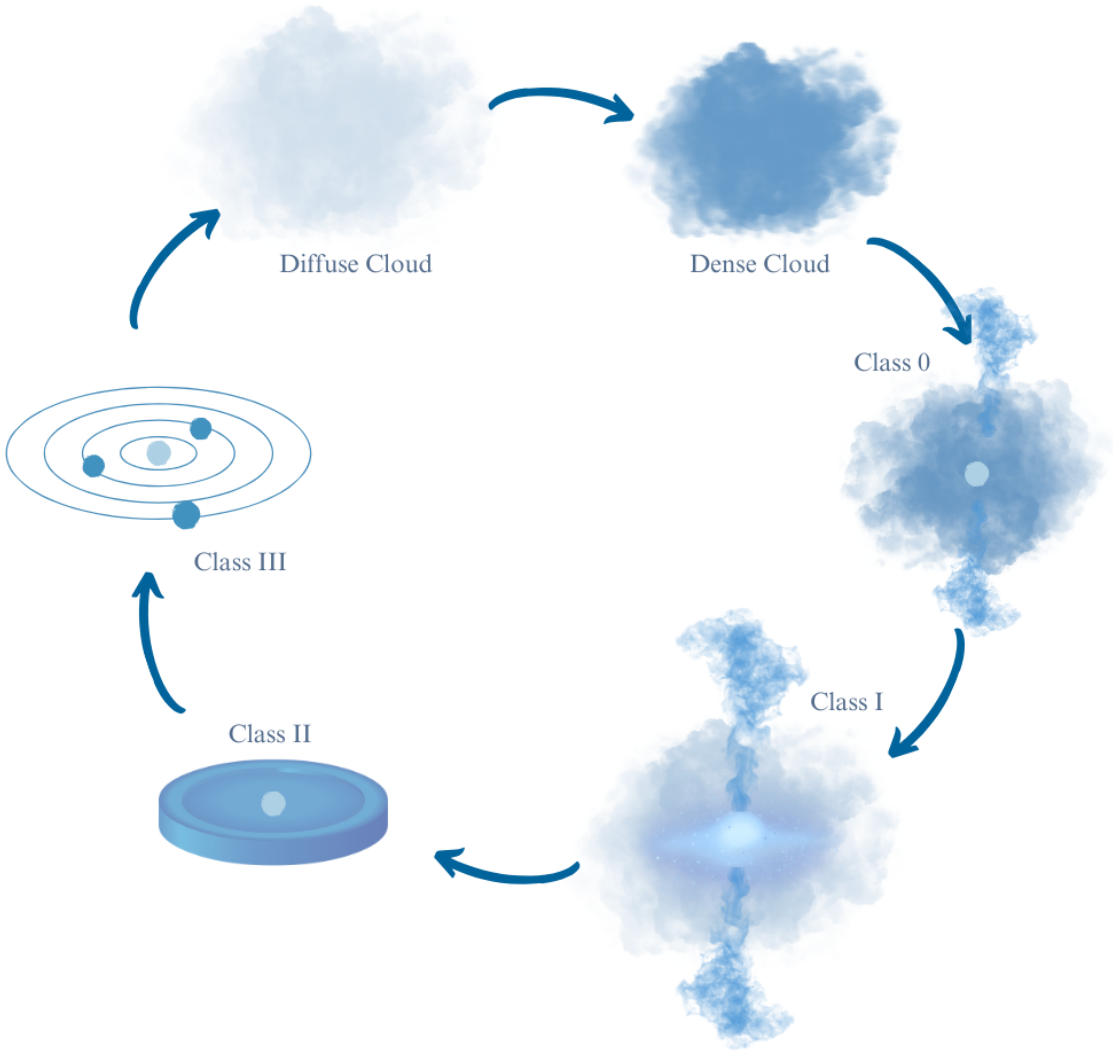

Figure 1.4: Artistic impression of star formation cycle. A diffuse cloud (top left) condensates, resulting in a dense cloud (top right). Upon contraction of the core, a protostar is formed. The gas and dust start accreting into the central protostar, generating feedback such as outflows (middle right, Class 0). The accretion onto the central protostar continues, and the outflows become less collimated (bottom right, Class I). At some point, the envelope clears out, revealing the disk (bottom left, Class II). In the next stage, the disk clears out, revealing the planets in the solar system (middle left, Class III). Finally, the star dies, resulting in a supernova explosion, which scatters the material back into the ISM, where it will be available for new star formation.

1.2.1 L1544

L1544 is a pre-stellar core located in the Taurus molecular cloud at 170 pc distance (Galli et al. 2019). Figure 1.5 shows a multi-wavelength *Herschel* image of the Taurus molecular cloud with L1544 highlighted on the edge of the cloud.

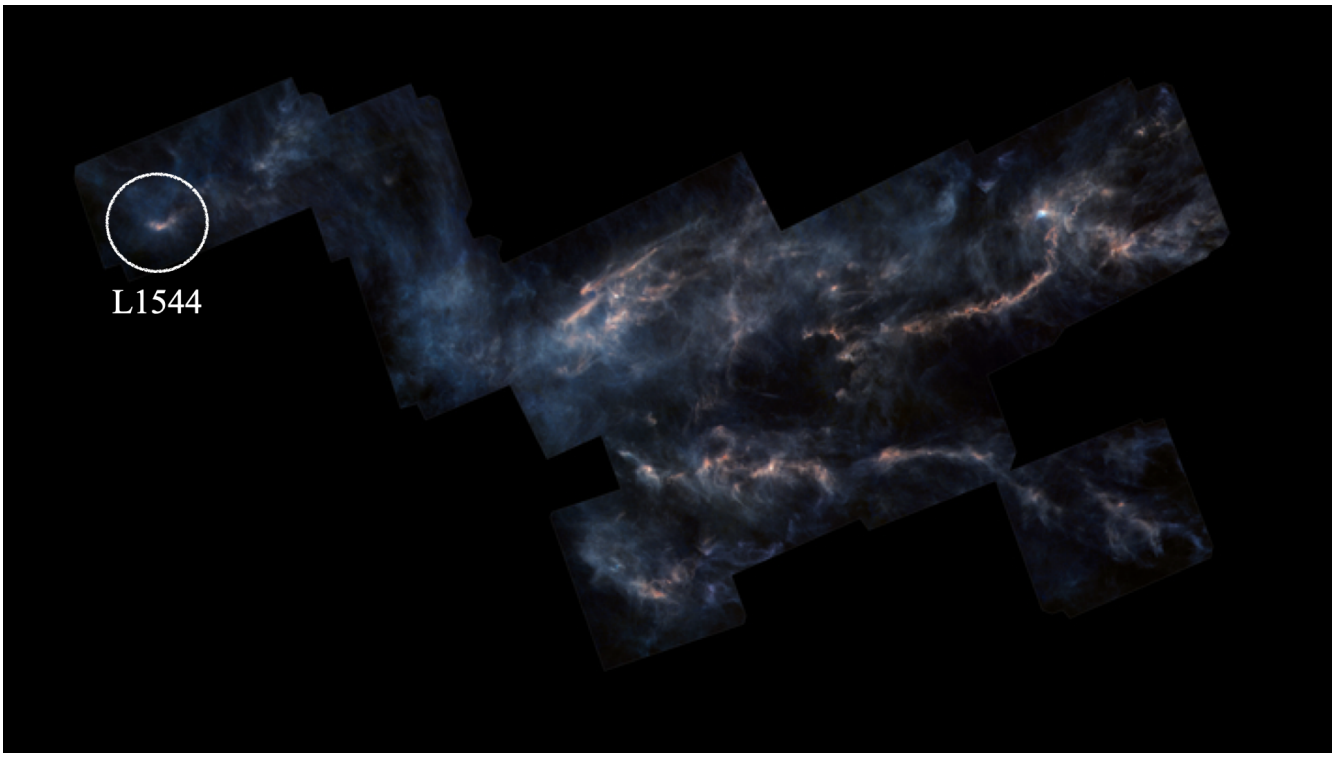

Figure 1.5: *Herschel* four-colour image of the Taurus Molecular Cloud (160 μm, blue; 250 μm, green, 350 μm, green + red and 500 μm, red). The pre-stellar L1544 is seen as the orange spot inside the white circle on the top left of this image. Credit: ESA/Herschel/NASA/JPL-Caltech, R. Hurt.

Contraction motions (Crapsi et al. 2005; Redaelli et al. 2022) and high deuteration levels (Crapsi et al. 2005; Redaelli et al. 2019) have been observed towards L1544. Example of highly-deuterated molecules, w.r.t. the local ISM D/H ratio $\sim 10^{-5}$; Linsky 2003, include $[N_2D^+]/[N_2H^+] = 0.2$, $[DCO^+]/[HCO^+] = 0.04$, [c-C_3HD]/[c-C_3H_2] = 0.12 - 0.17 and [HDCS]/[H_2CS] = 0.3 Caselli et al. (2002b); Spezzano et al. (2013, 2022). It is characterised by a high molecular hydrogen volume density ($n \sim 10^7$ cm^{-3}) and low temperatures ($T \sim 7$ K) at the centre (Crapsi et al. 2007; Keto et al. 2015). These conditions give rise to a "complete depletion zone" within the $\simeq$ 1800 au radius where 99.9% of the species heavier than He are frozen out onto dust grains (Caselli et al. 2022). Moreover, it is a chemically rich pre-stellar core which exhibits spatial chemical differentiation (Spezzano et al. 2017; Redaelli et al. 2019; Chacón-Tanarro et al. 2019; Jensen et al. 2023). This distinct spatial distribution of molecules is partly attributed to an uneven illumination of the core on the south, coinciding with the edge of the Taurus Molecular Cloud (Figure 1.5). The interstellar

radiation field causes the molecules in this area to dissociate. The location of this core on the edge of the Taurus Molecular Cloud makes its study simpler as protostellar feedback, present in other parts of this cloud, does not need to be considered (Figure 1.5).

Even though we have an idea of how the star formation process starts, many crucial details remain to be clarified. To better understand the first stages of star formation, I deepen the research on the physical, kinematic and chemical structure of the pre-stellar L1544 core in Chapters 2 and 4 through the study of molecular lines.

1.2.2 IRAS 16293-2422

IRAS 16293-2422 is a widely studied Class 0 triple (A1, A2 and B) protostellar system located in the ρ-Ophiuchus molecular cloud at a distance of $\sim$ 120 pc (Knude & Hog 1998; Lombardi et al. 2008; Loinard et al. 2008; Maureira et al. 2022). Figure 1.6 shows an ALMA image of the IRAS 16293-2422 source. The A and B protostars have a separation of $\sim$ 800 AU (Mundy et al. 1992). Each protostar has a circumstellar disk of $\sim$ 50 au, and is embedded in a low-density envelope (Jørgensen et al. 2005). IRAS 16293-2422 presents a complex quadrupole outflow system featuring a collimated pair of lobes aligned in the NE-SW direction and another set of less collimated lobes in the E-W direction.

This source has increased interest in the scientific community due to its chemical richness. Many COMs have been observed towards it, including many first detections (e.g. glycolaldehyde, Jørgensen et al. 2012). Moreover, components A and B present chemical differentiation. Components A1 and A2 are more rich in nitrogen-bearing molecules than component B. In contrast, some oxygen-bearing molecules like acetaldehyde (CH_3CHO) are seen mostly towards component B (Bisschop et al. 2008; Jørgensen et al. 2011). Furthermore, molecular emission towards A appears brighter than towards B.

The observed chemical inventory towards Class 0 objects differs from the one towards pre-stellar cores due to the different physical conditions of these objects. The main factor that plays a role in Class 0 stage chemistry is the increase in temperature mostly due to accretion into the central protostar. The increase in temperature results in the desorption of molecules trapped in the icy mantles of dust grains. The released species can further react, changing the composition and abundances of the gas phase. Moreover, with the increased temperature, some reactions with a moderate activation energy can proceed. The mobility of radicals on the surface of grains is also enhanced, increasing the production of COMs.

Amongst all the COMs observed towards IRAS 16293 - 2422, those of particular interest for this Thesis are the deuterated forms of COMs. In recent years, the number of detected singly-, doubly- and triply-deuterated molecules in the ISM has increased (e.g. Parise et al. 2002, 2004; Spezzano et al. 2013; Turner 1990; Manigand et al. 2019; Butner et al. 2007; Richard et al. 2021). Nowadays, the detection of multi-deuterated molecules has become more attainable due to the high spatial-resolution observations that facilities like the Atacama Large Millimeter/submillimeter Array (ALMA) provide (more on ALMA in Section 1.3.4). Surprisingly, the abundance of doubly-deuterated molecules w.r.t. the singly-deuterated isotopologues is higher than that of the singly-deuterated ones w.r.t. the main isotopologues. The average observed COMs D_2/D ratios in IRAS 16293-2422 is of 20%, (methyl formate, 22%, Manigand et al. 2019; dimethylether, 15-20%, Richard et al. 2021 and methanol, 25%, Drozdovskaya et al. 2022).

As mentioned in Section 1.2.1, multi-deuterated COMs formation is only efficient at extremely low temperatures, for example, in pre-stellar cores. In these objects, deuterated molecules are thought to be trapped into ice mantles of grains, alongside other COMs, and released into the gas phase in the Class 0 stage. It is difficult to observe deuterated COMs towards pre-stellar cores as these molecules are mainly trapped on the icy mantles of interstellar grains. Therefore, in a number of cases, deuterium fractionation is studied indirectly in the pre-stellar core stage through observations towards Class 0 objects.

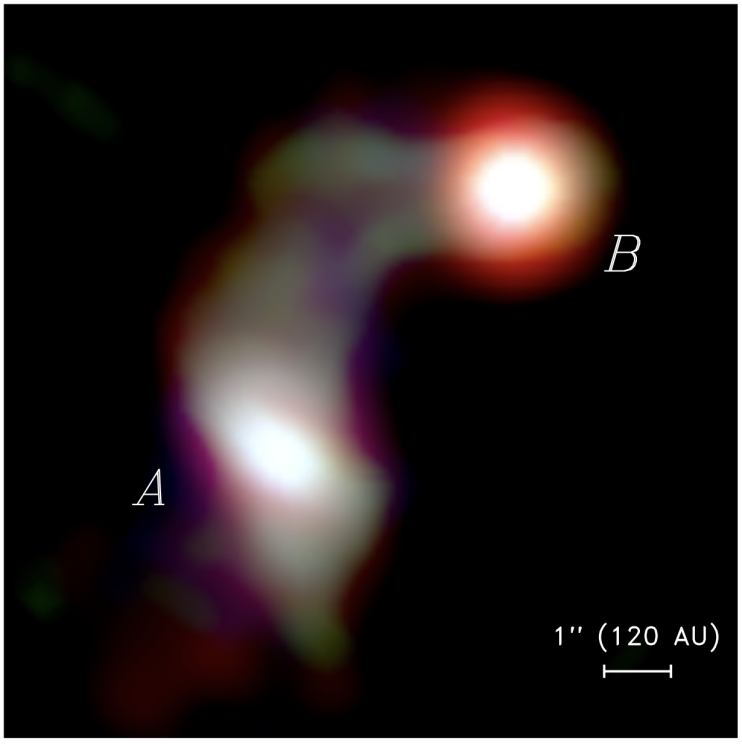

Figure 1.6: Three-color ALMA image of the IRAS 16293-2422 protostellar system. The red, green and blue colours indicate the continuum emission at 3.0 mm, 1.3 mm and 0.87 mm. The A1 and A2 protostars are located in the southeast (labelled with "A" as they are unresolved in this image), and the B protostar is marked with the "B" label in the northwest of this image. This Figure is taken from Jørgensen et al. (2016).

The similar D_2/D ratios for the COMs observed towards IRAS16293-2422 point to a common origin. Since the pre-stellar environment is ideal for enhanced deuteration, this could indicate that molecular complexity starts early in the star and planet formation process and it is at least partially inherited at later stages of the star formation process.

With the aim of further assessing the COMs inheritance scenario on the early stages of star formation, I observe a doubly-deuterated COM towards the protostellar system IRAS 16293-2422 stage and compare its D_2/D ratio with the ones found for other COMs in Chapter 3.

1.3 Observations

The content of this Section is mostly based on the book "Introduction to Astrochemistry" (Yamamoto 2016) and Physics of the Interstellar and Intergalactic Medium (Draine 2011).

In this section, I introduce theoretical concepts needed for the understanding, acquiring and processing of astronomical observations for the study of the initial conditions of star formation, such as the interaction of molecules with radiation (Section 1.3.1), the transfer of radiation through the ISM (Section 1.3.2), the derivation of information from molecular lines (Sections 1.3.2 and 1.3.3) and the collection and processing of this radiation by telescopes (Section 1.3.4).

1.3.1 Level population

The presence of molecules in the ISM is inferred from the spectra collected with telescopes, as introduced in Section 1.1. The changes in energy a molecule undergoes, called transitions, are quantised and, therefore, can be seen as increases or decreases of the radiation received in the form of lines. The energy level population of the molecule determines which transitions are observed and how intense they are. The level population of a molecule, determined by the number of molecules in the different energy states, can be inferred by solving its statistical equilibrium equations.

Transitions between a molecule's energy states can happen through radiative and collisional processes. With the goal of describing such processes as well as deriving the statistical equilibrium equations, we are going to consider, from this point onwards, a molecule with two energy levels: l being the lower and u being the upper.

A molecule can spontaneously decay from the upper to the lower level. The rate of spontaneous radiative deexcitation is defined by the Einstein coefficient A_{ul} (left in Figure 1.7). Decay can also be induced by an external radiation field. In this case, the rate for stimulated radiative deexcitation is written as $B_{ul} \int_0^\infty J_\nu \phi_{ul}(\nu) d\nu$ (middle in Figure 1.7). An external radiation field can also cause the spontaneous absorption of a photon, exciting the molecule from the lower to the upper state. The radiative excitation rate is defined as $B_{lu} \int_0^\infty J_\nu \phi_{lu}(\nu) d\nu$ (right in Figure 1.7). In the expressions for stimulated radiative deexcitation as well as for radiative excitation, J_ν corresponds to the specific intensity at a frequency ν of the external radiation field and $\phi_{ul}(\nu)$ and $\phi_{lu}(\nu)$ are the line profiles (see Section 1.3.3).

Moreover, molecular excitation and deexcitation transitions can also happen as a result of particle collisions. The rate coefficients for collisional excitation and deexcitation are expressed by C_{lu} and C_{ul}, respectively.

When a molecular system is in a state of equilibrium, the rate of the processes populating and depopulating a state are equal. By taking into account both radiative and collisional processes, we can write:

$$n_l C_{lu} + n_l B l u \int_0^\infty J_\nu \phi_{lu}(\nu) d\nu = n_u C_{ul} + n_u B u l \int_0^\infty J_\nu \phi_{ul}(\nu) d\nu + n_u A_{ul} \tag{1.12}$$

where n_l corresponds to the number of molecules in the lower level l and n_u corresponds to the number of molecules in the upper level u. Thus, the left-hand side of Equation 1.12 represents the

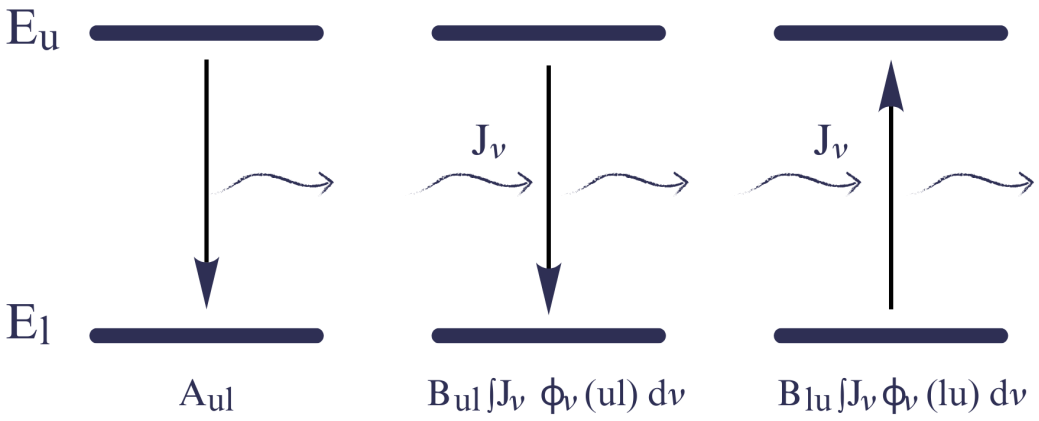

Figure 1.7: Scheme of the radiative spontaneous deexcitation, stimulated deexcitation and excitation (from left to right, respectively) for a two-level system characterised by a lower level with energy E_l and an upper level with energy E_u. Wavy arrows represent photons.

rate of populating processes, and the right-hand side represents the rate coefficients of depopulating processes.

To derive the relationship amongst the Einstein's coefficients, the collisional contribution to the statistical equilibrium equation is ignored. Moreover, the line profile function is normalised, $\int \phi_{lu}(\nu)\ \mathrm{d}\nu = \int \phi_{ul}(\nu)\mathrm{d}\nu = 1$. With these approximation Equation 1.12 results in:

$$n_l B_{lu} J_\nu \phi_{lu}(\nu) = n_u (B_{ul} J_\nu \phi_{ul}(\nu) + A_{ul}). \tag{1.13}$$

The population ratio of the upper and lower levels in thermal equilibrium is described by the Boltzmann distribution:

$$\frac{n_u}{n_l} = \frac{g_u}{g_l} e^{-\frac{h\nu}{kT_{ex}}} \tag{1.14}$$

where g_u and g_l correspond to the upper and lower level degeneracies, respectively, h is the Planck constant, k is the Boltzmann constant and T_{ex} is the excitation temperature of the system.

By substituting Equation 1.14 in Equation 1.13 we obtain:

$$J_\nu = \frac{A_{ul}/B_{ul}}{\frac{g_l}{g_u}\frac{B_{lu}}{B_{ul}} e^{\frac{h\nu}{kT_{ex}}} - 1}. \tag{1.15}$$

Moreover, if the external radiation field is assumed to be a blackbody, its intensity can be described by the Planck Function $B_\nu(T)$ as :

$$B_\nu(T) = \frac{2h\nu^3}{c^2}[e^{\frac{h\nu}{kT_{ex}}} - 1]^{-1}. \tag{1.16}$$

By substituting Equation 1.16 into Equation 1.15, one obtains:

$$A_{ul} = \frac{2h\nu^3}{c^2}B_{ul}, \tag{1.17}$$

$$g_l B_{lu} = g_u B_{ul}. \tag{1.18}$$

Note that the Einstein coefficients are independent of T_{ex} and, therefore, are intrinsic properties of the system. Furthermore, as they are all related, we can describe the state of the system with just one of these coefficients.

When taking only radiative transitions into account, we can estimate the typical lifetime of a state (the time before it spontaneously decays) using the Einstein A_{ul} coefficient as $t_u = A_{ul}^{-1}$. The higher energy of the upper state is, the shorter their lifetime ($A_{ul} \propto \nu_{ul}^3$).

We introduce the concept of optical depth τ_ν as $d\tau_\nu{=}\alpha_\nu dx$. Taking into account collisional induced transitions in an optically thin medium ($\tau_\nu << 1$) from Equations 1.12, 1.17 and 1.18, taking into account the collisional excitation and deexcitation rates follow a Boltzmann distribution:

$$\frac{C_{lu}}{C_{ul}} = \frac{g_u}{g_l}e^{-\frac{h\nu}{kT_k}} \tag{1.19}$$

where T_k is the kinetic temperature of the gas, and the external radiation field is the Cosmic Microwave Background (CMB; $T_b = 2.73$ K), the statistical equilibrium equation can be written as:

$$\frac{n_u g_l}{n_l g_u} = \frac{A_{ul}\{e^{(\frac{h\nu}{kT_b})} - 1\}^{-1} + C_{ul}e^{(-\frac{h\nu}{kT_k})}}{A_{ul}e^{(-\frac{h\nu}{kT_b})}\{e^{(\frac{h\nu}{kT_b})} - 1\}^{-1} + C_{ul}}. \tag{1.20}$$

The collisional deexcitation rate C_{ul} is related to the molecular hydrogen volume density n_{H_2} as $C_{ul} = n_{H_2}\ \sigma < v >$, where σ is the cross section for collisional de-excitation and $\langle v\langle$ is the mean relative velocity between the molecule and the H_2 molecule. Depending on the H_2 density of the medium, radiative processes, collisional processes, or the combination of both contribute to the level populations of a molecule. From Equation 1.20, we can infer the expression for the level populations in the two limiting cases of radiative-dominated (Equation 1.21) or collisionally-dominated (Equation 1.22) systems:

$$n_{H_2}C_{ul} << A_{ul} \rightarrow \frac{n_u g_l}{n_l g_u} \cong exp(-\frac{h\nu}{kT_b}) \tag{1.21}$$

$$n_{H_2}C_{ul} >> A_{ul} \rightarrow \frac{n_u g_l}{n_l g_u} \cong exp(-\frac{h\nu}{kT_k}). \tag{1.22}$$

In the case where spontaneous radiative deexcitation dominates (Equation 1.21), the excitation temperature of the transition (T_{ex}) equals the background temperature, T_b. In this case, level

populations deviate from a Boltzmann distribution and the system is said to be in non-LTE. In the case collisional deexcitation dominates, the excitation temperature of the transition, T_{ex}, equals the kinetic temperature, T_k. The level populations the are described by the Boltzmann distribution and the system is said to be in LTE.

For emission to be observed, a temperature higher than that of T_b is required. The equations above imply that the upper level needs to be adequately populated through collisions to generate strong emissions. This requires the equality A_{ul}=C_{ul}. This equality introduces the concept of critical density (n_{crit}), which works as a limit between the collisional deexcitation and the spontaneous radiative decay-dominated regime:

$$n_{crit} = \frac{A_{ul}}{\sigma < v >}. \tag{1.23}$$

If the volume density of a region is larger than the critical density ($n_{H_2} > n_{crit}$), the decay of a specific transition will be dominated by collisional deexcitation. If the volume density of the region is lower than the critical density ($n_{H_2} < n_{crit}$), the decay of the specific transition will be dominated by spontaneous radiative decay. The critical density is a useful approximation to predict whether a certain molecular transition will be observed in emission in a specific source.

In pre-stellar cores, there is a great range of molecular hydrogen volume densities (ranging from 10^7 cm^{-3}, at the centre, and 10^2 cm^{-3}, at the edge). Because of this, the level populations of a molecule may follow an LTE or a non-LTE treatment depending on which region within the pre-stellar core they emit from. For example, the $HC^{17}O^+$ J= 1 - 0 transition has a $n_{crit} \sim 10^5$ cm^{-3}, and therefore will only emit in the inner parts of a pre-stellar core where n_{H_2} is higher. In contrast, the CO J= 1 - 0 transition has a $n_{crit} \sim 10^3$ cm^{-3} making it emit from a larger radius in the pre-stellar core compared to $HC^{17}O^+$ (Chapter 2).

1.3.2 Radiative transfer

The content of this Section is mostly based on the book "Introduction to Astrochemistry" (Yamamoto 2016) and "Formalism for the CASSIS software" by Charlotte Vastel [2].

Before reaching the Earth, the radiation emitted, absorbed or scattered by a molecule in a pre-stellar core needs to propagate through the ISM. The change in intensity of electromagnetic radiation propagating through an emitting and absorbing gas for a specific frequency, dI_ν, and pathlength, dx, can be expressed as:

$$\frac{dI_\nu}{dx} = -\alpha_\nu I_\nu + j_\nu. \tag{1.24}$$

The first term in Equation 1.24 corresponds to the fraction of the initial radiation absorbed by the medium. The second term accounts for the emitted radiation by the medium. Thus, α_ν and j_ν are the absorption coefficient and the emissivity, respectively. In the approximation of the two-level system, they can be expressed as:

$$\alpha_\nu = n_l \sigma_{l\rightarrow u}(\nu)[1 - e^{-\frac{h\nu}{kT_{ex}}}] \tag{1.25}$$

and

$$j_\nu = \frac{1}{4\pi} n_u A_{ul} h\nu \phi_\nu \tag{1.26}$$

where n_l and n_u correspond to the lower and upper-level population, $\sigma_{lu}(\nu)$ corresponds to the absorption cross section at the frequency ν, T_{ex} is the excitation temperature and ϕ_ν is the line profile.

By introducing the source function $S_\nu = j_\nu/\alpha_\nu$, we can rewrite equation 1.24 as:

$$\frac{dI_\nu}{d\tau_\nu} = -I_\nu + S_\nu. \tag{1.27}$$

Assuming that the medium is uniform (S_ν = ct.), that the level population of the molecule is defined by T_{ex} and that the radiation field corresponds to a blackbody radiation field, $I_\nu = B_\nu(T_{ex})$, we can derive Kirchhoff's law:

$$S_\nu = B_\nu(T_{ex}). \tag{1.28}$$

Moreover, we can express the background radiation intensity $I_\nu(0)$ as a blackbody radiation at a certain background temperature (T_b) and write the radiative transfer equation as:

$$I_\nu(\tau_\nu) = B_\nu(T_{ex}) + e^{-\tau_\nu}[B_\nu(T_b) - B_\nu(T_{ex})]. \tag{1.29}$$

From this equation, we can explore the behaviour of radiation for different optical depth regimes:

- Optically thin medium ($\tau_\nu << 1$) and negligible background radiation ($B_\nu(T_b) = 0$):

  $I_\nu(\tau_\nu) = \mathrm{B}_\nu\ (T_{ex})\tau_\nu$

[2] https://cassis.irap.omp.eu/docs/RadiativeTransfer.pdf

- Optically thin medium (τ_ν <<1) and non-negligible background radiation ($B_\nu(T_b) \neq 0$):
  $B_\nu(T_b) < B_\nu(T_{ex}) \rightarrow$ Emission line
  $B_\nu(T_b) > B_\nu(T_{ex}) \rightarrow$ Absorption line
- Optically thick medium (τ_ν >>1) and negligible background radiation ($B_\nu(T_b) = 0$):
  $I_\nu(\tau_\nu) = B_\nu(T_{ex})$.

Moreover, expressing the intensity in terms of the temperature at which a blackbody emits most of that intensity, and tking into account that in observations, the source and a close position with no emission are alternatively observed:

$$J_\nu(T) = \frac{c^2}{2k\nu^2}\Delta I_\nu(T), \tag{1.30}$$

we obtain:

$$T = [J_\nu(T_{ex}) - J_\nu(T_b)](1 - e^{(-\tau_\nu)}), \tag{1.31}$$

where T is the spectral line intensity in Kelvin units and J_ν(T) is the equivalent Rayleigh-Jeans temperature (J_ν(T) = $(h\nu/k) \times (\mathrm{e}^{h\nu/kT}\text{-}1)^{-1}$).

The intensity of an observed molecular line (Equation 1.31) is a key element for the study of the physical, chemical and kinematic conditions of an astronomical source. It is related to the number of molecules that emit, and therefore, we can connect the ΔT with the molecular column density, N. Molecular column densities refer to the number of molecules in the line of sight (cm^{-2}). By dividing molecular column densities by molecular hydrogen column densities, we obtain molecular fractional abundances, which tell us information about the chemistry and, indirectly, the physics of the source we are observing.

With the aim of deriving the relationship between the line intensity and the column density, the molecular column density of the upper level is expressed as:

$$N_u = \int n_u ds, \tag{1.32}$$

where ds is the pathlength on the line of sight.

The relationship between the upper-level column density of the molecule, N_u, and the optical depth of a molecular line can be written as:

$$N_u = \frac{3h}{8\pi^3|\mu_{lu}|^2}[e^{\frac{h\nu}{kT_{ex}}} - 1]^{-1} \int \tau_\nu d\nu, \tag{1.33}$$

where $|\mu_{lu}|^2$ is the dipole matrix of a particular transition. N_u is linked to the total column density of the molecule, N_{TOT}, through:

$$N_{TOT} = N_u \frac{Q_{rot}}{g_u} e^{(\frac{E_u}{kT_{ex}})}, \tag{1.34}$$

where Q_{rot} is the rotational partition function, $Q_{rot} = \sum_i \mathrm{g}_i \mathrm{e}^{\frac{E_i}{kT}}$, where i represents the energy levels of the molecule. By combining Equations 1.33 and 1.34 we obtain:

$$N_{TOT} = \frac{3h}{8\pi^3|\mu_{lu}|^2}\frac{Q_{rot}}{g_u}e^{(\frac{E_u}{kT_{ex}})} \times [e^{\frac{h\nu}{kT_{ex}}} - 1]^{-1} \int \tau_\nu d\nu. \tag{1.35}$$

In the optically thin case, Equation 1.31 becomes $T = \tau_\nu$ [$J_\nu(T_{ex})$-$J_\nu(T_b)$], and Equation 1.35 can be re-written as:

$$N_{TOT} = \frac{3h}{8\pi^3|\mu_{lu}|^2}\frac{Q_{rot}}{g_u}e^{(\frac{E_u}{kT_{ex}})} \times [e^{\frac{h\nu}{kT_{ex}}} - 1]^{-1} \frac{1}{[J_\nu(T_{ex}) - J_\nu(T_b)]} \int T d\nu. \tag{1.36}$$

1.3.3 Spectral Line Broadening

Lines are not infinitely thin. Multiple processes can contribute to spectral line broadening in the ISM, including the kinematics, temperature and turbulence of the gas.

Intrinsic Line Profile

The intrinsic line profile comes from the energy uncertainties of the levels involved in the transition and, more specifically, from the Heisenberg uncertainty principle $\Delta E \Delta t \geq \hbar$. Then, the energy uncertainty of the upper level is $\Delta E_u \geq \hbar/\tau_u$ where τ_u is the lifetime of the upper level. This line profile is described by a Lorentz profile ϕ_ν:

$$\phi_\nu = \frac{4\gamma_{ul}}{16\pi^2(\nu - \nu_{ul}^2) + \gamma_{ul}^2}, \tag{1.37}$$

where l and u refer to the lower and upper levels respectively, $\gamma_{ul} = \Delta\nu \times 2\pi$, where $\Delta\nu$ is the full-width half maximum (FWHM) of the line.

Doppler Broadening

Doppler broadening results from the motions of molecules. One case of Doppler broadening is caused by the thermal motion of the molecules (thermal broadening, $\Delta\nu_{thermal}$). Due to the intrinsic velocity of the molecules, their emitted radiation is red or blue-shifted with respect to the line centre, ν_0, making the line appear broader. Another type of Doppler broadening is caused by the random motions of molecules due to the presence of turbulence (turbulence broadening, $\Delta\nu_{turb}$).

The probability a molecule in the gas phase at a temperature T has a velocity v, taking into account the Maxwell-Boltzmann gas velocity distribution, is proportional to $e^{-mv^2/2kT}$. Therefore, the FWHM is:

$$\Delta\nu = \frac{\nu}{c}\sqrt{\frac{2kT}{m}ln2}. \tag{1.38}$$

The thermal and turbulent widths of molecular lines can be extracted from the line profile and tell us about the thermal and kinematic information of the emitting gas, which are key properties to understanding the nature and evolution of an astronomical source.

1.3.4 Radio astronomy

In order to analyse molecular lines and retrieve information on their column densities and turbulent and thermal widths, the radiation coming from the ISM needs to be collected and processed by a telescope. Before the radiation reaches ground telescopes, it has one last obstacle to overcome: the terrestrial atmosphere. Molecules present in the atmosphere, such as H_2O, CO_2, and O_3, absorb, emit and scatter specific radio wavelengths. The transmittance pattern of radio waves through the atmosphere results in regions of the frequency range where radiation is completely absorbed and others where the radiation fully reaches the telescopes, known as "atmospheric windows". Placing telescopes in high-altitude, dry environments increases the atmospheric transparency of radio waves as the effect of the atmosphere in these places is minimal.

The radiation that reaches the telescope is collected by a parabolic antenna. The parabolic shape of the antenna is required for an adequate directivity of the radio waves. The reflection of the radiation in the antenna creates a particular power spectrum named beam pattern. This beam pattern presents higher power values in a certain angle range. This area is called the main lobe or main beam. Smaller power profiles around the main lobe are called side lobes, which appear due to diffraction on the edges of the main dish. Figure 1.8 depicts a typical antenna beam pattern. The fraction of power observed in the main beam w.r.t. the total power collected by the telescope is defined as the Main Beam Efficiency (η_{MB}):

$$\eta_{MB} = \frac{\Omega_{MB}}{\Omega_A} \tag{1.39}$$

where Ω_{MB} and Ω_A are the solid angles of the Main Beam and the antenna, respectively. The Main Beam Efficiency allows us to take into account the radiation loss as a consequence of the antenna reflection pattern and, therefore, is important to not underestimate molecular line intensities.

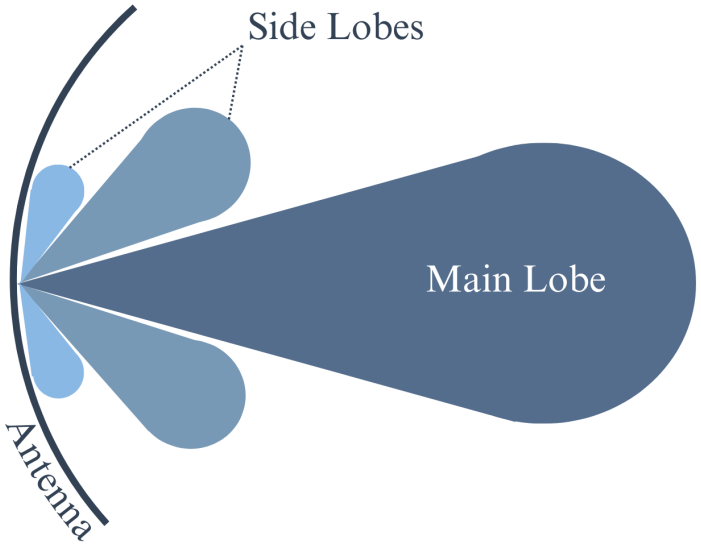

Figure 1.8: Schematics of the beam pattern. The main lobe is found in the horizontal plane in dark blue, and the side lobes are drawn around the main lobe in light blue shades.

Once the radiation is collected by the antenna, it is directed to the receiver.

Front-end receivers convert electromagnetic waves from free space to guided components and down-convert them to lower frequencies. The main frontend systems used are High Electron Mobility Transistors (HEMT) and Microwave Monolithic Integrated Circuits (MMIC) ($\nu < 150$ GHz), Superconducting Mixers (SIS) ($72 < \nu < 800$ GHz) and Hot Electron Bolometers (HEB) ($\nu > 900$ GHz).

The radiation is then directed to the backend. Backends mainly extract information on the continuum, spectra and polarization of the radiation. The backends of interest of this Thesis are spectrometers which allow the retrieval of the molecular spectra from the received radiation. High-frequency resolution is required for spectral features coming from cold, dense and low-turbulence environments to be resolved. The more resolved the molecular lines are, the more accurate the parameters derived from them will be.

An important feature of telescopes is their angular resolution, θ. The angular resolution of the observations corresponds to the minimum angle in the sky in which two objects can be discerned as separate. Thus, the greater the angular resolution, the smaller the spatial regions that will be resolved. The angular resolution depends on the diameter of the telescope antenna D and the wavelength of the observations λ as:

$$\theta = \frac{k\lambda}{D} \tag{1.40}$$

where k is a constant driven by the illumination pattern of the telescope. However, there exists an upper limit to the size of a telescope that can be built. In order to observe with higher angular resolution, we must then rely on interferometry. Interferometry is a technique that combines and analyzes the signals from multiple separate telescopes.

The choice between single-dish telescopes and interferometers depends on the nature of the research as well as the nature of the source observed. Below, the two observational facilities used in this Thesis, the Institute de Radioastronomie Millimétrique 30 m (IRAM 30m) single-dish telescope and the Atacama Large Millimeter and sub-millimeter Array (ALMA) interferometer, are described.

Institute de Radioastronomie Millimétrique 30 m telescope (IRAM 30m)

This subsection focuses on the IRAM 30m telescope (Figure 1.9) used for the observations towards the pre-stellar core L1544 presented in this Thesis (Chapters 2 and 4). For the study of the overall structure of nearby pre-stellar cores (with typical sizes of $\sim 10^4$ au), the spatial resolutions of single-dish telescopes ($\gtrsim$ 10 - 20") are sufficient.

Figure 1.9: Picture of the IRAM 30m Telescope antenna.

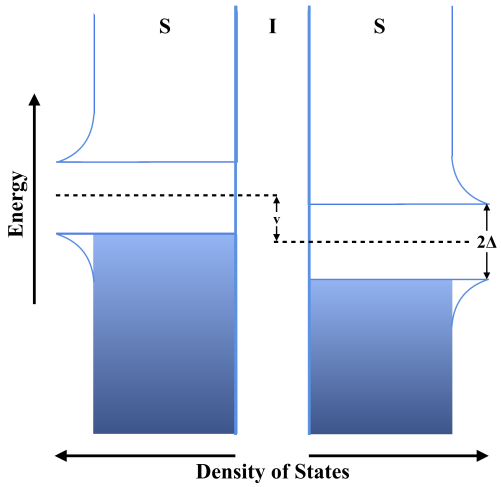

Figure 1.10: Superconducting mixer (SIS) diagram. The superconducting layers are denoted with "S", while the insulating layer is denoted with "I". The blue segments represent the filled bands. 2Δ indicates the gap between the filled and empty bands.

The IRAM 30m frontend used in this Thesis is the Eight MIxer Reciever (EMIR). EMIR operates in four bands: E090, E150, E230 and E330 [3], that cover the 3, 2, 1.3 and 0.9 mm atmospheric windows, respectively. In this Thesis, I used the E090 and E150 bands, which cover the 73 - 117 and 125 - 184 GHz frequency range (see Chapters 2 and 4). EMIR is a superconducting mixer (SIS). SIS down-convert the incoming radiation, ν, by mixing it with a local oscillator ν_{LO}, resulting in an intermediate frequency, ν_{IF}, a signal that can be more easily processed and analyzed.

This type of mixer is composed of two superconducting layers separated by a thin insulating layer (Figure 1.10). When voltage is applied, the electrons on the filled left-side superconductor band can quantum tunnel through the insulator layer into the empty right-side superconductor band. This phenomenon is known as the Josephson Effect. In this case, the resulting current between the two superconductor layers presents a non-linear relationship with the voltage applied as well as with the initial radiation phase. Consequently, the radiation is coherently converted to an intermediate frequency ν_{IF} when mixing it with the local oscillator signal ν_{LO}.

[3]Where the number approximately indicates in GHz the frequency centre of the bands

The IRAM 30m backend used for the research presented in this Thesis is the Versatile Spectrometric and Polarimetric Array (VESPA). VESPA is a correlator used for the observations presented in Chapters 2 and 4 due to its spectral resolving power (varying from 3.3 kHz and 1.25 MHz). The HCO^+, $HC^{17}O^+$, CS, $C^{34}S$, SO, ^{34}SO, c-C_3H_2 and H_2CO spectra presented in this Thesis have a spectral resolution of 10 kHz, which allows for line profiles to be resolved.

Atacama Large Millimeter and sub-millimeter Array (ALMA)

This subsection introduces the ALMA interferometer (Figure 1.11). ALMA observations towards the IRAS16293 - 2422 B protostar hot corino are used in Chapter 3. Hot corinos are typically $\leq$ 150 au in size, making them $\sim$ 100 times smaller than pre-stellar cores. In order to study them, high-spatial resolution observations are needed ($\gtrsim$ 1-5 "), and therefore, interferometry is used.

Figure 1.11: Picutre of the ALMA Interferometer. Credit: ESO/C.Malin.

ALMA comprises a network of 66 precision antennas configurable into different arrangements. The array includes 54 antennas with 12-meter diameter dishes and 12 smaller ones measuring 7 meters in diameter. ALMA has nine Bands spanning a frequency range between 35 and 950 GHz. Band 1 utilizes HEMT receivers, while Bands 3 to 10 employ SIS receivers. In this Thesis, Band 7 ALMA data is employed to investigate the transfer of molecular complexity in the early stages of star formation within the protostellar system IRAS16293-2422 (see Chapter 3).

1.4 Modelling

To get the full picture of the nature and evolution of the ISM, we require modelling alongside observations and laboratory experiments. Modelling allows to interpret the data better and to formulate predictions when the data acquisition is not possible. In the context of this Thesis, I focus on the modelling of molecular spectral line observations with 1D radiative-transfer techniques.

In order to model and interpret observed molecular emission, we need to take into account the physical, kinematic and chemical structure of the emitting source.

The physical structure of a source is characterised by its density, temperature and velocity profiles. These are constrained by a combination of theory and observations. Models are then tested and refined by comparison with additional observations in an iterative way.

The density structure of cores as a function of radius, ρ(r), can be described through different theoretical density profiles. The Singular Isothermal Sphere (SIS) and Bonnor-Ebert Sphere (BES) are commonly used density profiles (Shu 1977; Bonnor 1956; Ebert 1955). In the SIS model, the density is inversely proportional to r^2. The BES model is characterized by a flattened density profile towards the centre of the core and a profile scaling as r^{-2} in the outer parts of the core. The structure of the pre-stellar core L1544 is well described by a BES (Keto et al. 2015).

Temperature profiles are usually constrained by using "molecular thermometers", which are molecules that have a great number of accessible energy levels. For example, ammonia, NH_3, is a widely used molecular thermometer to derive gas temperatures. Due to the tunnelling of the nitrogen atom across the plane defined by the hydrogens (pyramidal inversion), the ammonia rotational levels split, which leads to a great number of closely spaced levels. Therefore, by observing NH_3 transitions, we can get precise gas temperature values. Crapsi et al. (2007) measured the gas temperature in the inner part of L1544 down to 5.5 K by observing the (1,1) and (2,2) transitions of NH_3.

Velocity profiles are constrained from a combination of theoretical pre-stellar core-collapse models and molecular line observations from which contraction velocities can be derived. For the case of L1544, Keto et al. (2015) compared the H_2O (1_{10} - 1_{01}) and $C^{18}O$ line observations with the predicted line profiles by considering different models of gravitational collapse. The models for gravitational collapse are closely related to the density structure of the pre-stellar core (e.g. the inside-out collapse of a Singular Isothermal Sphere and the quasi-equilibrium contraction of a Bonnor Ebert Sphere).

The chemical structure model of a source is described by the fractional abundance profiles of the molecules present. In the low-density and low-temperature conditions of the ISM, the chemistry is ruled by kinetics rather than by thermodynamics. In other words, the chemical abundances of a specific region will be dictated by which reactions are the fastest and not necessarily by which molecular products are the most stable.

The presence and abundance of a molecule will then depend on the kinetic competition between the reactions that form and destroy the molecule as a function of time. The differential equations that govern the molecular abundances can be solved at a steady state or as a function of time. To solve these equations in the steady state, we assume the abundance of the molecule has settled to a constant value, and therefore, the initial abundances of the molecules involved in the reactions are

not required. Nevertheless, as mentioned at the beginning of this subsection, in the typical ISM physical conditions, we can not assume a steady chemical composition. Therefore, the molecular number density equations are solved as a function of time. This method is called time-dependent chemical modelling, and in this case, the initial molecular abundances are required. As the reaction rates are dependent on the physical properties of the source, these need to be accounted for to compute molecular abundances. Within the time-dependent chemical models, we differentiate the pseudo-time dependent chemical models, which compute abundances over time with a fixed source physical structure, in contrast with real-time-dependent modelling, which takes into account the evolution of the physical properties of the source with time.

As explained in the paragraphs above and in Section 1.3.2, molecular emission depends on the chemical, kinematic and physical structure of the source it is emitting from. Thus, to be able to interpret an observed molecular line correctly we must take into account the source structure. This treatment is achieved through non-LTE Radiative Transfer Modelling. In this Thesis, I use 1D non-LTE radiative transfer modelling, which produces synthetic molecular lines with radial abundance and physical parameters profiles. The physical parameters used are those of a pre-stellar core model (Keto et al. 2015), which are plotted as a function of radius in Figure 1.12, and the abundance profiles of the molecules are obtained with the pseudo-time-dependent chemical model described in Sipilä et al. (2015), plotted in Figure 1.13.

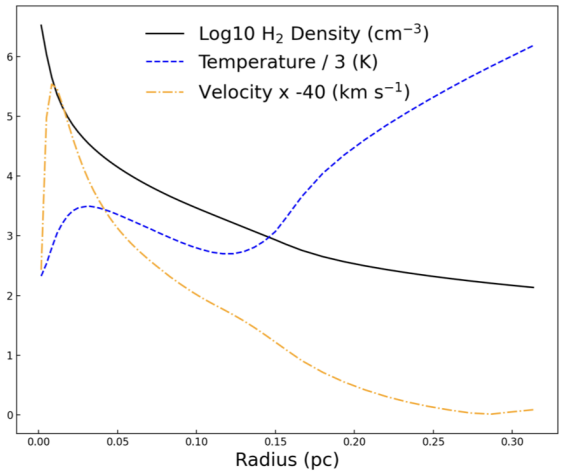

Figure 1.12: Pre-stellar core physical model profiles used in Chapter 2 and 4. The BES molecular hydrogen density profile is shown with a solid black line. The velocity profile is shown with a dash-dotted orange line. The temperature profile is plotted with a dashed blue line. The profiles have been rescaled so they fit in the same plot.

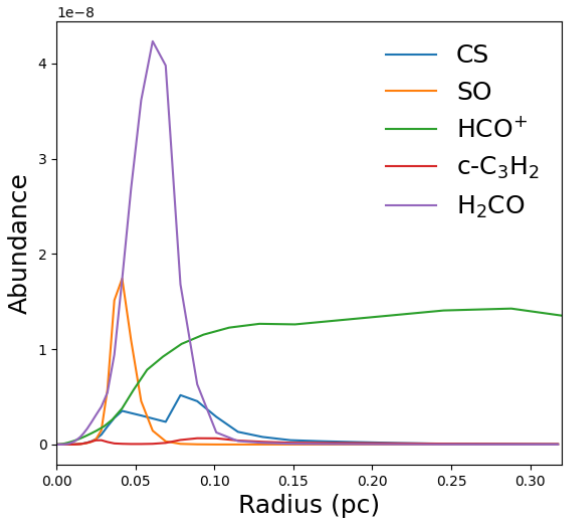

Figure 1.13: Molecular fractional abundance profiles at $\sim$ 5×10^5 years computed with the pseudo-time dependent gas grain chemical model in (Sipilä et al. 2015) used in Chapter 4. The abundance profiles for CS, SO, HCO$^+$, c-C$_3$H$_2$ and H$_2$CO are plotted in blue, orange, green, red and purple, respectively.

1D non-LTE radiative transfer modelling with LOC

The 1D non-LTE radiative transfer code used in this Thesis (Chapters 2 and 4) is the line transfer with OpenCL (LOC) program described in Juvela (2020). This software calculates the molecular level population equations (see Section 1.3.1) using an accelerated lambda iteration (ALI; Rybicki & Hummer 1991) and taking into account the radiative and collisional rates of the molecule. The 1D model is spherically symmetric and is sectioned into concentric shells with defined values for the pre-stellar core parameters: volume density, kinetic temperature, micro-turbulence level, radial velocity, and fractional abundance of different species.

The radiation transfer is simulated by tracing a set of rays throughout the model volume. Each set of rays represents a group of photons with different velocities determined by the division of the spectral line into channels. Upon entering the model, a ray carries information about the background radiation field. As the ray passes through a cell, induced upward transitions are computed, considering both photons entering from outside the cell and photons emitted within the cell. Due to absorption and emission within a cell, the number of photons within a specific ray changes. The software calculates the radiation field in each cell and solves the equilibrium state equations to compute the energy level population estimates. These calculations are performed iteratively until the energy level population estimates converge. Finally, spectral line maps are computed for the selected molecular transition. Afterwards, the spectral line maps are convoluted to give the final modelled line spectrum. This modelled spectrum can then be compared to observations.

1.5 Laboratory

The previous Sections have presented the theoretical background to understand the acquisition, interpretation and analysis of molecular rotational spectra through observational and modelling techniques in the context of star formation. The assignment of observed spectra to a molecule depends on the availability of accurate molecular spectroscopic catalogues, which are obtained from spectral measurements in the laboratory.

In this Section, I discuss the theoretical background of Rotational Spectroscopy and the Laboratory Techniques used in this Thesis for the recording of the rotational spectra of doubly-deuterated acetaldehyde (CHD_2CHO) (Chapter 3) in the Center for Astrochemical Studies (CAS) in the Max-Planck-Institute for Extraterrestrial Physics (MPE).

1.5.1 Rotational Spectroscopy

The content of this Section is primarily based on the "Fundamentals of Molecular Symmetry" book (Bunker & Jensen 2018).

Molecules can change their energy state by interacting with their surroundings. As introduced in Section 1.3.1, the change of their internal energy through interactions with electromagnetic radiation or through collisions results in the emission or absorption of a photon. The internal energy of a molecule is composed of rotational, vibrational and electronic energy. Rotational energy is linked to the change in orientation of the molecule in fixed space coordinates. Vibrational energy is related to the change in the distances of the atoms with respect to each other. Lastly, electronic energy arises from the electrons orbiting the nuclei. Thus, the internal energy of the molecule can also be regarded as rovibronic energy. The internal energy of a molecule is quantised, meaning that there are finite energy states the molecule can be in, and those levels are unique to the molecule. Consequently, spectra can be used as a fingerprint to identify molecules.

The state of a quantum mechanical system, such as a molecule, can be described by the Schrödinger equation:

$$\hat{\mathcal{H}}\Psi = E\Psi \tag{1.41}$$

where $\hat{\mathcal{H}}$ is the Hamiltonian operator, which encompasses the kinetic and potential energy of all the particles in the system, Ψ is the wavefunction which represents the state of the system, and E represents the possible values of the energy of the system. Due to the complexity of Equation 1.41, some approximations are introduced to be able to solve it. As electrons are lighter than nuclei, they move substantially faster. Due to this behaviour, we can decouple the motion of electrons from the motion of nuclei (Born-Oppenheimer approximation). The wavefunction (Ψ) can then be expressed as:

$$\Psi(r_i, R_i) = \Psi_e(r_i)\Psi_n(R_i) \tag{1.42}$$

where r_i expresses the position of i number of electrons, the R_i expresses the positions of i number of nuclei; and consequently Ψ_e is the electronic wavefunction and Ψ_n is the nuclear

wavefunciton.

The nuclear wavefunction Ψ_n describes the position of the nucleus in time. The position of the nuclei can change by altering the internuclear distance or by altering their orientation with respect to a frame of reference. By separating these two types of motions, we obtain:

$$\Psi_n(R_i) = \Psi_v(R_j)\Psi_r(\theta, \phi) \tag{1.43}$$

where $\Psi_v(R_j)$ corresponds to the vibrational wavefunction and R_j expresses the internuclear distances, and $\Psi_r(\theta, \phi)$ is the rotational wavefunction where θ and ϕ are the Eulerian angles which describe the orientation of the molecule w.r.t. a frame of reference.

The solution to the Schrödinger equation defines the three main transition types of a molecule: $\Psi_e(r_i)$, $\Psi_v(R_j)$ and $\Psi_r(\theta, \phi)$; electronic, vibrational and rotational. The energy necessary to change the electronic, vibrational and rotational state of the molecule decreases; being electronic transitions the most energetic and rotational transitions the least. This is the reason why rotational transitions dominate in low-temperature sources, such as pre-stellar cores.

Rotational transitions arise from the coupling of the rotating permanent dipole moment of a molecule with an electromagnetic field. The strength of rotational transitions is positively correlated with the dipole moment magnitude. Therefore, if a molecule does not have a permanent dipole moment, it has no rotational transitions. That is the case for the most abundant molecule in the interstellar medium, H_2. Due to its symmetry, it does not have a permanent dipole moment, and we can not detect it through rotational spectroscopy.

The moments of inertia of the molecule govern rotational transitions. The moments of inertia, I_j, can be described as:

$$I_j = \sum m_i r_i^2 \tag{1.44}$$

where j corresponds to the molecular axes (a, b and c), m_i are the masses of the different nuclei i and r_i are the positions of these atoms w.r.t. the molecular centre of mass. The total moment of inertia, I, is the sum of the individual moments of inertia of the molecular axes (I_a, I_b and I_c). In rotational spectroscopy, rotational constants, B_e, which are related to the moments of inertia, are used to describe rotors:

$$B_e = \frac{h}{8\pi^2 c I} \tag{1.45}$$

where h is Planck's constant, c is the speed of light and I is the moment of inertia. The rotational constant B_e becomes A, B or C when the moment of inertia is separated into its components along the molecular axes I_a, I_b and I_c.

The molecular axes (a, b and c) are labelled in a way that $I_c \geq I_b \geq I_a$. We can, therefore, classify the molecules into different groups depending on the relationship of their moments of inertia (Table 1.1). Classifying molecules into these groups helps to understand their rotational behaviour and spectra.

Table 1.1: Types of rotors

Rotor Type	Moment of inertia	Rotational constants
Linear Molecule	I_a=0, I_b=I_c	A = ∞, B = C
Spherical Top	I_a=I_b=I_c	A = B = C
Prolate Symmetric Top	$I_a < I_b$=I_c	$A > B$ = C
Oblate Symmetric Top	$I_a = I_b < I_c$	A = $B > C$
Asymmetric Top	$I_a < I_b < I_c$	$A > B > C$

The rotation of a molecule is described by solving the Schrödinger equation by using the rotational wavefunction, $\Psi_r(\theta, \phi)$. To ease solving this equation, the molecule is from now on considered to be a rigid rotor. The rigid rotor Hamiltonian, or the 0^{th} order Hamiltonian, $\hat{\mathcal{H}}_r^0$ describes a molecule rigidly rotating in space with geometry fixed at equilibrium:

$$\hat{\mathcal{H}}_r^0 = \hbar^{-2}(A\hat{J}_a^2 + B\hat{J}_b^2 + C\hat{J}_c^2) \tag{1.46}$$

where A, B, and C are the rotational constants, and $\hat{J}_i$ are the angular momentum operators in the three molecular axes a, b and c.

Nevertheless, the rotation cannot be completely separated from the vibrational and electronic motions:

$$\hat{\mathcal{H}}_r = \hat{\mathcal{H}}_r^0 + \hat{\mathcal{H}}_r'. \tag{1.47}$$

Then, we can add corrections to the 0^{th} order Hamiltonian, such as rotation-vibration coupling, centrifugal distortion and Coriolis coupling. These corrections are taken into account in $\hat{\mathcal{H}}_r'$ in Equation 1.47. To simplify, in the next subsections, the rigid rotor Hamiltonians for the different types of rotors will be presented.

For the interest of this Thesis, Linear, Symmetric, and Asymmetric Top molecule cases will be discussed. Moreover, hyperfine splitting and internal rotation, two phenomena that impact the rotational spectra of the molecules used in this Thesis, are also introduced.

Linear Molecules

Linear Molecules, as stated in Table 1.1, have two equal moments of inertia ($I_b = I_c$) and a third moment of inertia equal to 0 ($I_a = 0$). These molecules are described by only one rotational constant, B. The rigid-rotor Hamiltonian for linear molecules is written as:

$$\hat{\mathcal{H}}_r^0 = B\hbar^2(\hat{J}_b^{\,2} + \hat{J}_c^{\,2}) \tag{1.48}$$

with eigenvalues (energy levels):

$$E_r = B[J(J+1) - K^2]hc \tag{1.49}$$

where B is the rotational constant from the I_b moment of inertia and K is the projection of the quantum number J along the principal axis of symmetry.

An example of Linear Molecules in this Thesis includes CS and SO in Chapter 4.

Symmetric Top Molecules

Symmetric molecules present two moments of inertia that are equal and one that is different from the others (Table 1.1). Depending on the magnitude of the unique moment of inertia, we distinguish between prolate (A > B = C) and oblate (A = B > C) molecules (see Figure 1.14, left and right respectively).

For a prolate symmetric top, we have the rigid-rotor Hamiltonian form:

$$\hat{\mathcal{H}}_r^0 = \hbar^2[A\hat{J}_a^2 + B(\hat{J}_b^2 + \hat{J}_c^2)]. \tag{1.50}$$

The energy levels are then described by:

$$E_r = [BJ(J+1) + (A-B)K^2]hc \tag{1.51}$$

where A and B are the rotational constants arising from the I_a and I_b moment inertia components, and K is the projection of the quantum number J along the principal axis of symmetry.

For an oblate symmetric top, we have the rigid-rotor Hamiltonian form:

$$\hat{\mathcal{H}}_r^0 = \hbar^2[B(\hat{J}_a^2 + \hat{J}_b^2) + C\hat{J}_c^2]. \tag{1.52}$$

The energy levels are then described by:

$$E_r = [BJ(J+1) - (B-C)K^2]hc \tag{1.53}$$

where B and C are the rotational constants arising from the I_b and I_c moment inertia components.

Examples of Symmetric Top Molecules in this Thesis include HCO^+ (Chapter 4) and $HC^{17}O^+$ (Chapter 2).

Asymmetric Top Molecules

The asymmetric top molecule can be described with the rigid rotor rotational Hamiltonian:

$$\hat{\mathcal{H}}_r^0 = \hbar^{-2}(A\hat{J}_a^2 + B\hat{J}_b^2 + C\hat{J}_c^2). \tag{1.54}$$

The component of the angular momentum is not constant along any direction in the rotating asymmetric molecule, and therefore, K, which is the projection of J in the symmetry axis in symmetric tops, is not a good quantum number. The asymmetric top rotation can be analysed by diagonalizing the $\hat{\mathcal{H}}_r$ matrix with the symmetric top basis wavefunctions. We can, therefore, consider it a deviation from the symmetric top prolate and oblate cases.

We can assess the degree of asymmetry (degree of prolate or oblate deviation) with Ray's asymmetry parameter κ:

$$\kappa = \frac{2B - A - C}{A - C}. \tag{1.55}$$

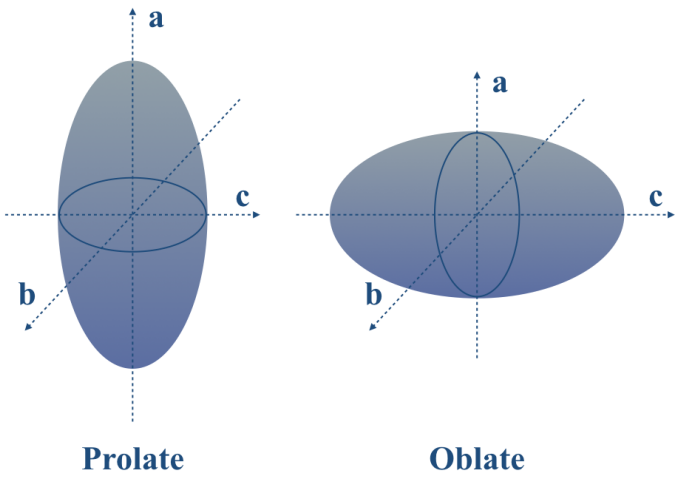

Figure 1.14: Prolate (left) and Oblate (right) symmetries. The molecular axes are shown with dotted arrows. For the prolate case $I_b = I_c < I_a$. For the oblate case $I_a = I_b < I_c$

The asymmetry parameter κ ranges from -1 (prolate, B=C) to 1 (oblate, B=A). The range of B between A and C gives different asymmetry conditions, making the $\pm k$ levels degenerate in symmetric tops split. To express asymmetric rotational levels, we use the nomenclature J, K_a, K_c, where K_a and K_c correspond to the prolate and oblate levels respectively that the asymmetric energy level connects with.

The "permitted" transitions are dictated by non-vanishing dipole matrix elements. The selection rules for asymmetric top molecules are the following: $\Delta J = 0, \pm 1$ ($0 \not\leftrightarrow 0$). Selection rules for the pseudo-quantum number K_a and K_b result from symmetry properties of the ellipsoid of inertia and are the following:

Table 1.2: K_a and K_c selection rules

Dipole Component	ΔK_a	ΔK_c
$\mu_a \neq 0$	0, ±2, ... (even)	± 1, ± 3, ... (odd)
$\mu_b \neq 0$	± 1, ± 3, ... (odd)	± 1, ± 3, ... (odd)
$\mu_c \neq 0$	± 1, ± 3, ... (odd)	0, ±2, ... (even)

Transitions are only due to one dipole component. For example, if a transition is due to the μ_a component, this transition is called an "a-type" transition. Thus, transition arising from the μ_b and μ_c components correspond to "b-type" and "c-type" transitions. The presence and intensity of the different types of transitions tell us information on the structure of the molecule. The intensity of these different transitions depends on several factors. First of all, the larger the value of the dipole moment component (μ_i; i = a, b, c), the more intense these types of lines ("i-type") will be. The greater the ΔK_a and ΔK_c, the weaker the lines will be. Moreover, if the molecule is close to

the prolate symmetric-top limit, only the transitions with $\Delta K_a = 0, \pm 1$ will be significant. In this case, transitions with large changes in ΔK_c may also be observable. In the oblate symmetric-top limit, the opposite holds. The only significant transitions will arise from $\Delta K_c = 0, \pm 1$, while transitions with large changes in ΔK_a can be observable.

Examples of Asymmetric Top Molecules in this Thesis include doubly-deuterated acetaldehyde, CHD_2CHO, (Chapter 3), H_2CO and c-C_3H_2 (Chapter 4).

Hyperfine Splitting

Nuclear hyperfine structure arises from magnetic or electric interactions of electrons with nuclear moments. For atoms with a nuclear spin statistical weight greater than one, hyperfine splitting of transitions occurs. On the other hand, hyperfine splitting does not happen with nuclei with spins 0 and 1/2 as they are spherically symmetric and, therefore, do not have quadrupole moments. The rotation of the molecule creates a weak magnetic field that can interact with the nuclear magnetic moment. In other words, the molecular rotational angular momentum, J, couples with the nuclear spin, I, to give the total angular momentum with nuclear coupling, F. The resulting levels from hyperfine splitting are labelled with the total angular quantum number F. The allowed values of F are $J + I$, $J + I$ - 1, to $\mid J$ - $I \mid$. The electric dipole transitions have to obey: $\Delta F = 0$ or $\pm$ 1 ($F = 0 \leftrightarrow 0$ is not allowed). The transitions that fulfil the condition: $\Delta F = \Delta J$ are the most intense.

To treat hyperfine splitting, $\hat{\mathcal{H}}_{hfs}$ is added to the rotational Hamiltonian the same way that $\hat{\mathcal{H}}'_r$ is. $\hat{\mathcal{H}}_{hfs}$ makes the rovibronic energy levels that have a nuclear spin statistical weight greater than unity to split into closely spaced sub-levels named hyperfine structure, and thus transitions between these levels are also split into hyperfine components.

$HC^{17}O^+$, introduced in Chapter 2, is a clear example of a molecule showing hyperfine splitting. The molecular angular momentum, J, couples with the nuclear spin, I, of the ^{17}O atom (I = 5/2), resulting in the splitting of its energy levels into hyperfine components. The J= 1 - 0 transition of $HC^{17}O^+$ results into the ground level (J = 0) with $F = 5/2$ and the upper level (J = 1) split into three levels with $F' = 3/2$, 5/2 and 7/2 (Figure 1.15). Because of this, the J= 1 - 0 transition is split into three transitions between F and the three F' levels (Figure 1.16).

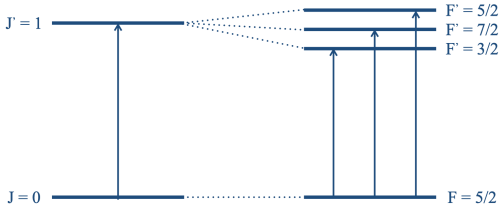

Figure 1.15: Non-hyperfine (left) and hyperfine (right) levels and transitions of the J= 1 - 0 $HC^{17}O^+$ line. On the non-hyperfine split case (left), there is a single transition between the lower J= 0 and the upper $J^{'}$ = 1 levels. On the hyperfine case (right), we can see three transitions happening between the lower level $F = 5/2$ and three upper levels $F^{'} = 3/2$, 5/2 and 7/2.

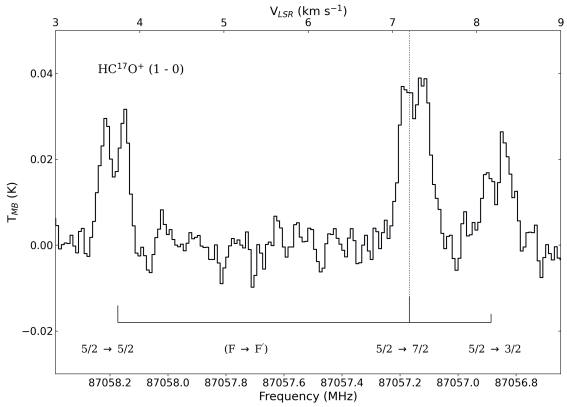

Figure 1.16: The hyperfine structure of the J= 1 - 0 $HC^{17}O^+$ transition observed towards the pre-stellar core L1544. From higher (left) to lower (right) frequencies, we have the 5/2 → 5/2, 7/2 → 5/2 and 3/2 → 5/2 transitions. The double-peaked hyperfine components are not due to quantum but physical reasons and are discussed in Chapter 2.

Internal rotation

All of the Hamiltonians presented up to this point describe rigid molecules. The energy barriers between the different conformers of a rigid molecule are insuperable. On the other hand, the nuclei of the so-called "non-rigid molecules" are able to tunnel through barriers that separate accessible minima in the potential energy surface and, therefore, can shift between configurations. In other words, non-rigid molecules are the ones that present large amplitude distortions of the order of the bond length or bond angle. This includes internal rotation, inversion, bending and pseudorotation. Upon the tunnelling of the barrier, each rotational transition will exhibit fine structure caused by the interaction of internal and overall rotation of the molecule. The separation between the components of the fine structure depends on the height of the potential barrier between the tunnelled minima.

The Hamiltonian for non-rigid molecules is constructed in a similar way as for the rigid one, but taking into account the internal rotation constant as well as the internal rotation potential function. First, an appropriate 0^{th} order Hamiltonian must be chosen so its eigenvalues are close enough to the real ones. The goal is to have the least non-vanishing cross terms in the Hamiltonian as possible. This is achieved by selecting an adequate method, which depends on the symmetry of the molecule. We have three main axis-defining methods: Principal Axis Method (PAM), Rho Axis Method (RAM) and Internal Axis Method (IAM) (Kleiner 2010).

In line with the content of this Thesis, I will focus specifically on the "non-rigid molecule" internal rotation behaviour of the rotation of a methyl group ($-CH_3$). The rotation of a methyl

group w.r.t. the rest of the molecule results in different equivalent configurations. The internal rotation of this functional group can be described by the torsional angle (α). The number of equivalent configurations depends on the symmetry of the molecule itself. The potential function V_N of the internal rotation is a periodic function of α with N equal configurations and can be expressed as:

$$V_N(\alpha) = \frac{V_N}{2}(1 - \cos N\alpha) + \frac{V_{2N}}{2}(1 - \cos 2N\alpha) + ... \tag{1.56}$$

To assess the behaviour of the torsional levels for the rotating methyl group, we include $V_3(\alpha)$ to the wave equation and solve it for two extreme cases, taking into account the height of the barrier V_N.

In the case of a very low barrier ($V_3 \to 0$), the molecule can be considered to present a free rotation of the methyl group w.r.t. the fixed molecular frame (left-hand vertical axis in Figure 1.17). In this case, the energy levels are defined by the quantum number m, which takes the values: $m = 0, \pm 1, \pm 2$, etc. The levels in the low barrier case appear to be doubly degenerate (except for $m = 0$, which is non-degenerate). The sign of m refers to the two potential directions of the internal rotation.

In the case of an infinitely high barrier ($V_3 \to \infty$), the molecule oscillates around one of the potential minima and, therefore, can be characterized with the harmonic oscillator description (right-hand vertical axis in Figure 1.17). The torsional states for this case (now defined with v) are triply degenerate, as the molecule could be oscillating in any of the three equivalent potential minima.

In the high barrier case, where the molecule can tunnel between equivalent minima, the three-fold degeneracy of the $V_3 \to \infty$ case is broken, resulting in two levels: a non-degenerate level, A, and a doubly degenerate level, E, (between the left- and right-hand vertical axes in Figure 1.17). The A and E level spacing increases with increasing v, making the levels with low v values move towards the Harmonic Oscillator case and levels with high v approach the Free Rotor case.

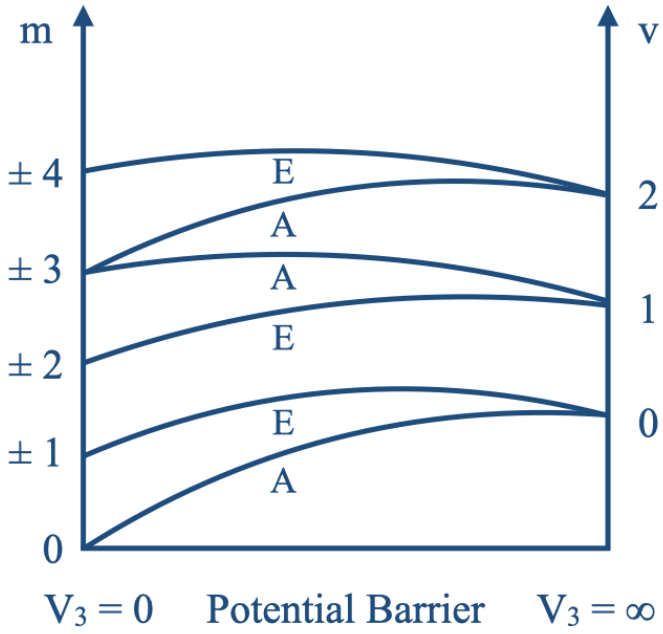

Figure 1.17: Torsional sub-level behaviour as a function of the potential barrier height (V_3) for a system with $N = 3$ equal configurations. On the left-hand axis, there are the Free Rotor levels quantised with the quantum number m. On the right-hand axis, there are the Harmonic Oscillator levels quantised with v. The lines connecting the $V_3 = 0$ and $V_3 = \infty$ represent the torsional sub-levels in the intermediate case. The labels of the intermediate states are found just below each of the curves. This scheme has been inspired by Figure 12.4 in Gordy & Cook (1970).

The treatment of internal rotation is specific to the molecule under study. The form of the Hamiltonian and the number and symmetry of resulting torsional sub-states are distinct for each case. In this Thesis, I worked on the rotational spectroscopy of the doubly-deuterated acetaldehyde (CHD_2CHO) molecule, which, as well as its main isotopologue, displays the rotation of its methyl group. In the case of CHD_2CHO, the description of the internal rotation is more complicated, as the methyl group is not symmetric ($-CHD_2$) as is the case for the main isotopologue. Depending on the orientation of the methyl group, we can distinguish two conformers, the symmetric and the asymmetric ones (Figure 1.18). When the H is in the plane defined by the aldehyde group ($-CHO$), the molecule presents a symmetry plane (left, Figure 1.18). If the deuterium is on the plane defined by the aldehyde group, there is no longer a symmetry plane and the conformer is called asymmetric (Figure 1.18). The asymmetric conformer has two equivalent configurations corresponding to the presence of one of the two deuteriums in the aldehyde-group plane. There is tunnelling between the asymmetric equivalent configurations. In the case of doubly-deuterated acetaldehyde, due to its symmetry, three torsional sublevels arise, one from the symmetric and two from the tunnelling between the equivalent asymmetric configurations.

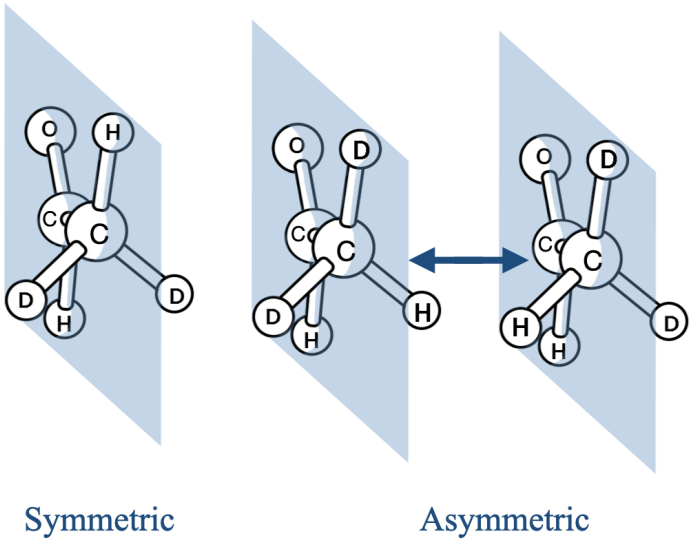

Figure 1.18: Doubly-deuterated acetaldehyde (CHD_2CHO) symmetric (left) and asymmetric (middle and right) conformers. The blue area depicts the plane defined by the aldehyde ($-CHO$) group. The symmetric conformer has the hydrogen on the blue plane and, therefore, is symmetric. The asymmetric conformers have one of the deuteriums on the blue plane, and there is no longer a symmetry plane.

1.5.2 Laboratory Molecular Spectra Measurements

In this Thesis, two experimental techniques have been involved in the recording of molecular rotational spectra: Chirped-Pulse Fourier Transform Spectroscopy and Frequency Modulation Absorption Spectroscopy, which I describe in this section.

Chirped-Pulse Fourier Transform Spectrometer (CP-FTS)

The Chirped-Pulse Fourier Transform Spectrometer (CP-FTS) set-up at the Center for Astrochemical Studies (CAS) at the Max-Planck-Institute for Extraterrestrial Physics (MPE) has been used for this Thesis to record part of the millimetre and sub-millimetre molecular spectra presented in Chapter 3.

A high power ($>$ 1 kW) frequency-swept (chirped) microwave pulse is used to simultaneously polarize all the molecular transitions that lie in a broad spectral region ($\sim$ 10 GHz). The high power of the pulse is required to produce a sufficient degree of polarization of all the transitions present in a specific frequency range. The radiation pulse induces the polarization of the molecular sample, which is treated as a global dipole moment. This phenomenon is described in the two-level system density matrix formalism by the Optical Bloch equations. The magnitude for the polarization response $|P|$ for each molecular transition is described as:

$$|P| = \frac{2|\mu_{ab}|^2 \varepsilon \Delta N_0}{\hbar} \sqrt{\frac{\pi}{\alpha}} \tag{1.57}$$

where μ_{ab} is the dipole moment of a transition between the levels a and b, ε is the magnitude of the oscillating electric field, ΔN_0 is the initial population difference and α is the rate of frequency sweep of the pulse. When the pulse stops, the molecules precess back to their equilibrium positions, emitting broad-band transient free induction decay (FID) radiation. This radiation exponentially decays with time in the form of a sinusoidal wave. The time constant T determines the rate of coherence decay. To avoid signal loss, the pulse duration, t_p, has to be smaller than $T \sim 10$ μs.

Thereafter, the Fourier Transform Spectrometer converts the FID time-domain signal into a frequency-domain spectrum (e.g. Figure 1.19). This technique is based on the Fourier Theorem, which states that any periodic function can be expanded as an infinite sum of linearly independent functions of sine and cosine terms. By performing spectroscopy in the time domain, we can achieve higher frequency resolutions, which is key to fully resolving the rotational lines. Moreover, if the microwave source is phase-stable, multiple scans can be averaged in the time domain, increasing the spectrum sensitivity.

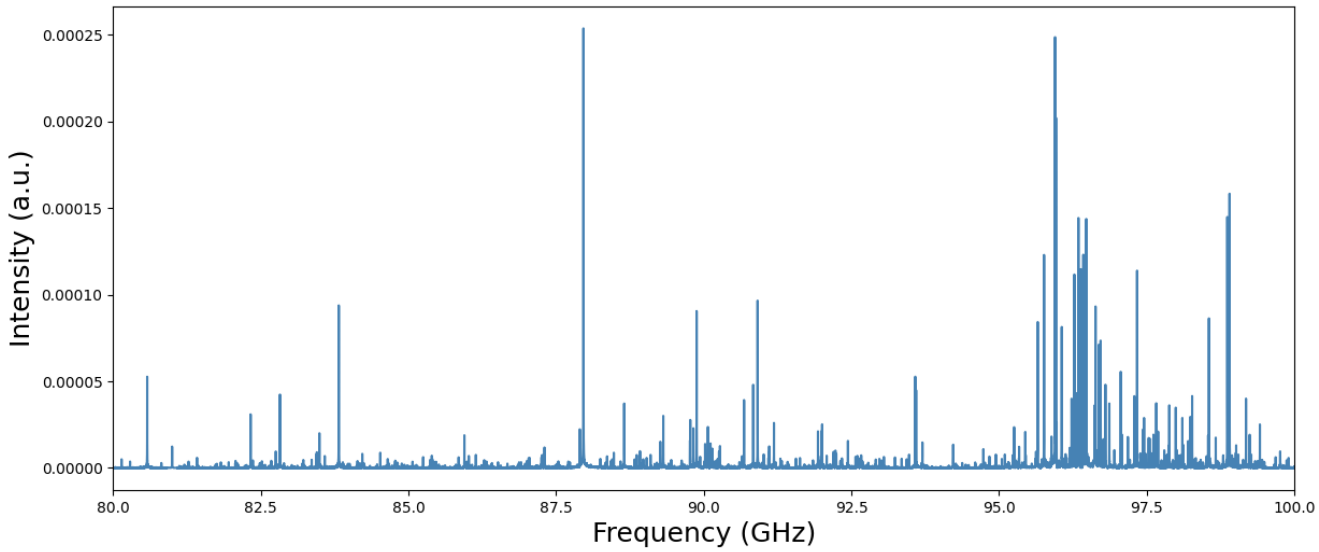

Figure 1.19: Portion of a spectrum (80 to 100 GHz) taken with the CP-FTS of a mixture of acetaldehyde (CH_3CHO) and its deuterated isotopologues.

CAS Absorption Cell (CASAC) Experiment

The CAS Absorption Cell (CASAC) Experiment in the Center for Astrochemical Studies (CAS) at the Max-Planck-Institute for Extraterrestrial Physics (MPE) has been used for this Thesis to record part of the millimetre and sub-millimetre molecular spectra presented in Chapter 3.

The CASAC is a spectroscopic frequency modulation absorption experiment. This setup makes use of the molecular absorption process phenomena described in Section 1.3.1 to obtain molecular spectra. First, radiation is directed through a gaseous sample of the molecule under study. Then, the molecules in the sample absorb radiation at frequencies equal to the separation between its energy levels, causing the radiation intensity to decline at the end of the cell. The intensity decrease of the incident radiation after passing through the gas-filled cell, named absorbance, A, can be described in terms of Beer Lambert's law:

$$A = \varepsilon c l \tag{1.58}$$

where ε is the molar absorption coefficient (in units of M^{-1} cm^{-1}), c is the molar concentration of the sample, M, and l is the pathlength of the radiation through the sample.

In order to increase the sensitivity of the measurements, which is a key factor in building accurate spectroscopic catalogues, frequency modulation is applied. Frequency modulation reduces the noise and, therefore, increases the signal-to-noise (S/N) ratio. First, the inputting radiation is mixed with a carrier wave called modulation signal. Then, the output signal is demodulated with a lock-in amplifier. Demodulation involves mixing the output signal with a reference signal whose frequency is equal to or a multiple of the modulating signal. In the case of the $2f$ demodulation used in the measurements in Chapter 3, the output signal is mixed with a reference signal that has

double the modulation frequency. The $2f$ modulation removes baselines that increase or decrease linearly with time. Finally, the output signal in time-space is Fourier transformed into a spectrum in frequency space, which shows second-derivative line profiles due to the $2f$ modulation applied (Figure 1.21).

Moreover, for an even higher sensitivity, a liquid-He-cooled InSb Hot Electron Bolometer (HEB) detector is used (Figure 1.20). HEB are highly sensitive detectors which measure the power of incident radiation through temperature-dependent electrical resistance. These types of detectors were first introduced in this Thesis in Section 1.3.4, as they are also used as frontends in radio telescopes.

The incident radiation is adsorbed by a layer of semi-conducting material (in the HEB used for the measurements in this Thesis, a layer of Indium Antimonium, InSb). When kept at cryogenic temperatures, through liquid helium, He, cooling ($\sim$ 4 K), the electrons become weakly coupled to the crystal bulk. Upon the absorption of incident radiation, the electrons gain energy and are driven out of equilibrium with the crystal lattice, thus becoming Hot Electrons. The change in electron temperature affects their conductivity and, therefore, the electrical resistance of the material. The change in electrical resistance, proportional to the power of incident radiation, is measured, which leads to output molecular spectra.

Figure 1.20: The liquid-He-cooled InSb Hot Electron Bolometer (HEB) detector used for the measurements with the CASAC setup. The black circular components on the bottom of the detector are where the radiation gets in and out of the bolometer. The blue funnel corresponds to the liquid N_2 inlet.

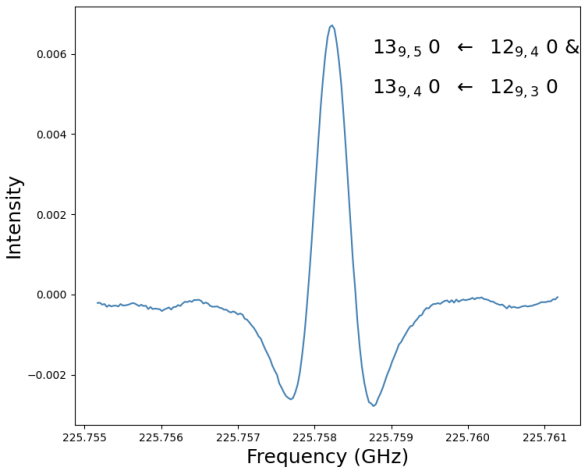

Figure 1.21: Scan of the $J_{K_a,K_c,v} \leftarrow J'_{K'_a,K'_c,v'}$ $13_{9,5,0} \leftarrow 12_{9,4,0}$ and $13_{9,4,0} \leftarrow 12_{9,3,0}$ (merged) transitions of CHD_2CHO taken with the CASAC experiment. This is an example of a second-derivative line profile due to the $2f$ modulation.

1.6 This Thesis

This Thesis presents the work carried out on the topics of the initial conditions of star formation and the origin and transfer of molecular complexity in space. It is constituted by the work published in two first-author papers (Chapters 2 and 3) and a work to be published in the future, also as a first-author paper (Chapter 4). The tasks included in this Thesis mainly done by coauthors are explicitly mentioned in the following paragraphs.

In Chapter 2, I study the origin of the double-peaked line profile of optically thin transitions observed towards the pre-stellar core L1544. This is done through the radiative transfer modelling of the optically thin $J = 1$ - 0 $HC^{17}O^+$ transition. The hyperfine collisional rate coefficients used for the radiative transfer modelling are computed by coauthors. I reproduced the line taking into account a prototypical pre-stellar core physical model and a molecular abundance profile derived from pseudo-time dependent chemical modelling but adopting an upscaled velocity profile and abundance. This may indicate the core is more evolved than previously thought and/or that the chemical modelling could be further improved. I concluded that double-peaked profiles of optically thin lines can be solely due to radiative transfer effects in a contracting dense core.

In Chapter 3, I measure and analyse the spectrum of doubly deuterated acetaldehyde (CHD_2CHO) in the laboratory using both Chirped and Absorption experiments. Doubly deuterated acetaldehyde is a molecule of astrophysical interest which was not detected towards the interstellar medium due to the lack of an accurate spectroscopic catalogue. I then measure the CHD_2CHO spectra in the laboratory, and the rotational constants are computed by a coauthor from these measurements. The resulting spectroscopic catalogue is used by a coauthor to compute a synthetic spectra which is compared to observations to detect CHD_2CHO molecule for the first time in the ISM. The molecule was detected in the protostellar source IRAS 16293-2422 with an abundance w.r.t. the singly deuterated variant of 20%. This D_2/D value is similar to other COMs detected in this source, which points to a common origin for these molecules, probably from the pre-stellar core phase, as is the only one that can account for the increased deuterium fractionation, indicating at least a partial inheritance of these molecules.

In Chapter 4, I use 1D non-LTE radiative transfer modelling coupled with Markov Chain Monte Carlo (MCMC) methods to reproduce the high-sensitivity and high-spectral resolution spectra of the $C^{34}S$ (2 - 1), ^{34}SO (2,3 - 1,2), CS (2 - 1), SO (2,3 - 1,2), HCO^+ (1 -0), $HC^{17}O^+$ (1 - 0), H_2CO ($2_{1,2}$ - $1_{1,1}$) and c-C_3H_2 ($2_{1,2}$ - $1_{0,1}$) transitions observed towards the dust peak of pre-stellar core L1544 to deepen the knowledge of the physical, chemical and kinematic structure of this source. The modelling approach used in this Chapter results in well-constrained parameters for the optically thin lines, but less constrained for the optically thick lines. Additionally, I constrain simple step fractional abundance profiles for the molecules. These profiles are then compared to fractional abundance profiles computed with chemical models. The aim is to assess the completeness of the chemical networks used in calculating these abundances. The radiative transfer modelling showed that all of the transitions trace different parts of L1544 with different physical, chemical and kinematic properties, with optically thin lines tracing the inner regions and optically thick lines the outer regions of L1544. The 1D radiative transfer modelling of increasingly sensitive and spectrally resolved molecular observations towards L1544 supports the idea that this pre-stellar

core is not spherically symmetric as conventionally treated in models and points at the need to use 3D radiative transfer models to understand the complexity of L1544 fully.

Finally, in Chapter 5, I summarise the findings presented, and I reflect on the future of the topics discussed in this Thesis.

2

Tracing the contraction of the pre-stellar core L1544 with $HC^{17}O^+$ $J = 1$ - 0 emission.[1]

The content of this chapter was published in the Astronomy & Astrophysics Journal. Credit: Ferrer Asensio et al., 2022, A&A, 667, A119, 32 pp, reproduced with permission ©AAS.

Spectral line profiles of several molecules observed towards the pre-stellar core L1544 appear double-peaked. For abundant molecular species this line morphology has been linked to self-absorption. However, the physical process behind the double-peaked morphology for less abundant species is still under debate.
In order to understand the cause behind the double-peaked spectra of optically thin transitions and their link to the physical structure of pre-stellar cores, we present high-sensitivity and high spectral resolution $HC^{17}O^+$ J =1-0 observations towards the dust peak in L1544. We observed the $HC^{17}O^+$(1-0) spectrum with the Institut de Radioastronomie Millimétrique (IRAM) 30m telescope. By using state-of-the-art collisional rate coefficients, a physical model for the core and the fractional abundance profile of $HC^{17}O^+$, the hyperfine structure of this molecular ion is modelled for the first time with the radiative transfer code LOC applied to the predicted chemical structure of a contracting pre-stellar core. We applied the same analysis to the chemically related $C^{17}O$ molecule.
The observed $HC^{17}O^+$(1-0) and $C^{17}O$(1-0) lines were successfully reproduced with a non-local thermal equilibrium (LTE) radiative transfer model applied to chemical model predictions for a contracting pre-stellar core. An upscaled velocity profile (by 30%) is needed to reproduce the $HC^{17}O^+$(1-0) observations. The double peaks observed in the $HC^{17}O^+$(1-0) hyperfine components are due to the contraction motions at densities close to the critical density of the transition ($\sim 10^5$ cm^{-3}) and to the decreasing HCO^+ fractional abundance towards the centre.

2.1 Introduction

Pre-stellar cores are gravitationally bound cores seen as sub-structures within molecular clouds. They present high central densities ($n_{H_2} > 10^5$ cm^{-3}) and low temperatures at the centre (< 10 K) (Keto & Caselli 2008). These sources are on the verge of contraction, but have yet not formed a protostar. The combined study of the physical structure and kinematics of pre-stellar cores, which represent the earliest stages of star formation (André et al. 2014), is crucial to achieve a comprehensive view of the initial conditions for core collapse. Molecular spectra have been widely used as diagnostics of dense cloud cores. The intensities, widths, rest frequencies, and profiles of spectral lines allow the physical, chemical, and kinematic structure of the source they originate from to be characterised. Transitions with hyperfine structure are especially useful for deriving physical properties such as optical depth and excitation temperature ($T_{\rm ex}$) of the line emitting area. The column density can then be derived without the need for assumptions on $T_{\rm ex}$ or of observations of other transitions, making hyperfine transitions useful probes of the physics and chemistry of molecular clouds (e.g. Caselli et al. 1995; Sohn et al. 2007; Lique et al. 2015).

L1544 is a widely studied pre-stellar core in the Taurus Molecular Cloud at a distance of 170 pc (Galli et al. 2019). Its chemical composition and structure have been constrained in multiple studies (Tafalla et al. 1998; Caselli et al. 2002a; Crapsi et al. 2005; Keto & Caselli 2010; Vastel et al. 2014; Spezzano et al. 2017; Caselli et al. 2019; Chacón-Tanarro et al. 2019; Jin & Garrod 2020). L1544 shows signs of contraction motions, which resemble the quasi-equilibrium contraction of a Bonnor-Ebert sphere (Keto et al. 2015). The core is also centrally concentrated, with central H_2 column densities close to 10^{23} cm^{-2} (Ward-Thompson et al. 1999; Crapsi et al. 2005), low central temperatures (~ 7 K, Crapsi et al. 2007), large amount of freeze-out (Caselli et al. 2022), large deuterium fractions, (Crapsi et al. 2005; Redaelli et al. 2019) and a rich chemical composition (Vastel et al. 2014; Jiménez-Serra et al. 2016; Spezzano et al. 2017). Due to its characteristics, L1544 is an ideal source to study the dynamics of a dense core on the verge of star formation.

Previous observations towards the dust peak of L1544 recorded spectral line transitions that present a double-peaked structure (Tafalla et al. 1998; Caselli et al. 1999; Williams et al. 1999; Dore et al. 2001a; Caselli et al. 2002a). This line morphology can be explained for some cases, for example, the N_2H^+(1-0) line (Williams et al. 1999), by self-absorption from a less dense, contracting envelope (Keto & Rybicki 2010). Self-absorption is expected to arise for optically thick transitions of abundant molecules (Tafalla et al. 1998). However, lines of rare isotopologues, such as $D^{13}CO^+$(1-0) and $HC^{17}O^+$(1-0), are expected to be optically thin, and their double-peaked profile is not expected to arise from self-absorption. Possible reasons for these features are the presence of dense material at different velocities along the line of sight (Tafalla et al. 1998) or the depletion of the targeted molecules towards the inner part of the core (Caselli et al. 2002a).

In order to reveal the nature of the process responsible for double-peaked line profiles of optically thin species, we obtained new high-sensitivity observations of the $HC^{17}O^+$(1-0) line towards L1544. The hyperfine structure of the line occurs because the nuclear spin of ^{17}O ($I = 5/2$) and the molecular rotation are coupled, resulting in the splitting of the $J = 1$ rotational level. The reason for choosing this particular isotope of HCO^+ is that it is expected to have optically thin lines that should not be affected by self-absorption and will allow us to see across the totality of the core.

$HC^{17}O^+$ was first observed in the interstellar medium by Guélin et al. (1982) towards Sagittarius B2 with the Bell Laboratories (BTL) 7m telescope at Crawford Hill Laboratory, New Jersey. They detected the $J = 1$ - 0 rotational transition centred at 87.1 GHz with an angular resolution of $2'$ and spectral resolution of 1 MHz (3.5 km s^{-1}). $HC^{17}O^+$(1-0) was detected more recently with the Institut de Radioastronomie Millimétrique (IRAM) 30m telescope towards the dust peak in L1544 (we refer to Figure 2 in Dore et al. 2001a and Figure 1 in Caselli et al. 2002a).

In this work, we present a new high-sensitivity and high spectral resolution $HC^{17}O^+$(1-0) spectrum towards the dust peak of L1544 observed with the IRAM 30m telescope. With the aid of predictions from a chemical model, applied to the physical structure of L1544 and the non-local thermodynamic equilibrium (LTE) radiative transfer code LOC, we reproduce the observed spectrum and discuss the results. This work is structured as follows. In Section 2.2, we describe the observational details of the data obtained with the IRAM 30m telescope. In Section 2.3, we present the determination of the collisional rate coefficients required for the modelling, and we describe the non-LTE radiative transfer code, the pre-stellar core model, and the fractional abundance profiles used. The results are presented in Section 2.4. In Section 2.5, we discuss the results obtained in the context of past works, and our conclusions can be found in Section 2.6.

2.2 Observations

We observed the ground state ($J = 1 - 0$) rotational transition of $HC^{17}O^+$ in a single pointing towards the dust peak of L1544 ($\alpha_{2000} = 05^h04^m17^s.21$, $\delta_{2000} = +25°10'42''.8$). These observations were carried out from Oct 10 to 15, 2018, using the IRAM 30m telescope at Pico Veleta, with a total on-source integration time of 22.6 hr. The telescope pointing was checked frequently against the nearby bright quasar B0316+413 and found to be accurate within 4". We used the E090 band of the EMIR receiver. The half power beam width (HPBW) of these observations is 28". The tuning frequency was 87.060 GHz and the observations were performed in frequency switching mode. We used the VESPA backend to achieve a spectral resolution of 10 kHz, equivalent to $\Delta v = 0.034$ km s^{-1} at this frequency. Both horizontal and vertical polarisations were observed simultaneously. The final spectrum is shown in Figure 2.1.

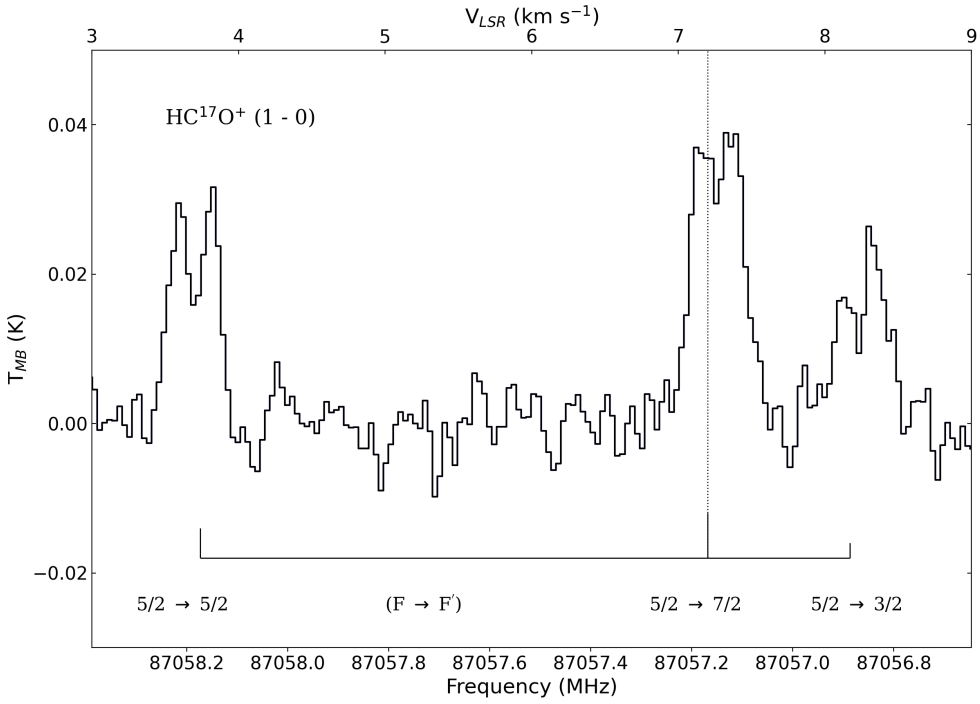

Figure 2.1: Spectrum of $HC^{17}O^+$(1-0) at the dust peak of L1544. The hyperfine structure is shown by vertical solid lines with heights proportional to their relative intensities (see Table 2.1). The vertical dotted line represents the LSR velocity of L1544 (7.2 km s^{-1}).

The observational data was processed and then averaged with the Continuum and Line Analysis Single-dish Software (CLASS), an application from the GILDAS[2] software (Pety 2005). A F_{eff}/B_{eff} ratio of 1.17 was used for the T_A^* to $T_{\rm MB}$ conversion. Figure 2.1 shows the observed $HC^{17}O^+$(1-

[2] https://www.iram.fr/IRAMFR/GILDAS/

0) rotational transition split into three hyperfine components that present a clear double-peaked structure. Each hyperfine level is labelled by a quantum number F ($\mathbf{F} = \mathbf{I} + \mathbf{J}$) varying between $|I - J|$ and $I + J$. The quantum number F corresponds to the lower level while the F' corresponds to the upper level of the transition. Table 2.1 reports the hyperfine transition frequencies measured in the laboratory, relative intensities, and upper energies. A signal-to-noise ratio (S/N) of 7 was obtained for the least bright component with a rms of 2.8 mK. The intensity difference between the two peaks in the $F - F^{'} = 5/2 \rightarrow 3/2$ transition centred at a frequency of 87.057 GHz is comparable to the noise level.

Table 2.1: Hyperfine transition frequencies measured in the laboratory (Dore et al. 2001a), upper energies of $HC^{17}O^+$(1-0) and relative intensities.

$F \rightarrow F^{'}$	Frequency (MHz)	$E_{\rm up}$ (K)	Relative intensity
5/2→3/2	87056.966(20)	4.18	2
5/2→7/2	87057.258(20)	4.18	4
5/2→5/2	87058.294(20)	4.18	3

Moreover, we use $C^{17}O$(1-0) observations towards the dust peak of L1544 from Chacón-Tanarro et al. (2019), for which an on-the-fly (OTF) map was taken with the IRAM 30m telescope with a spectral resolution of 20 kHz (Δv = 0.05 km s^{-1}). For $C^{17}O$, a single pointing spectrum was extracted towards the dust peak within a beam of 22" which corresponds to the IRAM 30m beam at the $C^{17}O$(1-0) transition frequency, 112.360 GHz. A F_{eff}/B_{eff} ratio of 1.20 was used for the T_A^* to $T_{\rm MB}$ conversion. The resulting spectrum has a rms of 75 mK (See Section 2.4.2).

2.3 Radiative transfer

In order to fully understand the observed spectra, we need to take into account the transfer of radiation across the source. Physical conditions can vary along the radiation's path which will affect the observed line intensity and profile. To derive information carried by spectral line profiles, we need to carry out a full radiative transfer modelling of the emission. Radiative transfer accounting for the physical structure of the observed object is crucial for the correct interpretation of spectra, as has been shown in past works, including those on pre-stellar cores (Caselli et al. 2002a; Sohn et al. 2007; Keto et al. 2015; Redaelli et al. 2019).

The present work focuses on L1544, a pre-stellar core with well-studied density, temperature and velocity profiles (Ward-Thompson et al. 1999; Crapsi et al. 2005, 2007; Keto et al. 2015). In such environments, LTE conditions do not generally apply across the source. In LTE, the energy level populations of molecules are described by the Boltzmann distribution. LTE applies when the critical density of the transition (n_{crit}= A_{ul}/k_{ul}, where A_{ul} is the Einstein A coefficient and k_{ul} is the collisional coefficient, where 'u' and 'l' are the upper and lower levels, respectively) is equal to

or lower than the volume density of the emitting region. In pre-stellar cores, volume densities can range from $\gtrsim 10^6$ cm^{-3} at the centre to $\lesssim 10^2$ cm^{-3} at the edge. For example, the CO 1-0 transition has a n_{crit} of about 10^3 cm^{-3}, making LTE not applicable in the outer parts of the core. For transitions with high n_{crit}, LTE applies only in a small region near the centre of the core. When departing from LTE, collisional rate coefficients are needed to study the transfer of radiation.

Furthermore, in non-LTE conditions, the hyperfine component intensity ratio may diverge from statistical weights (e.g. Caselli et al. 1995; Bizzocchi et al. 2013; Faure & Lique 2012; Mullins et al. 2016). In order to accurately predict line intensities resulting from different physical conditions, a full non-LTE radiative transfer treatment with accurate collisional rate coefficients is required.

In Section 2.3.1 we describe the methodology for the hyperfine collisional rate coefficients calculations, in Section 2.3.2 we describe the physical model adopted for L1544 and the LOC radiative transfer code, and in Section 2.3.3 we present the chemical code used to compute the molecular fractional abundance profile.

2.3.1 Hyperfine collisional rate coefficient calculations

We determined $HC^{17}O^+$–H_2 rate coefficients from the close coupling (CC) HCO^+–H_2 rate coefficients ($k^{CC}_{J\rightarrow J'}(T)$) of Yazidi et al. (2014) using the infinite order sudden (IOS) approximation described in Faure & Lique (2012). We use HCO^+–H_2 collisional rate coefficients for $HC^{17}O^+$ as we do not expect a significant difference, as seen in Daniel et al. (2016) where the collisional rate coefficients for N_2H^+ (isoelectronic of HCO^+) and its ^{15}N isotopologues have been found to be similar.

In $HC^{17}O^+$, the coupling between the nuclear spin ($I = 5/2$) of the ^{17}O atom and the molecular rotation results in a weak splitting (Alexander 1985) of each rotational level J, into hyperfine levels. Each hyperfine level is designated by a quantum number F ($F = I + J$) varying between $|I - J|$ and $I + J$.

Within the IOS approximation, inelastic rotational rate coefficients $k^{IOS}_{J\rightarrow J'}(T)$ can be calculated from the 'fundamental' rates (those from the lowest $J = 0$ level) as follows (Corey & McCourt 1983):

$$k^{IOS}_{J\rightarrow J'}(T) = (2J'+1)\sum_L \begin{pmatrix} J' & J & L \\ 0 & 0 & 0 \end{pmatrix}^2 k^{IOS}_{0\rightarrow L}(T). \tag{2.1}$$

Similarly, IOS rate coefficients among hyperfine structure levels can be obtained from the $k^{IOS}_{0\rightarrow L}(T)$ rate coefficients using the following formula (Corey & McCourt 1983):

$$k^{IOS}_{jF\rightarrow j'F'}(T) = (2j+1)(2j'+1)(2F'+1)\sum_L \begin{pmatrix} j' & j & L \\ 0 & 0 & 0 \end{pmatrix}^2 \times \begin{Bmatrix} j & j' & L \\ F' & F & I \end{Bmatrix}^2 k^{IOS}_{0\rightarrow L}(T). \tag{2.2}$$

In the above, ( ) and { } are respectively the 3-j and 6-j Wigner symbols.

The IOS approximation, however, is expected to be only moderately accurate at low temperatures. As a result, we compute the hyperfine rate coefficients as (Faure & Lique 2012)

$$k^{INF}_{JF\to J'F'}(T) = \frac{k^{IOS}_{JF\to J'F'}(T)}{k^{IOS}_{J\to J'}(T)} k^{CC}_{J\to J'}(T), \tag{2.3}$$

using the CC rate coefficients $k^{CC}(0 \to L)$ of Yazidi et al. (2014) for the IOS fundamental rates ($k^{IOS}_{J\to J'}(T)$) in Eqs. 2.1-2.2.

In addition, we note that the fundamental excitation rates $k^{CC}_{0\to L}$ were replaced by the de-excitation fundamental rates using the detailed balance relation:

$$k^{CC}_{0\to L} = (2L+1)k^{CC}_{L\to 0}. \tag{2.4}$$

This procedure is found to significantly improve the results at low temperatures due to important threshold effects. The calculated rate coefficients can be found in Appendix A.3.

2.3.2 The LOC radiative transfer code

Using the radiative transfer code LOC (line transfer with OpenCL; Juvela 2020), we calculate the strength and shape of the $HC^{17}O^+$(1-0) spectrum, taking into account its hyperfine structure. The level populations are calculated with the statistical equilibrium equations, which are solved using an accelerated lambda iteration (ALI) (Rybicki & Hummer 1991) and the molecule's radiative and collisional rates. The radiative transfer is calculated using the 1D model in LOC, which takes into account the volume density, kinetic temperature, radial velocity, and microturbulence of a spherically symmetric physical structure (see below for physical parameter ranges).

The physical parameters for the modelling are extracted from a pre-stellar core physical model based on Keto et al. (2015). This 1D model of an unstable quasi-equilibrium Bonnor–Ebert sphere has been shown to be successful in reproducing the profile of several molecular transitions observed towards the dust peak in L1544 (Keto & Rybicki 2010; Keto & Caselli 2010; Caselli et al. 2012; Bizzocchi et al. 2013; Caselli et al. 2017; Redaelli et al. 2018, 2019, 2021; Caselli et al. 2022).

The radial profiles of the physical properties of the model are plotted in Figure 2.2. We note that in order to include these three parameters in this one plot, we show the logarithm of the molecular hydrogen number density, the gas temperature divided by 3, and the velocity scaled by -40. The value of n(H_2) ranges from 8×10^6 cm^{-3} at the centre of the core to 1×10^2 cm^{-3} at the edge of the core (0.32 pc); T ranges from 6 K at the centre of the core to 18 K at the edge; and v ranges from -0.14 km s^{-1} at the velocity peak ($\sim$ 0.01 pc) to -0.01 km s^{-1} at the edge of the core.

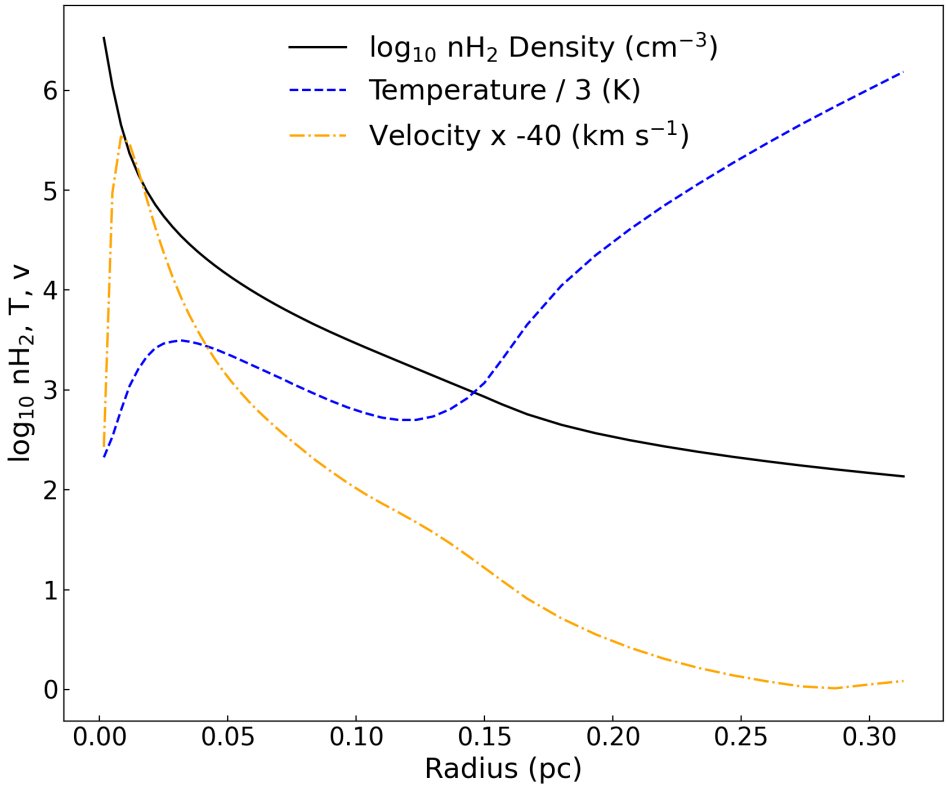

Figure 2.2: The radial profiles of the Keto et al. (2015) model physical parameters are plotted. The black solid line represents the number density of molecular hydrogen, the blue dashed line the gas temperature, and the orange dash-dotted line the velocity profile of the Keto et al. (2015) physical model. In order to display the various parameters in a single plot, the base 10 logarithm of the number density of molecular hydrogen, the temperature divided by 3, and the velocity scaled by -40 are shown.

2.3.3 Chemical code

The fractional abundance profile of $HC^{17}O^+$ is simulated using the pseudo-time dependent gas-grain chemical model described in Sipilä et al. (2015). Here, we used the same approach to simulate the chemical fractional abundances in L1544 as laid out in Sipilä et al. (2019). Briefly, we adopt the physical model for L1544 of Keto et al. (2015), which is separated into concentric shells; the results of chemical simulations carried out in each shell are combined, yielding time-dependent fractional abundance profiles for the various molecules in the chemical network. The physical structure of the core is thus fixed, while the chemistry evolves in a time-dependent manner. We refer the reader to Sipilä et al. (2015, 2019) for more details on the model, for example the initial fractional abundances. For the present work, we extracted several HCO^+ fractional abundance

profiles in a time interval between 10^4 and 10^7 years. The model does not treat oxygen isotope chemistry; to obtain the $HC^{17}O^+$ fractional abundance, we scaled the HCO^+ fractional abundance by the isotopic ratio $[^{16}O/^{17}O] = 2044$ (Penzias 1981; Wilson & Rood 1994). The same procedure was also followed for $C^{17}O$.

2.4 Results

2.4.1 $HC^{17}O^+$

The observed $HC^{17}O^+$(1-0) can be reproduced by using the pre-stellar core model and the $HC^{17}O^+$ fractional abundance profile at 5×10^5 yrs with small modifications. The results are shown in the two panels of Figure 2.3. The top left panel shows the original model (OM) LOC fit and the adopted model 1 (AM 1) LOC fit over the observations. The OM histogram is the spectrum LOC produces when using the original pre-stellar core model (from Keto et al. 2015) and the original $HC^{17}O^+$ fractional abundance profile. The AM 1 histogram is the spectrum LOC produces when using the original pre-stellar core model Keto et al. (2015) and a scaled-up (by a factor of 4) $HC^{17}O^+$ fractional abundance profile. We use AM 1 to compute the residuals, which can be found in the panel under the spectra. In order to reproduce the intensity of the hyperfine components, we had to scale up the $HC^{17}O^+$ fractional abundance profile by a factor of 4. However, this model fails to reproduce the double-peak morphology of the lines, and for this, a further change is needed.

The top right panel of Figure 2.3 shows (solid red histogram) a different adopted model 2 (AM 2) LOC fit overlaid on the observations (in black). The AM 2 corresponds to AM 1 with a scaled-up (by 30%, ranging from -0.4 at the velocity peak to -0.01 km s^{-1} at the edge of the core) velocity profile instead of the velocity profile from the pre-stellar core physical model of Keto et al. (2015). We use the AM 2 to compute the residuals, which can be found in the panel under the spectra. There is a reduction of the residual standard deviation of 0.7 mK compared to the AM 1 in the left panel, which only takes into account the $HC^{17}O^+$ fractional abundance profile scaling. The reasons behind the adjustments of the original pre-stellar core model are discussed in Section 2.5.

Using the $HC^{17}O^+$ fractional abundance profile in the adopted models of Fig. 2.3 and the physical structure given in input to LOC, we can derive the column density of $HC^{17}O^+$. This is done by integrating the multiplication of the fractional abundance profile (see Figure 2.4) by the gas density and convolving to the beam size (28"). The column density derived from the fractional abundance profile used to model the observations in Figure 2.3 is $5.4^{+0.7}_{-0.9} \times 10^{10}$ cm^{-2}. The column density uncertainty is derived with the approach used in Redaelli et al. (2018). We compute several models from scaled fractional abundance profiles, from which we derive the corresponding column density values. The χ^2 values are derived from the comparison of these models with the observations. We then plot χ^2 versus the column density values. The column density uncertainties are derived by setting a χ^2 upper and lower limits to 15%. The excitation temperature computed by LOC for the three $HC^{17}O^+$(1-0) hyperfine transitions throughout the core is plotted in Figure 2.5 in black. We can see that the T_{ex} profiles of the different hyperfine components do not vary significantly. In order to compare this method with the column density calculation from the line

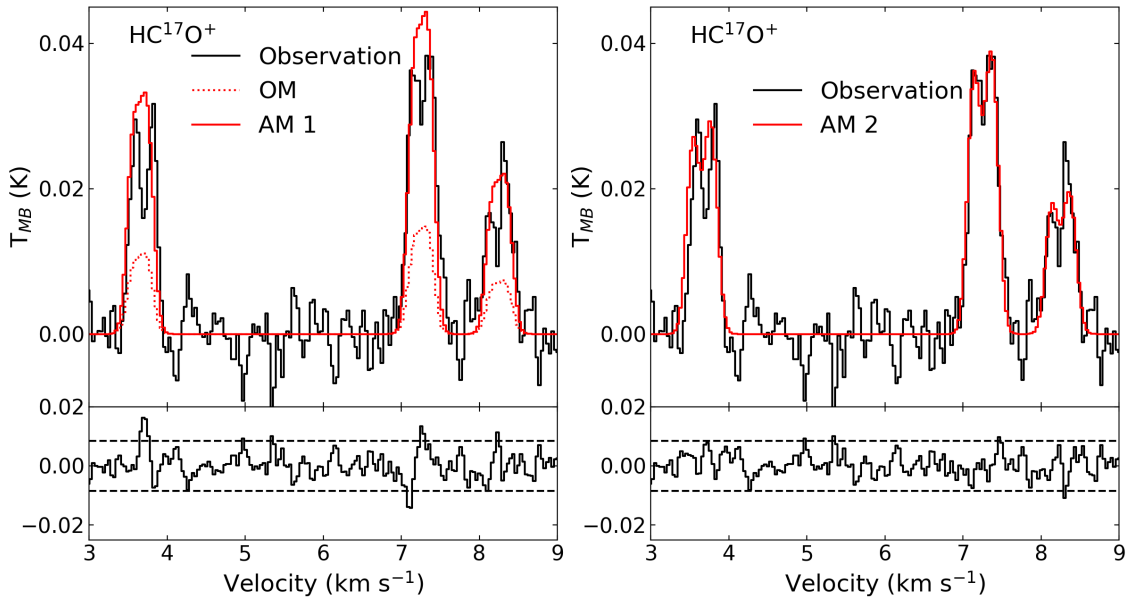

Figure 2.3: The results of the $HC^{17}O^+$ observed spectrum modelling with LOC are displayed. *Left.* Observed spectrum of the $HC^{17}O^+$(1-0) (black), the result of a simulation using the original $HC^{17}O^+$ fractional abundance profile at 5×10^5 yrs and the original pre-stellar core model (OM; dotted red) and the result of a simulation using the $HC^{17}O^+$ fractional abundance profile at 5×10^5 yrs upscaled by a factor of 4 times that of the original pre-stellar core model (AM 1; solid red). Residuals are computed with the adopted model and are shown in the lower panel. The dashed lines represent the 3σ levels. *Right.* Observed spectrum of the $HC^{17}O^+$(1-0) (black) and the result of a simulation using the $HC^{17}O^+$ fractional abundance profile at 5×10^5 yrs upscaled by a factor of 3 and an upscaled velocity profile by 30% (AM 2; solid red). Residuals are computed with the adopted model and are shown in the lower panel. The dashed lines represent the 3σ levels.

fitting with Gaussians in a C$T_{\rm ex}$ (constant $T_{\rm ex}$) approximation (see Caselli et al. 2002a), we perform hyperfine structure (HFS) fits in CLASS. Next, assuming an excitation temperature of 5 K, we calculate a $HC^{17}O^+$ column density of $4.1 \pm 0.3 \times 10^{10}$ cm^{-2}. The choice for $T_{\rm ex}$ comes from N_2H^+(1-0), which has a similar critical density to $HC^{17}O^+$(1-0) (1.4×10^5 and 1.5×10^5 cm^{-3}, respectively), observed towards L1544 in Crapsi et al. (2005). For this calculation, we use the optically thin approximation as we have confirmed the $HC^{17}O^+$ $J = 1$ - 0 transition to be optically thin (details of the calculation can be found in Appendix A.2). The column density derived with the simple C$T_{\rm ex}$ method is in agreement within the errors with the value derived with our model. Furthermore, we compare these two column density values with that obtained by scaling the $HC^{18}O^+$ column density derived in Redaelli et al. (2019) by [^{18}O/^{17}O]= 3.67, yielding a $HC^{17}O^+$ column density of $4.6 \pm 0.3 \times 10^{10}$ cm^{-2}.

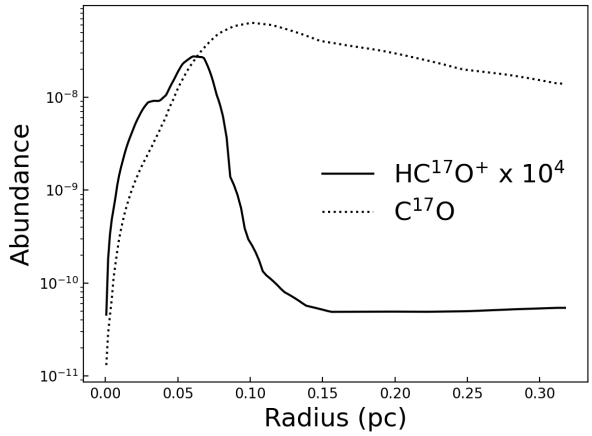

Figure 2.4: Comparison between the $HC^{17}O^+$ and $C^{17}O$ radial abundance profiles. The dotted curve shows the $C^{17}O$ fractional abundance (abundance with respect to H_2) as a function of radius. The solid curve shows the fractional abundance of $HC^{17}O^+$, scaled by 10^4 computed with the chemical code from Sipilä et al. (2015, 2019) by scaling the CO and HCO^+ fractional abundance profiles by the isotope ratio $[^{16}O/^{17}O]$ = 2044 (Penzias 1981; Wilson & Rood 1994).

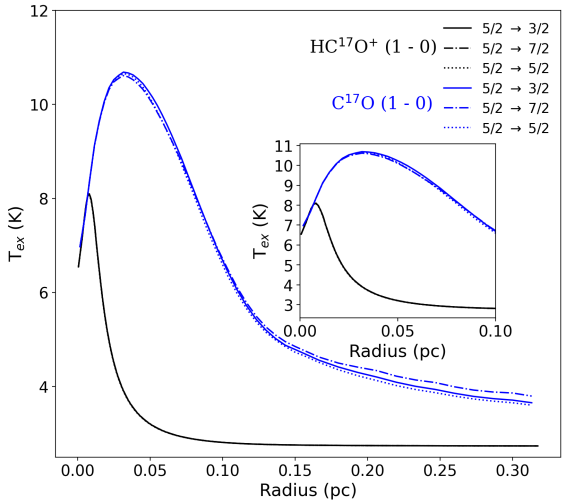

Figure 2.5: Excitation temperature profile of the three $HC^{17}O^+$(1-0) and $C^{17}O$(1-0) hyperfine transitions across the core. The $HC^{17}O^+$(1-0) $5/2 \rightarrow 3/2$, $5/2 \rightarrow 7/2$, and $5/2 \rightarrow 5/2$ transitions are plotted as a black solid line, a black dash-dotted line, and a black dotted line, respectively. The profiles for $HC^{17}O^+$ are superimposed. The $C^{17}O$(1-0) $5/2 \rightarrow 3/2$, $5/2 \rightarrow 7/2$, and $5/2 \rightarrow 5/2$ transitions are plotted as a blue solid line, a blue dash-dotted line, and a blue dotted line, respectively. The inset presents a zoom-in of the radial T_{ex} profile from 0 to 0.1 pc.

2.4.2 $C^{17}O$

The $J = 1$ - 0 transition of $C^{17}O$ has been observed towards L1544 by Chacón-Tanarro et al. (2019). Contrary to $HC^{17}O^+$, $C^{17}O$ presents single-peaked hyperfine components, even though it is also an optically thin transition. The critical densities of $HC^{17}O^+$(1-0) and $C^{17}O$(1-0) are 1.5×10^5 cm^{-3} and 2.0×10^3 cm^{-3}, respectively, as calculated from the Einstein and collisional coefficients at 10 K from the Leiden Atomic and Molecular Database (LAMDA)[3]. To model the hyperfine $C^{17}O$ emission, the hyperfine collisional rate coefficients were required, which we approximated from the non-hyperfine collisional rate coefficients available at LAMDA **(Yang et al. 2010)** with a Mj randomisation approach (Appendix A.4). We note that Dagdigian (2022) has recently also computed hyperfine $C^{17}O$ collisional rate coefficients using the recoupling technique. As in the case of $HC^{17}O^+$, we are able to reproduce the observed spectrum with the pre-stellar core model detailed in Section 2.3.2, and the fractional abundance profile at 5×10^5 yrs described in Section 2.3.3 with a scaling factor of 3. Results are shown in the two panels of Figure 2.6. The top left panel shows the OM LOC fit and the AM 1 LOC fit over the observations. The OM histogram is the spectrum LOC produces with the original pre-stellar core model and original $C^{17}O$ fractional abundance profile. The AM 1 histogram is the spectrum LOC produces with the original pre-stellar core model and a fractional abundance profile of $C^{17}O$ scaled up by a factor of 3, needed to fit the intensity of the observed lines (similar to those found in the case of $HC^{17}O^+$). The AM 1 is the model we use to compute the residuals, which can be found in the panel under the spectra. They show an overall good agreement between the AM 1 and the observations.

The top right panel of Figure 2.6 shows the AM 2 LOC spectrum overlaid on the observations. The AM 2 corresponds to the AM 1 with a velocity profile scaled up by 30% (ranging from -0.4 at the velocity peak to -0.01 km s^{-1} at the edge of the core). We use the AM 2 to compute the residuals, which can be found in the panel under the spectra. The bottom right panel shows the residuals obtained by subtracting the observed spectrum from the AM 2 spectrum. Contrarily to $HC^{17}O^+$, there is an increase in the residual standard deviation of 1.5 mK when a scaled-up velocity profile is adopted. Therefore, the best model for reproducing the $C^{17}O$ observed spectrum is the one that uses the increased (by a factor of 3) $C^{17}O$ fractional abundance profile and the original pre-stellar core velocity profile (AM 1 in the upper left panel of Figure 2.6). The reason behind this difference between $HC^{17}O^+$(1-0) and $C^{17}O$(1-0) observations is discussed in Section 2.5.

We have also computed the $C^{17}O$ column density from the fractional abundance profile used in LOC to fit the observations as done with $HC^{17}O^+$. The excitation temperature computed by LOC for the three $C^{17}O$(1-0) hyperfine transitions throughout the core is plotted in Figure 2.5 in blue. The T_{ex} profiles of the different hyperfine components do not vary significantly from each other. The calculated $C^{17}O$ column density is $4.8^{+0.7}_{-0.8} \times 10^{14}$ cm^{-2} (the uncertainty is calculated in the same way as for $HC^{17}O^+$). The column density calculated in Chacón-Tanarro et al. (2019) is $6.8 \pm 0.6 \times 10^{14}$ cm^{-2}, 41% higher than the column density extracted from the $C^{17}O$ fractional abundance profile used for the modelling with LOC. This difference in column densities could be due to the T_{ex} used; Chacón-Tanarro et al. (2019) assume a constant T_{ex} of 10 K across the core,

[3] https://home.strw.leidenuniv.nl/~moldata/

while LOC computes the column density using the T_{ex} radial profile (Figure 2.5).

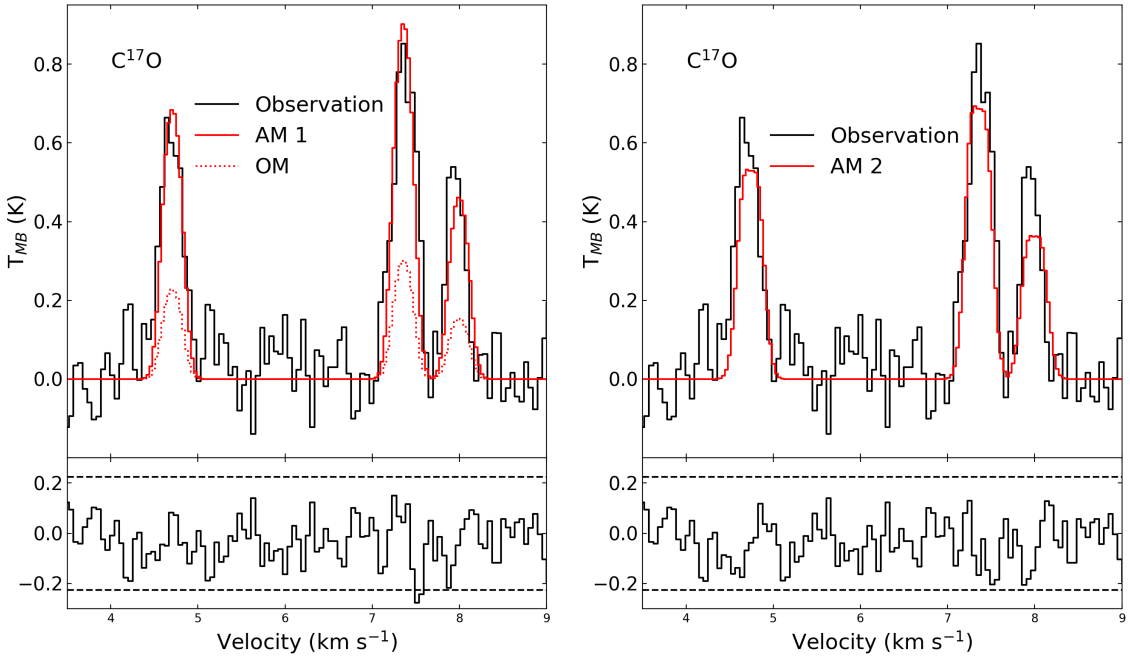

Figure 2.6: The results of the $C^{17}O$ observed spectrum modelling with LOC are displayed. *Left.* Observed spectrum of the $C^{17}O$ (1-0) (black). This spectrum is the result of a simulation using the original $C^{17}O$ fractional abundance profile at 5×10^5 yrs and the original pre-stellar core model (OM; dotted red) and the result of a simulation using the $C^{17}O$ fractional abundance profile at 5×10^5 yrs upscaled by a factor of 3 and the original pre-stellar core model (AM 1; solid red). The residuals are computed with the adopted model and are shown in the lower panel. The dashed lines represent the 3σ levels. *Right.* Observed spectrum of the $C^{17}O$ (1-0) (black) and the result of a simulation using the $C^{17}O$ fractional abundance profile at 5×10^5 yrs increased by a factor of 3 and a scaled-up velocity profile by 30% (AM 2; solid red). Residuals are computed with the adopted model and are shown in the lower panel. The dashed lines represent the 3σ levels.

2.5 Discussion

In past works, two scenarios have been discussed to explain the double-peaked morphology in optically thin transitions observed towards L1544 (Tafalla et al. 1998; Caselli et al. 2002a): the presence of two velocity components in the line of sight and the depletion of the molecules towards the centre of the core.

The double-peaked structure of the optically thin $C^{34}S$ (2-1) line is thought to arise from two separate velocity components on the line of sight at 7.10 and 7.25 km s^{-1} that overlap in the centre (Tafalla et al. 1998). We discard the two velocity component scenario for our case as this would produce double-peaked lines also from $C^{17}O$(1-0), in disagreement with observations, as shown in Fig. 2.6. Moreover, we are able to reproduce the $HC^{17}O^+$(1-0) line profile using a simple model of an individual object in contraction, as also found in the past using other molecular lines.

In Caselli et al. (2002a) it is suggested that the optically thin double-peaked line profiles of the $F_1, F = 1,0 \rightarrow 1,1$ line of N_2H^+ (1-0) and $HC^{18}O^+$ (1-0) towards L1544 arise from the depletion of these molecules towards the centre of the core. To mimic this depletion, the fractional abundances of N_2H^+ and $HC^{18}O^+$ were set to 0 between the centre and 2000 au and 1400 au, respectively. The size of these gaps in the fractional abundance profiles are related to the radius from the centre of the core at which these molecules present significant depletion. This artificial depletion reproduced the $F_1, F = 1,0 \rightarrow 1,1$ line of N_2H^+ (1-0) and $HC^{18}O^+$ (1-0) line profiles. To test whether an enhanced depletion of $HC^{17}O^+$ towards the core centre would reproduce the observations, we created a 'hole' in the fractional abundance profile, similarly to Caselli et al. (2002a) (more information in Appendix A.1.1), but the central depletion of $HC^{17}O^+$ does not reproduce the observed line profile (e.g. Figure A.1). This was expected as the chemical model already naturally predicts the depletion of HCO^+ towards the central part of the core.

Self-absorption is not expected to produce double peaks in lines of low species, as their concentration in the low-density foreground layer is not large enough to absorb photons emitted in the dense core. Nevertheless, self-absorption has been considered as a possible contribution to double-peaked line morphologies for some transitions in past works (Caselli et al. 1999, 2002a). To make sure that a sufficient of $HC^{17}O^+$ in a foreground layer would not induce self-absorption, we modelled the observations by adding a profile from 0.3 to 1.5 pc with a $HC^{17}O^+$ layer corresponding to a visual extinction of A_v=4 mag (more information in the Appendix A.1.2). This test also did not reproduce the observed spectrum, as shown in Figure A.2.

One of the parameters that improved the fitting of lines in L1544 in past works is the velocity profile. In Bizzocchi et al. (2013), upscaling the velocity profile by 75% was necessary to reproduce the high-sensitivity observations of N_2H^+(1-0) towards L1544. Both the observed linewidth and line profiles are well reproduced with LOC using a constant alongside the upscaled velocity profile from the Keto & Caselli (2008) physical structure model (Figure 5 in Bizzocchi et al. 2013). The upscaling of the velocity profile allows the further splitting in velocity of the two contracting parts of the cloud lying in front and behind the core centre where the density is close to the critical density of the transition (1.5×10^5 cm^{-3}). As in Bizzocchi et al. (2013), in our case, this is reflected in the split of the $HC^{17}O^+$(1-0) hyperfine components in agreement with the observed spectrum shown in Figure 2.1.

Infall motions were also invoked to explain the double-peaked profiles of $HC^{18}O^+$ 1-0 and N_2H^+ 1-0 towards the dust peak of L1544 in van der Tak et al. (2005). $HC^{18}O^+$ presents a line split where the two peaks appear with the same intensity, while N_2H^+ presents the well-known blue asymmetry in the peak intensity, indicating that the line is self-absorbed. In this paper, they combine the core physical model from Galli et al. (2002) with infall models at the t3 and t5 time steps from Ciolek & Basu (2000), which correspond respectively to 2.660 and 2.684 Myr after the start of the core collapse. Nevertheless, this model was not able to reproduce the H_2D^+ 1_{10}-1_{11}spectral line profile. In our work, we used a physical core model (Keto & Caselli 2010), which was tailored specifically for L1544 and includes infall dynamics which are consistent with the physical structure, as well as a state-of-the-art chemical model (Sipilä et al. 2015). Our model reproduced a great number of molecular lines (see Section 2.3.2) including $HC^{18}O^+$ (1-0) and N_2H^+ (1-0) in Redaelli et al. (2019). Moreover, the higher spectral resolution (by 0.02 km s^{-1}) of our $HC^{17}O^+$ (1-0) spectrum and the hyperfine splitting allows us to refine the physical model by fitting the line profile, compared to previous $HC^{18}O^+$ (1-0) observations. The velocity profiles used in van der Tak et al. (2005) range for t3 and t5 are respectively from -0.01 to -0.14 and -0.01 to -0.19 km s^{-1} (see Figure 2 in Ciolek & Basu 2000). These velocity profiles differ from the one we used to model $HC^{17}O^+$, where the velocity peak has an average of 2.5 times higher velocity than the maximum velocity in the profiles used for the modelling in van der Tak et al. (2005).

The different line profiles of $HC^{17}O^+$(1-0) and $C^{17}O$(1-0) arise from their different critical densities and spatial distributions in the core. $HC^{17}O^+$ and $C^{17}O$ have different critical densities (1.5×10^5 cm^{-3} and 2.0×10^3 cm^{-3}, respectively). The profile and critical density combination causes the $HC^{17}O^+$ line to emit preferentially closer to the core centre (see its excitation temperature profile in Fig. 2.5, in black), while $C^{17}O$ has a more extended emission (see its excitation temperature profile in Fig. 2.5, in blue). As $HC^{17}O^+$ emits in a small region close to the centre, where the contraction velocity also has a peak, the spectrum results in a double peak, where the local contraction velocity is 30% higher than in the original model of Keto et al. (2015). Unlike $HC^{17}O^+$, the $C^{17}O$ emission arises from lower density gas further away from the core centre where the contraction velocity is lower (see Fig. 2.2), resulting in a single peak. The fact that an upscaled velocity profile fits the $HC^{17}O^+$(1-0) line profile but not $C^{17}O$ simply tells us that the infall velocity is higher towards the inner part of the core, as expected in a contracting Bonnor–Ebert sphere (Keto & Rybicki 2010) at a more evolved stage compared to the one adopted by Keto et al. (2015). We estimate that it would take an additional 1×10^4 yrs for the infall velocity peak to increase by 30%. We also note that L1544 is not spherically symmetric, as assumed so far, but has an elongated structure (Caselli et al. 2002a). More complex simulations have been done taking into account a flattened structure for L1544, which more closely resembles reality (Caselli et al. 2019). Nevertheless, Caselli et al. (2022) show that the density and velocity profiles along the major and minor axes of the 3D simulation are very close to the same profiles in the spherically symmetric model of Keto et al. (2014), reinforcing the accuracy of the Keto et al. (2015) model, despite its simplicity. The need to take into account the physical structure and kinematics of a source when interpreting its spectra is made evident in this work. Using a slab model that does not take into account the physical or the kinematic structure of the core can lead to the derivation of non-accurate parameters and, in this case, does not allow us to reach any conclusions about the nature of the physical process behind the double-peaked profiles. As we show in Section 2.4, the

$HC^{17}O^+$ and $C^{17}O$ models both required an upscaling of the fractional abundance profile used to fit the observations. The necessary $HC^{17}O^+$ fractional abundance adjustment required to fit the observations is done by adjusting the HCO^+ profile predicted by our chemical code (see Section 2.3.3). We note that the HCO^+ fractional abundance profile resulting from a static model, where the physical structure is kept fixed while the chemistry is evolving, differs from the profile computed with a dynamic model, as can be seen in the central upper panel in Figure 12 in Sipilä & Caselli (2018). The fractional abundance profile of HCO^+ in the static model appears approximately three times higher than the profile obtained with the dynamic model at the very centre of the core (until 2.0×10^4 au) and about four times lower from 2.0×10^4 to 2.5×10^4 au. However, the physical model discussed in Sipilä & Caselli (2018) refers to a dense core with a mass of 7.2 $M_\odot$, which is significantly lower than that of L1544 described by Keto & Caselli (2010) (10 $M_\odot$), so the dynamic model results cannot be used here. We are currently preparing a new dynamical model for L1544 that will help to constrain the issue of static versus dynamic models (Sipilä et al. 2022 Submitted). Finally, the fact that the fractional abundances of $HC^{17}O^+$ and $C^{17}O$ needed to be upscaled by a similar factor can be the consequence of too large CO depletion compared to the observations, also suggesting that dynamics could help in better reproducing our data (as less CO-depleted material keeps moving towards the central regions, unlike in the static model).

2.6 Conclusions

In this work, we have presented new high-sensitivity and high-resolution $HC^{17}O^+$ $J = 1$ - 0 observations towards the dust peak of L1544, which has revealed the double-peaked nature of its hyperfine components. By carrying out a full non-LTE radiative transfer modelling of $HC^{17}O^+$(1-0) with new hyperfine collisional rate coefficients, we have explored what is causing the double-peaked profile observed in optically thin transitions of high-density tracers. The power of fully taking into account radiative transfer is made evident in this work, where modelling of the entire source is needed to reproduce the observed line profile. Moreover, we have tested the model by reproducing previous observations of the $C^{17}O$(1-0) line, which presents a single-peaked line morphology. Our main conclusions are as follows:

- The $HC^{17}O^+$(1-0) line profile can be reproduced with a model of a contracting pre-stellar core; there is no evidence for separate velocity components along the line of sight. This indicates that a double-peaked profile towards a centrally condensed core can be solely an effect of radiative transfer in a contracting centrally concentrated dense core. In the present work, the reason for the double peak lies in the infall velocity and the critical density of the line. This makes the line sensitive to the motions at radii of about 0.01 pc where the volume density is close to the critical density, and the contraction velocity has a peak.

- The fact that an upscaled velocity profile was required to reproduce $HC^{17}O^+$ but not $C^{17}O$ suggests that the L1544 pre-stellar core is more dynamically evolved than previously thought (1×10^4 yrs), as higher velocities (30% higher than the original physical model) are required towards the core centre to reproduce the splitting. Higher central velocities are, in fact, expected in contracting BE spheres at later stages of evolution (Keto & Caselli 2010).

- Both the $HC^{17}O^+$ and $C^{17}O$ fractional abundances are underproduced by our chemical models by a factor of 4 and 3, respectively. This suggests that the predicted CO freeze-out is too large, possibly due to the physical model not evolving dynamically.

Line profiles are shown to be powerful tools to gain insight into the physical, chemical, and kinematic structure of pre-stellar cores. In the future, we will build upon the results of this manuscript with the study of complementary transition line profiles towards L1544.

Acknowledgements. J.F.A., S.S., P.C., F.O.A., O.S, E.R. and L.B gratefully acknowledge the support of the Max Planck Society.

3

Millimetre and sub-millimetre spectroscopy of doubly deuterated acetaldehyde (CHD_2CHO) and first detection towards IRAS 16293-2422

The content of this chapter was published in the Astronomy & Astrophysics Journal. Credit: Ferrer Asensio et al., 2023, A&A, A177, 12 pp, (reproduced with permission ©AAS.)

The abundances of deuterated molecules with respect to their main isotopologue counterparts have been determined to be orders of magnitude higher than expected from the cosmic abundance of deuterium relative to hydrogen. The increasing number of singly and multi-deuterated species detections helps us to constrain the interplay between gas-phase and solid-state chemistry and to understand better deuterium fractionation in the early stages of star formation. Acetaldehyde is one of the most abundant complex organic molecules (COMs) in star-forming regions, and its singly deuterated isotopologues have already been observed towards protostars.
A spectroscopic catalogue for astrophysical purposes is built for doubly deuterated acetaldehyde (CHD_2CHO) from measurements in the laboratory. With this accurate catalogue, we aim to search for and detect this species in the interstellar medium and retrieve its column density and abundance. Sub-millimetre wave transitions were measured for the non-rigid doubly deuterated acetaldehyde CHD_2CHO displaying hindered internal rotation of its asymmetrical CHD_2 methyl group. An analysis of a dataset consisting of previously measured microwave transitions and of the newly measured ones was carried out with an effective Hamiltonian, which accounts for the tunnelling of the asymmetrical methyl group.
A line position analysis was carried out, allowing us to reproduce 853 transition frequencies with a weighted root mean square standard deviation of 1.7, varying 40 spectroscopic constants. A spectroscopic catalogue for astrophysical purposes was built from the analysis results. Using this catalogue, we were able to detect, for the first time, CHD_2CHO towards the low-mass proto-stellar system IRAS 16293-2422 utilising data from the ALMA Proto-stellar Interferometric Line Survey. The first detection of the CHD_2CHO species allowed for the derivation of its column density with a value of 1.3×10^{15} cm^{-2} and an uncertainty of 10-20%. The resulting D_2/D ratio of $\sim$ 20% is found to be coincident with D_2/D ratios derived for other COMs towards IRAS 16293-2422, pointing to a common formation environment with enhanced deuterium fractionation.

3.1 Introduction

The number of multi-deuterated molecules detected in the interstellar medium (ISM) has increased substantially in the last years (e.g. CHD_2OH and CD_3OH (Parise et al. 2002, 2004), c-C_3D_2 (Spezzano et al. 2013), D_2CO (Turner 1990), CHD_2OHCHO(Manigand et al. 2019), D_2O (Butner et al. 2007), and CH_3OCHD_2 (Richard et al. 2021)). In recent years, the Atacama Large Millimeter/submillimeter Array (ALMA) telescope opened up the possibility of measuring the abundances of these species in a more unambiguous manner. The high spatial resolution of the interferometer allowed the warm gas around protostars to be zoomed into where these molecules appear. The ALMA Proto-stellar Interferometric Line Survey (PILS) towards the proto-stellar system IRAS 16293-2422 (Jørgensen et al. 2016) has allowed for the detection and accurate column density derivation of several multi-deuterated species (e.g. Persson et al. 2018 and Jensen et al. 2021). Doubly deuterated molecules are found to be more abundant than expected when taking the local ISM deuterium abundance into account (D/H = $2.0 \pm 0.1 \times 10^{-5}$, Linsky (2003); Caselli & Ceccarelli (2012); Ceccarelli et al. (2014) and references therein). The enrichment of molecules with deuterium, known as deuterium fractionation, is an interesting diagnostics tool that can be used as a clock to trace molecules to the time and environment of their formation (Ceccarelli et al. 2014). For example, the D/H ratio for methanol found in comets agrees with the ratio derived in pre-stellar cores and low-mass proto-stellar regions linking the cometary methanol to the first stages of star formation (Drozdovskaya et al. 2021). Furthermore, the water D/H ratio on Earth is found to be more similar to the one observed in proto-stellar cores, in clustered star-forming regions, than that in isolated proto-stellar cores (Jensen et al. 2019), supporting the interpretation that the Sun was formed in a clustered star-forming environment (Adams 2010). I am running a few minutes late; my previous meeting is running over.

Deuteration is most effective in the pre-stellar core environment due to the low temperatures present (< 10 K) (e.g. Caselli et al. 2002b and Crapsi et al. 2007). Due to the lower zero point energy (ZPE) of deuterium, this forms stronger bonds than hydrogen at low temperatures, making the equilibrium of the reaction $H_3^+ + HD \rightleftharpoons H_2D^+ + H_2$ shift to the right-hand side in pre-stellar cores (e.g. Pagani et al. 1992). Moreover, in these environments, CO, which is the main destructor of H_3^+ and H_2D^+, is heavily frozen onto the surface of dust grains (e.g. Caselli et al. 1999). As a consequence, pre-stellar cores have a higher H_2D^+/H_3^+ ratio (Dalgarno & Lepp 1984). The H_2D^+ and other multi-deuterated forms of H_3^+ are the main deuteration agents in the gas phase. On the other hand, H-D substitution reactions on the surface of dust grains have been proposed to explain the observed deuterium fractionation (Drozdovskaya et al. 2022 and references therein). In Ambrose et al. (2021), deuterated methanol (CH_2DOH) was observed towards nine of the 12 starless and pre-stellar sources observed, deriving a median value $[CH_2DOH]/[CH_3OH]$ ratio of 0.11.

Deuterated molecules found in sources at later stages of the star formation process are thought to be inherited from the pre-stellar core phase. The molecules trapped in the ice mantles of dust grains are released into the gas phase due to the heating of the central protostar, making their detection possible (Taquet et al. 2014). Observation of the D/H ratios towards the proto-stellar system IRAS 16293-2422 has revealed a generalised trend with smaller molecules (e.g. methanol,

formic acid, formaldehyde) having a D/H ∼2% and larger molecules (e.g. dimethyl ether, ethanol) displaying a D/H ∼4–8% (Jørgensen et al. 2018). van Gelder et al. (2022) compared observations of deuterated methanol towards high-mass protostars with literature observations encompassing multiple stages and masses of the star formation process. They observe that the $[CH_2DOH]/[CH_3OH]$ ratio for high-mass protostars is lower than the one for the low-mass protostars. However, the $[CHD_2OH]/[CH_2DOH]$ ratio is found to be similar amongst high- and low-mass protostars. In the same paper, by using the gas-grain chemical model GRAINOBLE (Taquet et al. 2012, 2013 and Taquet et al. 2014), the authors suggest that the methanol deuteration levels in high-mass protostars could indicate that this molecule was formed in a warm environment (>20K) or that the pre-stellar phase within which they formed was short-lived.

The fact that D_2/D ratios are observed to be higher than D/H ratios implies that multiple deuteration is more favourable than the first deuteration, which is supported by laboratory experiments (Nagaoka et al. 2005, 2007, and Hidaka et al. 2009). In the case of methanol, from the observed D/H and D_2/D column density ratios in the comet 67P/Churyumov–Gerasimenko, the formation of singly deuterated methanol (CH_2DOH) is constrained to happen via the H-D substitution of the main isotopologue (CH_3OH) (Drozdovskaya et al. 2021). On the other hand, doubly deuterated methanol (CHD_2OH) is deduced to form from the hydrogenation of doubly deuterated formaldehyde (D_2CO) (Drozdovskaya et al. 2021). The study of methanol deuteration sets an example as to the importance of deriving column density ratios of singly and multi-deuterated species for the purpose of understanding the nature of deuterium fractionation and the interplay of the chemistry in the gas phase and on the surface of dust grains.

The astrophysically relevant molecule acetaldehyde and its isotopologues have been the focus of numerous spectroscopic studies due to the internal rotation of their methyl group. The microwave spectrum of the main isotopologue (CH_3CHO) was first analysed by Kilb et al. (1957). Subsequently, its analysis was extended up to the $\upsilon_t = 4$ torsional state (Hershbach 1959; Iijima & Tsuchiya 1972, and Bauder & Günthard 1976), enabling its first detection in the ISM by Gilmore et al. (1976). The isotopic species with either a deuterated COD aldehyde group or a fully deuterated CD_3 methyl group were also investigated (Coudert & López 2006; Elkeurti et al. 2010, and Zaleski et al. 2017), of which the CH_3CDO species has been detected in the ISM by Jørgensen et al. (2018). Spectroscopic results are also available for isotopic species with a partially deuterated CH_2D or CHD_2 asymmetrical methyl group. The monodeuterated species CH_2DCHO has been the subject of several investigations (Turner & Cox 1976; Turner et al. 1981, and Coudert et al. 2019), which led to its detection in the ISM (Coudert et al. 2019). The doubly deuterated species CHD_2CHO has also been studied (Turner & Cox 1976 and Turner et al. 1981), but only a few transitions characterised by low K_a values were assigned in a microwave spectrum. Due to the high levels of confusion in the observational spectra towards star-forming regions, high-accuracy spectroscopic catalogues are crucial for the detection of species in the ISM, which stresses the need to extend the study on CHD_2CHO beyond the work done by Turner & Cox (1976) and Turner et al. (1981) towards higher J and K_a.

The doubly deuterated isotopic variant of acetaldehyde CHD_2CHO is investigated in this work. The analysis of its microwave and sub-millimetre wave spectra is reported in Section 3.2, where a spectroscopic catalogue is also built. Section 3.3 deals with the astrophysical search in ALMA PILS and the detection of this species. In Section 3.4, we present the discussion. Lastly, our

conclusions can be found in Section 3.5.

3.2 Spectroscopic investigation of CHD_2CHO

Theoretical models aimed at accounting for the internal rotation of molecules displaying internal rotation of a symmetrical CH_3 or CD_3 methyl group were developed a long time ago (Koehler & Dennison 1940; Burkhard & Dennison 1951; Ivash & Dennison 1953; Hecht & Dennison 1957a,b; Lees & Baker 1968, and De Lucia et al. 1989) and successfully applied to the main isotopic species of methanol and acetaldehyde. The efforts to characterise the internal rotation of symmetrical methyl groups are still under study Ilyushin et al. 2020; Kleiner & Hougen 2020, and Xu et al. 2021). These models cannot be used for molecules displaying internal rotation of a partially deuterated CH_2D or CHD_2 methyl group. Alternate models were designed for such molecules and applied to mono- and doubly deuterated methyl formate and methanol (Margulès et al. 2009; Coudert et al. 2012; Pearson et al. 2012; Coudert et al. 2014; Ndao et al. 2015, and Coudert et al. 2021). The Hamiltonian used in the present investigation is based on the theoretical model developed for monodeuterated methyl formate by Margulès et al. (2009), which relies on the high-barrier internal axis method (IAM) approach of Hougen (1985) and Coudert & Hougen (1988). In this section, the experimental spectrum is described and after briefly outlining the IAM approach, the fitting of previously available microwave transitions (Turner & Cox 1976 and Turner et al. 1981) and of the newly measured sub-millimetre ones are reported.

3.2.1 Experimental

The rotational transitions were recorded in the 82.5–450 GHz frequency range using the broadband Chirped-Pulse Fourier Transform Spectrometre (CP-FTS) as well as the high-resolution absorption experiment in the Center for Astrochemical Studies Laboratory of the Max-Planck-Institute für Extraterrestrische Physik in Garching, Germany.

The doubly deuterated acetaldehyde sample was synthesised by warming up a mixture of equal weights of CH_3CHO and D_2O in an acidic medium ($KHSO_4$, pH=1) with a silicone bath at 38°C for 2 weeks. Separation of the organic phase, where the molecule is dissolved in, from the water phase was done by manual decantation. The first low J and K_a line recordings were done with CP-FTS, which allows for an instantaneous bandwidth of 20 GHz in the frequency range of 75–110 GHz. The Chirped-Pulse was produced by an arbitrary waveform generator (Keysight, M8190A). The signal was then upconverted and amplified by an image quality (IQ) modulator and a solid-state amplifier, respectively, before entering the chamber. Thereafter, the signal was amplified, downconverted, and digitised.

For lines at higher J and K_a, which require an increased sensitivity, we moved on to recording with the frequency-modulated absorption spectrometre (Bizzocchi et al. 2017). The radiation source is an active multiplier chain (Virginia Diodes, Inc.) connected to a synthesiser (Keysight E8257D PSG Analog Signal Generator) operating between 250 kHz and 67 GHz. The synthesiser is also connected to a 10 MHz rubidium frequency clock. A combination of frequency multipliers allowed us to access the range between 82.5 and 450 GHz covered by the measurements. The

detector used is a liquid-He-cooled InSb hot electron bolometre (QMC Instr. Ltd.). Frequency modulation of the signal was applied to reduce the noise, and then the output signal was demodulated at $2f$ (where f denotes the modulation frequency) with a lock-in amplifier (Standford Research Systems SR830). The sample was at an average pressure of 1.2×10^{-2} mbar in the cell during measurements with both setups, and the linewidth was limited by Doppler broadening. All of the measurements were carried out at room temperature. Figure 3.1 shows a sample of the measurement scans, and Figure 3.2 shows the Out configuration a-type $17_{K_a} \rightarrow 16_{K_a}$ transitions for K_a ranging from 6 to 9 (see Figure 3.3 for a structural reference of the in and Out configurations.)

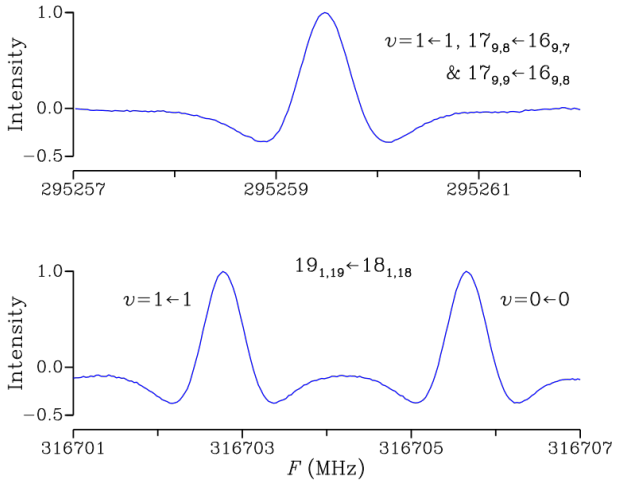

Figure 3.1: $\upsilon = 0$ and 1 tunnelling components, arising from the two isoenergetic Out configurations of several a-type transitions. The upper panel shows the $\upsilon = 1$ component of the unresolved K-type doublet $17_9 \leftarrow 16_9$. The lower panel depicts the $\upsilon = 0$ and 1 tunnelling components of the $19_{1,19} \leftarrow 18_{1,18}$ transition.

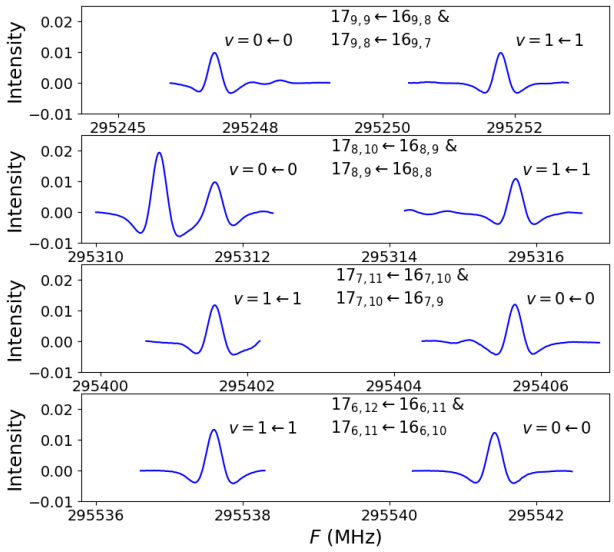

Figure 3.2: $\upsilon = 0$ and 1 tunnelling components of the a-type $17K_a \leftarrow 16K_a$ transitions, displaying no resolved asymmetry splitting, with $6 \leq K_a \leq 9$. The line at 295 312 MHz in the second panel is unidentified.

3.2.2 Theory

The theoretical model developed previously for monodeuterated methyl formate (Margulès et al. 2009) can be applied to doubly deuterated acetaldehyde CHD_2CHO with only a few changes. The main one concerns the relative energy of the non-superimposable equilibrium configurations, defined in agreement with the IAM approach of Hougen (1985) and Coudert & Hougen (1988). As emphasised by Fig. 3.3, in doubly deuterated acetaldehyde, just as in monodeuterated methyl formate, there arise three equilibrium configurations which can be identified by their configuration number n, with $n = 1$, 2, and 3, and characterised by $\alpha_{\rm eq}^{(n)}$, the value of the torsional angle $\alpha = \angle$HCCO about which the reference function is localised. Configurations 1 and 2 are the two

C_1 symmetry Out configurations with the hydrogen atom outside the CCO plane. They are lower in energy than Configuration 3, the C_s symmetry In configuration with the hydrogen atom in the CCO plane. The energy difference E_d between the In and Out configurations is not known exactly as of yet, but it is expected to be very close to the zero-point vibrational energy difference:

$$E_d = E_{\text{zpe}}(\text{In}, \text{CHD}_2\text{CHO}) - E_{\text{zpe}}(\text{Out}, \text{CHD}_2\text{CHO}) \; . \tag{3.1}$$

An approximate value of this difference was retrieved from E'_d, the equivalent energy difference for the monodeuterated species CH_2DCHO (we refer to Figure 2 in Coudert et al. 2019 for a visual representation of these conformers):

$$E'_d = E_{\text{zpe}}(\text{Out}, \text{CH}_2\text{DCHO}) - E_{\text{zpe}}(\text{In}, \text{CH}_2\text{DCHO}) \; . \tag{3.2}$$

The ratio $r = E_d/E'_d$ was computed using ab initio calculations. A calculation at the B3LYP/6-31G(d) level of theory with the Gaussian 16 package (Frisch et al. 2016) yielded $r = 0.9311$. Since E'_d, which was first estimated by Turner et al. (1981) and Cox et al. (2003) and determined later with a higher accuracy by Coudert et al. (2019), is 15.558 66(4) cm^{-1}, we obtain $E_d = 14.487\ \text{cm}^{-1}$.

The theoretical results in Sections 3.2 and 3.3 of Margulès et al. (2009) can be used in the case of CHD_2CHO provided a few changes, due to the definition of E_d in this work, are made. Equation (8) of these authors should be changed to:

$$\langle \psi_3 | H_t | \psi_3 \rangle = \langle \psi_1 | H_t | \psi_1 \rangle + E_d = \langle \psi_2 | H_t | \psi_2 \rangle + E_d \tag{3.3}$$

and E_d should be ignored in their Eq. (21) and in their Table 2; in their Table 1, it should only appear for diagonal matrix elements involving two wavefunctions corresponding to Configuration 3. Table 3.1 of the present work lists the computed values for the rotational constants and dipole moment components of the In and Out configurations as retrieved from the structure of Kilb et al. (1957) and the dipole moment components reported in Table 16 of Turner & Cox (1978) for CH_3CHO. Equations (12) and (13) of Margulès et al. (2009) should be used with no change being made to obtain the tunnelling matrix element $H_{JK\gamma 1;JK'\gamma' 2}$ of the $1 \rightarrow 2$ tunnelling path connecting the isoenergetic Configurations 1 and 2. Similarly, Eqs. (14) and (15) should be used for the tunnelling of matrix element $H_{JK\gamma 1;JK'\gamma' 3}$ of the $1 \rightarrow 3$ tunnelling path connecting Configurations 1 and 3. The rotational dependence of these tunnelling matrix elements was parameterised by two sets of Eulerian-type angles, θ_2, ϕ_2 and χ_3, θ_3, ϕ_3, which were numerically evaluated using the structure of Kilb et al. (1957) and which are also given in Table 3.1. In Eqs. (12)–(15) of Margulès et al. (2009), h_2 and h_3 are the magnitude of the tunnelling splittings. These parameters – the Eulerian-type angles $\theta_2, \phi_2, \chi_3, \theta_3$, and ϕ_3; the rotational constants of the In and Out configurations; and the energy difference E_d – allowed us to compute the rotation-torsion energy of the first three torsional states of CHD_2CHO to zeroth order.

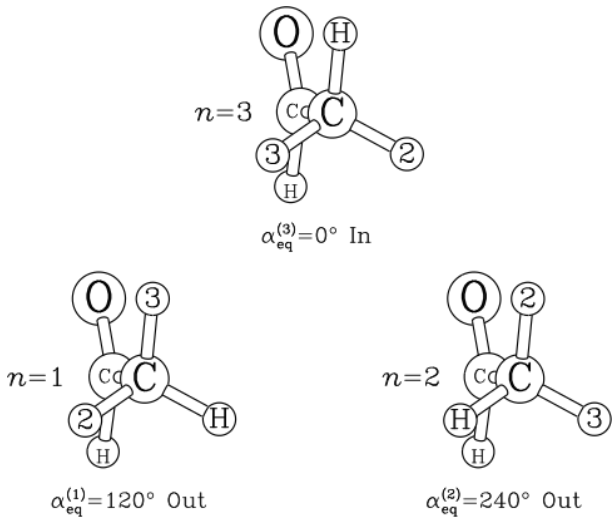

Figure 3.3: Two energetically equivalent out configurations and the higher energy In configuration are identified by their configuration number $n = 1$, 2, and 3. The two deuterium atoms are labelled 2 and 3. Furthermore, $\alpha_{eq}^{(n)}$ is the equilibrium value of the torsional angle $\alpha = \angle$HCCO. Configuration 3, displaying a symmetry plane and therefore having C_s symmetry, is approximately 14.487 cm^{-1} above Configurations 1 and 2 with C_1 symmetry.

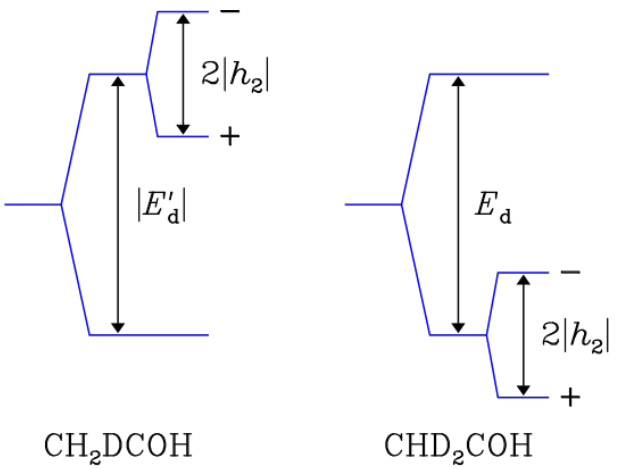

Figure 3.4: $J = 0$ tunnelling pattern of CH_2DCHO and CHD_2CHO as retrieved by Margulès et al. (2009). The tunnelling parameter h_2 and the energy differences E_d and E'_d are defined in Section 3.2.2. The tunnelling sub-levels for CHD_2CHO are also labelled with the quantum number υ such that $\upsilon = 0$ and 1 correspond to the + and - tunnelling sub-levels, respectively, and $\upsilon = 2$ to the In conformation level.

When tunnelling effects are small, the In configuration displays asymmetric-top rotational energies shifted by $+E_d$. For the + and − sub-levels arising from the Out configurations, Eq. (21) of Margulès et al. (2009) shows that $\pm h_2$ should be added to the asymmetric-top rotational energies, where the upper (lower) sign is for the + (−) sub-level. As h_2 is negative (Hougen 1985 and Coudert & Hougen 1988), the + sub-level is below the − sub-level. The resulting tunnelling pattern for $J = 0$ is drawn in Fig. 3.4 where it is compared to that of the monodeuterated species CH_2DCHO. In agreement with the energy level diagram for CHD_2CHO in this figure, the vibrational quantum number υ, with $0 \leq \upsilon \leq 2$, was introduced. Furthermore, $\upsilon = 0$ and 1 refer to rotational levels arising from the + and – tunnelling sub-levels, respectively, and $\upsilon = 2$ to those arising from the In configuration. The results presented for CH_2DCHO by Coudert et al. (2019) concerning selection rules, distortion terms for the tunnelling matrix elements, and the assignment of the levels arising from numerical diagonalisation of the Hamiltonian matrix also apply for CHD_2CHO and readers are referred to that paper for further information.

Table 3.1: Calculated molecular parameters

Parameter	Value	Parameter	Value
χ_2	241.9	χ_3	241.3
θ_2	4.7	θ_3	3.7
ϕ_2	61.9	ϕ_3	68.9
$A^{\mathrm{In}} \times 10^{-3}$	47.937	$A^{\mathrm{Out}} \times 10^{-3}$	45.149
$B^{\mathrm{In}} \times 10^{-3}$	8.784	$B^{\mathrm{Out}} \times 10^{-3}$	9.174
$C^{\mathrm{In}} \times 10^{-3}$	8.154	$C^{\mathrm{Out}} \times 10^{-3}$	8.184
μ_x^{In}	1.043	μ_x^{Out}	1.136
μ_y^{In}	-	μ_y^{Out}	0.111
μ_z^{In}	2.544	μ_z^{Out}	2.502

The Eulerian-type angles (in degrees) involved in the rotational dependence of the tunnelling matrix elements, the rotational constants (in MHz), and the dipole moments components (in Debye) are listed for the in and Out configurations. For symmetry reasons, the relation $\chi_2 = \phi_2 + \pi$ is fulfilled and μ_y^{In} is zero. Superscripted 'In' and 'Out' labels identify the rotational constants and dipole moment components.

3.2.3 Line assignment and line analysis

Starting from the results of Turner & Cox (1976), parallel a-type and perpendicular b-type transitions within the In configuration were assigned up to $J = 20$ and $K_a = 5$. This first set of transitions was fitted with a Watson-type Hamiltonian. Parallel a-type and perpendicular b- and c-type transitions within and between the $+$ and $-$ sub-levels of the Out configurations were assigned afterwards up to $J = 27$ and $K_a = 16$, using the results of Turner et al. (1981). Fitting this second set of transitions yielded rotational constants for the Out configurations, the magnitude of the tunnelling splitting h_2, and the Eulerian-type angles θ_2 and ϕ_2. No unaccountably large residuals, which could have been attributed to couplings between the In and Out configurations, were found. As a result, unlike in the monodeuterated species CH_2DCHO, the value of E_d and of the parameters describing the $1 \rightarrow 3$ tunnelling parameter could not be retrieved. Both sets of transitions were then fitted and new transitions were predicted and searched for. For the In configuration, it was possible to assign a- and b-type transitions up to $J = 26$ and $K_a = 17$. For the Out configurations, a-, b-, and c-type transitions were assigned up to $J = 27$ and $K_a = 14$. Table 3.2 lists the number of assigned transitions for each configuration, counting even forbidden ΔK_a and ΔK_c transitions (Turner et al. 1981) of the Out configurations as a-type transitions.

Table 3.2: Assigned transitions

	In		Out			
References	*a*-type	*b*-type	*a*-type	*b*-type	*c*-type	All
1	17	30	-	-	-	47
2	-	-	24	28	12	64
This work	176	36	445	75	2	742
All	193	66	469	103	14	853

The number of assigned *a*-, *b*-, and *c*-type transitions for each configuration in the two previous investigations (Turner & Cox 1976 and Turner et al. 1981) and in this work. Any *c*-type transitions within the In configuration are not allowed. No transitions were assigned between the In and Out configurations.

In the final analysis, experimental frequencies were introduced in a least-squares-fit procedure where they were given a weight equal to the inverse of their experimental uncertainty squared. Unresolved K-type doublets were treated as in Margulès et al. (2009). The rotational Watson-type Hamiltonians used for the In and Out configurations were written using Watson's A set of distortion parameters (Watson 1967, 1968a,b). The root mean square value of the observed minus calculated frequency is 81 kHz for transitions within the In configuration, 88 kHz for transitions within the Out configurations, and 83 kHz for all transitions. The unitless standard deviation of this final analysis is 1.7. With the selected set of spectroscopic parameters, most line frequencies are reproduced within their experimental uncertainty of 50 kHz. Also, *a*-type lines characterised by a large J and K_a value tend to display residuals larger than this value, and this may be due to the effects that are unaccounted for from the $1 \rightarrow 3$ tunnelling motion. For the whole dataset, assignments, observed and calculated frequencies, and residuals are listed in Table 3.3, available at the Centre de Données astronomiques de Strasbourg (CDS)[1]. Table 3.4 lists the parameters determined in the analysis. This table displays two columns. Column 1 gives the parameter name and column 2 its value and uncertainty. For the rotational constants, the calculated values in Table 3.1 are within 300 MHz from the experimental values in Table 3.4. For the Eulerian-type angles describing the rotational dependence of the tunnelling matrix elements, the discrepancies

[1] https://cdsweb.u-strasbg.fr/index-fr.gml

are 0.2 and 1° for θ_2 and ϕ_2, respectively.

Table 3.4: Spectroscopic parameters

Parameter[a]		Value	Parameter[a]		Value
θ_2		4.864(12)	H_{KKJ}	$\times10^4$	0.514(21)
ϕ_2		60.828 7(36)	H_{JKK}	$\times10^5$	0.112(81)
θ_{2j}	$\times10^3$	0.293(34)	H_J	$\times10^8$	0.26(25)
ϕ_{2j}	$\times10^3$	0.187(40)	h_K	$\times10^3$	0.434(63)
h_2		91.824(22)	h_{KJ}	$\times10^5$	0.396(39)
h_{2k}		0.116 7(23)	h_J	$\times10^9$	0.7(13)
h_{2j}	$\times10^2$	0.949(81)			
f_2	$\times10$	0.180 7(72)	A^{Out}	$\times10^{-3}$	45.141 639 0(39)
s_{2xz}	$\times10$	0.194(11)	B^{Out}	$\times10^{-3}$	9.176 200 44(90)
h_{2kk}	$\times10^3$	0.298(20)	C^{Out}	$\times10^{-3}$	8.187 146 15(81)
h_{2kj}	$\times10^3$	0.130 7(81)	Δ_K		0.353 84(15)
h_{2jj}	$\times10^5$	0.277(81)	Δ_{KJ}	$\times10$	0.168 73(14)
			Δ_J	$\times10^2$	0.666 13(20)
A^{In}	$\times10^{-3}$	47.940 411 5(57)	δ_K	$\times10$	0.902 4(17)
B^{In}	$\times10^{-3}$	8.778 690 6(14)	δ_J	$\times10^3$	0.853 2(12)
C^{In}	$\times10^{-3}$	8.175 064 5(13)	H_{KKJ}	$\times10^4$	0.238 0(90)
Δ_K		0.292 10(24)	H_{JKK}	$\times10^6$	0.31(29)
Δ_{KJ}	$\times10$	0.778 46(42)	H_J	$\times10^8$	0.70(22)
Δ_J	$\times10^2$	0.517 80(26)	h_K	$\times10^5$	0.3 174(13)
δ_K		0.353 56(51)	h_{KJ}	$\times10^5$	0.113 (21)
δ_J	$\times10^3$	0.592 2(14)	h_J	$\times10^8$	0.16(12)

[a] Parameters are in MHz, except for the angles θ_2 and ϕ_2; their distortion constants are in degrees. Uncertainties are given in parentheses in the same units as the last quoted digit.

Table 3.5: Partition functions (Q_{rot}) of CHD_2CHO

T/K	Q_{rot}	T/K	Q_{rot}
2.725	27.3	75	5186.2
5.000	66.9	150	15262.5
9.375	177.5	225	28438.5
18.75	550.6	300	44014.5
37.50	1714.4		

The partition functions are given for each temperature T in Kelvin.

3.2.4 Spectroscopic catalogue

The spectroscopic catalogue was built using the results of the previous sections. The energy difference E_d was set to the value computed in Section 3.2.2. Transitions were calculated up to $J = 28$ and their line strength and line intensity were computed using the dipole moment

components in Table 3.1. The partition functions $Q_{\rm rot}$, listed in Table 3.5, were computed for several temperatures using degeneracy factors equal to $(2J+1)$. A zero energy was taken for the Out configurations 0_{00}, + level. Lines were selected using an intensity cutoff depending on the line frequency (as is commonly done in the Jet Propulsion Laboratory (JPL) database catalogue line files; Pickett et al. 1998). Its value in $\mathrm{nm}^2 \cdot \mathrm{MHz}$ units at 300 K is

$$10^{\mathrm{LOGSTR0}} + (F/300\ 000)^2 \times 10^{\mathrm{LOGSTR1}}, \tag{3.4}$$

where F is the frequency in MHz, and LOGSTR0 and LOGSTR1 are two dimensionless constants both set to -8. The linelist, given in Table 3.6, is available at the CDS and is formatted in the same way as the catalogue line files of the JPL database (Pickett et al. 1998). A minimum value of 10 kHz was selected for the calculated error (ERR). For observed unblended microwave lines, the line frequency (FREQ) and the error (ERR) were replaced by their experimental values. This is then indicated by a negative species tag. The catalogue is available on CDMS [2] (Endres et al. 2016).

3.3 Astrophysical observations

Based on the new spectroscopic measurements, we searched for CHD_2CHO towards the B component of the proto-stellar system IRAS 16293–2422 in data from the ALMA PILS (Jørgensen et al. 2016). PILS represents an unbiased molecular line survey of IRAS 16293–2422 which was carried out during ALMA's Cycle 2 (project id: 2013.1.00278.S, PI: J. K. Jørgensen), covering one of the prominent atmospheric windows in ALMA's Band 7 between 329.1 and 362.9 GHz with a spectral resolution of ≈0.2 km s^{-1} and angular resolution of ≈0.5″ (70 au at the distance of IRAS 16293–2422). The high sensitivity of the PILS data and relatively narrow lines towards one component of IRAS 16293–2422 have enabled the detections of a number of species for the first time in the ISM (e.g. CH_3Cl by Fayolle et al. (2017) and HONO by Coutens et al. (2019)) as well as having made it possible to systematically survey the content of deuterated isotopologues of complex organic molecules (Jørgensen et al. 2018). The latter also includes the detection of doubly deuterated organics, including CHD_2CN (Calcutt et al. 2018), CHD_2OCHO (Manigand et al. 2019), and CHD_2OCH_3 (Richard et al. 2021) as well as new and better constraints on the column densities of doubly and triply deuterated methanol (Drozdovskaya et al. 2022 and Ilyushin et al. 2022). For details about the data and their reduction, we refer readers to Jørgensen et al. (2016).

For our search, we analysed the position offset by one beam (0.5″) from the B component of IRAS 16293–2422, where line and continuum opacity are limited. This position was also the one studied in the above-mentioned papers from PILS (Jørgensen et al. 2016 and Jørgensen et al. 2018). We adopted a similar approach to previous works by fitting synthetic spectra for CHD_2CHO calculated under the assumption that its excitation is characterised by local thermodynamical equilibrium (LTE), which is reasonable at the densities of the warm gas where these species are present (Jørgensen et al. 2016). The free parameters in the fits are the column density of the

[2] https://cdms.astro.uni-koeln.de

molecule N, and its rotational temperature, $T_{\rm rot}$. For the line width and velocity offset relative to the local standard of rest, we adopted values of 1 km s^{-1} (FWHM) and of 2.6 km s^{-1}, respectively, which match the spectra well at this position. For $T_{\rm rot}$, we assumed a temperature of 125 K similar to that of the non-deuterated and singly deuterated isotopologues of acetaldehyde. An example of the fit to a selected frequency range is shown in Fig. 3.5 while the fits to the lines predicted to be brighter than 40 mJy beam^{-1} km s^{-1} (68 transitions; the root mean square noise in the spectra is about 4–5 mJy beam^{-1} per 1 km s^{-1}) over the entire frequency range are shown in Fig. B.1 (in Appendix B.1). Several clean and unblended transitions are seen to provide a good constraint on the CHD_2CHO column density of 1.3×10^{15} cm^{-2} with an uncertainty of 10-20% (for the discussion on the uncertainty derivation, we refer readers to Jørgensen et al. (2018)). The few lines that are either under- or over-produced with the synthetic spectra are due to blends with brighter lines of more prominent species (e.g. the two lines seen at 330.71 GHz with an upper energy level of 202 K that are blended with glycolaldehyde) or absorption due to optically thick emission (e.g. the transition at 347.86 GHz falling close to a transition of formic acid).

The derived column density can be compared to that of the singly deuterated variant, CH_2DCHO, of 6.2×10^{15} cm^{-2} (Manigand et al. 2020). The ratio between the singly and doubly deuterated variants of 20% is very close to those for methyl formate (CHD_2OCHO/CH_2DOCHO) of 22% (Manigand et al. 2019), dimethylether (CH_3OCHD_2/CH_2OCH_2D) of 15-20% (Richard et al. 2021), and methanol (CHD_2OH/CH_2DOH) of 25% (Drozdovskaya et al. 2022) – in all cases it is significantly above the ratios for the singly deuterated to non-deuterated isotopologues (Jørgensen et al. 2018) by factors of 4–5.

3.4 Discussion of astronomical observational results

The similar doubly to singly deuterated column density ratios for acetaldehyde, methyl formate, dimethylether, and methanol presented in Section 3.3 suggest that doubly deuterated acetaldehyde shares a common origin and was formed in an environment resembling the physical conditions with which doubly deuterated methyl formate, dimethylether, and methanol were formed. The pre-stellar core phase is a good candidate due to the low temperatures that promote deuterium fractionation through the enhancement of the H_2D^+/ H_3^+ ratio as well as the larger atomic D/H ratio in the gas phase, which promotes deuteration of surface species.

Mechanisms for acetaldehyde main isotopologue formation have been suggested for both the gas phase as well as for the surface of grains. For the gas phase, Vazart et al. (2020) concluded that C_2H_5 + O(^{3}P) and CH_3CH_2OH + OH / CH_3CHOH + O(^{3}P) are potentially efficient gas-phase formation routes. Fedoseev et al. (2022) studied grain surface reactions and proposed CH_2CO + 2H as a plausible way of forming CH_3CHO. Contrarily to deuterated methanol, whose formation pathway has been constrained (Drozdovskaya et al. 2021), the formation of deuterated acetaldehyde is still not clear. In the same line as doubly deuterated methanol, doubly deuterated acetaldehyde could be formed from a doubly deuterated reactant. The acetaldehyde D_2/D ratio found in this work and the D/H ratio from Manigand et al. 2020 combined with a gas-grain chemical model can potentially shed light on the formation mechanism of singly and multi-deuterated acetaldehyde.

Contrary to deuterated methanol, which has been observed in a variety of sources, deuterated

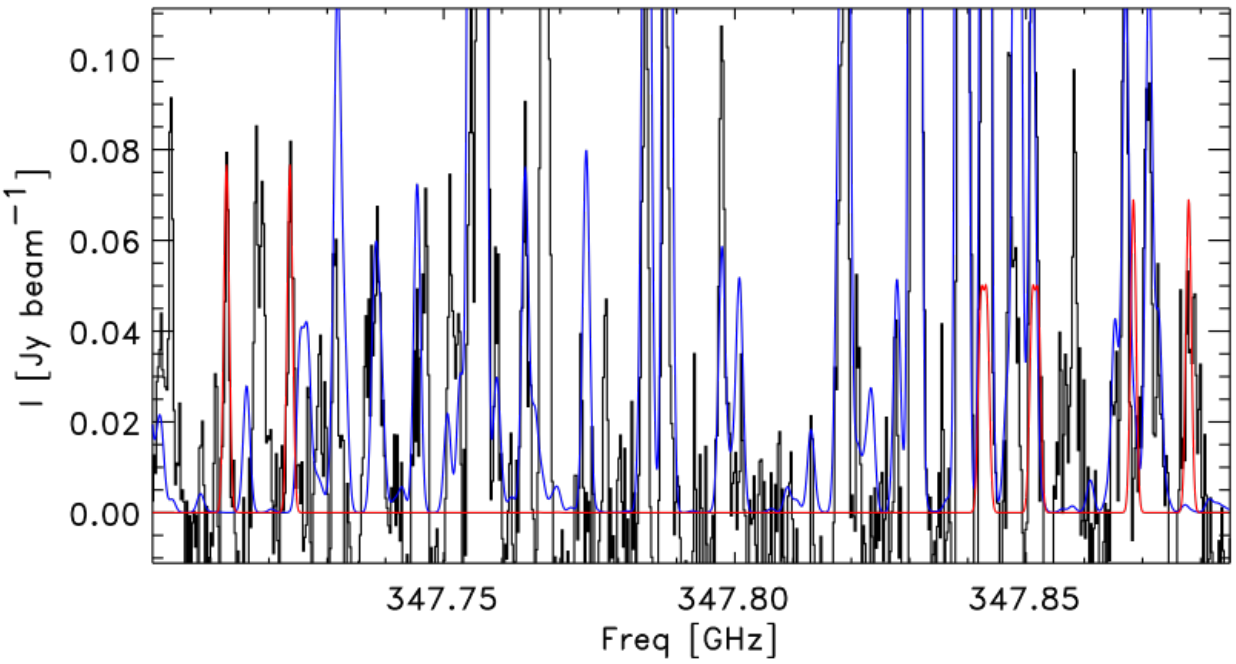

Figure 3.5: Example of the CHD_2CHO fits in a selected frequency range. The synthetic spectra fitted to CHD_2CHO is shown in red and all other species identified in PILS are in blue.

acetaldehyde counts fewer detections. Acetaldehyde is less abundant than methanol in pre-stellar cores with $[CH_3CHO]/[CH_3OH]$ ratios between 0.02 and 0.26 (Scibelli & Shirley 2020). We estimate the line brightness of the most intense lines of the singly and doubly deuterated acetaldehyde in the 3 mm band towards pre-stellar cores to be 4.3 mK and 0.5 mK, respectively. We base our estimate on the average column density of CH_3CHO observed towards starless cores in Scibelli & Shirley 2020 (2×10^{12} cm^{-2}), and assuming the D/H and D_2/H ratio observed towards IRAS16293.

Based on our predictions, it will be unlikely to detect the doubly deuterated acetaldehyde towards pre-stellar cores, and this is possibly also true for other COMs. Nevertheless, one can use the diagnostic power of deuteration and derive information on inheritance from pre-stellar cores by using state-of-the-art chemical models.

3.5 Conclusions

The rotation-torsion spectrum of doubly deuterated acetaldehyde (CHD_2CHO) was experimentally and theoretically studied. Due to the tunnelling of the CHD_2 methyl group, the ground state is split into three torsional sub-levels. Transitions were measured in the millimetre and sub-millimetre range (82.5 – 450 GHz), as described in Section 3.2.1. These, alongside previously measured ones, were fitted using IAM. A total of 853 transitions were fitted with a weighted root mean square deviation of 1.7. The resulting spectroscopic parameters computed with this fit can

be found in Table 3.4. We built a spectroscopic catalogue for astrophysical purposes from the results of the analysis, which we publish in CDMS.

We present the first detection of CHD_2CHO in the ISM through comparisons to observations of the B component of the proto-stellar system IRAS 16293-2422 from the ALMA PILS programme. This doubly deuterated variant is enhanced compared to its singly and non-deuterated counterparts at the same level as for other complex organics seen towards this source. Further comparison to chemical models may shed further light on the acetaldehyde formation during the earliest stages of star formation.

Acknowledgements. J.F.A., S.S., V.L., C.P.E. and P.C. gratefully acknowledge the support of the Max Planck Society. The research of J.K.J. is supported by the Independent Research Fund Denmark (grant No. 0135-00123B). This paper makes use of the following ALMA data: ADS/JAO.ALMA#2013.0.00278.S. ALMA is a partnership of ESO (representing its member states), NSF (USA) and NINS (Japan), together with NRC (Canada), MOST and ASIAA (Taiwan), and KASI (Republic of Korea), in cooperation with the Republic of Chile. The Joint ALMA Observatory is operated by ESO, AUI/NRAO and NAOJ. We also thank the anonymous referee for their insightful comments.

4

High sensitivity and spectral resolution molecular line observations towards the L1544 pre-stellar core: challenges to current models [1]

The content of this chapter will be submitted in the Astronomy & Astrophysics Journal. Credit: Ferrer Asensio et al., 2024, in prep., (reproduced with permission ©AAS.)

The increased sensitivity and spectral resolution of observed spectra towards the pre-stellar core L1544 are challenging the current physical and chemical models. These spectra show complex line profiles, which tell us information on the structure and evolutionary state of pre-stellar cores. The high sensitivity and high spectral resolution spectra of the HCO^+ (J = 1 - 0), CS (J = 2 - 1), $C^{34}S$ (J = 2 - 1), H_2CO (J_{K_a,K_c} = $2_{1,2}$ - $1_{1,1}$), c-C_3H2 (J_{K_a,K_c} = $2_{1,2}$ - $1_{0,1}$), SO (N,J = 2,3 - 1,2) and ^{34}SO (N,J = 2,3 - 1,2) transitions are taken with the IRAM 30 m telescope towards the dust peak of L1544. A non-Local Thermodynamic Equilibrium (non-LTE) radiative transfer code, using a pre-stellar core physical model, is coupled to the Markov Chain Monte Carlo (MCMC) method to model the observed molecular transitions. Selected physical and chemical parameters are explored to find the best fit with observations. This approach gives good constraints on the models for the optically thin lines, supporting the findings for an increase of the gas contraction velocity in the inner parts of L1544. On the other hand, this 1D non-LTE radiative transfer modelling coupled with the MCMC method results in less-constrained models for the observed optically thick lines. The derived step fractional abundance profiles are compared to fractional abundance profiles computed with chemical models. All of the transitions observed trace different gas components with different gas dynamics at different distances along the radius of the core, pointing to the need to use 3D radiative transfer modelling to understand the small-scale structure of the L1544 pre-stellar core fully.

4.1 Introduction

Pre-stellar cores are high-density regions formed from the fragmentation of filamentary structures that constitute molecular clouds (Palmeirim et al. 2013; Hacar et al. 2022). While pre-stellar cores are in the early stages of gravitational contraction, they have not yet formed a protostar. These objects are characterised by high densities ($n_{H_2} > 10^5$ cm^{-3}) and low temperatures (< 10 K) at their centre (Keto & Caselli 2008). The study of the physical, chemical and kinematic properties of these cores and their surroundings helps us gain a comprehensive understanding of the initial conditions that lead to core collapse and, therefore, to understand the first stages of the star formation process (André et al. 2014).

Molecular spectra have proven to be valuable tools for characterizing dense cloud cores. Molecular line intensities, widths, and profiles are influenced by the physical conditions along the path of the emitted radiation. The information embedded within observed spectral lines is extracted through a comprehensive radiative transfer modelling of the emission accounting for the physical structure of the observed source (Caselli et al. 2002a; Sohn et al. 2007; Keto et al. 2015; Redaelli et al. 2019; Ferrer Asensio et al. 2022).

L1544 is a well-known pre-stellar core in the Taurus Molecular Cloud at a distance of 170 pc (Galli et al. 2019). Extensive research has focused on the study of its physical and chemical properties, revealing it is centrally concentrated, with low central temperatures and signs of contraction motions (Ward-Thompson et al. 1999; Crapsi et al. 2005, 2007). A substantial part of the knowledge on L1544 has been obtained via radiative transfer modelling of molecular lines. The radiative transfer modelling is carried out by calculating the energy level population of the molecule of interest and computing the transfer of its emitted radiation, taking into account the pre-stellar core physical model Keto & Rybicki (2010); Keto et al. (2015) and the molecular abundance profiles obtained with a pseudo-time-dependent gas-grain chemical model (Sipilä et al. 2015).

With access to increasingly high-sensitive and high-spectral resolution spectra of molecules, we are challenging the current models and knowledge on L1544, learning about its small-scale non-homogeneous structure and its relationship with its surroundings. For example, past studies showed the need for adjusting the velocity profile of the pre-stellar core physical model (Keto et al. 2015) to fit the line profile of specific lines (Bizzocchi et al. 2013; Ferrer Asensio et al. 2022). In addition, spatially extended abundant molecules such as HCO^+ have shown the need to take into account a diffuse envelope around L1544 to be able to reproduce their molecular profiles (Redaelli et al. 2019). Moreover, Lin et al. (2022) found a local gas density enhancement towards L1544 deviating from the commonly assumed Bonnor Ebert (BE) sphere structure, which could be the result of an accretion flow impact.

Molecular line profiles harbour invaluable information. For instance, the characteristic blue asymmetry profile of optically thick lines is commonly used to trace contraction motions in star-forming regions. This profile is characterised by a double-peaked line where the blue peak, at lower velocities, is more intense than the red peak, at higher velocities. This occurs due to the combination of the self-absorption of the line coupled with the contraction of the source. The relative intensity of the two components is, therefore, indicative of the optical thickness of the line observed as well as the contraction velocity (Myers et al. 1996). Self-absorption occurs when

a molecule present in a less dense foreground layer absorbs the radiation emitted by the same molecule in a denser layer in the background. This self-absorption results in a double-peaked line profile with the dip aligning with the velocity of the absorbing layer. If the absorbing layer has the same velocity as the emitting layer, the line dip will be found in the centre of the line. In the case the absorbing layer has a different velocity w.r.t. the emitting layer, the dip will shift to lower or higher velocities accordingly. Double-peaked line profiles can also be due to the presence of two separated gas components along the line of sight as well as an effect of radiative transfer tracing the contraction of a core for optically thin lines.

In this work, we deepen our comprehension of the physical, chemical and kinematic structure of L1544 through the radiative transfer modelling of unprecedented high-sensitivity and high-spectral resolution molecular line observations towards this pre-stellar core. Intending to probe the entirety of the core, we observe optically thin transitions, $C^{34}S$ (J = 2 - 1) and ^{34}SO (N,J = 2,3 - 1,2), which are expected to trace the whole core, and optically thick transitions, HCO^+ (J = 1 - 0), CS (J = 2 - 1), H_2CO (J_{K_a,K_c} = $2_{1,2}$ - $1_{1,1}$), c-C_3H2 (J_{K_a,K_c} = $2_{1,2}$ - $1_{0,1}$) and SO (N,J = 2,3 - 1,2), which are expected to trace the outer parts of the core. Owing to the need to adjust the pre-stellar core model as a consequence of the new information provided by the new observations (Ferrer Asensio et al. 2022), we adopt a non-LTE approach coupled with an MCMC method. This allows to explore the parameter space of selected physical and chemical model variables to provide the highest-probability model solutions to fit the observations. The molecular fractional abundance profiles commonly used for radiative transfer modelling are computed using chemical networks. Incomplete chemical networks can produce incorrect abundance profiles, leading to poor fits in observed spectra and, consequently, incorrect conclusions. In this Chapter, we assess the molecular fractional abundance profiles computed with the pseudo-time dependent chemical modelling described in Sipilä et al. (2015) (pyRate) by comparing them to simple step-abundance profiles found to give the best fits of observed transitions towards L1544. Through this comparison, we can notice issues with chemical networks.

This manuscript is structured as follows: the observations are presented in Section 4.2, the radiative transfer methodology used to reproduce the observed molecular transitions is described in Section 4.3, the modelling results are introduced in Section 4.4, these results are interpreted and placed in the context of past works in Section 4.5 and we summarize our conclusions in Section 4.6. Additionally, we include an Appendix C with further tests.

4.2 Observations

The single-pointing observations of the HCO^+ (J = 1 - 0), CS (J = 2 - 1), $C^{34}S$ (J = 2 - 1), H_2CO (J_{K_a,K_c} = $2_{1,2}$ - $1_{1,1}$), c-C_3H2 (J_{K_a,K_c} = $2_{1,2}$ - $1_{0,1}$), SO (N,J = 2,3 - 1,2) and ^{34}SO (N,J = 2,3 - 1,2) rotational transitions are obtained towards the dust peak of L1544 (α_{2000} = $05^h04^m17^s.21$, δ_{2000} = +25°10′42″.8). These observations were carried out in August and October of 2021, using the IRAM 30m telescope at Pico Veleta. The telescope pointing was frequently checked against the nearby bright quasars B0316+413, B0851+202, and B0439+360, depending on the elevation of the source. We used the E090 and E150 bands of the EMIR receiver. The observations were performed in frequency-switching mode. We used the VESPA backend to achieve a spectral resolution of 10 kHz. Both horizontal and vertical polarisations were observed simultaneously. The summary of the observed transitions in this project alongside $HC^{17}O^+$ observed in Ferrer Asensio et al. (2022) can be found in Table 4.1.

Table 4.1: Observed Molecular Transitions

Molecule	Transition	Frequency (MHz)	E_{up} (K)	A (x 10^{-5} s^{-1})	rms (mK)	HPBW (")	Velocity resolution (km s^{-1})
HCO^+	J = 1 - 0	89188.525	4.28	4.19	64	27.6	0.033
$HC^{17}O^+$	J = 1 - 0	87057.53	4.18	3.9	2.8	28.3	0.034
CS	J = 2 - 1	97980.95	7.05	1.68	44	25.1	0.029
$C^{34}S$	J = 2 - 1	96412.94	6.94	1.60	16	25.5	0.030
H_2CO	J_{K_a,K_c} = $2_{1,2}$ - $1_{1,1}$	140839.50	21.92	5.30	61	17.5	0.020
c-C_3H_2	J_{K_a,K_c} = $2_{1,2}$ - $1_{0,1}$	85338.89	6.44	2.32	52	28.8	0.034
SO	N,J = 2,3 - 1,2	99299.87	9.22	1.12	16	24.7	0.029
^{34}SO	N,J = 2,3 - 1,2	97715.39[b]	9.09	1.07	19	25.1	0.030

The spectral information for the molecular transitions including the frequency, the upper energy, E_{up}, and the Einstein coefficient, A, was taken from The Cologne Database for Molecular Spectroscopy (CDMS)[2] (HCO^+, Tinti et al. (2007), $HC^{17}O^+$, Dore et al. (2001b), CS and $C^{34}S$, Bogey et al. (1981), H_2CO, Brünken et al. (2003), c-C_3H_2, Bogey et al. (1986), SO, Clark & De Lucia (1976) and ^{34}SO, Tiemann (1974)). [b] The ^{34}SO frequency was directly measured in the Center for Astrochemical Studies (CAS) laboratory.

The observational data was processed and then averaged with the Continuum and Line Analysis Single-dish Software (CLASS), an application from the GILDAS[3] software (Pety 2005). The resulting spectra are presented in Figure 4.1.

[3] https://www.iram.fr/IRAMFR/GILDAS/

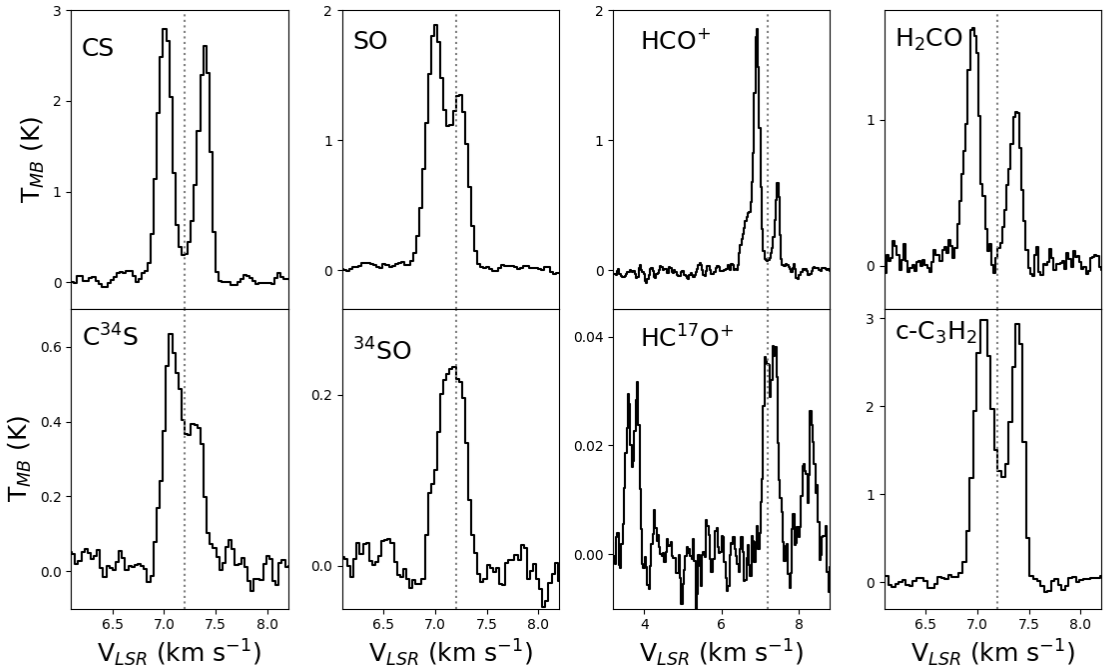

Figure 4.1: Spectrum of the transitions taken towards the dust peak of L1544. $HC^{17}O^+$ is included from previous works (Ferrer Asensio et al. 2022). The vertical dotted grey line represents the LSR velocity of L1544 (7.2 km s^{-1}).

Signal-to-noise ratio (S/N) values are 11 for ^{34}SO, 13 for the least bright component of H_2CO, 26 for HCO^+, 28 for $C^{34}S$, 48 for the least bright component of CS, 49 for the least bright component of c-C_3H2, and 69 for the least bright component of SO. The spectral velocity resolution is 0.03 km s^{-1} for all the spectra.

4.3 Radiative transfer

In pre-stellar cores, where the molecular hydrogen volume density (n_{H_2}) and gas temperature (T_{gas}) can span between $\gtrsim 10^6$ cm^{-3} and $\sim$ 5 K at the centre and $\lesssim 10^2$ cm^{-3} and $\sim$ 20 K at the edge, we cannot assume the condition of LTE throughout the core. The LTE regime is valid when the critical density of the transition ($n_{crit} = A_{ul}/C_{ul}$), where A_{ul} is the Einstein A coefficient and C_{ul} is the collisional coefficient at a specific temperature, where 'u' and 'l' are the upper and lower levels, respectively) is equal to or lower than the volume density of the emitting region. Thus, for high n_{crit} transitions, LTE applies only in a reduced area on the pre-stellar core centre where the n_{H_2} exceeds n_{crit}. In non-LTE conditions, namely, when the critical density of the transition is higher than the volume density, the energy level populations deviate from the Boltzmann distribution and need to be calculated using the statistical equilibrium equations.

The environment radiation crosses from its emission origin to the observer and has an impact on the radiation itself and, therefore, on the observed line intensity and profile. To be able to model these observations and properly interpret the results, we need to take into account the physical, chemical and kinematic changes in the radiation's path. This is done with Radiative Transfer Modelling. Therefore, in order to reproduce the observation of intrinsically diverse transitions towards a source, we need to perform non-LTE radiative transfer modelling.

In the next Section, we introduce the non-LTE radiative transfer modelling approach used in this work.

4.3.1 The LOC radiative transfer code + MCMC

In previous works, the adjustment of physical and chemical model parameters, such as the fractional abundance or the velocity profile scaling, aided the fit and understanding of the nature of some molecular emission towards L1544 (Bizzocchi et al. 2013; Ferrer Asensio et al. 2022; Redaelli et al. 2022). In this work, we explore the parameter space of specific physical and chemical parameters when performing the radiative transfer modelling of the observations to ensure the best possible fit. With this aim in mind, we combine non-LTE radiative transfer modelling with the Markov Chain Monte Carlo method (MCMC) to calculate probability distributions of the physical and chemical parameters, which produce the closest modelled spectra w.r.t. the observed spectra.

The radiative transfer modelling of the observed molecular lines is carried with the Line transfer with OpenCL (LOC) code (Juvela 2020). As a first step, LOC solves the statistical equilibrium equations with the radiative and collisional coefficients of the molecule with an accelerated lambda iteration (ALI) (Rybicki & Hummer 1991). Then, the radiative transfer is computed using a 1D model of the source, taking into account the molecular hydrogen volume density, n_{H_2}, the gas temperature, T_{gas}, the velocity of the gas, v, the turbulent velocity, v_{turb}, and the fractional abundance profiles of the desired molecule. The 1D radial profiles of the physical properties are taken from the unstable quasi-static Bonnor Ebert sphere pre-stellar core physical model in Keto et al. (2015).

The pre-stellar core physical model radial profiles are presented in Figure 4.2. The molecular hydrogen volume density (solid black line) ranges from 8×10^6 cm^{-3} at the centre to 1×10^2 cm^{-3}

at the edge of the core (0.32 pc). The gas temperature (blue dashed line) ranges from 6 K at the centre to 18 K at the edge. Finally, the gas velocity (orange dash and dotted line) ranges from -0.14 km s^{-1} at the velocity peak ($\sim$ 0.01 pc) to -0.01 km s^{-1} at the edge of the core. The negative sign of the velocity indicates that the pre-stellar core model is contracting. This model has been successful at reproducing many molecular transitions observations towards the dust peak in L1544 (Keto & Rybicki 2010; Keto & Caselli 2010; Caselli et al. 2012; Bizzocchi et al. 2013; Caselli et al. 2017; Redaelli et al. 2018, 2019, 2022; Caselli et al. 2022; Ferrer Asensio et al. 2022).

Additionally to the pre-stellar core physical model, the LOC software also requires information on the fractional abundance profile of the molecules. The fractional abundance profiles for the molecules can be simulated using chemical models. Commonly, the fractional abundance profiles computed with the pyRate chemical model (Sipilä et al. 2015) are used when performing radiative transfer modelling of L1544 observations. These abundance profiles are simulated using the pre-stellar core physical model described in Keto et al. (2015), which is separated into concentric shells where chemical simulations, based on a chemical network, are conducted. The physical structure of the core is fixed, and the chemistry evolves with time. As one of the objectives is to assess fractional abundance profiles computed with the pyRate chemical model (Sipilä et al. 2015), we use simple step abundance profiles described in Section 4.3.2.

The Markov Chain Monte Carlo method, as the name suggests, combines the Markov Chain process with Monte Carlo simulations. The MCMC code EMCEE is used (Foreman-Mackey et al. 2013). The MCMC method involves randomly sampling high-dimensional probability distributions while considering the probabilistic dependence between samples using the Markov Chain. The density estimation for probability distributions is done, taking into account both the observations and the model. The value of the parameters that have the lowest χ^2 minimization w.r.t. the observations is the value with the highest likelihood.

First of all, we define the parameters to be explored by the MCMC and a sensible range for their values. The limits for the values are set from the source's physical and chemical structure information in the literature. Then, initial values, from where the random walk starts, are defined. The MCMC, starting from the initial values, generates a sequence of models using random parameter values. Depending on the χ^2 minimization of the resulting model w.r.t. the observations, the parameters used are accepted or rejected. If they are accepted, these parameter values are used for the next step on the modelling chain. If the parameters are rejected, the previous values in the chain are used. This procedure is repeated for a defined number of steps until the chain converges. As a product, we obtain the probability distribution of the parameter values as constrained by the comparison of the produced spectral models with the observed spectra in the form of histograms. In the corner plots, the parameter histograms are arranged to give information on the correlation between the parameters in pairs. The highest-probability parameter value is then used to model the observed spectra.

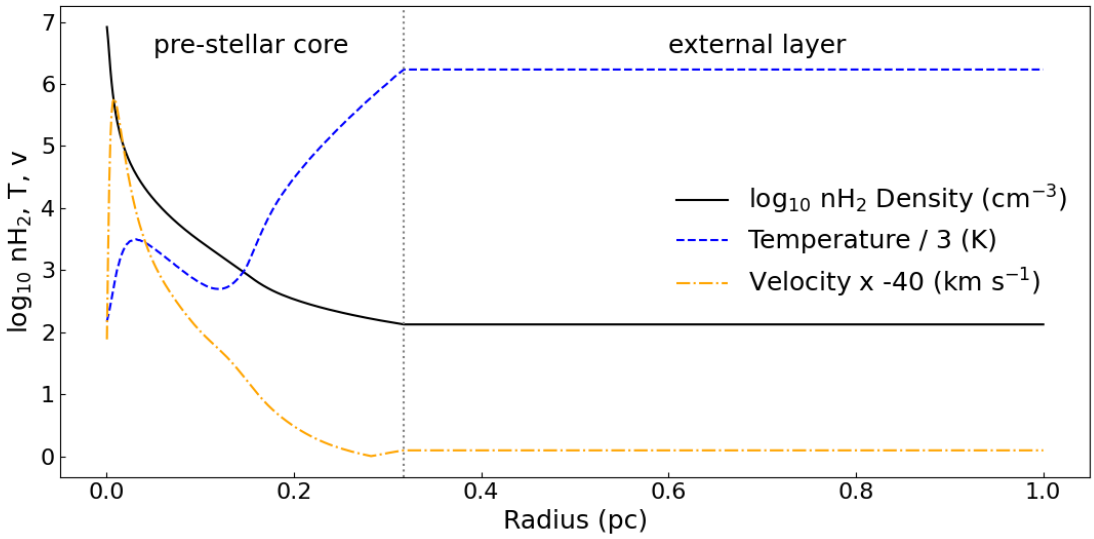

Figure 4.2: The 1D pre-stellar core physical model profiles used for the radiative transfer modelling are presented. The pre-stellar core physical model described in Keto et al. (2015) is plotted between 0 to 0.32 pc. The vertical dotted black line marks the radius at 0.32 pc. The physical profiles between 0.32 and 1 pc correspond to an "external layer" used for some of the transition modelling. The physical parameters in this external layer are constant profiles with values equal to the value at the edge (0.32 pc) of the pre-stellar core model in Keto et al. (2015). The physical parameters have been scaled to be presented in the same plot. The molecular hydrogen column density, n_{H_2}, is plotted logarithmically (black solid line). The gas temperature, T, is divided by a factor of 3 (blue dashed line). The velocity profile has been multiplied by a factor of -40 (orange dash-dotted line).

4.3.2 Models and Parameter Space

Past works required small adjustments of the velocity profile scaling to reproduce some observed molecular transitions towards L1544 (Bizzocchi et al. 2013; Ferrer Asensio et al. 2022). Thus, for the modelling in this manuscript, we set the velocity profile scaling, f_v, as a parameter to be explored by the MCMC. Moreover, we include the turbulent velocity, v_{turb}, as another parameter, as we expect the turbulent velocity to vary in different parts of the core and surroundings.

Several articles in the literature have also shown the need to scale the fractional abundance profiles computed from pseudo-time-dependent chemical models. In order to gain insight into the molecular radial distributions directly from observations, we use simple step abundance profiles for the modelling. This choice of abundance profile takes into account the almost total molecular depletion observed towards the centre of the core (Caselli et al. 2022), which has an impact on the observed molecular emission. The abrupt depletion of a molecule is a simplification of reality as we expect molecules to gradually deplete towards the centre of the core.

Depending on the nature of the observed molecular transition, we use either a "non-extended"

or an "extended" model.

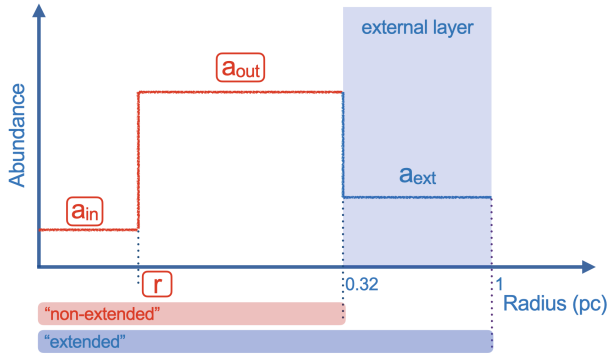

Figure 4.3: Schematics of the abundance profiles used for the radiative transfer modelling. The vertical axis represents the abundance, and the horizontal axis the radius in units of parsec. From the centre of the core (left) to the parameter r, we have the inner fractional abundance a_{in} and from r to 0.32 pc, there is the outer fractional abundance a_{out} regime. This constitutes the spatial extent of the "non-extended" model, as indicated by the red stripe at the bottom of the plot. From 0.32 to 1 pc, we have the shaded blue area representing the external layer characterised by an external fractional abundance a_{ext}, which we set to the molecular fractional abundance found towards diffuse clouds. Thus, the "extended" model (from the centre to 1 pc) is indicated by the blue stripe at the bottom of the plot. The parameters framed in a box (a_{in}, a_{out} and r) are those explored by the MCMC.

The "non-extended" model corresponds to a pre-stellar core physical and chemical model 1D profiles that extend to 0.32 pc as used for the majority of the radiative transfer modelling of molecules towards L1544 (Giers et al. 2022; Ferrer Asensio et al. 2022). This model uses the pre-stellar core physical model described in Keto et al. (2015) but sets the f_v and v_{turb} as parameters to be explored by the MCMC. The molecular abundance profile is constructed with two constant abundance values, one representing the abundance in the inner part of the core, a_{in}, and another for the outer part of the core, a_{out}. The separation of the inner abundance and outer abundance regions is defined by a radius, r. Consequentially, the abundance profile has two zones: a_{in} between 0 and r pc and a_{out} between r and 0.32 pc (red stripe in Figure 4.3).

The spectra of some abundant molecules, such as HCO^+ (Redaelli et al. 2022), trace the structure beyond the pre-stellar core, considered to have its edge at 0.32 pc in previous L1544 modelling. Thus, for molecules suspected to be present in this extended structure, we adopt the "extended" model. The extended model consists of the "non-extended" model structure (0 - 0.32 pc) with an additional layer spanning from 0.32 to 1 pc. The physical parameter profiles in this extended layer are assumed to be constant with the values given at the edge (0.32 pc) of the Keto et al. (2015) model. The f_v parameter scales the velocity in the entire model from 0 to 1 pc. The abundance is kept constant in this external layer and is set to the observed value towards diffuse clouds. Thus, for the "extended" model, the abundance profile is defined by a_{in} (between 0 and r pc), a_{out} (between r and 0.32 pc), and diffuse cloud observed abundance a_{ext} (between 0.32 and 1 pc) (blue stripe in Figure 4.3). From this point on, the spectra resulting from the "non-extended"

model are plotted with a solid red line, and the spectra resulting from the "extended" model are plotted with a dash-dotted blue line.

For both the "non-extended" and "extended" models, we have 5 parameters explored by the MCMC: a_{in}, a_{out}, r, f_v and v_{turb}. The prior probability distributions are set such as:

- $10^{-15} < a_{in} < 10^{-6.5}$
- $10^{-15} < a_{out} < 10^{-6.5}$
- $500 < r < 20000$ (au)
- $0 < f_v < 2$
- $0.00 < v_{turb} < 0.35$ (km/s).

These limits are set from previous knowledge of the physical, kinematic and chemical nature of the source. We also impose the condition that a_{in} cannot be larger than a_{out} as we expect the molecules to be depleted towards the centre of the core and, therefore, be less abundant in that area.

4.4 Results

The modelling results for the observed molecular transitions are separated into two Sections: optically thin transitions and optically thick transitions (Sections 4.4.1 and 4.4.2, respectively). Generally, the modelling of optically thin transitions with the LOC + MCMC approach results in better-constrained parameters than the modelling of the optically thick transitions.

4.4.1 Optically Thin Transitions

Due to the intrinsic lower fractional abundances of the rare isotopologues, $C^{34}S$, ^{34}SO and $HC^{17}O^+$ are expected to emit only from the core (i.e. within 0.32 pc). We do not expect these transitions to trace the extended structure, as traced with the HCO^+ $J = 1$ - 0 transition (Redaelli et al. 2022). Thus, for the modelling of optically thin transitions presented in the next subsections, we use the "non-extended" model described in Section 4.3.2.

$C^{34}S$

The $C^{34}S$ (2 - 1) transition presents a double-peaked line profile (Figure 4.1). The LOC + MCMC approach reproduces well the observations (observations in black, model in red; Figure 4.4). The best model parameter values are presented in Table 4.2. The resulting corner plot shows Gaussian-like profiles for the explored parameters (Figure 4.5).

Table 4.2: $C^{34}S$ (2 - 1) best model parameters

a_{in}	$1.98^{+1.20}_{-1.43} \times 10^{-11}$
a_{out}	$6.38^{+2.30}_{-1.32} \times 10^{-10}$
r (au)	6293^{+991}_{-675}
f_v	$1.29^{+0.06}_{-0.09}$
v_{turb} (km/s)	$0.072^{+0.01}_{-0.01}$

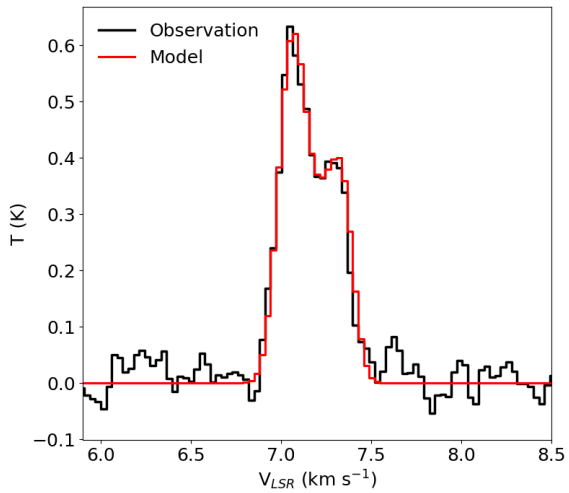

Figure 4.4: $C^{34}S$ (2 - 1) observations in black and modelling results in red towards the L1544 dust peak. The corner plot of the parameter exploration corresponding to these results is shown in Figure 4.5.

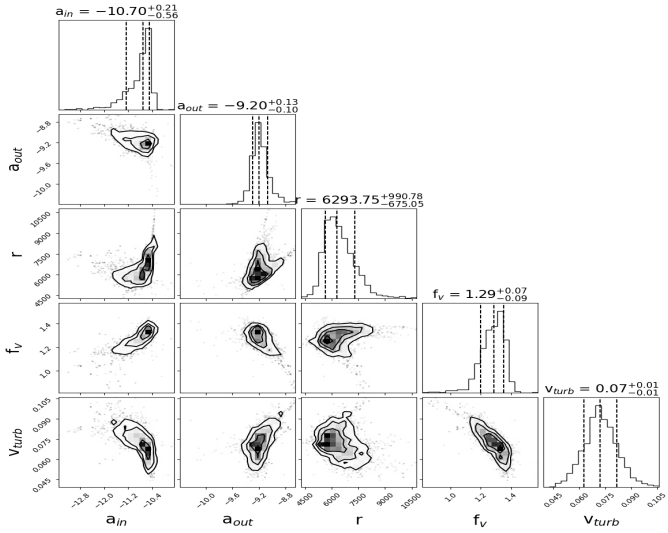

Figure 4.5: Corner plot of the parameters used for the model displayed in Figure 4.4. The top left subplot corresponds to the inner abundance values explored in the modelling. The second column is the outer abundance. The third corresponds to the radius separating the abundance regions. The fourth shows the velocity profile scaling, and the fifth the turbulent velocity. The rest of the panels show the correlation between the different variables.

The comparison of the step fractional abundance profile used for the line profile model in Figure 4.4 and the fractional abundance profile computed with the pyRate chemical model (Sipilä et al. 2015) is presented in Figure 4.6. As the chemical model in Sipilä et al. (2015) does not take into account sulphur isotope chemistry, we scale down the CS fractional abundance profile by the $[^{32}S/^{34}S] = 22$ ratio (Wilson & Rood 1994).

The radius where the $C^{34}S$ abundance drops due to depletion in the centre of the core found with the LOC + MCMC modelling agrees with the radius of the fractional abundance profile computed with chemical models. The $C^{34}S$ a_{out} value found with the LOC + MCMC modelling is a factor ~ 3 larger than the highest $C^{34}S$ chemically modelled abundance.

In order to see the effect of the abundance profile used on the output line profile, I present Figure 4.7. In this Figure, I compare the results of our LOC + MCMC modelling approach (red solid line) with the spectrum computed with the original abundance profile and the best f_v and v_{turb} values found with our LOC + MCMC approach (dotted grey line). Thus, the difference between the solid red and the dotted grey spectra in Figure 4.7 is the abundance profile used (see Figure 4.6). The spectrum computed with the original chemical model and the best f_v and v_{turb} LOC + MCMC values shows a hint of a double peak and under-reproduces the observed line intensity w.r.t. the observations.

Moreover, to see the effect of the best f_v and v_{turb} LOC + MCMC values on the modelled line profile w.r.t. to the line profile computed by using the original velocity profile and commonly assumed $v_{turb} = 0.075$ km/s, I compute a third spectrum by using both the original abundance and velocity profiles and setting $v_{turb} = 0.075$ km/s (dashed grey line in Figure 4.7). This spectrum shows a line profile tending to a single-peak morphology and underestimates the line intensity w.r.t. the observations.

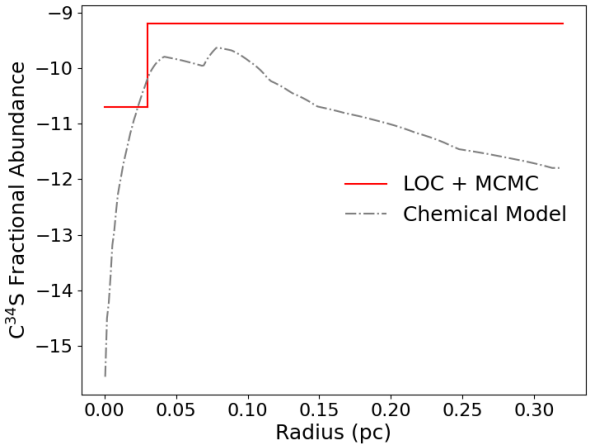

Figure 4.6: $C^{34}S$ step fractional abundance profile obtained from the LOC + MCMC modelling of the observed line profile is plotted in a solid red over the fractional abundance profile obtained from the pyRate chemical model (Sipilä et al. 2015) in a grey dashed-dotted line.

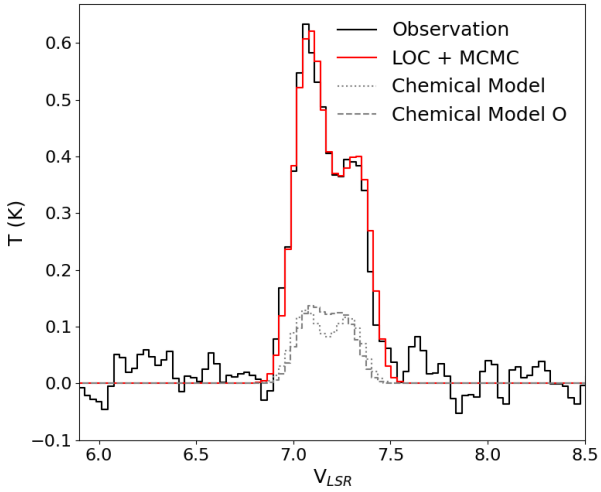

Figure 4.7: Comparison of the $C^{34}S$ spectra computed with different models. The spectrum computed with our LOC + MCMC approach (Figure 4.4) is plotted in a red solid line. The $C^{34}S$ spectrum computed with the original pyRate chemical model fractional abundance profile (Sipilä et al. 2015) and the original pre-stellar core physical model velocity profile and $v_{turb} = 0.075$ km/s, is plotted in a grey dashed line. The spectrum computed with the original fractional abundance profile and the best f_v and v_{turb} values found with our LOC + MCMC approach is plotted with a dotted grey line. Finally, the observations are plotted with a black solid line.

^{34}SO

The ^{34}SO (2,3 - 1,2) transition appears as a single-peaked component with an asymmetric protuberance at $\sim$ 6.9 km/s. The ^{34}SO observed line appears shifted when using the frequency value taken from the CDMS (97715.3170 $\pm$ 0.0500 MHz). The ^{34}SO (2,3 - 1,2) transition was remeasured in the laboratory of the Center for Astrochemical Studies (CAS), finding a value of 97715.395 $\pm$ 0.023 MHz, which we use to centre this line with the V_{LSR} of L1544 (Figure 4.1). This transition is modelled with the "non-extended" model described in Section 1.4.

The resulting model fits the observed transition well, excluding the asymmetric protuberance (observations in black, model in red in Figure 4.8). Nevertheless, not all the variables are well constrained (Table 4.3), making the corner plot deviate from Gaussian profiles to more flattened profiles (Figure 4.9). The a_{in} parameter was not constrained, appearing as a flat profile in the corner plot. The a_{out} and r parameters are less well constrained than f_v and v_{turb}, appearing broader in the corner plot.

Table 4.3: ^{34}SO (2,3-1,2) best model parameters

a_{in}	$2.67^{+82.94}_{-2.62} \times 10^{-13}$
a_{out}	$1.62^{+4.47}_{-1.45} \times 10^{-9}$
r (au)	11405^{+4497}_{-5364}
f_v	$1.00^{+0.15}_{-0.12}$
v_{turb} (km/s)	$0.099^{+0.020}_{-0.017}$

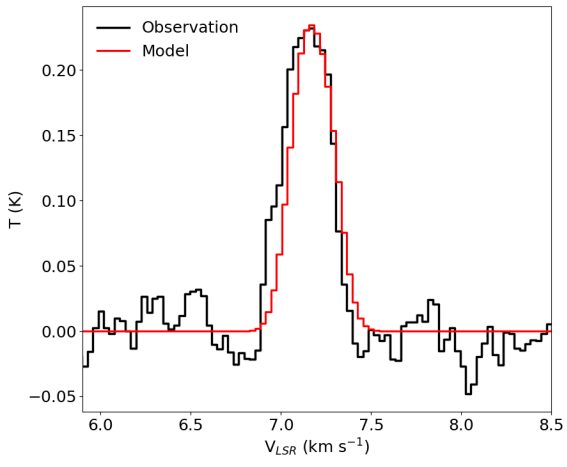

Figure 4.8: ^{34}SO (2,3 - 1,2) observations in black and modelling results in red towards the L1544 dust peak. The corner plot of the parameter exploration corresponding to these results is shown in Figure 4.9.

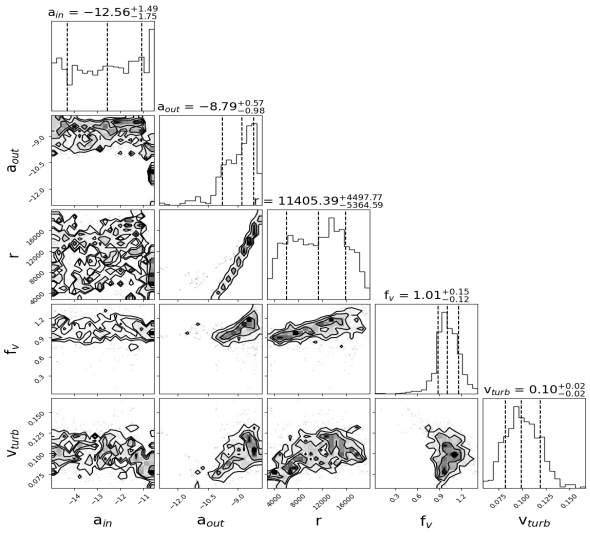

Figure 4.9: Corner plot of the parameters used for the model displayed in Figure 4.8.

The comparison of the step fractional abundance profile used for the line profile modelling in Figure 4.8 and the fractional abundance profile computed with the pyRate chemical model (Sipilä et al. 2015) is presented in Figure 4.10. Like in the case of $C^{34}S$, we scale down the SO fractional abundance profile by the $[^{32}S/^{34}S] = 22$ ratio (Wilson & Rood 1994).

The radius where the ^{34}SO abundance drops due to depletion in the centre of the core found with the LOC + MCMC modelling does not agree with the radius of the fractional abundance profile computed with chemical models, being the first at larger radii (~ 0.05 pc). The ^{34}SO a_{out} value found with the LOC + MCMC modelling is a factor of ~ 2 higher than the highest ^{34}SO chemically modelled abundance.

As done for $C^{34}S$, I compare the spectra computed with our LOC + MCMC approach with the one computed with the original abundance and the best f_v and v_{turb} values found with the LOC + MCMC (Figure 4.11). This spectrum (dotted grey line) overestimates the intensity w.r.t. the spectrum computed with the LOC + MCMC approach (red solid line).

Moreover, I compute a third spectrum by using both the original abundance and velocity profiles and setting $v_{turb} = 0.075$ km/s. The spectrum is single-peaked and overestimates the line intensity (dashed grey line in Figure 4.11).

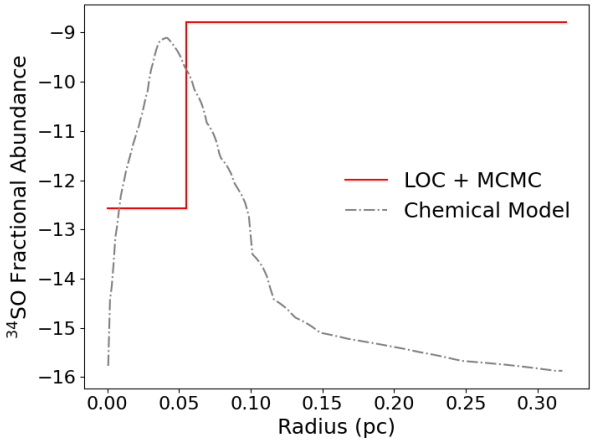

Figure 4.10: ^{34}SO step fractional abundance profile obtained from the LOC + MCMC modelling of the observed line profile is plotted in logarithmic scale in a red solid line over the fractional abundance profile obtained from the pyRate chemical model in (Sipilä et al. 2015) in a grey dashed-dotted line.

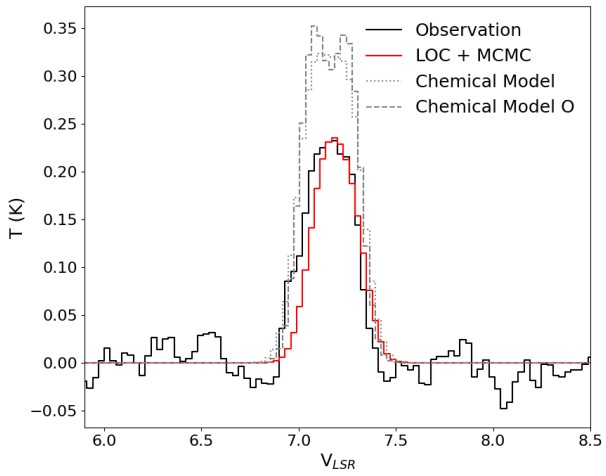

Figure 4.11: Comparison of the ^{34}SO spectra computed with different models. The spectrum computed with our LOC + MCMC approach (Figure 4.8) is plotted in a red solid line. The ^{34}SO spectrum computed with the original pyRate chemical model fractional abundance profile (Sipilä et al. 2015) and the original velocity profile and $v_{turb} = 0.075$ km/s is plotted in a grey dashed line. The spectrum computed with the original fractional abundance profile and the f_v and v_{turb} values found with our LOC + MCMC approach is plotted with a dotted grey line. Finally, the observations are plotted with a black solid line.

$HC^{17}O^+$

The $HC^{17}O^+$ (1-0) transition, first presented in Ferrer Asensio et al. (2022), is split into three hyperfine components ($F \rightarrow F'$ $5/2 \rightarrow 5/2$, $5/2 \rightarrow 7/2$ and $5/2 \rightarrow 3/2$, from lower to higher velocity), which are in turn displaying a double-peaked line profile (Figure 4.1). In Ferrer Asensio et al. (2022), the observations were successfully reproduced with LOC using the pre-stellar core physical model described in Keto et al. (2015) and the $HC^{17}O^+$ fractional abundance profiled scaled from the HCO^+ fractional abundance profile computed with the pyRate chemical model (Sipilä et al. 2015). In this work, we test the LOC + MCMC approach using a step abundance profile (Figure 4.12). Thus, the results presented in this Section are computed with the "non-extended" model described in Section 1.4

The model fits the line double-peaked profile well but underestimates the line intensity. The variable values are well-constrained (Table 4.4), and the corner plot appears to have a Gaussian tendency (Figure 4.12).

Table 4.4: $HC^{17}O^+$ (1-0) best model parameters

a_{in}	$5.81^{+31.86}_{-5.44} \times 10^{-14}$
a_{out}	$7.65^{+32.16}_{-4.91} \times 10^{-12}$
r (au)	4941^{+3590}_{-2079}
f_v	$1.37^{+0.14}_{-0.05}$
v_{turb} (km/s)	$0.070^{+0.010}_{-0.012}$

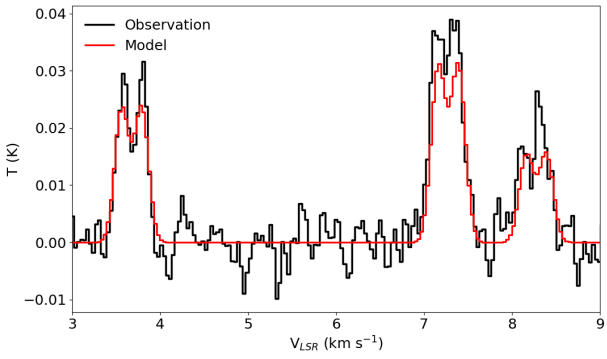

Figure 4.12: $HC^{17}O^+$ (1 - 0) observations in black and modelling results in red towards the L1544 dust peak. The corner plot of the parameter exploration corresponding to these results is shown in Figure 4.12.

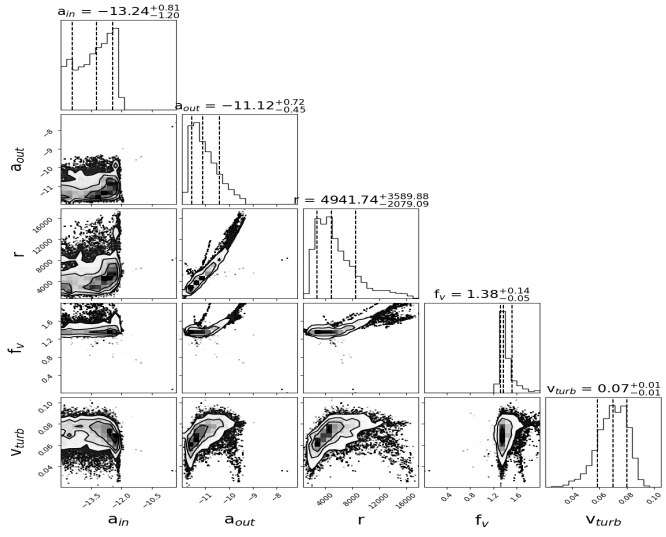

Figure 4.13: Corner plot of the parameters used for the model displayed in Figure 4.12.

The comparison of the step fractional abundance profile used for the line profile model in Figure 4.12 and the fractional abundance profile computed with the pyRate chemical model (Sipilä et al. 2015) is presented in Figure 4.14. As the chemical model in Sipilä et al. (2015) does not take into account oxygen isotope chemistry, I scaled down the HCO^+ fractional abundance profile by the $[^{16}O/^{17}O] = 2044$ ratio (Penzias 1981; Wilson & Rood 1994)). The HCO^+ abundance profile used in this comparison is an updated abundance profile w.r.t. Ferrer Asensio et al. (2022) seen to better fit the HCO^+ observations towards L1544 (Redaelli et al. 2022).

The radius where the $HC^{17}O^+$ abundance drops due to depletion in the centre of the core found with the LOC + MCMC modelling agrees with the radius of the fractional abundance profile computed with chemical models. The $HC^{17}O^+$ a_{out} value found with the LOC + MCMC modelling is a factor ~ 1.3 weaker than the highest $HC^{17}O^+$ chemically modelled abundance.

As done for the previous molecules, I compare the spectra computed with our LOC + MCMC approach with the spectrum computed with the original abundance and the best f_v and v_{turb} values found with the LOC + MCMC in Figure 4.15. This spectrum (dotted grey line) underestimates the intensity and gives double-peaked hyperfine components.

Moreover, I compute a third spectrum by using both the original abundance and velocity profiles and setting $v_{turb} = 0.075$ km/s. This spectrum is also underproduced, and the hyperfine components appear single-peaked (dashed grey line in Figure 4.15).

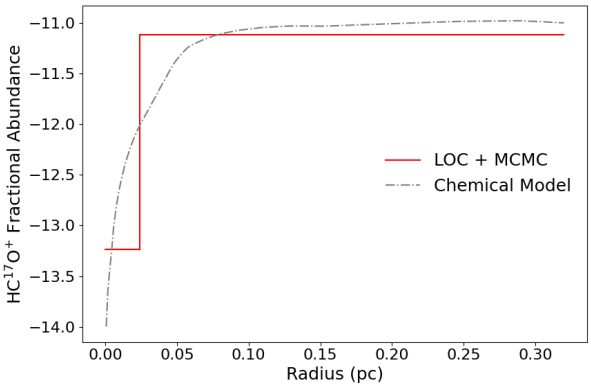

Figure 4.14: $HC^{17}O^+$ step fractional abundance profile obtained from the LOC + MCMC modelling of the observed line profile is plotted in logarithmic scale in a solid red line over the fractional abundance profile obtained from the pyRate chemical model in Sipilä et al. (2015) in a grey dashed-dotted line.

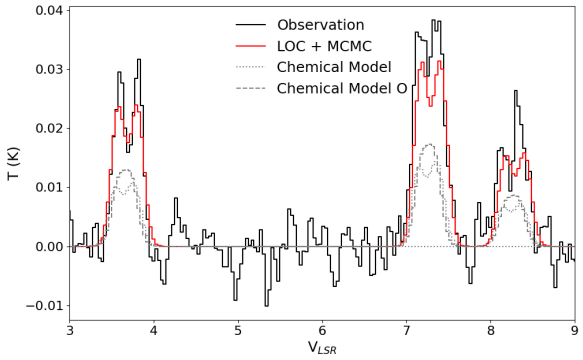

Figure 4.15: Comparison of the $HC^{17}O^+$ spectra computed with different models. Our LOC + MCMC approach (Figure 4.12) is plotted in a red solid line. The $HC^{17}O^+$ spectrum computed with the original pyRate chemical model fractional abundance profile (Sipilä et al. 2015) and the original velocity profile and $v_{turb} = 0.075$ km/s, is plotted in a grey dashed line. The spectrum computed with the original fractional abundance profile and the f_v and v_{turb} values found with our LOC + MCMC approach is plotted with a dotted grey line. Finally, the observations are plotted with a black solid line.

4.4.2 Optically Thick Transitions

The molecules included in the next subsections are abundant enough to also emit (absorb) from the extended structure beyond 0.32 pc. Our approach is first to model the optically thick transitions arising from abundant molecules with the "non-extended" model and then test the "extended" model if the previous fails to reproduce the observations.

CS

The CS (2 - 1) transition appears double-peaked with a dip that almost reaches the baseline (Figure 4.1). The blue and red peaks have similar intensities. This transition was first fit with the "non-extended" model described in Section 4.3.2, and the results are presented in the red spectra in Figure 4.16. The model fits well the observed line profile (black spectra in Figure 4.16). On the other hand, the variables are less constrained (Table 4.5) than the ones found for the optically Thin lines. In this case, the f_v, with a value lower than 1 ($0.22^{+0.92}_{-0.01}$), indicates the need to downscale the velocity profile to reproduce the observations. This is in contrast with the $C^{34}S$ and $HC^{17}O^+$ transitions modelling in Section 4.4.1, which showed f_v values higher than one, indicating the need to upscale the velocity profile to be able to fit the observations. Moreover, the v_{turb} is also higher ($0.115^{+0.001}_{-0.038}$ km/s) than seen in Section 4.4.1. The histograms in the corner plot appear as a single peak instead of the expected Gaussian profile. Given these results, and knowing the presence of a diffuse extended layer around L1544 Redaelli et al. (2022), we run the "extended" model described in Section 4.3.2 to assess whether the parameters and the corner plot can be better constrained taking into account an extended layer. The CS abundance is kept constant in the extended layer, assuming a value of 1×10^{-9} as seen towards diffuse clouds (Snow & McCall 2006). The "extended" model (blue dash-dotted spectra Figure 4.16) gives similar results to the "non-extended" model (red solid spectra in Figure 4.16). The resulting spectrum of the "non-extended" model shows a slightly more pronounced asymmetry. The parameters of the "extended" model (Table 4.6) are, within errors, the same results as the "non-extended" model ones (Table 4.5). The corner plot of the "extended" model (Figure 4.18) also looks really similar to the "non-extended" model corner plot (Figure 4.17). The "extended" model does not improve the results w.r.t. the "non-extended" model.

Table 4.5: CS (2 - 1) best "non-extended" model parameters

a_{in}	$2.17^{+151.64}_{-2.28} \times 10^{-12}$
a_{out}	$5.10^{+1.43}_{-0.42} \times 10^{-9}$
r (au)	3026^{+3168}_{-252}
f_v	$0.22^{+0.92}_{-0.01}$
v_{turb} (km/s)	$0.115^{+0.001}_{-0.038}$

Table 4.6: CS (2 - 1) best "extended" model parameters

a_{in}	$1.25^{+37.39}_{-1.22} \times 10^{-12}$
a_{out}	$4.61^{+22.74}_{-0.31} \times 10^{-9}$
r (au)	2624^{+3170}_{-163}
f_v	$0.22^{+1.16}_{-0.01}$
v_{turb} (km/s)	$0.115^{+0.002}_{-0.044}$

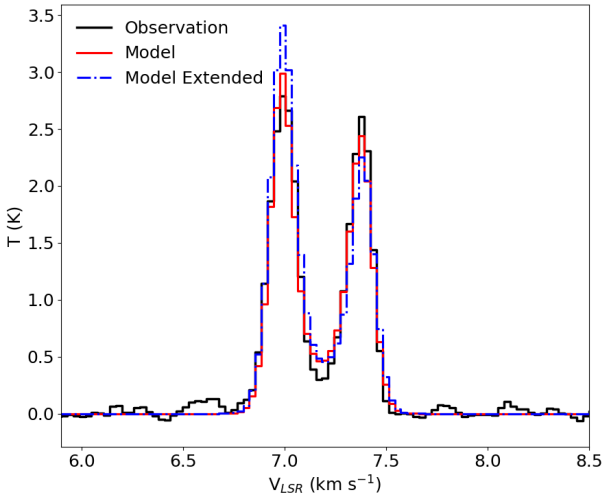

Figure 4.16: CS (2 -1) observations towards the L1544 dust peak in black. The "non-extended" model is plotted in the solid red spectra, and the "extended" model is plotted in the dash-dotted blue spectra. The corner plot of the parameter exploration corresponding to these results is shown in Figure 4.17.

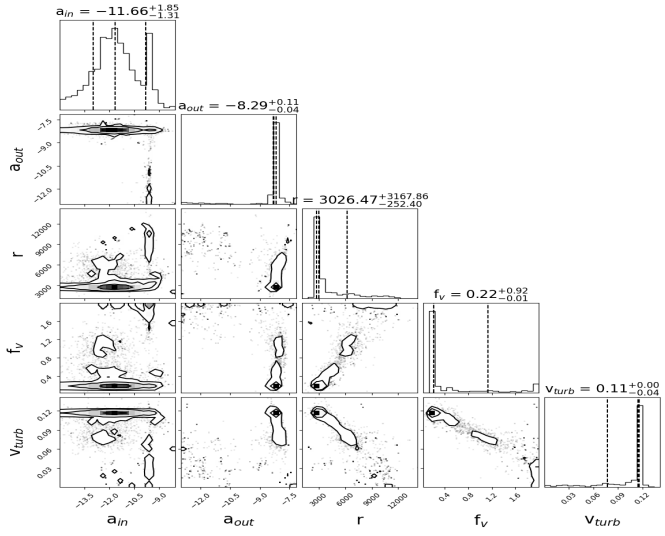

Figure 4.17: Corner plot of the parameters used for the "non-extended" model displayed in a solid red line in Figure 4.16.

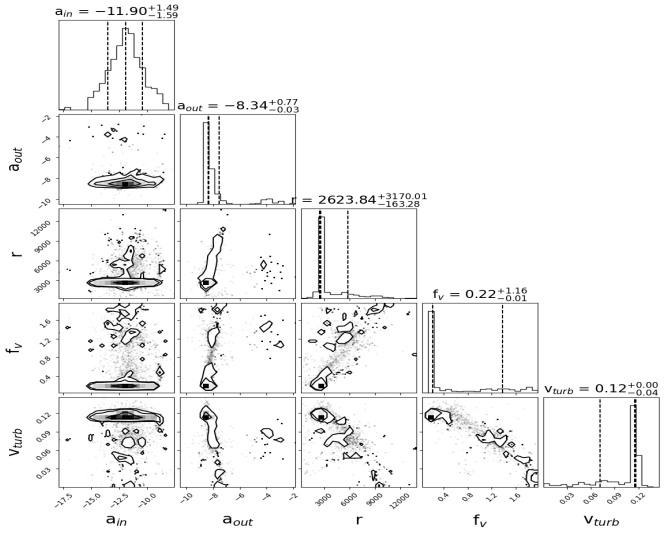

Figure 4.18: Corner plot of the parameters used for the "extended" model displayed in a dash-dotted blue line in Figure 4.16.

The comparison of the step fractional abundance profile used for the line profile "non-extended" and "extended" models in Figure 4.16 and the fractional abundance profile computed with the pyRate chemical model (Sipilä et al. 2015) are presented in Figures 4.19 and 4.20.

The radius where the CS abundance drops due to depletion in the centre of the core found with the "non-extended" LOC + MCMC modelling is shifted by ~ 0.01 pc w.r.t. the chemical models. The CS a_{out} value found with the LOC + MCMC modelling agrees with the largest abundance from the chemical model.

The "extended" step abundance profile behaves within errors the same way the "non-extended" model does. For comparison, we have plotted the extended layer with the fixed fractional abundance value of 1×10^{-9}. In Figure 4.22, I compare the CS spectrum computed with our "extended" LOC + MCMC approach with the CS spectrum computed with LOC with the fractional abundance profile computed with the pyRate chemical model (Sipilä et al. 2015), plotted in black in Figure 4.20. The spectrum computed with the chemical model (grey dashed line in Figure 4.22) shows similar features as the "non-extended" model (Figure 4.21).

As done with the other molecules, I compare the spectra computed with our LOC + MCMC approach with the spectrum computed with the original abundance and the best f_v and v_{turb} values found with the LOC + MCMC ("non-extended" and "extended" models in Figures 4.21 and 4.22). For the "non-extended" model, the spectrum computed with the original fractional abundance profile and the best f_v and v_{turb} values (dotted grey line) underestimates the line strength and does not reproduce the self-absorption dip.

Moreover, I compute a third spectrum by using both the original abundance and velocity profiles and setting $v_{turb} = 0.075$ km/s. This approach for the "non-extended" model also underproduces the line intensity, but less than for the model using the best f_v and v_{turb} values. This model results in a similar self-absorption dip as for our LOC + MCMC approach model.

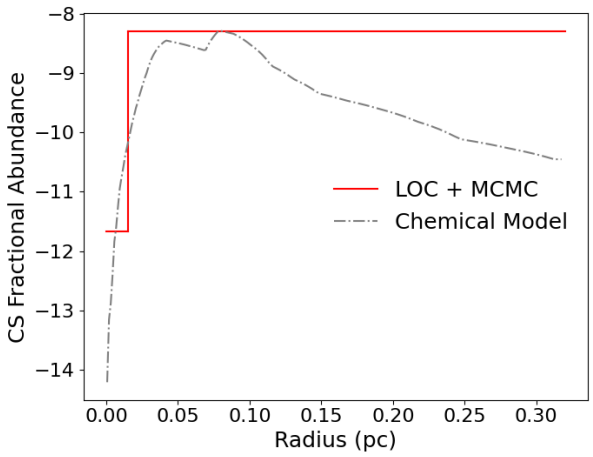

Figure 4.19: CS step fractional abundance profile obtained from the "non-extended" LOC + MCMC modelling of the observed line profile is plotted in logarithmic scale in a solid red line over the fractional abundance profile obtained from the pyRate chemical model in Sipilä et al. (2015) plotted with a dashed-dotted grey line.

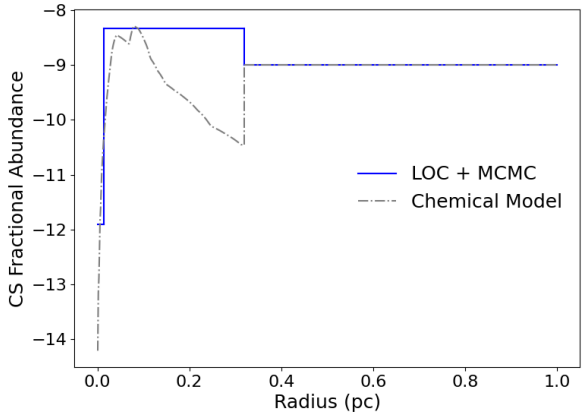

Figure 4.20: CS step fractional abundance profile obtained from the "extended" LOC + MCMC modelling of the observed line profile is plotted in logarithmic scale in a solid blue line over the fractional abundance profile obtained from the pyRate chemical model in Sipilä et al. (2015) with a dashed-dotted grey line.

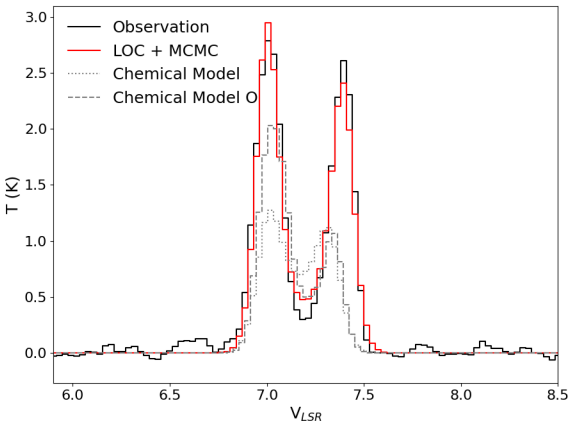

Figure 4.21: Comparison of the CS spectra computed with different models. Our "non-extended" LOC + MCMC approach (red spectrum in Figure 4.16) is plotted in a red solid line. The CS spectrum computed with the original pyRate chemical model fractional abundance profile (Sipilä et al. 2015) and the original velocity profile and v_{turb} = 0.075 km/s, is plotted in a grey dashed line. The spectrum computed with the original fractional abundance profile and the f_v and v_{turb} values found with our LOC + MCMC approach is plotted with a dotted grey line. Finally, the observations are plotted with a black solid line.

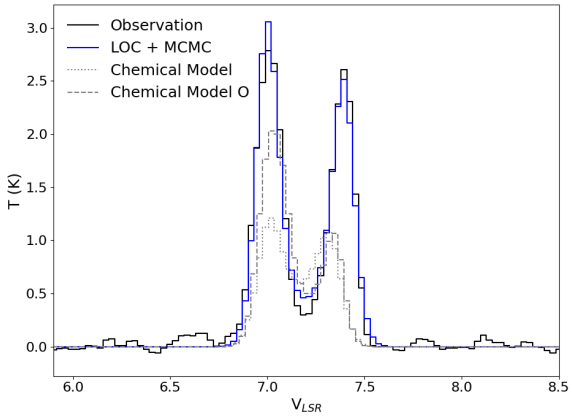

Figure 4.22: Comparison of the CS spectra computed with different models. Our "extended" LOC + MCMC approach (blue spectrum in Figure 4.16) is plotted in a blue solid line. The CS spectrum computed with the original pyRate chemical model fractional abundance profile (Sipilä et al. 2015) and the original velocity profile and v_{turb} = 0.075 km/s, is plotted in a grey dashed line. The spectrum computed with the original fractional abundance profile and the f_v and v_{turb} values found with our LOC + MCMC approach is plotted with a dotted grey line. Finally, the observations are plotted with a black solid line.

With the idea of better constraining the CS model parameters, we perform a combined modelling of the CS and $C^{34}S$ (2 - 1) transitions. These tests do not bring new information to the information obtained from the CS and $C^{34}S$ separated models. For more information, refer to section C.1 in the Appendix.

4.4.3 SO

The SO (2,3 - 1,2) transition presents the characteristic blue asymmetry line profile (Figure 4.1). Unlike other optically thick lines introduced in this work (CS, HCO^+ and H_2CO), SO presents a shallower self-absorption feature. The SO (2,3 - 1,2) transition is fitted with the "non-extended" model. As we can see in Figure 4.23, the model (in red) fits well the observations (in black). The model parameters are well-constrained (Table 4.7). The corner plot is displayed in Figure 4.24.

Table 4.7: SO (2,3 - 1,2) best model parameters

a_{in}	$1.07^{+6.82}_{-0.92} \times 10^{-12}$
a_{out}	$1.97^{+0.74}_{-0.21} \times 10^{-9}$
r (au)	4987^{+737}_{-242}
f_v	$1.30^{+0.02}_{-0.01}$
v_{turb} (km/s)	$0.084^{+0.002}_{-0.004}$

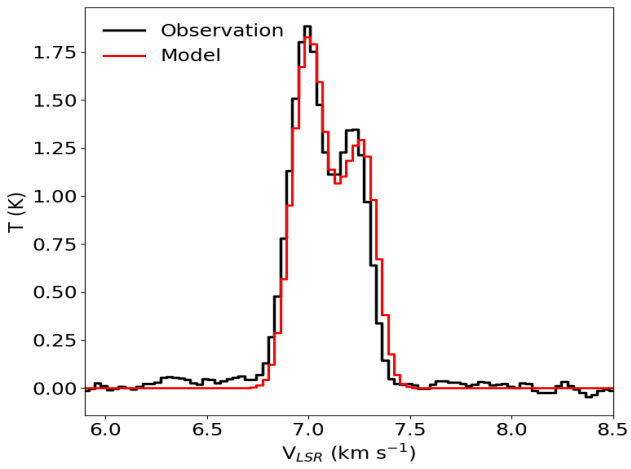

Figure 4.23: SO (2,3 - 1,2) observations in black and modelling results in red towards the L1544 dust peak. The corner plot of the parameter exploration corresponding to these results is shown in Figure 4.24.

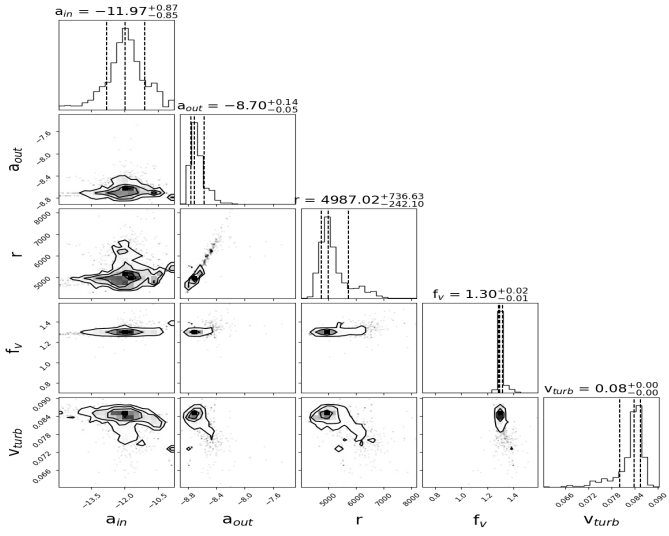

Figure 4.24: Corner plot of the parameters used for the "non-extended" model displayed in Figure 4.23.

The comparison of the step fractional abundance profile used to model the spectrum in Figure 4.23 and the fractional abundance profile computed with the pyRate chemical model described in Sipilä et al. (2015) are presented in Figure 4.25.

The radius where the SO abundance drops due to depletion in the centre of the core found with the LOC + MCMC modelling agrees with the radius of the fractional abundance profile computed with chemical models. The a_{out} SO value found with the LOC + MCMC modelling is a factor of ~ 8 lower compared to the highest SO chemically modelled abundance.

As done with the other molecules, I compare the spectra computed with our LOC + MCMC approach with the original abundance and the best f_v and v_{turb} values found with the LOC + MCMC in Figure 4.26. The spectrum computed with the original fractional abundance profile and the best f_v and v_{turb} values (dotted grey line) overestimates the line strength.

Moreover, I compute a third spectrum by using both the original abundance and velocity profiles and setting $v_{turb} = 0.075$ km/s. This approach also overestimates the line intensity and shows less-separated peaks.

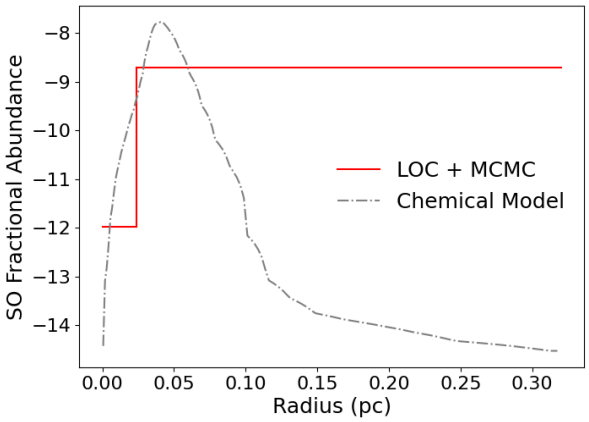

Figure 4.25: SO step fractional abundance profile obtained from the "non-extended" LOC + MCMC modelling of the observed line profile is plotted in logarithm scale in a solid red line over the fractional abundance profile obtained from the pyRate chemical model in Sipilä et al. (2015) in a dashed grey line.

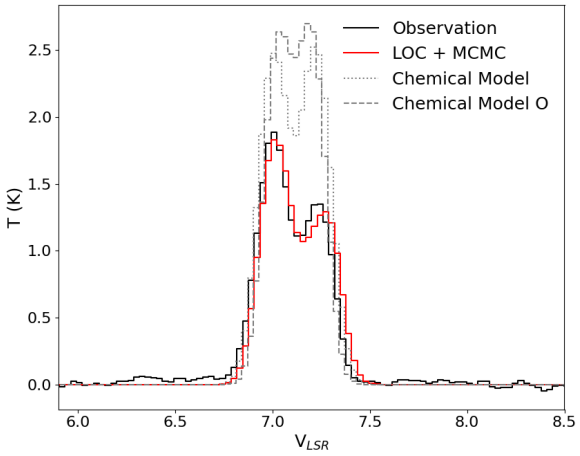

Figure 4.26: Comparison of the SO spectra computed with different models. Our LOC + MCMC approach (Figure 4.23) is plotted in a red solid line. The SO spectrum computed with the original pyRate chemical model fractional abundance profile (Sipilä et al. 2015) and the original velocity profile and $v_{turb} = 0.075$ km/s is plotted in a grey dashed line. The spectrum computed with the original fractional abundance profile and the f_v and v_{turb} values found with our LOC + MCMC approach is plotted with a dotted grey line. Finally, the observations are plotted with a black solid line.

Moreover, as for the case of CS, we perform a combined fit of SO and ^{34}SO to try to better constrain the parameters found with the individual models of the molecules. This test does not present new information (see Section C.2 in the Appendix).

The LOC + MCMC fitting approach was not able to give good constraints on the parameters for the HCO^+ (1 - 0), the H_2CO $2_{1,2}$ - $1_{1,1}$ and the c-C_3H2 $2_{1,2}$ - $1_{0,1}$ transitions. Thus, as these line fits were not conclusive, they are presented in the Appendix C.

4.5 Discussion

In Section 4.4, I have presented the results of the radiative transfer modelling using the LOC + MCMC approach described in Section 4.3. The first general trend is that this modelling approach reproduces the observed spectra and results in better-constrained parameters for optically thin lines w.r.t. optically thick lines. Moreover, fitting the main and rare isotopologues together has been shown not to improve the constraints on the modelled fractional abundance profiles (refer to Appendix C). Having a higher number of lines could help to constrain the fractional abundance profiles better. Unfortunately, we cannot try this approach in this manuscript as just one line of each isotopologue has been observed.

The optically thin lines presented in this work are well fit with the "non-extended" model described in Section 4.3.2, with the exception of ^{34}SO (2,3 - 1,2), which has less well-constrained parameters than C^{34}S (2 - 1) and HC^{17}O$^+$ (1 - 0). This can be due to the lower level of line profile complexity for ^{34}SO, which represents fewer constraints for the modelling, resulting in broader histograms in the corner plot. The C^{34}S and HC^{17}O$^+$ lines present double-peaked profiles which are well fitted with a f_v value of $\sim$ 1.3. The need for upscaling the pre-stellar core velocity profile indicates that these optically thin transitions trace the inner region of the L1544 pre-stellar core, where the gas velocity is the highest. This agrees with what was found for the HC^{17}O$^+$ (1-0) transition in Ferrer Asensio et al. (2022) with a different modelling approach. On the other hand, ^{34}SO appears single-peaked and f_v has a value of $\sim$ 1.0. Thus, ^{34}SO seems to be tracing a region at larger radii than C^{34}S and HC^{17}O$^+$.

The radius where C^{34}S and HC^{17}O$^+$ deplete, as computed with the LOC + MCMC model, agrees with the radius where the abundance decreases in the fractional molecular abundance profiles computed with the pyRate chemical model (Sipilä et al. 2015). Nevertheless, the modelled a_{out} abundances are a factor $\sim$ 1.75 on average higher than the highest value in the fractional molecular abundance profiles computed with chemical modelling.

On the other hand, the radius where ^{34}SO depletes computed with the LOC + MCMC model lays at larger radii than the one shown in the fractional molecular abundance profile computed with chemical modelling. We have to keep in mind that r was not well-constrained, but these results could also be pointing at a problem with the chemical network used to compute the SO, and consequently ^{34}SO, fractional abundance profile. Moreover, the modelled a_{out} abundance is a factor $\sim$ 2 higher than the highest value in the fractional molecular abundance profiles computed with chemical modelling.

The drop in the outer parts of the core in the SO fractional abundance profile shown in a grey dashed line in Figure 4.10 could be the result of the "depleted" initial abundances assumption in the pyRate chemical model described (Sipilä et al. 2015). This assumption involves reducing the initial S abundance to avoid an excess of sulphur-bearing species in the inner part of the core to reproduce the observed sulphur depletion known as "the sulphur depletion problem" (Ruffle et al. 1999). This results in an underestimation of the sulphur-bearing abundances on the outer parts of the core. Observationally, SO has shown to have an extended morphology in some pre-stellar cores (e.g. in L134N, Swade 1989, and in L183, Lattanzi et al. 2020) and it could also be the case for L1544.

From these results, $C^{34}S$ and $HC^{17}O^+$ seem to trace a region at similar radii in the innermost part of L1544, while ^{34}SO traces a region at larger radii. These optically thin transitions provide constraints on the molecular fractional abundance profiles and on the kinematic structure of the inner parts of L1544.

The optically thick lines presented in Section 4.4 show less well-constrained parameters compared to the optically thin transition models.

The CS (2 - 1) "non-extended" and "extended" models result, within errors, in the same fit. The low-velocity profile scaling value alongside the high turbulent velocity value found in both "extended" and "non-extended" models point to CS tracing slow-contracting less quiescent gas. Thus, CS seems to be tracing the outer parts of the core, where the gas contraction velocity decreases and the turbulent velocity increases. Moreover, the comparable intensity of the two components in the CS transition suggests that the line self-absorption occurs in a static layer within the core, one that moves with the systemic velocity of the L1544 core (V_{LSR} = 7.2 km/s). The computed r where the CS depletes in the centre of the core as well as the highest a_{out} values agree with the fractional abundance profile computed with chemical modelling.

The typical core contraction blue asymmetry line profile of the SO (2,3 - 1,2) transition is well-fitted with the "non-extended" model. This molecule is not abundant enough in the outer parts of the core for self-absorption of the magnitude of the CS (2 - 1) line to occur. In this case, contrarily with what was found for ^{34}SO, the radius at which the molecule depletes in the centre of the core computed with the LOC + MCMC approach agrees with the one seen in the fractional abundance profile computed with chemical modelling. Nevertheless, SO (2,3 - 1,2) is an optically thick line and should not be sensitive to the innermost core structure like ^{34}SO is. The computed a_{out} value is a factor of $\sim$ 8 lower than the highest abundance in the fractional abundance profile computed with chemical modelling.

The CS (2 - 1) and SO (2,3 - 1,2) transitions fit well with the "non-extended" model, showing they are tracing a region within the pre-stellar core.

The line profiles of the other optically thick lines hint at the properties of the gas they trace but, with a lack of well-constrained radiative transfer models, do not provide strong constraints on their fractional abundance profiles. For more details, refer to Appendix C.

All of the transitions presented in this manuscript trace different parts of the L1544 core, which have different physical, chemical and kinematic properties. The optically thin $C^{34}S$ (2 - 1) and $HC^{17}O^+$ (1 - 0) transitions trace the innermost part of the core where the gas contracts at high velocities. The optically thin ^{34}SO (2,3 - 1,2) traces a region at larger radii than the other optically thin lines tracing slower contraction velocities. Then, the SO (2,3 - 1,2) transition traces material that is contracting. Lastly, the CS (2 - 1) transition traces the outer part of the core that is static.

The comparison between the spectra computed with our LOC + MCMC approach, with the original fractional abundance profiles computed with the chemical model described in Sipilä et al. (2015) and the best f_v and v_{turb} values, and the original fractional abundance and velocity profiles and v_{turb} = 0.075 km/s, showed us the need of slightly modifying the abundance profiles and physical parameters used for the modelling of the high-sensitivity and high-spectral resolution observed lines towards L1544.

Chemical differentiation towards the L1544 pre-stellar core has been observed, showing the spatial distributions of the molecules not to be radially symmetric but to be present in different

regions of the core (Spezzano et al. 2017) as different "molecular peaks". This observed chemical segregation towards L1544 was successfully modelled with a pre-stellar core embedded in a dynamic star-forming cloud using a three-dimensional magnetohydrodynamic approach (Jensen et al. 2023). Moreover, multi-line observations towards L1544 showed the need for a local enhancement of the molecular hydrogen column density, showing that pre-stellar cores can show a clumpy structure deviating from the BES ideal (Lin et al. 2022).

4.6 Conclusions

This work has presented new high-sensitivity and high-spectral resolution observations of the HCO^+ (J = 1 - 0), CS (J = 2 - 1), $C^{34}S$ (J = 2 - 1), H_2CO ($J_{K_a,K_c} = 2_{1,2}$ - $1_{1,1}$), c-C_3H2 ($J_{K_a,K_c} = 2_{1,2}$ - $1_{0,1}$), SO (N,J = 2,3 - 1,2) and ^{34}SO (N,J = 2,3 - 1,2) as well as $HC^{17}O^+$ (J = 1 - 0) (Ferrer Asensio et al. 2022) rotational transitions towards the dust peak of the L1544 pre-stellar core.

Reproducing the optically thin lines through radiative transfer modelling was generally successful, providing good constraints on the abundance profiles for these species, in contrast to optically thick lines. In order to better constrain the fit for optically thick lines, more transitions are needed to be fitted simultaneously. The CS (J = 2 - 1), $C^{34}S$ (J = 2 - 1), SO (N,J = 2,3 - 1,2), ^{34}SO (N,J = 2,3 - 1,2) and $HC^{17}O^+$ (J = 1 - 0) observed transitions are successfully reproduced with a 1D non-LTE radiative transfer model coupled to the Markov Chain Monte Carlo approach using a pre-stellar core physical model. The optically thin transitions modelling constrained the innermost region of the L1544 pre-stellar core. On the other hand, the optically thick transitions constrained the outer parts of L1544.

The fractional abundance profiles of these molecules are constrained and compared to the fractional abundance profiles computed with a pseudo-time-dependent chemical model, pointing to the possible incompleteness of the chemical networks used or to the uncertainties in elemental abundances input in chemical models.

The results presented in this manuscript show that all of the molecular transitions trace different parts of the L1544 core with different physical, chemical and kinematic properties, strengthening the idea that L1544 deviates from the homogeneous spherically-symmetric ideal generally used for modelling this source. Thus, these results point to the need to use 3D radiative transfer modelling to be able to interpret increasingly sensitive and spectrally resolved spectra towards L1544.

5

Conclusions and future work

5.1 Summary

This thesis presents relevant results for the understanding of the initial conditions of the star formation process through the study of the physical, chemical and kinematic structure of the L1544 pre-stellar core using observational and modelling techniques. Moreover, results on the origin and transfer of COMs in the first stages of the star formation process through spectroscopic measurements of a deuterated molecule in the laboratory and observations towards the proto-stellar system IRAS 16293-2422 are presented.

Tracing the contraction of the pre-stellar core L1544 with $HC^{17}O^+$ $J = 1$ - 0 emission. In order to understand the cause of the double-peaked line profile observed for several optically thin transitions towards the prestellar core L1544, I performed non-LTE radiative transfer modelling to reproduce the high spectral resolution and sensitivity $HC^{17}O^+$ J=1-0 transition. This line was well fitted with the Keto Caselli contracting core model (Keto et al. 2015) alongside the molecule's abundance profile by scaling the velocity profile by 1.3 and the abundance profile by 4. I was also able to reproduce the optically thin $C^{17}O$ J=1-0 line, which does not appear double peaked, with the same physical and chemical model just by upscaling the abundance profile by 3. I found that due to a combination of the critical density of the transition and the spatial distribution of the molecules, $HC^{17}O^+$ (1 - 0) traces the innermost part of the core where the contracting velocity is higher, while $C^{17}O$ (1 - 0) traces mostly the outer parts of the core where the gas moves slower. The fact that I needed a higher velocity towards the centre of the core may indicate that this is more evolved than we previously thought.

Millimetre and sub-millimetre spectroscopy of doubly deuterated acetaldehyde (CHD_2CHO) and first detection towards IRAS 16293-2422. I measured the rotational spectra of the doubly-deuterated form of the astrophysically relevant molecule acetaldehyde. The measurements were carried out with the Chirped-Pulse Fourier Transform Spectrometer (CP-FTS) alongside the high-resolution absorption experiment in the frequency range of 82.5 to 450 GHz. Over 700 new lines were recorded. The transitions were fitted with a modified Internal Axis Method (IAM) approach which takes into account the coupling of the internal with the overall rotation obtaining a weighted root mean square standard deviation of 1.7. From these results, I built an accurate spectroscopic catalogue for CHD_2CHO that I made available in the CDMS. With this catalogue, I detected doubly deuterated acetaldehyde for the first time in the Interstellar Medium towards the protostellar system IRAS 16293-2422 in the PILS data (Jørgensen et al. 2016). From these observations a column density of 1.3×10^{15} cm^{-2} was retrieved for CHD_2CHO giving a D_2/D ratio of $\sim$ 20% consistent with D_2/D ratios retrieved for other COMs towards IRAS 16293-2422. The similarity of the D_2/D ratios suggests a common formation environment for these molecules where deuterium fractionation is enhanced, possibly the pre-stellar core.

High sensitivity and spectral resolution molecular line observations towards the L1544 pre-stellar core: challenges to current models I observed the CS J = 2 - 1, the $C^{34}S$ J = 2 - 1, the SO N,J = 2,3 - 1,2, the ^{34}SO N,J = 2,3 - 1,2, the H_2CO $J_{K_a,K_c} = 2_{1,2}$ - $1_{1,1}$, the c$-C_3H_2$ $J_{K_a,K_c} = 2_{1,2}$ - $1_{0,1}$ and the HCO^+ J = 1 - 0 transitions with the IRAM 30m telescope towards the dust peak of the L1544 pre-stellar core. Moreover, previous $HC^{17}O^+$ observations also taken with the IRAM 30m telescope towards the dust peak of L1544 were used. I then performed

1D non-LTE radiative transfer modelling coupled with Markov Chain Monte Carlo methods of these transitions by using a pre-stellar core physical model. The radiative transfer modelling for optically thin lines resulted in better constrained parameters than for optically thick lines. The joint modelling of the main and rare isotopologues does not improve the fit as the parameters were not constrained. This points to the need for more transitions to constrain some of the optically thick line fits. Each of the transitions studied in this project traces a different part of the L1544 core with different physical, chemical and kinematic properties. This work further highlights the non-homogenous and non-spherically-symmetric nature of L1544 as commonly assumed for modelling and highlights the need to perform 3D radiative transfer modelling in the future for the interpretation of highly-sensitive and highly spectrally resolved molecular line observations towards L1544.

5.2 Future work

The work presented in this Thesis adds to the current knowledge on the initial conditions of the star formation process through the study of the physical, chemical and kinematic structure of the pre-stellar core L1544 and through the first detection of CHD_2CHO towards the protostellar system IRAS 16293 - 2422. The study of the topics presented in this Thesis will be continued in future projects which are described below.

The observations presented in both Chapters 2 and 4 hint at the possibility of L1544 being a more evolved pre-stellar core than previously thought. On the one hand, in Chapter 2, I showed the need to use an upscaled velocity profile w.r.t. the velocity profile suggested in the pre-stellar core physical model in Keto et al. (2015) to reproduce the observed double-peaked line profile of the $HC^{17}O^+$ (1 - 0) transition. This result potentially points at the gas-contraction velocity in the innermost part of the core is higher than expected, and thus that L1544 is dynamically more evolved than previously thought. In Chapter 4, I present the high-sensitivity and high-spectral resolution HCO^+ (1 - 0) observed spectrum which displays a blue excess feature. This feature, which traces emission at really high velocities, could be a hint of a faster contraction of L1544 than predicted, aligning with the results presented in Chapter 2.

The blue excess feature seen in HCO^+ (1 - 0) (Chapter 4) was seen for the first time in the ortho-H_2O (1_{10} - 1_{01}) transition, observed with the *Herschel Space Telescope* towards L1544 (Figure 5.1). In order to understand the nature of this blue excess feature and its link with the evolutionary state of pre-stellar cores, I have submitted a proposal to the IRAM 30 m telescope which has been accepted. This research proposes observing high-resolution and high-sensitivity spectra of HCO^+ (1-0) towards various cores: Oph D, L429, L694-2, L1517B, and L1521F a Very Low-Luminosity Object (VeLLO). The selected cores represent distinct evolutionary stages, ranging from starless to protostellar which will facilitate a comprehensive analysis of the blue excess feature's association with the ongoing formation of central structures. The objective is to see the presence or absence of the blue excess feature and understand its correlation with the evolutionary state of the cores. Additionally, radiative transfer modelling of the HCO^+ emission, including observations of the rarer isotopologue $HC^{18}O^+$ (1-0) transition, will be conducted to elucidate the physicochemical conditions responsible for the observed blue excess feature. A possible follow-up to this project

will involve extending the observations to map the blue excess feature, providing insights into the formation of a flattened central structure, possibly evolving into a protoplanetary disk.

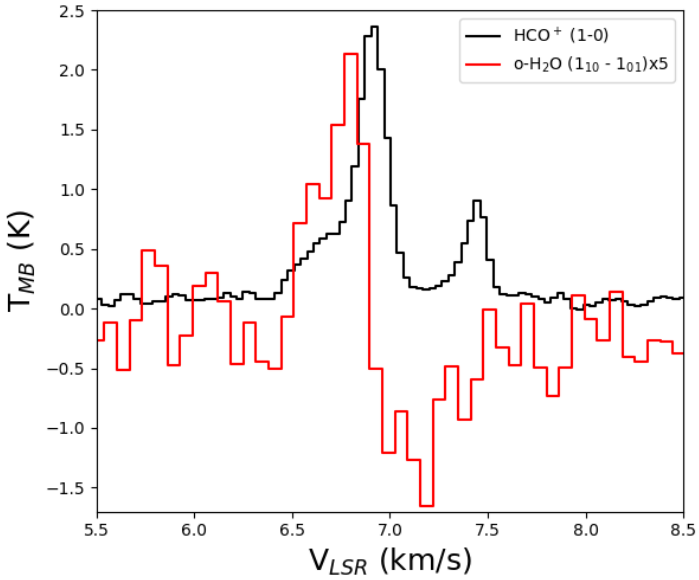

Figure 5.1: Overlaid spectra of ortho-H_2O (1_{10} - 1_{01}) upscaled by a factor of 5 taken with Herschel in red (Caselli et al 2012) and HCO^+ (1-0) taken with the IRAM 30m telescope in black (Ferrer Asensio et al. 2024 in prep.) towards the dust peak of L1544.

The work contained in Chapter 3 has highlighted the importance of accurate molecular spectroscopic catalogues for the detection of molecules in the ISM. Moreover, through this work, I have reaffirmed the power of doubly deuterated molecules as COMs journey tracers in the early stages of the star formation process.

In the next phase of this research, I propose an in-depth exploration of the journey of interstellar COMs across the early stages of star formation, employing deuterium fractionation as a key investigative tool. The primary focus will be on two significant COMs, methyl formate and ethanol, integrating observations, modelling, and laboratory experiments. This multifaceted approach will aim to shed further light on the implications of observed deuterium abundance ratios of COMs and their correlation with the early physical conditions of star formation.

The choice of COMs for this project lies on the prevalence in space and potential role as precursors to more complex molecular species that methyl formate ($HCOOCH_3$) and ethanol (CH_3CH_2OH) have. First, contained in a first project, I will widen the sample of observed singly- and doubly-deuterated methyl formate abundance ratios across both low- and high-mass star prestellar and protostellar objects. This will provide insights into the journey of this molecule during the early stages of star formation and enhance our understanding of the associated physical conditions. Secondly, as included in a second project, I will construct, for the first time, an accurate spectroscopic catalogue for doubly deuterated ethanol through laboratory measurements.

This will enable the detection of doubly deuterated ethanol in the interstellar medium (ISM), allowing for a comparison of its D_2/D ratio with that of other COMs. As an additional result, the observed D_2/D ratios of methyl formate and ethanol, will aid the understanding formation mechanisms of their main as well as their deuterated isotopologues, which to date, are still under debate.

A

Tracing the contraction of the pre-stellar core L1544 with $HC^{17}O^+$ $J = 1$ - 0 emission.

In this Section of the Appendix, I present complementary material to the content introduced in Chapter 2. This includes additional radiative transfer models, the assessment of the calculated column density dependency of T_{ex} assumed and the hyperfine collisional rate coefficients for $HC^{17}O^+$ and $C^{17}O$.

A.1 Results of the considered scenarios

In this Section, we present complementary results obtained to evaluate the viability of the different possible scenarios for the $HC^{17}O^+(1$ - $0)$ double-peaked structure. All the models presented were computed with a HCO^+ fractional abundance profile at $t = 5 \times 10^5$ yrs, and thus are comparable with the best-fit results (AM 2 in Figure 2.3). Fractional abundance profiles at time steps between 10^4 and 10^7 yrs were also tested and led to less accurate fits with larger residual standard deviations.

A.1.1 Depletion

The chemical model takes into account the CO depletion by freeze-out at the centre of the core. This affects the HCO^+ fractional abundance (Figure 2.4) as this molecule is formed by the reaction of CO with H_3^+. Following the idea that the model flat-topped profiles in the OM of Figure 2.3 could be the result of the enhanced $HC^{17}O^+$ depletion towards the core centre, we tested larger depletions than those taken into account in the chemical model to see whether we could fit the observed line profiles better. To this end, we modelled the radiative transfer of the molecule with a modified fractional abundance profile, creating fractional abundance holes with different radii. We tested the effect of a 7000 au radius hole, and show the resulting spectra from a model with $HC^{17}O^+$ depletion from 0 to 7000 au in Figure A.1. We note that in order to distinguish the feature of the lines properly, the $HC^{17}O^+$ fractional abundance had to be increased by a factor of 16 to make the spectrum visible in the figure. We obtain a faint line emission with a double-peaked feature, which is not enhanced from the OM profile in Figure 2.3. Therefore, the $HC^{17}O^+$ depletion towards the centre of the core alone cannot explain the observed double-peaked structure.

A.1.2 Self-absorption

Self-absorption is not expected for an optically thin transition such as $HC^{17}O^+(1$ - $0)$. Nevertheless, we tested the effects of an envelope-like extension added to the fractional abundance profile corresponding to a visual extinction of A_v=4 mag, which lengthens the fractional abundance profile from 0.3 to 1.7 pc. In Figure A.2, we present the A_v=4 mag extended model spectrum with a $HC^{17}O^+$ fractional abundance profile scaled up by a factor of 3 to be able to distinguish possible self-absorption features in the line profiles. This trial does not show signs of $HC^{17}O^+(1$ - $0)$ self-absorption nor does it reproduce the observed line profile, which gives evidence that an enhanced $HC^{17}O^+$ molecular fractional abundance in the foreground does not account for the observed line shape.

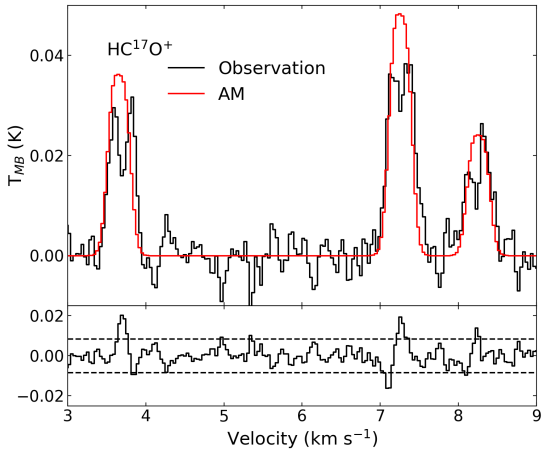

Figure A.1: Spectrum of the HC^{17}O$^+$ (1 - 0) observation (black) and product of model with the upscaled by a factor of 16 fractional abundance profile at 5×10^5 yrs and modified to have 0 fractional abundance from 0 to 7000 au (red).

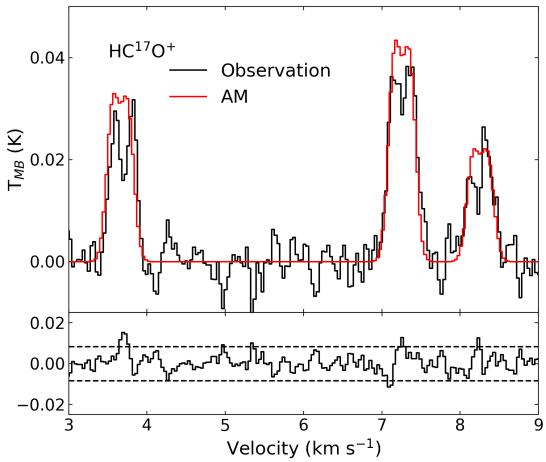

Figure A.2: Spectrum of the HC^{17}O$^+$ (1 - 0) observation (black) and product of model with an upscaled by a factor of 3 extended fractional abundance profile with A$_v$=4 at 5×10^5 yrs.

A.2 Comparison with constant $T_{\rm ex}$ (C$T_{\rm ex}$) approximation

To derive the column density from the observations we first checked that the HC^{17}O$^+$(1 - 0) transition is optically thin. A first fit with CLASS returns larger optical depth uncertainties than optical depth values. In the optically thin approximation (τ_ν<0.1, where τ_ν represents the total optical depth) τ_ν is not included in the radiative transfer equation, and thus the problem degenerates, resulting in the large optical depth uncertainties observed. As the optical depth derivation for this case with CLASS is not possible, we estimate its value with the following equation, assuming three different $T_{\rm ex}$ values (5, 7 and 9 K):

$$\tau_\nu = -ln[1 - \frac{T_{\rm MB}}{[J_\nu(T_{ex}) - J_\nu(T_{bg})]}]. \quad \text{(A.1)}$$

The total optical depth is represented by τ_ν, and the line brightness temperature by $T_{\rm MB}$; $J_\nu(T_{ex})$ and $J_\nu(T_{bg})$ correspond to the Rayleigh-Jeans equivalent temperature at T_{ex} and T_{bg}, respectively. The optical depth obtained for the line lies between 0.03 and 0.08, which confirms that the $J = 1$ - 0 rotational transition of HC^{17}O$^+$ is optically thin.

We then proceed to fit the observations with the hyperfine structure (HFS) tool in CLASS. This tool fits the hyperfine components of a transition using laboratory-calculated frequencies, assuming a Gaussian velocity distribution, the same excitation temperature of the hyperfine components, and local standard of rest (LSR) velocity. In our particular case, we also fixed the optical depth to the minimum value allowed (0.1) to indicate that the line is optically thin. In order to reproduce

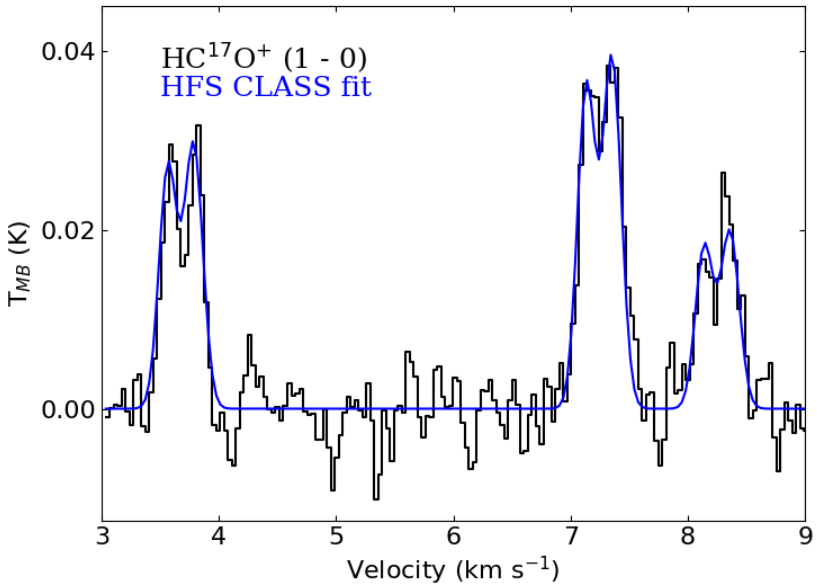

Figure A.3: Spectrum of the $HC^{17}O^+$ $J = 1$ - 0 at the dust peak of L1544 (black). The HFS fit was done with CLASS (blue).

Table A.1: Results of the CLASS HFS fit of the observed $HC^{17}O^+$(1 - 0) rotational transition towards L1544, treating the two peaks of each hyperfine line as separate velocity components.

v_{LSR} (km s^{-1})	T_{MB} (K)	Δv (km s^{-1})
7.13±0.07	8.2±0.4 × 10^{-2}	0.177±0.018
7.35±0.07	9.0±0.4 × 10^{-2}	0.186±0.017

the double peak, as kinematic information cannot be included in CLASS, we applied this tool taking into account two separate velocity components. This fit results in a hyperfine component model that follows the statistical intensity ratios. In non-CT_{ex} conditions, the relative intensity amongst hyperfine components can differ from the statistical value. In our case, however, the ratio of intensities does not differ significantly from the statistical values.

With the parameters derived from HFS fittings (Table A.1) and the $HC^{17}O^+$ molecular constants extracted from the Cologne Database for Molecular Spectroscopy (CDMS)[1], we calculated the column density of the molecule assuming that the transition is optically thin. For this purpose, we use Equation A.2 (Mangum & Shirley 2015),

$$N_{\rm TOT} = \frac{8\pi k_B \nu^2 W}{A_{ul} h c^3} \frac{Q_{rot}}{g_u} \frac{J_\nu(T_{ex})}{J_\nu(T_{ex}) - J_\nu(T_{bg})} \exp\left(\frac{E_u}{k_B T_{ex}}\right), \tag{A.2}$$

[1]https://cdms.astro.uni-koeln.de

Table A.2: Derived column densities from HFS fitting.

V_{lsr} (km s^{-1})	N_{col} (T_{ex}=5 K) (cm^{-2})	N_{col} (T_{ex}=7 K) (cm^{-2})	N_{col} (T_{ex}=9 K) (cm^{-2})
7.13±0.03	$1.9\pm0.2 \times 10^{10}$	$1.7\pm0.2 \times 10^{10}$	$1.7\pm0.2 \times 10^{10}$
7.35±0.03	$2.2\pm0.2 \times 10^{10}$	$1.9\pm0.2 \times 10^{10}$	$2.0\pm0.2 \times 10^{10}$

where $N_{\rm TOT}$ is the total column density, $k_{\rm B}$ is the Boltzmann constant, ν is the transition frequency, $A_{\rm ul}$ is the Einstein coefficient, h is the Planck constant, c is the light speed, $E_{\rm u}$ is the upper level energy, and W is the integrated intensity. As seen in Table A.1, the HFS fit returns, for each velocity component, the summed $T_{\rm MB}$ of the three hyperfine lines and the average linewidth Δv. We calculated a global W for each velocity component from the $T_{\rm MB}$ and Δv assuming a Gaussian profile. In Equation A.2, $g_{\rm u}$ represents the combined upper-level degeneracy of the hyperfine transitions, which equals 18. Lastly, $Q_{\rm rot}$ represents the partition function. We used three different $Q_{\rm rot}$ values, 16.54, 22.23, and 27.94, for three different $T_{\rm ex}$ values, 5, 7, and 9 K, used for the calculations. The result is six column density values, corresponding to two velocity components and three assumed $T_{\rm ex}$ (Table A.2).

The column density of the two fitted velocity components are then summed for each $T_{\rm ex}$ resulting in the calculated total $HC^{17}O^+$ column density. The derived total column densities are the same for all $T_{\rm ex}$ within the uncertainties. We conclude that the column densities do not strongly depend on the $T_{\rm ex}$ used in the range of values considered here. The derived column density of $HC^{17}O^+$ at $T_{\rm ex}$= 5 K towards L1544 is $4.1\pm0.3\times10^{10}$ cm^{-2}. On the other hand, the extracted column density from the $HC^{17}O^+$ fractional abundance profile used to fit the observational spectrum with LOC is $5.4^{+0.7}_{-0.9} \times 10^{10}$ cm^{-2}, consistent within the errors with the column density obtained with CLASS. Contrary to a C$T_{\rm ex}$ approach where a single excitation temperature is used, the column density derivation from the fractional abundance profile integration takes into account the excitation temperature profile across the core (Figure 2.5).

A.3 $HC^{17}O^+$ hyperfine collisional rate coefficients

In this section, we present for the first time the $HC^{17}O^+$–H_2 hyperfine collisional rate coefficients calculated with the method described in Section 2.3.1. For each transition J, $F \rightarrow J^{'}$, $F^{'}$, where the $J^{'}$ and $F^{'}$ quantum numbers refer to the final energy levels and J and F indicate the initial energy levels, collisional coefficient values in units of cm^3 s^{-1} are given for five temperatures: 10, 20, 30, 40, and 50 K (Table A.3).

Table A.3: $HC^{17}O^+$ hyperfine collisional rate coefficients given in units of cm^3 s^{-1} for 10, 20, 30, 40, and 50 K. Transitions are labelled with the J, $F \rightarrow J^{'}$,$F^{'}$ quantum numbers, where the $J^{'}$ and $F^{'}$ quantum numbers refer to the final energy levels and J and F indicate initial energy levels.

Quantum Numbers	T				
J, $F \rightarrow J^{'}$,$F^{'}$	10 K	20 K	30 K	40 K	50 K
0, 5/2 → 1, 3/2	2.390000×10^{-10}	2.145000×10^{-10}	2.037000×10^{-10}	1.985000×10^{-10}	1.962000×10^{-10}
0, 5/2 → 1, 5/2	2.390000×10^{-10}	2.145000×10^{-10}	2.037000×10^{-10}	1.985000×10^{-10}	1.962000×10^{-10}
1, 3/2 → 1, 5/2	3.871328×10^{-11}	3.444551×10^{-11}	3.146681×10^{-11}	2.914492×10^{-11}	2.729761×10^{-11}
1, 7/2 → 1, 5/2	1.659141×10^{-10}	1.476236×10^{-10}	1.348578×10^{-10}	1.249068×10^{-10}	1.169897×10^{-10}
0, 5/2 → 1, 7/2	2.390000×10^{-10}	2.145000×10^{-10}	2.037000×10^{-10}	1.985000×10^{-10}	1.962000×10^{-10}
1, 3/2 → 1, 7/2	1.290443×10^{-10}	1.148184×10^{-10}	1.048894×10^{-10}	9.714972×10^{-11}	9.099203×10^{-11}
0, 5/2 → 2, 1/2	1.685000×10^{-10}	1.456000×10^{-10}	1.317000×10^{-10}	1.215000×10^{-10}	1.136000×10^{-10}
1, 3/2 → 2, 1/2	2.738739×10^{-10}	2.491296×10^{-10}	2.389575×10^{-10}	2.346329×10^{-10}	2.332109×10^{-10}
1, 5/2 → 2, 1/2	7.906003×10^{-12}	6.798591×10^{-12}	6.092502×10^{-12}	5.622241×10^{-12}	5.285196×10^{-12}
1, 7/2 → 2, 1/2	1.581201×10^{-10}	1.359718×10^{-10}	1.218500×10^{-10}	1.124448×10^{-10}	1.057039×10^{-10}
0, 5/2 → 2, 3/2	1.685000×10^{-10}	1.456000×10^{-10}	1.317000×10^{-10}	1.215000×10^{-10}	1.136000×10^{-10}
1, 3/2 → 2, 3/2	1.932930×10^{-10}	1.757504×10^{-10}	1.684887×10^{-10}	1.653675×10^{-10}	1.643047×10^{-10}
1, 5/2 → 2, 3/2	1.110756×10^{-10}	9.960229×10^{-11}	9.396839×10^{-11}	9.095122×10^{-11}	8.929198×10^{-11}
1, 7/2 → 2, 3/2	1.355315×10^{-10}	1.165473×10^{-10}	1.044429×10^{-10}	9.638127×10^{-11}	9.060336×10^{-11}
2, 1/2 → 2, 3/2	2.200436×10^{-11}	2.004954×10^{-11}	1.847141×10^{-11}	1.718948×10^{-11}	1.614980×10^{-11}
2, 9/2 → 2, 3/2	1.107463×10^{-10}	1.072935×10^{-10}	9.949162×10^{-11}	9.272650×10^{-11}	8.729360×10^{-11}
0, 5/2 → 2, 5/2	1.685000×10^{-10}	1.456000×10^{-10}	1.317000×10^{-10}	1.215000×10^{-10}	1.136000×10^{-10}
1, 3/2 → 2, 5/2	9.469243×10^{-11}	8.566529×10^{-11}	8.165332×10^{-11}	7.974360×10^{-11}	7.889673×10^{-11}
1, 5/2 → 2, 5/2	2.218229×10^{-10}	1.990521×10^{-10}	1.879496×10^{-10}	1.820488×10^{-10}	1.788419×10^{-10}
1, 7/2 → 2, 5/2	1.233846×10^{-10}	1.071826×10^{-10}	9.729705×10^{-11}	9.090762×10^{-11}	8.646132×10^{-11}
2, 3/2 → 2, 5/2	1.807560×10^{-11}	1.664894×10^{-11}	1.535652×10^{-11}	1.429468×10^{-11}	1.343501×10^{-11}

Table A.3: continued.

Quantum Numbers	T				
J, $F \rightarrow J^{'}$,$F^{'}$	10 K	20 K	30 K	40 K	50 K
2, 9/2 → 2, 5/2	1.086164×10^{-10}	1.030723×10^{-10}	9.537286×10^{-11}	8.884370×10^{-11}	8.358296×10^{-11}
0, 5/2 → 2, 7/2	1.685000×10^{-10}	1.456000×10^{-10}	1.317000×10^{-10}	1.215000×10^{-10}	1.136000×10^{-10}
1, 3/2 → 2, 7/2	3.162401×10^{-11}	2.719436×10^{-11}	2.437001×10^{-11}	2.248896×10^{-11}	2.114079×10^{-11}
1, 5/2 → 2, 7/2	2.483453×10^{-10}	2.223133×10^{-10}	2.093184×10^{-10}	2.022388×10^{-10}	1.982431×10^{-10}
1, 7/2 → 2, 7/2	1.599307×10^{-10}	1.423924×10^{-10}	1.332116×10^{-10}	1.279722×10^{-10}	1.248161×10^{-10}
2, 1/2 → 2, 7/2	2.818996×10^{-12}	2.731108×10^{-12}	2.532514×10^{-12}	2.360311×10^{-12}	2.222019×10^{-12}
2, 3/2 → 2, 7/2	6.690918×10^{-11}	6.202664×10^{-11}	5.725136×10^{-11}	5.330129×10^{-11}	5.010662×10^{-11}
2, 5/2 → 2, 7/2	1.076068×10^{-10}	1.005103×10^{-10}	9.284715×10^{-11}	8.645735×10^{-11}	8.129582×10^{-11}
2, 9/2 → 2, 7/2	1.371902×10^{-10}	1.269790×10^{-10}	1.171834×10^{-10}	1.090940×10^{-10}	1.025500×10^{-10}
0, 5/2 → 2, 9/5	1.685000×10^{-10}	1.456000×10^{-10}	1.317000×10^{-10}	1.215000×10^{-10}	1.136000×10^{-10}
1, 3/2 → 2, 9/2	7.906003×10^{-11}	6.798591×10^{-11}	6.092502×10^{-11}	5.622241×10^{-11}	5.285196×10^{-11}
1, 5/2 → 2, 9/2	6.211859×10^{-11}	5.341750×10^{-11}	4.786966×10^{-11}	4.417475×10^{-11}	4.152654×10^{-11}
1, 7/2 → 2, 9/2	2.987214×10^{-10}	2.704966×10^{-10}	2.581053×10^{-10}	2.523028×10^{-10}	2.498215×10^{-10}
2, 1/2 → 2, 9/2	2.818996×10^{-11}	2.731108×10^{-11}	2.532514×10^{-11}	2.360311×10^{-11}	2.222019×10^{-11}
0, 5/2 → 3, 1/2	9.659000×10^{-11}	8.195000×10^{-11}	7.271000×10^{-11}	6.659000×10^{-11}	6.225000×10^{-11}
1, 3/2 → 3, 1/2	1.724803×10^{-10}	1.489832×10^{-10}	1.361045×10^{-10}	1.271759×10^{-10}	1.202824×10^{-10}
1, 5/2 → 3, 1/2	1.232002×10^{-11}	1.064166×10^{-11}	9.721750×10^{-12}	9.083991×10^{-12}	8.591597×10^{-12}
1, 7/2 → 3, 1/2	9.469966×10^{-11}	8.697510×10^{-11}	7.997376×10^{-11}	7.484013×10^{-11}	7.092605×10^{-11}
2, 1/2 → 3, 1/2	2.029112×10^{-10}	1.893532×10^{-10}	1.831264×10^{-10}	1.809263×10^{-10}	1.808661×10^{-10}
2, 3/2 → 3, 1/2	5.797464×10^{-11}	5.410092×10^{-11}	5.232183×10^{-11}	5.169323×10^{-11}	5.167603×10^{-11}
2, 5/2 → 3, 1/2	9.372001×10^{-11}	8.267731×10^{-11}	7.470437×10^{-11}	6.936529×10^{-11}	6.558273×10^{-11}
2, 7/2 → 3, 1/2	1.562000×10^{-11}	1.377955×10^{-11}	1.245073×10^{-11}	1.156088×10^{-11}	1.093046×10^{-11}
2, 9/2 → 3, 1/2	7.867410×10^{-11}	8.068898×10^{-11}	8.009666×10^{-11}	7.925428×10^{-11}	7.844467×10^{-11}
0, 5/2 → 3, 3/2	9.659000×10^{-11}	8.195000×10^{-11}	7.271000×10^{-11}	6.659000×10^{-11}	6.225000×10^{-11}
1, 3/2 → 3, 3/2	1.379843×10^{-10}	1.191866×10^{-10}	1.088836×10^{-10}	1.017407×10^{-10}	9.622588×10^{-11}
1, 5/2 → 3, 3/2	5.520247×10^{-11}	4.823683×10^{-11}	4.412244×10^{-11}	4.124004×10^{-11}	3.901992×10^{-11}
1, 7/2 → 3, 3/2	8.631327×10^{-11}	7.917658×10^{-11}	7.279396×10^{-11}	6.811926×10^{-11}	6.455420×10^{-11}
2, 1/2 → 3, 3/2	8.116450×10^{-11}	7.574129×10^{-11}	7.325056×10^{-11}	7.237053×10^{-11}	7.234644×10^{-11}
2, 3/2 → 3, 3/2	1.821543×10^{-10}	1.682622×10^{-10}	1.608375×10^{-10}	1.573062×10^{-10}	1.559004×10^{-10}
2, 5/2 → 3, 3/2	5.965661×10^{-11}	5.422438×10^{-11}	5.085186×10^{-11}	4.889735×10^{-11}	4.774383×10^{-11}

Table A.3: continued.

Quantum Numbers	T				
J, $F \rightarrow J^{'}$,$F^{'}$	10 K	20 K	30 K	40 K	50 K
2, 7/2 → 3, 3/2	5.710869×10^{-11}	5.226057×10^{-11}	4.841900×10^{-11}	4.577220×10^{-11}	4.386156×10^{-11}
2, 9/2 → 3, 3/2	6.881591×10^{-11}	7.011156×10^{-11}	6.934112×10^{-11}	6.845375×10^{-11}	6.764774×10^{-11}
3, 1/2 → 3, 3/2	5.977317×10^{-11}	5.528093×10^{-11}	5.131498×10^{-11}	4.794228×10^{-11}	4.514606×10^{-11}
3, 11/2→ 3, 3/2	6.861673×10^{-11}	7.620402×10^{-11}	7.593822×10^{-11}	7.348592×10^{-11}	7.047374×10^{-11}
0, 5/2 → 3, 5/2	9.659000×10^{-11}	8.195000×10^{-11}	7.271000×10^{-11}	6.659000×10^{-11}	6.225000×10^{-11}
1, 3/2 → 3, 5/2	9.045786×10^{-11}	7.823060×10^{-11}	7.147759×10^{-11}	6.679067×10^{-11}	6.317294×10^{-11}
1, 5/2 → 3, 5/2	1.095869×10^{-10}	9.597244×10^{-11}	8.780751×10^{-11}	8.207587×10^{-11}	7.766319×10^{-11}
1, 7/2 → 3, 5/2	7.945528×10^{-11}	7.239696×10^{-11}	6.651489×10^{-11}	6.223346×10^{-11}	5.896387×10^{-11}
2, 1/2 → 3, 5/2	1.457867×10^{-11}	1.286091×10^{-11}	1.162068×10^{-11}	1.079016×10^{-11}	1.020176×10^{-11}
2, 3/2 → 3, 5/2	1.553198×10^{-10}	1.434066×10^{-10}	1.370036×10^{-10}	1.339313×10^{-10}	1.326796×10^{-10}
2, 5/2 → 3, 5/2	1.255400×10^{-10}	1.175793×10^{-10}	1.138296×10^{-10}	1.124642×10^{-10}	1.123760×10^{-10}
2, 7/2 → 3, 5/2	9.020214×10^{-11}	8.415567×10^{-11}	7.935858×10^{-11}	7.613998×10^{-11}	7.389774×10^{-11}
2, 9/2 → 3, 5/2	6.325941×10^{-11}	6.259754×10^{-11}	6.088762×10^{-11}	5.947431×10^{-11}	5.834494×10^{-11}
3, 1/2 → 3, 5/2	2.656586×10^{-11}	2.456930×10^{-11}	2.280666×10^{-11}	2.130768×10^{-11}	2.006491×10^{-11}
3, 3/2 → 3, 5/2	7.945319×10^{-11}	7.492245×10^{-11}	6.969361×10^{-11}	6.514485×10^{-11}	6.138543×10^{-11}
3, 11/2 → 3, 5/2	6.140773×10^{-11}	6.620547×10^{-11}	6.501631×10^{-11}	6.245588×10^{-11}	5.968795×10^{-11}
0, 5/2 → 3, 7/2	9.659000×10^{-11}	8.195000×10^{-11}	7.271000×10^{-11}	6.659000×10^{-11}	6.225000×10^{-11}
1, 3/2 → 3, 7/2	4.485171×10^{-11}	3.917290×10^{-11}	3.582973×10^{-11}	3.348865×10^{-11}	3.168529×10^{-11}
1, 5/2 → 3, 7/2	1.498436×10^{-10}	1.314640×10^{-10}	1.203028×10^{-10}	1.124551×10^{-10}	1.064155×10^{-10}
1, 7/2 → 3, 7/2	8.480465×10^{-11}	7.596313×10^{-11}	6.966744×10^{-11}	6.515623×10^{-11}	6.169916×10^{-11}
2, 1/2 → 3, 7/2	2.733500×10^{-11}	2.411422×10^{-11}	2.178878×10^{-11}	2.023154×10^{-11}	1.912830×10^{-11}
2, 3/2 → 3, 7/2	3.924137×10^{-12}	3.837929×10^{-12}	3.707450×10^{-12}	3.605216×10^{-12}	3.525694×10^{-12}
2, 5/2 → 3, 7/2	2.063152×10^{-10}	1.927370×10^{-10}	1.854829×10^{-10}	1.821672×10^{-10}	1.810157×10^{-10}
2, 7/2 → 3, 7/2	1.399021×10^{-10}	1.325814×10^{-10}	1.280018×10^{-10}	1.256087×10^{-10}	1.244779×10^{-10}
2, 9/2 → 3, 7/2	7.142354×10^{-11}	6.732945×10^{-11}	6.371906×10^{-11}	6.118730×10^{-11}	5.935247×10^{-11}
3, 1/2 → 3, 7/2	1.914397×10^{-11}	1.882564×10^{-11}	1.758879×10^{-11}	1.645755×10^{-11}	1.552889×10^{-11}
3, 3/2 → 3, 7/2	3.108678×10^{-11}	2.907058×10^{-11}	2.701750×10^{-11}	2.524885×10^{-11}	2.378514×10^{-11}
3, 5/2 → 3, 7/2	7.658633×10^{-11}	7.218317×10^{-11}	6.748307×10^{-11}	6.327467×10^{-11}	5.970209×10^{-11}
3, 9/2 → 3, 7/2	1.250383×10^{-10}	1.221175×10^{-10}	1.159677×10^{-10}	1.096174×10^{-10}	1.038638×10^{-10}
3, 11/2 → 3, 7/2	7.096953×10^{-11}	7.224497×10^{-11}	6.912224×10^{-11}	6.552781×10^{-11}	6.221674×10^{-11}

Table A.3: continued.

Quantum Numbers	T				
J, $F \rightarrow J^{'}$,$F^{'}$	10 K	20 K	30 K	40 K	50 K
0, 5/2 → 3, 9/2	9.659000×10^{-11}	8.195000×10^{-11}	7.271000×10^{-11}	6.659000×10^{-11}	6.225000×10^{-11}
1, 3/2 → 3, 9/2	2.209659×10^{-11}	2.029419×10^{-11}	1.866054×10^{-11}	1.746270×10^{-11}	1.654941×10^{-11}
1, 5/2 → 3, 9/2	1.400915×10^{-10}	1.233731×10^{-10}	1.129446×10^{-10}	1.055868×10^{-10}	9.992874×10^{-11}
1, 7/2 → 3, 9/2	1.173120×10^{-10}	1.029327×10^{-10}	9.419485×10^{-11}	8.805045×10^{-11}	8.332185×10^{-11}
2, 1/2 → 3, 9/2	2.002613×10^{-12}	2.053901×10^{-12}	2.038824×10^{-12}	2.017382×10^{-12}	1.996773×10^{-12}
2, 3/2 → 3, 9/2	4.084308×10^{-11}	3.778153×10^{-11}	3.525346×10^{-11}	3.349137×10^{-11}	3.220998×10^{-11}
2, 5/2 → 3, 9/2	4.853419×10^{-11}	4.641645×10^{-11}	4.423421×10^{-11}	4.263064×10^{-11}	4.142666×10^{-11}
2, 7/2 → 3, 9/2	2.398887×10^{-10}	2.262601×10^{-10}	2.194638×10^{-10}	2.168264×10^{-10}	2.164561×10^{-10}
2, 9/2 → 3, 9/2	1.176314×10^{-10}	1.080880×10^{-10}	1.017097×10^{-10}	9.783423×10^{-11}	9.541047×10^{-11}
3, 1/2 → 3, 9/2	3.480722×10^{-12}	3.422843×10^{-12}	3.197962×10^{-12}	2.992282×10^{-12}	2.823435×10^{-12}
3, 3/2 → 3, 9/2	2.335744×10^{-11}	2.386681×10^{-11}	2.278639×10^{-11}	2.157098×10^{-11}	2.047047×10^{-11}
3, 5/2 → 3, 9/2	5.524542×10^{-11}	5.579146×10^{-11}	5.337726×10^{-11}	5.061490×10^{-11}	4.805504×10^{-11}
3, 11/2 → 3, 9/2	1.163184×10^{-10}	1.117551×10^{-10}	1.046986×10^{-10}	9.821969×10^{-11}	9.273370×10^{-11}
0, 5/2 → 3, 11/2	9.659000×10^{-11}	8.195000×10^{-11}	7.271000×10^{-11}	6.659000×10^{-11}	6.225000×10^{-11}
1, 3/2 → 3, 11/2	4.910353×10^{-11}	4.509820×10^{-11}	4.146787×10^{-11}	3.880599×10^{-11}	3.677647×10^{-11}
1, 5/2 → 3, 11/2	3.419710×10^{-11}	3.140768×10^{-11}	2.887941×10^{-11}	2.702560×10^{-11}	2.561218×10^{-11}
1, 7/2 → 3, 11/2	1.961994×10^{-10}	1.700941×10^{-10}	1.554527×10^{-10}	1.452684×10^{-10}	1.374113×10^{-10}
2, 1/2 → 3, 11/2	1.668844×10^{-11}	1.711585×10^{-11}	1.699020×10^{-11}	1.681151×10^{-11}	1.663978×10^{-11}
2, 3/2 → 3, 11/2	2.479426×10^{-11}	2.542926×10^{-11}	2.524259×10^{-11}	2.497711×10^{-11}	2.472196×10^{-11}
2, 5/2 → 3, 11/2	3.796581×10^{-11}	3.660430×10^{-11}	3.505677×10^{-11}	3.389755×10^{-11}	3.301760×10^{-11}
2, 7/2 → 3, 11/2	5.905740×10^{-11}	5.382769×10^{-11}	4.973817×10^{-11}	4.693134×10^{-11}	4.491019×10^{-11}
2, 9/2 → 3, 11/2	3.103941×10^{-10}	2.876229×10^{-10}	2.756723×10^{-10}	2.701825×10^{-10}	2.682105×10^{-10}
3, 1/2 → 3, 11/2	1.348180×10^{-11}	1.508640×10^{-11}	1.508853×10^{-11}	1.462761×10^{-11}	1.403990×10^{-11}
0, 5/2 → 4, 3/2	6.476000×10^{-11}	5.950000×10^{-11}	5.417000×10^{-11}	5.005000×10^{-11}	4.689000×10^{-11}
1, 3/2 → 4, 3/2	1.000976×10^{-10}	8.654839×10^{-11}	7.703968×10^{-11}	7.068534×10^{-11}	6.626915×10^{-11}
1, 5/2 → 4, 3/2	1.608711×10^{-11}	1.390956×10^{-11}	1.238138×10^{-11}	1.136014×10^{-11}	1.065040×10^{-11}
1, 7/2 → 4, 3/2	5.941529×10^{-11}	5.964205×10^{-11}	5.827894×10^{-11}	5.695451×10^{-11}	5.588045×10^{-11}
2, 1/2 → 4, 3/2	1.214262×10^{-10}	1.065431×10^{-10}	9.709880×10^{-11}	9.043036×10^{-11}	8.536090×10^{-11}
2, 3/2 → 4, 3/2	6.938639×10^{-11}	6.088175×10^{-11}	5.548503×10^{-11}	5.167449×10^{-11}	4.877766×10^{-11}
2, 5/2 → 4, 3/2	6.075598×10^{-11}	5.606351×10^{-11}	5.136840×10^{-11}	4.790023×10^{-11}	4.529028×10^{-11}

Table A.3: continued.

Quantum Numbers	T				
J, $F \rightarrow J^{'}$,$F^{'}$	10 K	20 K	30 K	40 K	50 K
2, 7/2 → 4, 3/2	2.025485×10^{-11}	1.887397×10^{-11}	1.731073×10^{-11}	1.614575×10^{-11}	1.527075×10^{-11}
2, 9/2 → 4, 3/2	5.877659×10^{-11}	6.223771×10^{-11}	6.103703×10^{-11}	5.894917×10^{-11}	5.670042×10^{-11}
3, 1/2 → 4, 3/2	1.522410×10^{-10}	1.454889×10^{-10}	1.431467×10^{-10}	1.429769×10^{-10}	1.439454×10^{-10}
3, 3/2 → 4, 3/2	1.068840×10^{-10}	1.005365×10^{-10}	9.712121×10^{-11}	9.547041×10^{-11}	9.480810×10^{-11}
3, 5/2 → 4, 3/2	5.460310×10^{-11}	4.977087×10^{-11}	4.627438×10^{-11}	4.391609×10^{-11}	4.225004×10^{-11}
3, 7/2 → 4, 3/2	4.121902×10^{-11}	4.128402×10^{-11}	4.057268×10^{-11}	3.988628×10^{-11}	3.928378×10^{-11}
3, 9/2 → 4, 3/2	1.642819×10^{-11}	1.714044×10^{-11}	1.724633×10^{-11}	1.721222×10^{-11}	1.713047×10^{-11}
3, 11/2 → 4, 3/2	5.422465×10^{-11}	5.527929×10^{-11}	5.463870×10^{-11}	5.313807×10^{-11}	5.138216×10^{-11}
4, 13/2 → 4, 3/2	5.037171×10^{-11}	5.194548×10^{-11}	5.215658×10^{-11}	5.189176×10^{-11}	5.137140×10^{-11}
0, 5/2 → 4, 5/2	6.476000×10^{-11}	5.950000×10^{-11}	5.417000×10^{-11}	5.005000×10^{-11}	4.689000×10^{-11}
1, 3/2 → 4, 5/2	7.507320×10^{-11}	6.491129×10^{-11}	5.777976×10^{-11}	5.301401×10^{-11}	4.970186×10^{-11}
1, 5/2 → 4, 5/2	4.653520×10^{-11}	4.141751×10^{-11}	3.760850×10^{-11}	3.500400×10^{-11}	3.317196×10^{-11}
1, 7/2 → 4, 5/2	5.399160×10^{-11}	5.377120×10^{-11}	5.231174×10^{-11}	5.098199×10^{-11}	4.992618×10^{-11}
2, 1/2 → 4, 5/2	4.047539×10^{-11}	3.551435×10^{-11}	3.236627×10^{-11}	3.014345×10^{-11}	2.845363×10^{-11}
2, 3/2 → 4, 5/2	1.295418×10^{-10}	1.149861×10^{-10}	1.049252×10^{-10}	9.774787×10^{-11}	9.230434×10^{-11}
2, 5/2 → 4, 5/2	5.811796×10^{-11}	5.143518×10^{-11}	4.691975×10^{-11}	4.370699×10^{-11}	4.126886×10^{-11}
2, 7/2 → 4, 5/2	5.112332×10^{-11}	4.901451×10^{-11}	4.580702×10^{-11}	4.316739×10^{-11}	4.103096×10^{-11}
2, 9/2 → 4, 5/2	5.134148×10^{-11}	5.364988×10^{-11}	5.228179×10^{-11}	5.033428×10^{-11}	4.834220×10^{-11}
3, 1/2 → 4, 5/2	2.050901×10^{-11}	1.852807×10^{-11}	1.703190×10^{-11}	1.598797×10^{-11}	1.522359×10^{-11}
3, 3/2 → 4, 5/2	1.624955×10^{-10}	1.547529×10^{-10}	1.516627×10^{-10}	1.509709×10^{-10}	1.515572×10^{-10}
3, 5/2 → 4, 5/2	1.104189×10^{-10}	1.063943×10^{-10}	1.042664×10^{-10}	1.034034×10^{-10}	1.032623×10^{-10}
3, 7/2 → 4, 5/2	4.436590×10^{-11}	4.055569×10^{-11}	3.779112×10^{-11}	3.592737×10^{-11}	3.461238×10^{-11}
3, 9/2 → 4, 5/2	4.299808×10^{-11}	4.345636×10^{-11}	4.286642×10^{-11}	4.203142×10^{-11}	4.116931×10^{-11}
3, 11/2 → 4, 5/2	4.481261×10^{-11}	4.581272×10^{-11}	4.538149×10^{-11}	4.427896×10^{-11}	4.297518×10^{-11}
4, 3/2 → 4, 5/2	7.774785×10^{-11}	7.317440×10^{-11}	6.830180×10^{-11}	6.400149×10^{-11}	6.039409×10^{-11}
4, 13/2 → 4, 5/2	4.207317×10^{-11}	4.401253×10^{-11}	4.416566×10^{-11}	4.374305×10^{-11}	4.307520×10^{-11}
0, 5/2 → 4, 7/2	6.476000×10^{-11}	5.950000×10^{-11}	5.417000×10^{-11}	5.005000×10^{-11}	4.689000×10^{-11}
1, 3/2 → 4, 7/2	4.737529×10^{-11}	4.117306×10^{-11}	3.678164×10^{-11}	3.383649×10^{-11}	3.178573×10^{-11}
1, 5/2 → 4, 7/2	7.658609×10^{-11}	6.869372×10^{-11}	6.269944×10^{-11}	5.856994×10^{-11}	5.565402×10^{-11}
1, 7/2 → 4, 7/2	5.163862×10^{-11}	5.023322×10^{-11}	4.821892×10^{-11}	4.659357×10^{-11}	4.536025×10^{-11}

Table A.3: continued.

Quantum Numbers	T				
J, $F \rightarrow J^{'}$,$F^{'}$	10 K	20 K	30 K	40 K	50 K
2, 1/2 → 4, 7/2	1.060637×10^{-11}	9.895280×10^{-12}	9.076831×10^{-12}	8.466217×10^{-12}	8.007707×10^{-12}
2, 3/2 → 4, 7/2	8.377550×10^{-11}	7.437497×10^{-11}	6.786866×10^{-11}	6.322644×10^{-11}	5.970574×10^{-11}
2, 5/2 → 4, 7/2	1.091332×10^{-10}	9.674627×10^{-11}	8.853521×10^{-11}	8.262956×10^{-11}	7.808699×10^{-11}
2, 7/2 → 4, 7/2	7.781004×10^{-11}	7.378260×10^{-11}	6.905332×10^{-11}	6.515677×10^{-11}	6.195122×10^{-11}
2, 9/2 → 4, 7/2	4.927485×10^{-11}	4.980088×10^{-11}	4.776599×10^{-11}	4.562101×10^{-11}	4.364835×10^{-11}
3, 1/2 → 4, 7/2	1.398342×10^{-11}	1.263277×10^{-11}	1.161266×10^{-11}	1.090089×10^{-11}	1.037972×10^{-11}
3, 3/2 → 4, 7/2	2.895058×10^{-11}	2.794200×10^{-11}	2.684427×10^{-11}	2.599437×10^{-11}	2.532791×10^{-11}
3, 5/2 → 4, 7/2	1.744500×10^{-10}	1.666782×10^{-10}	1.637425×10^{-10}	1.632735×10^{-10}	1.641127×10^{-10}
3, 7/2 → 4, 7/2	1.036723×10^{-10}	9.887777×10^{-11}	9.609942×10^{-11}	9.462151×10^{-11}	9.390938×10^{-11}
3, 9/2 → 4, 7/2	6.395416×10^{-11}	6.193153×10^{-11}	5.963346×10^{-11}	5.756512×10^{-11}	5.577156×10^{-11}
3, 11/2 → 4, 7/2	4.058949×10^{-11}	4.143771×10^{-11}	4.106767×10^{-11}	4.024465×10^{-11}	3.929869×10^{-11}
4, 3/2 → 4, 7/2	3.162127×10^{-11}	3.072928×10^{-11}	2.878070×10^{-11}	2.698997×10^{-11}	2.549558×10^{-11}
4, 5/2 → 4, 7/2	8.317058×10^{-11}	8.046003×10^{-11}	7.622321×10^{-11}	7.199367×10^{-11}	6.820865×10^{-11}
4, 13/2→ 4, 7/2	4.046700×10^{-11}	4.304797×10^{-11}	4.293278×10^{-11}	4.206422×10^{-11}	4.096794×10^{-11}
0, 5/2 → 4, 9/2	6.476000×10^{-11}	5.950000×10^{-11}	5.417000×10^{-11}	5.005000×10^{-11}	4.689000×10^{-11}
1, 3/2 → 4, 9/2	2.434012×10^{-11}	2.188740×10^{-11}	2.001111×10^{-11}	1.871514×10^{-11}	1.779883×10^{-11}
1, 5/2 → 4, 9/2	9.366336×10^{-11}	8.450327×10^{-11}	7.742715×10^{-11}	7.252250×10^{-11}	6.904847×10^{-11}
1, 7/2 → 4, 9/2	5.759652×10^{-11}	5.370934×10^{-11}	5.026174×10^{-11}	4.776236×10^{-11}	4.595270×10^{-11}
2, 1/2 → 4, 9/2	1.697018×10^{-11}	1.583245×10^{-11}	1.452293×10^{-11}	1.354595×10^{-11}	1.281233×10^{-11}
2, 3/2 → 4, 9/2	2.564797×10^{-12}	2.715827×10^{-12}	2.663434×10^{-12}	2.572327×10^{-12}	2.474200×10^{-12}
2, 5/2 → 4, 9/2	1.334717×10^{-10}	1.205431×10^{-10}	1.109450×10^{-10}	1.038291×10^{-10}	9.827738×10^{-11}
2, 7/2 → 4, 9/2	1.182738×10^{-10}	1.085921×10^{-10}	1.008263×10^{-10}	9.480074×10^{-11}	8.994217×10^{-11}
2, 9/2 → 4, 9/2	5.931946×10^{-11}	5.691655×10^{-11}	5.334231×10^{-11}	5.035192×10^{-11}	4.789392×10^{-11}
3, 1/2 → 4, 9/2	9.015170×10^{-12}	9.468645×10^{-12}	9.562279×10^{-12}	9.565409×10^{-12}	9.535001×10^{-12}
3, 3/2 → 4, 9/2	1.645436×10^{-11}	1.506369×10^{-11}	1.397602×10^{-11}	1.320777×10^{-11}	1.264035×10^{-11}
3, 5/2 → 4, 9/2	3.343967×10^{-11}	3.138070×10^{-11}	2.958240×10^{-11}	2.820373×10^{-11}	2.711973×10^{-11}
3, 7/2 → 4, 9/2	2.118848×10^{-10}	2.044106×10^{-10}	2.014471×10^{-10}	2.007949×10^{-10}	2.014263×10^{-10}
3, 9/2 → 4, 9/2	1.069472×10^{-10}	1.015944×10^{-10}	9.789043×10^{-11}	9.536810×10^{-11}	9.361765×10^{-11}
3, 11/2 → 4, 9/2	4.785886×10^{-11}	4.758193×10^{-11}	4.654179×10^{-11}	4.546006×10^{-11}	4.446093×10^{-11}
4, 3/2 → 4, 9/2	1.782512×10^{-11}	1.913040×10^{-11}	1.876123×10^{-11}	1.801811×10^{-11}	1.722513×10^{-11}

Table A.3: continued.

Quantum Numbers	T				
J, $F \rightarrow J^{'}$,$F^{'}$	10 K	20 K	30 K	40 K	50 K
4, 5/2 → 4, 9/2	3.057954×10^{-11}	2.965202×10^{-11}	2.776540×10^{-11}	2.603647×10^{-11}	2.459313×10^{-11}
4, 7/2 → 4, 9/2	8.617205×10^{-11}	8.283720×10^{-11}	7.839712×10^{-11}	7.415826×10^{-11}	7.043602×10^{-11}
4, 11/2 → 4, 9/2	1.105011×10^{-10}	1.060641×10^{-10}	1.003759×10^{-10}	9.516387×10^{-11}	9.068792×10^{-11}
4, 13/2 → 4, 9/2	5.222774×10^{-11}	5.459719×10^{-11}	5.334134×10^{-11}	5.135453×10^{-11}	4.931816×10^{-11}
0, 5/2 → 4, 11/2	6.476000×10^{-11}	5.950000×10^{-11}	5.417000×10^{-11}	5.005000×10^{-11}	4.689000×10^{-11}
1, 3/2 → 4, 11/2	1.540001×10^{-11}	1.548049×10^{-11}	1.513843×10^{-11}	1.480157×10^{-11}	1.452724×10^{-11}
1, 5/2 → 4, 11/2	8.159732×10^{-11}	7.440125×10^{-11}	6.864258×10^{-11}	6.460179×10^{-11}	6.172200×10^{-11}
1, 7/2 → 4, 11/2	7.860267×10^{-11}	7.021826×10^{-11}	6.391899×10^{-11}	5.959664×10^{-11}	5.655076×10^{-11}
2, 1/2 → 4, 11/2	1.769659×10^{-12}	1.878760×10^{-12}	1.844814×10^{-12}	1.782809×10^{-12}	1.715296×10^{-12}
2, 3/2 → 4, 11/2	3.035187×10^{-11}	2.964204×10^{-11}	2.789693×10^{-11}	2.638155×10^{-11}	2.512175×10^{-11}
2, 5/2 → 4, 11/2	3.114941×10^{-11}	3.157659×10^{-11}	3.030631×10^{-11}	2.895346×10^{-11}	2.770617×10^{-11}
2, 7/2 → 4, 11/2	1.673581×10^{-10}	1.503778×10^{-10}	1.384354×10^{-10}	1.296007×10^{-10}	1.226752×10^{-10}
2, 9/2 → 4, 11/2	9.997091×10^{-11}	9.112478×10^{-11}	8.381655×10^{-11}	7.838148×10^{-11}	7.418158×10^{-11}
3, 1/2 → 4, 11/2	2.022634×10^{-12}	2.124376×10^{-12}	2.145383×10^{-12}	2.146085×10^{-12}	2.139263×10^{-12}
3, 3/2 → 4, 11/2	1.397517×10^{-11}	1.451269×10^{-11}	1.453878×10^{-11}	1.439336×10^{-11}	1.419065×10^{-11}
3, 5/2 → 4, 11/2	3.301015×10^{-11}	3.254352×10^{-11}	3.161445×10^{-11}	3.064447×10^{-11}	2.973871×10^{-11}
3, 7/2 → 4, 11/2	5.045683×10^{-11}	4.760824×10^{-11}	4.499317×10^{-11}	4.282620×10^{-11}	4.102592×10^{-11}
3, 9/2 → 4, 11/2	2.372040×10^{-10}	2.278138×10^{-10}	2.239830×10^{-10}	2.230294×10^{-10}	2.236558×10^{-10}
3, 11/2 → 4, 11/2	8.893120×10^{-11}	8.489735×10^{-11}	8.172519×10^{-11}	7.956047×10^{-11}	7.804962×10^{-11}
4, 3/2 → 4, 11/2	6.686128×10^{-12}	7.475260×10^{-12}	7.481734×10^{-12}	7.259562×10^{-12}	6.973930×10^{-12}
4, 5/2 → 4, 11/2	2.339345×10^{-11}	2.482134×10^{-11}	2.454929×10^{-11}	2.386395×10^{-11}	2.308954×10^{-11}
4, 7/2 → 4, 11/2	4.512494×10^{-11}	4.531003×10^{-11}	4.372919×10^{-11}	4.201451×10^{-11}	4.044192×10^{-11}
4, 13/2 → 4, 11/2	1.006772×10^{-10}	9.930827×10^{-11}	9.431005×10^{-11}	8.920331×10^{-11}	8.466317×10^{-11}
0, 5/2 → 4, 13/2	6.476000×10^{-11}	5.950000×10^{-11}	5.417000×10^{-11}	5.005000×10^{-11}	4.689000×10^{-11}
1, 3/2 → 4, 13/2	3.208335×10^{-11}	3.225102×10^{-11}	3.153839×10^{-11}	3.083660×10^{-11}	3.026509×10^{-11}
1, 5/2 → 4, 13/2	2.062501×10^{-11}	2.073280×10^{-11}	2.027468×10^{-11}	1.982353×10^{-11}	1.945613×10^{-11}
1, 7/2 → 4, 13/2	1.228916×10^{-10}	1.071162×10^{-10}	9.588694×10^{-11}	8.833987×10^{-11}	8.307878×10^{-11}
2, 1/2 → 4, 13/2	1.327245×10^{-11}	1.409070×10^{-11}	1.383611×10^{-11}	1.337107×10^{-11}	1.286472×10^{-11}
2, 3/2 → 4, 13/2	1.896064×10^{-11}	2.012957×10^{-11}	1.976587×10^{-11}	1.910152×10^{-11}	1.837817×10^{-11}
2, 5/2 → 4, 13/2	2.836945×10^{-11}	2.846393×10^{-11}	2.717429×10^{-11}	2.589060×10^{-11}	2.474300×10^{-11}

Table A.3: continued.

Quantum Numbers	T				
J, $F \rightarrow J^{'}$,$F^{'}$	10 K	20 K	30 K	40 K	50 K
2, 7/2 → 4, 13/2	3.995458×10^{-11}	3.828152×10^{-11}	3.565148×10^{-11}	3.352735×10^{-11}	3.183981×10^{-11}
2, 9/2 → 4, 13/2	2.300429×10^{-10}	2.036343×10^{-10}	1.858723×10^{-10}	1.732095×10^{-10}	1.635743×10^{-10}
3, 1/2 → 4, 13/2	9.720805×10^{-12}	9.902501×10^{-12}	9.782362×10^{-12}	9.506653×10^{-12}	9.184945×10^{-12}
3, 3/2 → 4, 13/2	1.588861×10^{-11}	1.621510×10^{-11}	1.603996×10^{-11}	1.561612×10^{-11}	1.511804×10^{-11}
3, 5/2 → 4, 13/2	1.972539×10^{-11}	2.027114×10^{-11}	2.015475×10^{-11}	1.975609×10^{-11}	1.926976×10^{-11}
3, 7/2 → 4, 13/2	2.805861×10^{-11}	2.836445×10^{-11}	2.798417×10^{-11}	2.744473×10^{-11}	2.688762×10^{-11}
3, 9/2 → 4, 13/2	5.148182×10^{-11}	4.932415×10^{-11}	4.714628×10^{-11}	4.543729×10^{-11}	4.407859×10^{-11}
3, 11/2 → 4, 13/2	3.007248×10^{-10}	2.854227×10^{-10}	2.778925×10^{-10}	2.748391×10^{-10}	2.742610×10^{-10}
0, 5/2 → 5, 5/2	3.892000×10^{-11}	3.839000×10^{-11}	3.742000×10^{-11}	3.652000×10^{-11}	3.574000×10^{-11}
1, 3/2 → 5, 5/2	7.003921×10^{-11}	6.350285×10^{-11}	5.807572×10^{-11}	5.398829×10^{-11}	5.080547×10^{-11}
1, 5/2 → 5, 5/2	1.500840×10^{-11}	1.360775×10^{-11}	1.244480×10^{-11}	1.156892×10^{-11}	1.088689×10^{-11}
1, 7/2 → 5, 5/2	4.885238×10^{-11}	5.028940×10^{-11}	4.917948×10^{-11}	4.734279×10^{-11}	4.530764×10^{-11}
2, 1/2 → 5, 5/2	6.842358×10^{-11}	5.895339×10^{-11}	5.275891×10^{-11}	4.859136×10^{-11}	4.561476×10^{-11}
2, 3/2 → 5, 5/2	4.887399×10^{-11}	4.210956×10^{-11}	3.768494×10^{-11}	3.470812×10^{-11}	3.258197×10^{-11}
2, 5/2 → 5, 5/2	3.978911×10^{-11}	3.814448×10^{-11}	3.657346×10^{-11}	3.532602×10^{-11}	3.433459×10^{-11}
2, 7/2 → 5, 5/2	1.640310×10^{-11}	1.627860×10^{-11}	1.592201×10^{-11}	1.557629×10^{-11}	1.527354×10^{-11}
2, 9/2 → 5, 5/2	5.071022×10^{-11}	4.931396×10^{-11}	4.746068×10^{-11}	4.529821×10^{-11}	4.319514×10^{-11}
3, 1/2 → 5, 5/2	1.023504×10^{-10}	9.148680×10^{-11}	8.422513×10^{-11}	7.876190×10^{-11}	7.452987×10^{-11}
3, 3/2 → 5, 5/2	8.828010×10^{-11}	7.976820×10^{-11}	7.352309×10^{-11}	6.877289×10^{-11}	6.510145×10^{-11}
3, 5/2 → 5, 5/2	4.862221×10^{-11}	4.517789×10^{-11}	4.176476×10^{-11}	3.909341×10^{-11}	3.704056×10^{-11}
3, 7/2 → 5, 5/2	3.407422×10^{-11}	3.461841×10^{-11}	3.332198×10^{-11}	3.184881×10^{-11}	3.049733×10^{-11}
3, 9/2 → 5, 5/2	1.652350×10^{-11}	1.758971×10^{-11}	1.731549×10^{-11}	1.673873×10^{-11}	1.611590×10^{-11}
3, 11/2 → 5, 5/2	3.614959×10^{-11}	3.585899×10^{-11}	3.554955×10^{-11}	3.528427×10^{-11}	3.501489×10^{-11}
4, 3/2 → 5, 5/2	1.917424×10^{-10}	1.839385×10^{-10}	1.823983×10^{-10}	1.831070×10^{-10}	1.848756×10^{-10}
4, 5/2 → 5, 5/2	8.081082×10^{-11}	7.644061×10^{-11}	7.413205×10^{-11}	7.284832×10^{-11}	7.212740×10^{-11}
4, 7/2 → 5, 5/2	3.728886×10^{-11}	3.655470×10^{-11}	3.582186×10^{-11}	3.522122×10^{-11}	3.471846×10^{-11}
4, 9/2 → 5, 5/2	2.651691×10^{-11}	2.730981×10^{-11}	2.745528×10^{-11}	2.723270×10^{-11}	2.685281×10^{-11}
4, 11/2 → 5, 5/2	1.506815×10^{-11}	1.554845×10^{-11}	1.562079×10^{-11}	1.540166×10^{-11}	1.506008×10^{-11}
4, 13/2 → 5, 5/2	2.257286×10^{-11}	2.500794×10^{-11}	2.637168×10^{-11}	2.718906×10^{-11}	2.766560×10^{-11}
5, 15/2 → 5, 5/2	3.838313×10^{-11}	4.438482×10^{-11}	4.657395×10^{-11}	4.770678×10^{-11}	4.837201×10^{-11}

Table A.3: continued.

Quantum Numbers	T				
J, $F \rightarrow J^{'}$,$F^{'}$	10 K	20 K	30 K	40 K	50 K
0, 5/2 → 5, 7/2	3.892000×10^{-11}	3.839000×10^{-11}	3.742000×10^{-11}	3.652000×10^{-11}	3.574000×10^{-11}
1, 3/2 → 5, 7/2	5.042823×10^{-11}	4.572205×10^{-11}	4.181452×10^{-11}	3.887157×10^{-11}	3.657994×10^{-11}
1, 5/2 → 5, 7/2	3.942625×10^{-11}	3.674617×10^{-11}	3.413707×10^{-11}	3.200523×10^{-11}	3.024439×10^{-11}
1, 7/2 → 5, 7/2	4.404552×10^{-11}	4.493178×10^{-11}	4.374841×10^{-11}	4.202320×10^{-11}	4.017567×10^{-11}
2, 1/2 → 5, 7/2	2.052707×10^{-11}	1.768602×10^{-11}	1.582767×10^{-11}	1.457741×10^{-11}	1.368443×10^{-11}
2, 3/2 → 5, 7/2	7.799825×10^{-11}	6.936581×10^{-11}	6.344196×10^{-11}	5.934982×10^{-11}	5.637081×10^{-11}
2, 5/2 → 5, 7/2	4.206928×10^{-11}	3.659429×10^{-11}	3.296850×10^{-11}	3.051198×10^{-11}	2.874841×10^{-11}
2, 7/2 → 5, 7/2	4.072645×10^{-11}	3.934955×10^{-11}	3.784589×10^{-11}	3.645868×10^{-11}	3.525018×10^{-11}
2, 9/2 → 5, 7/2	4.287895×10^{-11}	4.180433×10^{-11}	4.031597×10^{-11}	3.860210×10^{-11}	3.694616×10^{-11}
3, 1/2 → 5, 7/2	1.180097×10^{-11}	1.121593×10^{-11}	1.039288×10^{-11}	9.733415×10^{-12}	9.228976×10^{-12}
3, 3/2 → 5, 7/2	1.084392×10^{-10}	9.748057×10^{-11}	8.979864×10^{-11}	8.398599×10^{-11}	7.948859×10^{-11}
3, 5/2 → 5, 7/2	9.594593×10^{-11}	8.852231×10^{-11}	8.254818×10^{-11}	7.770199×10^{-11}	7.378676×10^{-11}
3, 7/2 → 5, 7/2	4.227162×10^{-11}	3.918350×10^{-11}	3.621416×10^{-11}	3.389586×10^{-11}	3.211345×10^{-11}
3, 9/2 → 5, 7/2	3.658581×10^{-11}	3.693231×10^{-11}	3.589644×10^{-11}	3.473414×10^{-11}	3.365510×10^{-11}
3, 11/2 → 5, 7/2	3.095642×10^{-11}	3.116538×10^{-11}	3.084970×10^{-11}	3.044861×10^{-11}	3.002713×10^{-11}
4, 3/2 → 5, 7/2	3.089579×10^{-11}	2.879739×10^{-11}	2.725854×10^{-11}	2.614197×10^{-11}	2.528648×10^{-11}
4, 5/2 → 5, 7/2	1.770701×10^{-10}	1.716628×10^{-10}	1.715027×10^{-10}	1.730627×10^{-10}	1.753861×10^{-10}
4, 7/2 → 5, 7/2	8.499708×10^{-11}	8.103143×10^{-11}	7.904048×10^{-11}	7.786513×10^{-11}	7.715090×10^{-11}
4, 9/2 → 5, 7/2	3.261711×10^{-11}	3.166994×10^{-11}	3.085794×10^{-11}	3.022252×10^{-11}	2.970738×10^{-11}
4, 11/2 → 5, 7/2	2.763954×10^{-11}	2.909599×10^{-11}	2.969336×10^{-11}	2.982856×10^{-11}	2.972756×10^{-11}
4, 13/2 → 5, 7/2	2.078037×10^{-11}	2.254248×10^{-11}	2.344696×10^{-11}	2.387915×10^{-11}	2.404157×10^{-11}
5, 5/2 → 5, 7/2	7.852123×10^{-11}	7.580314×10^{-11}	7.133639×10^{-11}	6.715150×10^{-11}	6.355546×10^{-11}
5, 15/2 → 5, 7/2	3.095379×10^{-11}	3.501043×10^{-11}	3.639961×10^{-11}	3.703338×10^{-11}	3.733138×10^{-11}
0, 5/2 → 5, 9/2	3.892000×10^{-11}	3.839000×10^{-11}	3.742000×10^{-11}	3.652000×10^{-11}	3.574000×10^{-11}
1, 3/2 → 5, 9/2	3.127366×10^{-11}	2.853956×10^{-11}	2.619859×10^{-11}	2.440469×10^{-11}	2.298920×10^{-11}
1, 5/2 → 5, 9/2	6.043282×10^{-11}	5.676093×10^{-11}	5.295629×10^{-11}	4.976237×10^{-11}	4.707678×10^{-11}
1, 7/2 → 5, 9/2	4.219352×10^{-11}	4.209951×10^{-11}	4.054513×10^{-11}	3.873294×10^{-11}	3.693402×10^{-11}
2, 1/2 → 5, 9/2	7.125944×10^{-12}	7.137956×10^{-12}	7.017806×10^{-12}	6.887740×10^{-12}	6.768875×10^{-12}
2, 3/2 → 5, 9/2	4.389386×10^{-11}	3.898338×10^{-11}	3.562207×10^{-11}	3.330320×10^{-11}	3.161669×10^{-11}
2, 5/2 → 5, 9/2	7.322753×10^{-11}	6.402880×10^{-11}	5.787015×10^{-11}	5.361740×10^{-11}	5.051480×10^{-11}

Table A.3: continued.

Quantum Numbers	T				
J, $F \rightarrow J^{'}$,$F^{'}$	10 K	20 K	30 K	40 K	50 K
2, 7/2 → 5, 9/2	6.028815×10^{-11}	5.599755×10^{-11}	5.257999×10^{-11}	4.981475×10^{-11}	4.756245×10^{-11}
2, 9/2 → 5, 9/2	3.966452×10^{-11}	3.865231×10^{-11}	3.730999×10^{-11}	3.587691×10^{-11}	3.453719×10^{-11}
3, 1/2 → 5, 9/2	1.016699×10^{-11}	9.662955×10^{-12}	8.953868×10^{-12}	8.385711×10^{-12}	7.951118×10^{-12}
3, 3/2 → 5, 9/2	1.781412×10^{-11}	1.817287×10^{-11}	1.750830×10^{-11}	1.674080×10^{-11}	1.603421×10^{-11}
3, 5/2 → 5, 9/2	1.190798×10^{-10}	1.070369×10^{-10}	9.865987×10^{-11}	9.230744×10^{-11}	8.737808×10^{-11}
3, 7/2 → 5, 9/2	9.408418×10^{-11}	8.639087×10^{-11}	8.047517×10^{-11}	7.582445×10^{-11}	7.213781×10^{-11}
3, 9/2 → 5, 9/2	5.370814×10^{-11}	5.150728×10^{-11}	4.894350×10^{-11}	4.683776×10^{-11}	4.514870×10^{-11}
3, 11/2 → 5, 9/2	3.114672×10^{-11}	3.172909×10^{-11}	3.115930×10^{-11}	3.040383×10^{-11}	2.965008×10^{-11}
4, 3/2 → 5, 9/2	1.482392×10^{-11}	1.486311×10^{-11}	1.474149×10^{-11}	1.459727×10^{-11}	1.445143×10^{-11}
4, 5/2 → 5, 9/2	3.466383×10^{-11}	3.260798×10^{-11}	3.101622×10^{-11}	2.972170×10^{-11}	2.864036×10^{-11}
4, 7/2 → 5, 9/2	1.803131×10^{-10}	1.746274×10^{-10}	1.744118×10^{-10}	1.759944×10^{-10}	1.783769×10^{-10}
4, 9/2 → 5, 9/2	8.265280×10^{-11}	7.915830×10^{-11}	7.740093×10^{-11}	7.639896×10^{-11}	7.581101×10^{-11}
4, 11/2 → 5, 9/2	3.841645×10^{-11}	3.909828×10^{-11}	3.923530×10^{-11}	3.918964×10^{-11}	3.904479×10^{-11}
4, 13/2 → 5, 9/2	2.312988×10^{-11}	2.444496×10^{-11}	2.499430×10^{-11}	2.509807×10^{-11}	2.497549×10^{-11}
5, 5/2 → 5, 9/2	2.945741×10^{-11}	3.055133×10^{-11}	2.953792×10^{-11}	2.818409×10^{-11}	2.686770×10^{-11}
5, 7/2 → 5, 9/2	8.093865×10^{-11}	7.769268×10^{-11}	7.340331×10^{-11}	6.946155×10^{-11}	6.606866×10^{-11}
5, 13/2 → 5, 9/2	5.388127×10^{-11}	5.804955×10^{-11}	5.781065×10^{-11}	5.665173×10^{-11}	5.532132×10^{-11}
5, 15/2 → 5, 9/2	3.013817×10^{-11}	3.316016×10^{-11}	3.388155×10^{-11}	3.394655×10^{-11}	3.374718×10^{-11}
0, 5/2 → 5, 11/2	3.892000×10^{-11}	3.839000×10^{-11}	3.742000×10^{-11}	3.652000×10^{-11}	3.574000×10^{-11}
1, 3/2 → 5, 11/2	1.712017×10^{-11}	1.621430×10^{-11}	1.519642×10^{-11}	1.431434×10^{-11}	1.355767×10^{-11}
1, 5/2 → 5, 11/2	7.023728×10^{-11}	6.635104×10^{-11}	6.209931×10^{-11}	5.845174×10^{-11}	5.534219×10^{-11}
1, 7/2 → 5, 11/2	4.654256×10^{-11}	4.483466×10^{-11}	4.240427×10^{-11}	4.013393×10^{-11}	3.810014×10^{-11}
2, 1/2 → 5, 11/2	1.039200×10^{-11}	1.040952×10^{-11}	1.023430×10^{-11}	1.004462×10^{-11}	9.871276×10^{-12}
2, 3/2 → 5, 11/2	2.563167×10^{-12}	2.490905×10^{-12}	2.396066×10^{-12}	2.285260×10^{-12}	2.177409×10^{-12}
2, 5/2 → 5, 11/2	8.114148×10^{-11}	7.297245×10^{-11}	6.718081×10^{-11}	6.297096×10^{-11}	5.977966×10^{-11}
2, 7/2 → 5, 11/2	8.461991×10^{-11}	7.545593×10^{-11}	6.904151×10^{-11}	6.432776×10^{-11}	6.071870×10^{-11}
2, 9/2 → 5, 11/2	4.548345×10^{-11}	4.347119×10^{-11}	4.154732×10^{-11}	3.987140×10^{-11}	3.845295×10^{-11}
3, 1/2 → 5, 11/2	6.891422×10^{-12}	7.453265×10^{-12}	7.393029×10^{-12}	7.173790×10^{-12}	6.919146×10^{-12}
3, 3/2 → 5, 11/2	1.221862×10^{-11}	1.168797×10^{-11}	1.087073×10^{-11}	1.020171×10^{-11}	9.682742×10^{-12}
3, 5/2 → 5, 11/2	2.155173×10^{-11}	2.118392×10^{-11}	2.017013×10^{-11}	1.925404×10^{-11}	1.849430×10^{-11}

Table A.3: continued.

Quantum Numbers	T				
J, $F \rightarrow J^{'}$,$F^{'}$	10 K	20 K	30 K	40 K	50 K
3, 7/2 → 5, 11/2	1.511115×10^{-10}	1.374420×10^{-10}	1.278171×10^{-10}	1.204064×10^{-10}	1.145718×10^{-10}
3, 9/2 → 5, 11/2	9.300039×10^{-11}	8.555389×10^{-11}	7.981015×10^{-11}	7.542077×10^{-11}	7.201469×10^{-11}
3, 11/2 → 5, 11/2	4.122632×10^{-11}	4.117896×10^{-11}	3.963881×10^{-11}	3.804332×10^{-11}	3.661736×10^{-11}
4, 3/2 → 5, 11/2	9.678520×10^{-12}	1.006617×10^{-11}	1.017026×10^{-11}	1.009996×10^{-11}	9.952982×10^{-12}
4, 5/2 → 5, 11/2	1.489434×10^{-11}	1.481052×10^{-11}	1.461517×10^{-11}	1.442225×10^{-11}	1.424211×10^{-11}
4, 7/2 → 5, 11/2	3.732205×10^{-11}	3.548128×10^{-11}	3.402887×10^{-11}	3.286746×10^{-11}	3.190253×10^{-11}
4, 9/2 → 5, 11/2	2.023992×10^{-10}	1.967517×10^{-10}	1.966806×10^{-10}	1.983928×10^{-10}	2.008800×10^{-10}
4, 11/2 → 5, 11/2	7.721934×10^{-11}	7.445771×10^{-11}	7.296747×10^{-11}	7.211873×10^{-11}	7.161330×10^{-11}
4, 13/2 → 5, 11/2	3.248656×10^{-11}	3.323258×10^{-11}	3.333764×10^{-11}	3.309878×10^{-11}	3.270904×10^{-11}
5, 5/2 → 5, 11/2	1.537522×10^{-11}	1.653370×10^{-11}	1.650740×10^{-11}	1.615367×10^{-11}	1.570066×10^{-11}
5, 7/2 → 5, 11/2	2.845609×10^{-11}	2.908035×10^{-11}	2.795440×10^{-11}	2.661493×10^{-11}	2.536048×10^{-11}
5, 9/2 → 5, 11/2	8.540356×10^{-11}	8.326262×10^{-11}	7.935329×10^{-11}	7.562377×10^{-11}	7.237858×10^{-11}
5, 13/2 → 5, 11/2	9.947736×10^{-11}	9.844476×10^{-11}	9.426720×10^{-11}	9.005967×10^{-11}	8.634302×10^{-11}
5, 15/2 → 5, 11/2	4.085486×10^{-11}	4.359713×10^{-11}	4.336733×10^{-11}	4.242485×10^{-11}	4.130587×10^{-11}
0, 5/2 → 5, 13/2	3.892000×10^{-11}	3.839000×10^{-11}	3.742000×10^{-11}	3.652000×10^{-11}	3.574000×10^{-11}
1, 3/2 → 5, 13/2	1.352232×10^{-11}	1.395158×10^{-11}	1.365840×10^{-11}	1.315534×10^{-11}	1.259298×10^{-11}
1, 5/2 → 5, 13/2	5.931747×10^{-11}	5.659308×10^{-11}	5.325120×10^{-11}	5.026505×10^{-11}	4.765614×10^{-11}
1, 7/2 → 5, 13/2	6.106020×10^{-11}	5.685534×10^{-11}	5.279040×10^{-11}	4.947962×10^{-11}	4.675088×10^{-11}
2, 1/2 → 5, 13/2	1.712369×10^{-12}	1.663633×10^{-12}	1.599964×10^{-12}	1.525553×10^{-12}	1.453111×10^{-12}
2, 3/2 → 5, 13/2	2.284875×10^{-11}	2.259681×10^{-11}	2.201579×10^{-11}	2.135593×10^{-11}	2.072792×10^{-11}
2, 5/2 → 5, 13/2	2.314726×10^{-11}	2.266551×10^{-11}	2.192420×10^{-11}	2.106636×10^{-11}	2.023760×10^{-11}
2, 7/2 → 5, 13/2	1.052369×10^{-10}	9.276568×10^{-11}	8.427316×10^{-11}	7.826243×10^{-11}	7.378969×10^{-11}
2, 9/2 → 5, 13/2	7.125471×10^{-11}	6.510836×10^{-11}	6.058689×10^{-11}	5.728973×10^{-11}	5.479168×10^{-11}
3, 1/2 → 5, 13/2	1.772080×10^{-12}	1.916554×10^{-12}	1.901065×10^{-12}	1.844689×10^{-12}	1.779209×10^{-12}
3, 3/2 → 5, 13/2	1.090565×10^{-11}	1.143233×10^{-11}	1.133821×10^{-11}	1.109075×10^{-11}	1.080752×10^{-11}
3, 5/2 → 5, 13/2	2.425725×10^{-11}	2.408439×10^{-11}	2.328979×10^{-11}	2.253197×10^{-11}	2.187477×10^{-11}
3, 7/2 → 5, 13/2	3.266544×10^{-11}	3.144951×10^{-11}	2.985549×10^{-11}	2.858946×10^{-11}	2.760782×10^{-11}
3, 9/2 → 5, 13/2	1.763320×10^{-10}	1.597931×10^{-10}	1.482103×10^{-10}	1.393065×10^{-10}	1.323099×10^{-10}
3, 11/2 → 5, 13/2	8.006758×10^{-11}	7.582410×10^{-11}	7.110511×10^{-11}	6.713660×10^{-11}	6.392076×10^{-11}
4, 3/2 → 5, 13/2	4.365597×10^{-12}	4.496957×10^{-12}	4.511548×10^{-12}	4.438551×10^{-12}	4.329152×10^{-12}

Table A.3: continued.

Quantum Numbers	T				
J, $F \rightarrow J^{'}$,$F^{'}$	10 K	20 K	30 K	40 K	50 K
4, 5/2 → 5, 13/2	1.254442×10^{-11}	1.331417×10^{-11}	1.364481×10^{-11}	1.372503×10^{-11}	1.367760×10^{-11}
4, 7/2 → 5, 13/2	2.175601×10^{-11}	2.263833×10^{-11}	2.298858×10^{-11}	2.311718×10^{-11}	2.312349×10^{-11}
4, 9/2 → 5, 13/2	4.053663×10^{-11}	3.919347×10^{-11}	3.804899×10^{-11}	3.715155×10^{-11}	3.640934×10^{-11}
4, 11/2 → 5, 13/2	2.263889×10^{-10}	2.183938×10^{-10}	2.170472×10^{-10}	2.179596×10^{-10}	2.199256×10^{-10}
4, 13/2 → 5, 13/2	6.840845×10^{-11}	6.676325×10^{-11}	6.555885×10^{-11}	6.460813×10^{-11}	6.383486×10^{-11}
5, 5/2 → 5, 13/2	7.229668×10^{-12}	7.604719×10^{-12}	7.654261×10^{-12}	7.597828×10^{-12}	7.493179×10^{-12}
5, 7/2 → 5, 13/2	2.140387×10^{-11}	2.373856×10^{-11}	2.419172×10^{-11}	2.412723×10^{-11}	2.387598×10^{-11}
5, 15/2 → 5, 13/2	8.774371×10^{-11}	8.828888×10^{-11}	8.482177×10^{-11}	8.090653×10^{-11}	7.726682×10^{-11}
0, 5/2 → 5, 15/2	3.892000×10^{-11}	3.839000×10^{-11}	3.742000×10^{-11}	3.652000×10^{-11}	3.574000×10^{-11}
1, 3/2 → 5, 15/2	2.704465×10^{-11}	2.790316×10^{-11}	2.731681×10^{-11}	2.631067×10^{-11}	2.518595×10^{-11}
1, 5/2 → 5, 15/2	1.641996×10^{-11}	1.694120×10^{-11}	1.658521×10^{-11}	1.597434×10^{-11}	1.529147×10^{-11}
1, 7/2 → 5, 15/2	9.043539×10^{-11}	8.255564×10^{-11}	7.579799×10^{-11}	7.061499×10^{-11}	6.652257×10^{-11}
2, 1/2 → 5, 15/2	1.198658×10^{-11}	1.164543×10^{-11}	1.119975×10^{-11}	1.067887×10^{-11}	1.017178×10^{-11}
2, 3/2 → 5, 15/2	1.663444×10^{-11}	1.616100×10^{-11}	1.554251×10^{-11}	1.481966×10^{-11}	1.411594×10^{-11}
2, 5/2 → 5, 15/2	2.213228×10^{-11}	2.177902×10^{-11}	2.114258×10^{-11}	2.041209×10^{-11}	1.971093×10^{-11}
2, 7/2 → 5, 15/2	2.687828×10^{-11}	2.674036×10^{-11}	2.616366×10^{-11}	2.551989×10^{-11}	2.491579×10^{-11}
2, 9/2 → 5, 15/2	1.465684×10^{-10}	1.284742×10^{-10}	1.163515×10^{-10}	1.080695×10^{-10}	1.020856×10^{-10}
3, 1/2 → 5, 15/2	6.680329×10^{-12}	6.590704×10^{-12}	6.534406×10^{-12}	6.495994×10^{-12}	6.458694×10^{-12}
3, 3/2 → 5, 15/2	1.090653×10^{-11}	1.084433×10^{-11}	1.075214×10^{-11}	1.066634×10^{-11}	1.057765×10^{-11}
3, 5/2 → 5, 15/2	1.408705×10^{-11}	1.437476×10^{-11}	1.425447×10^{-11}	1.404261×10^{-11}	1.380646×10^{-11}
3, 7/2 → 5, 15/2	2.151070×10^{-11}	2.208223×10^{-11}	2.159235×10^{-11}	2.093365×10^{-11}	2.028498×10^{-11}
3, 9/2 → 5, 15/2	3.808097×10^{-11}	3.782376×10^{-11}	3.602533×10^{-11}	3.429316×10^{-11}	3.281636×10^{-11}
3, 11/2 → 5, 15/2	2.347344×10^{-10}	2.127842×10^{-10}	1.965413×10^{-10}	1.840682×10^{-10}	1.743559×10^{-10}
4, 3/2 → 5, 15/2	6.582743×10^{-12}	7.317127×10^{-12}	7.732621×10^{-12}	7.987438×10^{-12}	8.140725×10^{-12}
4, 5/2 → 5, 15/2	8.765542×10^{-12}	9.565605×10^{-12}	9.988395×10^{-12}	1.020671×10^{-11}	1.030530×10^{-11}
4, 7/2 → 5, 15/2	1.234994×10^{-11}	1.314801×10^{-11}	1.350255×10^{-11}	1.359598×10^{-11}	1.355404×10^{-11}
4, 9/2 → 5, 15/2	2.051511×10^{-11}	2.125849×10^{-11}	2.147142×10^{-11}	2.138879×10^{-11}	2.116948×10^{-11}
4, 11/2 → 5, 15/2	4.334794×10^{-11}	4.264704×10^{-11}	4.178154×10^{-11}	4.092959×10^{-11}	4.013252×10^{-11}
4, 13/2 → 5, 15/2	2.824387×10^{-10}	2.708637×10^{-10}	2.673235×10^{-10}	2.668915×10^{-10}	2.679979×10^{-10}

A.4 $C^{17}O$ hyperfine collisional rate coefficients

We approximated the $C^{17}O$-H_2 hyperfine collisional rate coefficients from the non-hyperfine collisional rate coefficients available in LAMDA using the Mj-randomisation method (Franz & Franz 1966). For each transition J, $F \rightarrow J^{'}$, $F^{'}$, where the $J^{'}$ and $F^{'}$ quantum numbers refer to the final energy levels and J and F indicate initial energy levels, collisional coefficient values with units of cm^3 s^{-1} are given for seven temperatures: 2, 5, 10, 20, 30, 40, and 50 K (Table A.4).

Table A.4: $C^{17}O$ hyperfine collisonal rate coefficients given in units of cm^3 s^{-1} for 2, 5, 10, 20, 30, 40, and 50 K. Transitions are labelled with the J, $F \rightarrow J^{'}$,$F^{'}$ quantum numbers, where the $J^{'}$ and $F^{'}$ quantum numbers refer to the final energy levels and J and F indicate the initial energy levels.

Quantum Numbers	T						
J, $F \rightarrow J^{'}$,$F^{'}$	2 K	5 K	10 K	20 K	30 K	40 K	50 K
0, 5/2 → 1, 3/2	2.950×10^{-11}	3.250×10^{-11}	3.300×10^{-11}	3.250×10^{-11}	3.260×10^{-11}	3.290×10^{-11}	3.340×10^{-11}
0, 5/2 → 1, 7/2	2.950×10^{-11}	3.250×10^{-11}	3.300×10^{-11}	3.250×10^{-11}	3.260×10^{-11}	3.290×10^{-11}	3.340×10^{-11}
0, 5/2 → 1, 5/2	2.950×10^{-11}	3.250×10^{-11}	3.300×10^{-11}	3.250×10^{-11}	3.260×10^{-11}	3.290×10^{-11}	3.340×10^{-11}
0, 5/2 → 2, 1/2	2.870×10^{-11}	2.880×10^{-11}	3.020×10^{-11}	3.090×10^{-11}	3.110×10^{-11}	3.120×10^{-11}	3.130×10^{-11}
0, 5/2 → 2, 9/2	2.870×10^{-11}	2.880×10^{-11}	3.020×10^{-11}	3.090×10^{-11}	3.110×10^{-11}	3.120×10^{-11}	3.130×10^{-11}
0, 5/2 → 2, 3/2	2.870×10^{-11}	2.880×10^{-11}	3.020×10^{-11}	3.090×10^{-11}	3.110×10^{-11}	3.120×10^{-11}	3.130×10^{-11}
0, 5/2 → 2, 5/2	2.870×10^{-11}	2.880×10^{-11}	3.020×10^{-11}	3.090×10^{-11}	3.110×10^{-11}	3.120×10^{-11}	3.130×10^{-11}
0, 5/2 → 2, 7/2	2.870×10^{-11}	2.880×10^{-11}	3.020×10^{-11}	3.090×10^{-11}	3.110×10^{-11}	3.120×10^{-11}	3.130×10^{-11}
1, 3/2 → 2, 1/2	1.980×10^{-11}	1.740×10^{-11}	1.590×10^{-11}	1.430×10^{-11}	1.360×10^{-11}	1.330×10^{-11}	1.330×10^{-11}
1, 7/2 → 2, 1/2	3.950×10^{-11}	3.480×10^{-11}	3.180×10^{-11}	2.860×10^{-11}	2.720×10^{-11}	2.660×10^{-11}	2.650×10^{-11}
1, 5/2 → 2, 1/2	2.960×10^{-11}	2.610×10^{-11}	2.380×10^{-11}	2.150×10^{-11}	2.040×10^{-11}	2.000×10^{-11}	1.990×10^{-11}
1, 3/2 → 2, 9/2	1.980×10^{-11}	1.740×10^{-11}	1.590×10^{-11}	1.430×10^{-11}	1.360×10^{-11}	1.330×10^{-11}	1.330×10^{-11}
1, 7/2 → 2, 9/2	3.950×10^{-11}	3.480×10^{-11}	3.180×10^{-11}	2.860×10^{-11}	2.720×10^{-11}	2.660×10^{-11}	2.650×10^{-11}
1, 5/2 → 2, 9/2	2.960×10^{-11}	2.610×10^{-11}	2.380×10^{-11}	2.150×10^{-11}	2.040×10^{-11}	2.000×10^{-11}	1.990×10^{-11}
1, 3/2 → 2, 3/2	1.980×10^{-11}	1.740×10^{-11}	1.590×10^{-11}	1.430×10^{-11}	1.360×10^{-11}	1.330×10^{-11}	1.330×10^{-11}
1, 7/2 → 2, 3/2	3.950×10^{-11}	3.480×10^{-11}	3.180×10^{-11}	2.860×10^{-11}	2.720×10^{-11}	2.660×10^{-11}	2.650×10^{-11}
1, 5/2 → 2, 3/2	2.960×10^{-11}	2.610×10^{-11}	2.380×10^{-11}	2.150×10^{-11}	2.040×10^{-11}	2.000×10^{-11}	1.990×10^{-11}
1, 3/2 → 2, 5/2	1.980×10^{-11}	1.740×10^{-11}	1.590×10^{-11}	1.430×10^{-11}	1.360×10^{-11}	1.330×10^{-11}	1.330×10^{-11}
1, 7/2 → 2, 5/2	3.950×10^{-11}	3.480×10^{-11}	3.180×10^{-11}	2.860×10^{-11}	2.720×10^{-11}	2.660×10^{-11}	2.650×10^{-11}
1, 5/2 → 2, 5/2	2.960×10^{-11}	2.610×10^{-11}	2.380×10^{-11}	2.150×10^{-11}	2.040×10^{-11}	2.000×10^{-11}	1.990×10^{-11}
1, 3/2 → 2, 7/2	1.980×10^{-11}	1.740×10^{-11}	1.590×10^{-11}	1.430×10^{-11}	1.360×10^{-11}	1.330×10^{-11}	1.330×10^{-11}
1, 7/2 → 2, 7/2	3.950×10^{-11}	3.480×10^{-11}	3.180×10^{-11}	2.860×10^{-11}	2.720×10^{-11}	2.660×10^{-11}	2.650×10^{-11}
1, 5/2 → 2, 7/2	2.960×10^{-11}	2.610×10^{-11}	2.380×10^{-11}	2.150×10^{-11}	2.040×10^{-11}	2.000×10^{-11}	1.990×10^{-11}
0, 5/2 → 3, 11/2	4.650×10^{-12}	4.820×10^{-12}	5.160×10^{-12}	5.520×10^{-12}	6.000×10^{-12}	6.590×10^{-12}	7.220×10^{-12}
0, 5/2 → 3, 1/2	4.650×10^{-12}	4.820×10^{-12}	5.160×10^{-12}	5.520×10^{-12}	6.000×10^{-12}	6.590×10^{-12}	7.220×10^{-12}
0, 5/2 → 3, 3/2	4.650×10^{-12}	4.820×10^{-12}	5.160×10^{-12}	5.520×10^{-12}	6.000×10^{-12}	6.590×10^{-12}	7.220×10^{-12}

Table A.4: continued.

Quantum Numbers	T						
J, $F \rightarrow J^{'}$,$F^{'}$	2 K	5 K	10 K	20 K	30 K	40 K	50 K
0, 5/2 → 3, 5/2	4.650×10^{-12}	4.820×10^{-12}	5.160×10^{-12}	5.520×10^{-12}	6.000×10^{-12}	6.590×10^{-12}	7.220×10^{-12}
0, 5/2 → 3, 9/2	4.650×10^{-12}	4.820×10^{-12}	5.160×10^{-12}	5.520×10^{-12}	6.000×10^{-12}	6.590×10^{-12}	7.220×10^{-12}
0, 5/2 → 3, 7/2	4.650×10^{-12}	4.820×10^{-12}	5.160×10^{-12}	5.520×10^{-12}	6.000×10^{-12}	6.590×10^{-12}	7.220×10^{-12}
1, 3/2 → 3, 11/2	1.050×10^{-11}	1.060×10^{-11}	1.110×10^{-11}	1.130×10^{-11}	1.130×10^{-11}	1.130×10^{-11}	1.120×10^{-11}
1, 7/2 → 3, 11/2	2.100×10^{-11}	2.110×10^{-11}	2.230×10^{-11}	2.260×10^{-11}	2.260×10^{-11}	2.250×10^{-11}	2.250×10^{-11}
1, 5/2 → 3, 11/2	1.580×10^{-11}	1.590×10^{-11}	1.670×10^{-11}	1.700×10^{-11}	1.690×10^{-11}	1.690×10^{-11}	1.690×10^{-11}
1, 3/2 → 3, 1/2	1.050×10^{-11}	1.060×10^{-11}	1.110×10^{-11}	1.130×10^{-11}	1.130×10^{-11}	1.130×10^{-11}	1.120×10^{-11}
1, 7/2 → 3, 1/2	2.100×10^{-11}	2.110×10^{-11}	2.230×10^{-11}	2.260×10^{-11}	2.260×10^{-11}	2.250×10^{-11}	2.250×10^{-11}
1, 5/2 → 3, 1/2	1.580×10^{-11}	1.590×10^{-11}	1.670×10^{-11}	1.700×10^{-11}	1.690×10^{-11}	1.690×10^{-11}	1.690×10^{-11}
1, 3/2 → 3, 3/2	1.050×10^{-11}	1.060×10^{-11}	1.110×10^{-11}	1.130×10^{-11}	1.130×10^{-11}	1.130×10^{-11}	1.120×10^{-11}
1, 7/2 → 3, 3/2	2.100×10^{-11}	2.110×10^{-11}	2.230×10^{-11}	2.260×10^{-11}	2.260×10^{-11}	2.250×10^{-11}	2.250×10^{-11}
1, 5/2 → 3, 3/2	1.580×10^{-11}	1.590×10^{-11}	1.670×10^{-11}	1.700×10^{-11}	1.690×10^{-11}	1.690×10^{-11}	1.690×10^{-11}
1, 3/2 → 3, 5/2	1.050×10^{-11}	1.060×10^{-11}	1.110×10^{-11}	1.130×10^{-11}	1.130×10^{-11}	1.130×10^{-11}	1.120×10^{-11}
1, 7/2 → 3, 5/2	2.100×10^{-11}	2.110×10^{-11}	2.230×10^{-11}	2.260×10^{-11}	2.260×10^{-11}	2.250×10^{-11}	2.250×10^{-11}
1, 5/2 → 3, 5/2	1.580×10^{-11}	1.590×10^{-11}	1.670×10^{-11}	1.700×10^{-11}	1.690×10^{-11}	1.690×10^{-11}	1.690×10^{-11}
1, 3/2 → 3, 9/2	1.050×10^{-11}	1.060×10^{-11}	1.110×10^{-11}	1.130×10^{-11}	1.130×10^{-11}	1.130×10^{-11}	1.120×10^{-11}
1, 7/2 → 3, 9/2	2.100×10^{-11}	2.110×10^{-11}	2.230×10^{-11}	2.260×10^{-11}	2.260×10^{-11}	2.250×10^{-11}	2.250×10^{-11}
1, 5/2 → 3, 9/2	1.580×10^{-11}	1.590×10^{-11}	1.670×10^{-11}	1.700×10^{-11}	1.690×10^{-11}	1.690×10^{-11}	1.690×10^{-11}
1, 3/2 → 3, 7/2	1.050×10^{-11}	1.060×10^{-11}	1.110×10^{-11}	1.130×10^{-11}	1.130×10^{-11}	1.130×10^{-11}	1.120×10^{-11}
1, 7/2 → 3, 7/2	2.100×10^{-11}	2.110×10^{-11}	2.230×10^{-11}	2.260×10^{-11}	2.260×10^{-11}	2.250×10^{-11}	2.250×10^{-11}
1, 5/2 → 3, 7/2	1.580×10^{-11}	1.590×10^{-11}	1.670×10^{-11}	1.700×10^{-11}	1.690×10^{-11}	1.690×10^{-11}	1.690×10^{-11}
2, 1/2 → 3, 11/2	7.390×10^{-12}	6.030×10^{-12}	5.300×10^{-12}	4.700×10^{-12}	4.460×10^{-12}	4.370×10^{-12}	4.350×10^{-12}
2, 9/2 → 3, 11/2	3.690×10^{-11}	3.020×10^{-11}	2.650×10^{-11}	2.350×10^{-11}	2.230×10^{-11}	2.190×10^{-11}	2.180×10^{-11}
2, 3/2 → 3, 11/2	1.480×10^{-11}	1.210×10^{-11}	1.060×10^{-11}	9.400×10^{-12}	8.920×10^{-12}	8.740×10^{-12}	8.710×10^{-12}
2, 5/2 → 3, 11/2	2.220×10^{-11}	1.810×10^{-11}	1.590×10^{-11}	1.410×10^{-11}	1.340×10^{-11}	1.310×10^{-11}	1.310×10^{-11}
2, 7/2 → 3, 11/2	2.950×10^{-11}	2.410×10^{-11}	2.120×10^{-11}	1.880×10^{-11}	1.780×10^{-11}	1.750×10^{-11}	1.740×10^{-11}
2, 1/2 → 3, 1/2	7.390×10^{-12}	6.030×10^{-12}	5.300×10^{-12}	4.700×10^{-12}	4.460×10^{-12}	4.370×10^{-12}	4.350×10^{-12}
2, 9/2 → 3, 1/2	3.690×10^{-11}	3.020×10^{-11}	2.650×10^{-11}	2.350×10^{-11}	2.230×10^{-11}	2.190×10^{-11}	2.180×10^{-11}
2, 3/2 → 3, 1/2	1.480×10^{-11}	1.210×10^{-11}	1.060×10^{-11}	9.400×10^{-12}	8.920×10^{-12}	8.740×10^{-12}	8.710×10^{-12}
2, 5/2 → 3, 1/2	2.220×10^{-11}	1.810×10^{-11}	1.590×10^{-11}	1.410×10^{-11}	1.340×10^{-11}	1.310×10^{-11}	1.310×10^{-11}
2, 7/2 → 3, 1/2	2.950×10^{-11}	2.410×10^{-11}	2.120×10^{-11}	1.880×10^{-11}	1.780×10^{-11}	1.750×10^{-11}	1.740×10^{-11}
2, 1/2 → 3, 3/2	7.390×10^{-12}	6.030×10^{-12}	5.300×10^{-12}	4.700×10^{-12}	4.460×10^{-12}	4.370×10^{-12}	4.350×10^{-12}
2, 9/2 → 3, 3/2	3.690×10^{-11}	3.020×10^{-11}	2.650×10^{-11}	2.350×10^{-11}	2.230×10^{-11}	2.190×10^{-11}	2.180×10^{-11}
2, 3/2 → 3, 3/2	1.480×10^{-11}	1.210×10^{-11}	1.060×10^{-11}	9.400×10^{-12}	8.920×10^{-12}	8.740×10^{-12}	8.710×10^{-12}
2, 5/2 → 3, 3/2	2.220×10^{-11}	1.810×10^{-11}	1.590×10^{-11}	1.410×10^{-11}	1.340×10^{-11}	1.310×10^{-11}	1.310×10^{-11}
2, 7/2 → 3, 3/2	2.950×10^{-11}	2.410×10^{-11}	2.120×10^{-11}	1.880×10^{-11}	1.780×10^{-11}	1.750×10^{-11}	1.740×10^{-11}
2, 1/2 → 3, 5/2	7.390×10^{-12}	6.030×10^{-12}	5.300×10^{-12}	4.700×10^{-12}	4.460×10^{-12}	4.370×10^{-12}	4.350×10^{-12}

Table A.4: continued.

Quantum Numbers	T						
J, $F \rightarrow J^{'}$,$F^{'}$	2 K	5 K	10 K	20 K	30 K	40 K	50 K
2, 9/2 → 3, 5/2	3.690×10^{-11}	3.020×10^{-11}	2.650×10^{-11}	2.350×10^{-11}	2.230×10^{-11}	2.190×10^{-11}	2.180×10^{-11}
2, 3/2 → 3, 5/2	1.480×10^{-11}	1.210×10^{-11}	1.060×10^{-11}	9.400×10^{-12}	8.920×10^{-12}	8.740×10^{-12}	8.710×10^{-12}
2, 5/2 → 3, 5/2	2.220×10^{-11}	1.810×10^{-11}	1.590×10^{-11}	1.410×10^{-11}	1.340×10^{-11}	1.310×10^{-11}	1.310×10^{-11}
2, 7/2 → 3, 5/2	2.950×10^{-11}	2.410×10^{-11}	2.120×10^{-11}	1.880×10^{-11}	1.780×10^{-11}	1.750×10^{-11}	1.740×10^{-11}
2, 1/2 → 3, 9/2	7.390×10^{-12}	6.030×10^{-12}	5.300×10^{-12}	4.700×10^{-12}	4.460×10^{-12}	4.370×10^{-12}	4.350×10^{-12}
2, 9/2 → 3, 9/2	3.690×10^{-11}	3.020×10^{-11}	2.650×10^{-11}	2.350×10^{-11}	2.230×10^{-11}	2.190×10^{-11}	2.180×10^{-11}
2, 3/2 → 3, 9/2	1.480×10^{-11}	1.210×10^{-11}	1.060×10^{-11}	9.400×10^{-12}	8.920×10^{-12}	8.740×10^{-12}	8.710×10^{-12}
2, 5/2 → 3, 9/2	2.220×10^{-11}	1.810×10^{-11}	1.590×10^{-11}	1.410×10^{-11}	1.340×10^{-11}	1.310×10^{-11}	1.310×10^{-11}
2, 7/2 → 3, 9/2	2.950×10^{-11}	2.410×10^{-11}	2.120×10^{-11}	1.880×10^{-11}	1.780×10^{-11}	1.750×10^{-11}	1.740×10^{-11}
2, 1/2 → 3, 7/2	7.390×10^{-12}	6.030×10^{-12}	5.300×10^{-12}	4.700×10^{-12}	4.460×10^{-12}	4.370×10^{-12}	4.350×10^{-12}
2, 9/2 → 3, 7/2	3.690×10^{-11}	3.020×10^{-11}	2.650×10^{-11}	2.350×10^{-11}	2.230×10^{-11}	2.190×10^{-11}	2.180×10^{-11}
2, 3/2 → 3, 7/2	1.480×10^{-11}	1.210×10^{-11}	1.060×10^{-11}	9.400×10^{-12}	8.920×10^{-12}	8.740×10^{-12}	8.710×10^{-12}
2, 5/2 → 3, 7/2	2.220×10^{-11}	1.810×10^{-11}	1.590×10^{-11}	1.410×10^{-11}	1.340×10^{-11}	1.310×10^{-11}	1.310×10^{-11}
2, 7/2 → 3, 7/2	2.950×10^{-11}	2.410×10^{-11}	2.120×10^{-11}	1.880×10^{-11}	1.780×10^{-11}	1.750×10^{-11}	1.740×10^{-11}
0, 5/2 → 4, 13/2	2.820×10^{-12}	2.830×10^{-12}	3.110×10^{-12}	3.420×10^{-12}	3.640×10^{-12}	3.850×10^{-12}	4.040×10^{-12}
0, 5/2 → 4, 3/2	2.820×10^{-12}	2.830×10^{-12}	3.110×10^{-12}	3.420×10^{-12}	3.640×10^{-12}	3.850×10^{-12}	4.040×10^{-12}
0, 5/2 → 4, 5/2	2.820×10^{-12}	2.830×10^{-12}	3.110×10^{-12}	3.420×10^{-12}	3.640×10^{-12}	3.850×10^{-12}	4.040×10^{-12}
0, 5/2 → 4, 11/2	2.820×10^{-12}	2.830×10^{-12}	3.110×10^{-12}	3.420×10^{-12}	3.640×10^{-12}	3.850×10^{-12}	4.040×10^{-12}
0, 5/2 → 4, 7/2	2.820×10^{-12}	2.830×10^{-12}	3.110×10^{-12}	3.420×10^{-12}	3.640×10^{-12}	3.850×10^{-12}	4.040×10^{-12}
0, 5/2 → 4, 9/2	2.820×10^{-12}	2.830×10^{-12}	3.110×10^{-12}	3.420×10^{-12}	3.640×10^{-12}	3.850×10^{-12}	4.040×10^{-12}
1, 3/2 → 4, 13/2	1.370×10^{-12}	1.770×10^{-12}	2.120×10^{-12}	2.390×10^{-12}	2.600×10^{-12}	2.830×10^{-12}	3.070×10^{-12}
1, 7/2 → 4, 13/2	2.730×10^{-12}	3.550×10^{-12}	4.250×10^{-12}	4.780×10^{-12}	5.200×10^{-12}	5.660×10^{-12}	6.150×10^{-12}
1, 5/2 → 4, 13/2	2.050×10^{-12}	2.660×10^{-12}	3.180×10^{-12}	3.590×10^{-12}	3.900×10^{-12}	4.240×10^{-12}	4.610×10^{-12}
1, 3/2 → 4, 3/2	1.370×10^{-12}	1.770×10^{-12}	2.120×10^{-12}	2.390×10^{-12}	2.600×10^{-12}	2.830×10^{-12}	3.070×10^{-12}
1, 7/2 → 4, 3/2	2.730×10^{-12}	3.550×10^{-12}	4.250×10^{-12}	4.780×10^{-12}	5.200×10^{-12}	5.660×10^{-12}	6.150×10^{-12}
1, 5/2 → 4, 3/2	2.050×10^{-12}	2.660×10^{-12}	3.180×10^{-12}	3.590×10^{-12}	3.900×10^{-12}	4.240×10^{-12}	4.610×10^{-12}
1, 3/2 → 4, 5/2	1.370×10^{-12}	1.770×10^{-12}	2.120×10^{-12}	2.390×10^{-12}	2.600×10^{-12}	2.830×10^{-12}	3.070×10^{-12}
1, 7/2 → 4, 5/2	2.730×10^{-12}	3.550×10^{-12}	4.250×10^{-12}	4.780×10^{-12}	5.200×10^{-12}	5.660×10^{-12}	6.150×10^{-12}
1, 5/2 → 4, 5/2	2.050×10^{-12}	2.660×10^{-12}	3.180×10^{-12}	3.590×10^{-12}	3.900×10^{-12}	4.240×10^{-12}	4.610×10^{-12}
1, 3/2 → 4, 11/2	1.370×10^{-12}	1.770×10^{-12}	2.120×10^{-12}	2.390×10^{-12}	2.600×10^{-12}	2.830×10^{-12}	3.070×10^{-12}
1, 7/2 → 4, 11/2	2.730×10^{-12}	3.550×10^{-12}	4.250×10^{-12}	4.780×10^{-12}	5.200×10^{-12}	5.660×10^{-12}	6.150×10^{-12}
1, 5/2 → 4, 11/2	2.050×10^{-12}	2.660×10^{-12}	3.180×10^{-12}	3.590×10^{-12}	3.900×10^{-12}	4.240×10^{-12}	4.610×10^{-12}
1, 3/2 → 4, 7/2	1.370×10^{-12}	1.770×10^{-12}	2.120×10^{-12}	2.390×10^{-12}	2.600×10^{-12}	2.830×10^{-12}	3.070×10^{-12}
1, 7/2 → 4, 7/2	2.730×10^{-12}	3.550×10^{-12}	4.250×10^{-12}	4.780×10^{-12}	5.200×10^{-12}	5.660×10^{-12}	6.150×10^{-12}
1, 5/2 → 4, 7/2	2.050×10^{-12}	2.660×10^{-12}	3.180×10^{-12}	3.590×10^{-12}	3.900×10^{-12}	4.240×10^{-12}	4.610×10^{-12}
1, 3/2 → 4, 9/2	1.370×10^{-12}	1.770×10^{-12}	2.120×10^{-12}	2.390×10^{-12}	2.600×10^{-12}	2.830×10^{-12}	3.070×10^{-12}
1, 7/2 → 4, 9/2	2.730×10^{-12}	3.550×10^{-12}	4.250×10^{-12}	4.780×10^{-12}	5.200×10^{-12}	5.660×10^{-12}	6.150×10^{-12}

Table A.4: continued.

Quantum Numbers	T						
J, $F \rightarrow J^{'}$,$F^{'}$	2 K	5 K	10 K	20 K	30 K	40 K	50 K
1, 5/2 → 4, 9/2	2.050×10^{-12}	2.660×10^{-12}	3.180×10^{-12}	3.590×10^{-12}	3.900×10^{-12}	4.240×10^{-12}	4.610×10^{-12}
2, 1/2 → 4, 13/2	4.040×10^{-12}	3.970×10^{-12}	4.150×10^{-12}	4.160×10^{-12}	4.080×10^{-12}	4.020×10^{-12}	3.980×10^{-12}
2, 9/2 → 4, 13/2	2.020×10^{-11}	1.980×10^{-11}	2.080×10^{-11}	2.080×10^{-11}	2.040×10^{-11}	2.010×10^{-11}	1.990×10^{-11}
2, 3/2 → 4, 13/2	8.080×10^{-12}	7.940×10^{-12}	8.310×10^{-12}	8.320×10^{-12}	8.160×10^{-12}	8.040×10^{-12}	7.960×10^{-12}
2, 5/2 → 4, 13/2	1.210×10^{-11}	1.190×10^{-11}	1.250×10^{-11}	1.250×10^{-11}	1.220×10^{-11}	1.210×10^{-11}	1.190×10^{-11}
2, 7/2 → 4, 13/2	1.620×10^{-11}	1.590×10^{-11}	1.660×10^{-11}	1.660×10^{-11}	1.630×10^{-11}	1.610×10^{-11}	1.590×10^{-11}
2, 1/2 → 4, 3/2	4.040×10^{-12}	3.970×10^{-12}	4.150×10^{-12}	4.160×10^{-12}	4.080×10^{-12}	4.020×10^{-12}	3.980×10^{-12}
2, 9/2 → 4, 3/2	2.020×10^{-11}	1.980×10^{-11}	2.080×10^{-11}	2.080×10^{-11}	2.040×10^{-11}	2.010×10^{-11}	1.990×10^{-11}
2, 3/2 → 4, 3/2	8.080×10^{-12}	7.940×10^{-12}	8.310×10^{-12}	8.320×10^{-12}	8.160×10^{-12}	8.040×10^{-12}	7.960×10^{-12}
2, 5/2 → 4, 3/2	1.210×10^{-11}	1.190×10^{-11}	1.250×10^{-11}	1.250×10^{-11}	1.220×10^{-11}	1.210×10^{-11}	1.190×10^{-11}
2, 7/2 → 4, 3/2	1.620×10^{-11}	1.590×10^{-11}	1.660×10^{-11}	1.660×10^{-11}	1.630×10^{-11}	1.610×10^{-11}	1.590×10^{-11}
2, 1/2 → 4, 5/2	4.040×10^{-12}	3.970×10^{-12}	4.150×10^{-12}	4.160×10^{-12}	4.080×10^{-12}	4.020×10^{-12}	3.980×10^{-12}
2, 9/2 → 4, 5/2	2.020×10^{-11}	1.980×10^{-11}	2.080×10^{-11}	2.080×10^{-11}	2.040×10^{-11}	2.010×10^{-11}	1.990×10^{-11}
2, 3/2 → 4, 5/2	8.080×10^{-12}	7.940×10^{-12}	8.310×10^{-12}	8.320×10^{-12}	8.160×10^{-12}	8.040×10^{-12}	7.960×10^{-12}
2, 5/2 → 4, 5/2	1.210×10^{-11}	1.190×10^{-11}	1.250×10^{-11}	1.250×10^{-11}	1.220×10^{-11}	1.210×10^{-11}	1.190×10^{-11}
2, 7/2 → 4, 5/2	1.620×10^{-11}	1.590×10^{-11}	1.660×10^{-11}	1.660×10^{-11}	1.630×10^{-11}	1.610×10^{-11}	1.590×10^{-11}
2, 1/2 → 4, 11/2	4.040×10^{-12}	3.970×10^{-12}	4.150×10^{-12}	4.160×10^{-12}	4.080×10^{-12}	4.020×10^{-12}	3.980×10^{-12}
2, 9/2 → 4, 11/2	2.020×10^{-11}	1.980×10^{-11}	2.080×10^{-11}	2.080×10^{-11}	2.040×10^{-11}	2.010×10^{-11}	1.990×10^{-11}
2, 3/2 → 4, 11/2	8.080×10^{-12}	7.940×10^{-12}	8.310×10^{-12}	8.320×10^{-12}	8.160×10^{-12}	8.040×10^{-12}	7.960×10^{-12}
2, 5/2 → 4, 11/2	1.210×10^{-11}	1.190×10^{-11}	1.250×10^{-11}	1.250×10^{-11}	1.220×10^{-11}	1.210×10^{-11}	1.190×10^{-11}
2, 7/2 → 4, 11/2	1.620×10^{-11}	1.590×10^{-11}	1.660×10^{-11}	1.660×10^{-11}	1.630×10^{-11}	1.610×10^{-11}	1.590×10^{-11}
2, 1/2 → 4, 7/2	4.040×10^{-12}	3.970×10^{-12}	4.150×10^{-12}	4.160×10^{-12}	4.080×10^{-12}	4.020×10^{-12}	3.980×10^{-12}
2, 9/2 → 4, 7/2	2.020×10^{-11}	1.980×10^{-11}	2.080×10^{-11}	2.080×10^{-11}	2.040×10^{-11}	2.010×10^{-11}	1.990×10^{-11}
2, 3/2 → 4, 7/2	8.080×10^{-12}	7.940×10^{-12}	8.310×10^{-12}	8.320×10^{-12}	8.160×10^{-12}	8.040×10^{-12}	7.960×10^{-12}
2, 5/2 → 4, 7/2	1.210×10^{-11}	1.190×10^{-11}	1.250×10^{-11}	1.250×10^{-11}	1.220×10^{-11}	1.210×10^{-11}	1.190×10^{-11}
2, 7/2 → 4, 7/2	1.620×10^{-11}	1.590×10^{-11}	1.660×10^{-11}	1.660×10^{-11}	1.630×10^{-11}	1.610×10^{-11}	1.590×10^{-11}
2, 1/2 → 4, 9/2	4.040×10^{-12}	3.970×10^{-12}	4.150×10^{-12}	4.160×10^{-12}	4.080×10^{-12}	4.020×10^{-12}	3.980×10^{-12}
2, 9/2 → 4, 9/2	2.020×10^{-11}	1.980×10^{-11}	2.080×10^{-11}	2.080×10^{-11}	2.040×10^{-11}	2.010×10^{-11}	1.990×10^{-11}
2, 3/2 → 4, 9/2	8.080×10^{-12}	7.940×10^{-12}	8.310×10^{-12}	8.320×10^{-12}	8.160×10^{-12}	8.040×10^{-12}	7.960×10^{-12}
2, 5/2 → 4, 9/2	1.210×10^{-11}	1.190×10^{-11}	1.250×10^{-11}	1.250×10^{-11}	1.220×10^{-11}	1.210×10^{-11}	1.190×10^{-11}
2, 7/2 → 4, 9/2	1.620×10^{-11}	1.590×10^{-11}	1.660×10^{-11}	1.660×10^{-11}	1.630×10^{-11}	1.610×10^{-11}	1.590×10^{-11}
3, 11/2 → 4, 13/2	2.360×10^{-11}	2.430×10^{-11}	2.320×10^{-11}	2.100×10^{-11}	1.990×10^{-11}	1.940×10^{-11}	1.930×10^{-11}
3, 1/2 → 4, 13/2	3.930×10^{-12}	4.050×10^{-12}	3.860×10^{-12}	3.490×10^{-12}	3.320×10^{-12}	3.240×10^{-12}	3.220×10^{-12}
3, 3/2 → 4, 13/2	7.850×10^{-12}	8.090×10^{-12}	7.730×10^{-12}	6.990×10^{-12}	6.630×10^{-12}	6.480×10^{-12}	6.440×10^{-12}
3, 5/2 → 4, 13/2	1.180×10^{-11}	1.210×10^{-11}	1.160×10^{-11}	1.050×10^{-11}	9.950×10^{-12}	9.720×10^{-12}	9.650×10^{-12}
3, 9/2 → 4, 13/2	1.960×10^{-11}	2.020×10^{-11}	1.930×10^{-11}	1.750×10^{-11}	1.660×10^{-11}	1.620×10^{-11}	1.610×10^{-11}
3, 7/2 → 4, 13/2	1.570×10^{-11}	1.620×10^{-11}	1.550×10^{-11}	1.400×10^{-11}	1.330×10^{-11}	1.300×10^{-11}	1.290×10^{-11}

Table A.4: continued.

Quantum Numbers	T						
J, $F \rightarrow J^{'}$,$F^{'}$	2 K	5 K	10 K	20 K	30 K	40 K	50 K
3, 11/2 → 4, 3/2	2.360×10^{-11}	2.430×10^{-11}	2.320×10^{-11}	2.100×10^{-11}	1.990×10^{-11}	1.940×10^{-11}	1.930×10^{-11}
3, 1/2 → 4, 3/2	3.930×10^{-12}	4.050×10^{-12}	3.860×10^{-12}	3.490×10^{-12}	3.320×10^{-12}	3.240×10^{-12}	3.220×10^{-12}
3, 3/2 → 4, 3/2	7.850×10^{-12}	8.090×10^{-12}	7.730×10^{-12}	6.990×10^{-12}	6.630×10^{-12}	6.480×10^{-12}	6.440×10^{-12}
3, 5/2 → 4, 3/2	1.180×10^{-11}	1.210×10^{-11}	1.160×10^{-11}	1.050×10^{-11}	9.950×10^{-12}	9.720×10^{-12}	9.650×10^{-12}
3, 9/2 → 4, 3/2	1.960×10^{-11}	2.020×10^{-11}	1.930×10^{-11}	1.750×10^{-11}	1.660×10^{-11}	1.620×10^{-11}	1.610×10^{-11}
3, 7/2 → 4, 3/2	1.570×10^{-11}	1.620×10^{-11}	1.550×10^{-11}	1.400×10^{-11}	1.330×10^{-11}	1.300×10^{-11}	1.290×10^{-11}
3, 11/2 → 4, 5/2	2.360×10^{-11}	2.430×10^{-11}	2.320×10^{-11}	2.100×10^{-11}	1.990×10^{-11}	1.940×10^{-11}	1.930×10^{-11}
3, 1/2 → 4, 5/2	3.930×10^{-12}	4.050×10^{-12}	3.860×10^{-12}	3.490×10^{-12}	3.320×10^{-12}	3.240×10^{-12}	3.220×10^{-12}
3, 3/2 → 4, 5/2	7.850×10^{-12}	8.090×10^{-12}	7.730×10^{-12}	6.990×10^{-12}	6.630×10^{-12}	6.480×10^{-12}	6.440×10^{-12}
3, 5/2 → 4, 5/2	1.180×10^{-11}	1.210×10^{-11}	1.160×10^{-11}	1.050×10^{-11}	9.950×10^{-12}	9.720×10^{-12}	9.650×10^{-12}
3, 9/2 → 4, 5/2	1.960×10^{-11}	2.020×10^{-11}	1.930×10^{-11}	1.750×10^{-11}	1.660×10^{-11}	1.620×10^{-11}	1.610×10^{-11}
3, 7/2 → 4, 5/2	1.570×10^{-11}	1.620×10^{-11}	1.550×10^{-11}	1.400×10^{-11}	1.330×10^{-11}	1.300×10^{-11}	1.290×10^{-11}
3, 11/2 → 4, 11/2	2.360×10^{-11}	2.430×10^{-11}	2.320×10^{-11}	2.100×10^{-11}	1.990×10^{-11}	1.940×10^{-11}	1.930×10^{-11}
3, 1/2 → 4, 11/2	3.930×10^{-12}	4.050×10^{-12}	3.860×10^{-12}	3.490×10^{-12}	3.320×10^{-12}	3.240×10^{-12}	3.220×10^{-12}
3, 3/2 → 4, 11/2	7.850×10^{-12}	8.090×10^{-12}	7.730×10^{-12}	6.990×10^{-12}	6.630×10^{-12}	6.480×10^{-12}	6.440×10^{-12}
3, 5/2 → 4, 11/2	1.180×10^{-11}	1.210×10^{-11}	1.160×10^{-11}	1.050×10^{-11}	9.950×10^{-12}	9.720×10^{-12}	9.650×10^{-12}
3, 9/2 → 4, 11/2	1.960×10^{-11}	2.020×10^{-11}	1.930×10^{-11}	1.750×10^{-11}	1.660×10^{-11}	1.620×10^{-11}	1.610×10^{-11}
3, 7/2 → 4, 11/2	1.570×10^{-11}	1.620×10^{-11}	1.550×10^{-11}	1.400×10^{-11}	1.330×10^{-11}	1.300×10^{-11}	1.290×10^{-11}
3, 11/2 → 4, 7/2	2.360×10^{-11}	2.430×10^{-11}	2.320×10^{-11}	2.100×10^{-11}	1.990×10^{-11}	1.940×10^{-11}	1.930×10^{-11}
3, 1/2 → 4, 7/2	3.930×10^{-12}	4.050×10^{-12}	3.860×10^{-12}	3.490×10^{-12}	3.320×10^{-12}	3.240×10^{-12}	3.220×10^{-12}
3, 3/2 → 4, 7/2	7.850×10^{-12}	8.090×10^{-12}	7.730×10^{-12}	6.990×10^{-12}	6.630×10^{-12}	6.480×10^{-12}	6.440×10^{-12}
3, 5/2 → 4, 7/2	1.180×10^{-11}	1.210×10^{-11}	1.160×10^{-11}	1.050×10^{-11}	9.950×10^{-12}	9.720×10^{-12}	9.650×10^{-12}
3, 9/2 → 4, 7/2	1.960×10^{-11}	2.020×10^{-11}	1.930×10^{-11}	1.750×10^{-11}	1.660×10^{-11}	1.620×10^{-11}	1.610×10^{-11}
3, 7/2 → 4, 7/2	1.570×10^{-11}	1.620×10^{-11}	1.550×10^{-11}	1.400×10^{-11}	1.330×10^{-11}	1.300×10^{-11}	1.290×10^{-11}
3, 11/2 → 4, 9/2	2.360×10^{-11}	2.430×10^{-11}	2.320×10^{-11}	2.100×10^{-11}	1.990×10^{-11}	1.940×10^{-11}	1.930×10^{-11}
3, 1/2 → 4, 9/2	3.930×10^{-12}	4.050×10^{-12}	3.860×10^{-12}	3.490×10^{-12}	3.320×10^{-12}	3.240×10^{-12}	3.220×10^{-12}
3, 3/2 → 4, 9/2	7.850×10^{-12}	8.090×10^{-12}	7.730×10^{-12}	6.990×10^{-12}	6.630×10^{-12}	6.480×10^{-12}	6.440×10^{-12}
3, 5/2 → 4, 9/2	1.180×10^{-11}	1.210×10^{-11}	1.160×10^{-11}	1.050×10^{-11}	9.950×10^{-12}	9.720×10^{-12}	9.650×10^{-12}
3, 9/2 → 4, 9/2	1.960×10^{-11}	2.020×10^{-11}	1.930×10^{-11}	1.750×10^{-11}	1.660×10^{-11}	1.620×10^{-11}	1.610×10^{-11}
3, 7/2 → 4, 9/2	1.570×10^{-11}	1.620×10^{-11}	1.550×10^{-11}	1.400×10^{-11}	1.330×10^{-11}	1.300×10^{-11}	1.290×10^{-11}
0, 5/2 → 5, 15/2	7.920×10^{-13}	8.220×10^{-13}	9.700×10^{-13}	1.180×10^{-12}	1.380×10^{-12}	1.590×10^{-12}	1.830×10^{-12}
0, 5/2 → 5, 5/2	7.920×10^{-13}	8.220×10^{-13}	9.700×10^{-13}	1.180×10^{-12}	1.380×10^{-12}	1.590×10^{-12}	1.830×10^{-12}
0, 5/2 → 5, 7/2	7.920×10^{-13}	8.220×10^{-13}	9.700×10^{-13}	1.180×10^{-12}	1.380×10^{-12}	1.590×10^{-12}	1.830×10^{-12}
0, 5/2 → 5, 13/2	7.920×10^{-13}	8.220×10^{-13}	9.700×10^{-13}	1.180×10^{-12}	1.380×10^{-12}	1.590×10^{-12}	1.830×10^{-12}
0, 5/2 → 5, 9/2	7.920×10^{-13}	8.220×10^{-13}	9.700×10^{-13}	1.180×10^{-12}	1.380×10^{-12}	1.590×10^{-12}	1.830×10^{-12}
0, 5/2 → 5, 11/2	7.920×10^{-13}	8.220×10^{-13}	9.700×10^{-13}	1.180×10^{-12}	1.380×10^{-12}	1.590×10^{-12}	1.830×10^{-12}
1, 3/2 → 5, 15/2	1.530×10^{-12}	1.380×10^{-12}	1.380×10^{-12}	1.440×10^{-12}	1.510×10^{-12}	1.570×10^{-12}	1.640×10^{-12}

Table A.4: continued.

Quantum Numbers	T						
J, $F \rightarrow J^{'}$,$F^{'}$	2 K	5 K	10 K	20 K	30 K	40 K	50 K
1, 7/2 → 5, 15/2	3.050×10^{-12}	2.760×10^{-12}	2.760×10^{-12}	2.890×10^{-12}	3.010×10^{-12}	3.140×10^{-12}	3.270×10^{-12}
1, 5/2 → 5, 15/2	2.290×10^{-12}	2.070×10^{-12}	2.070×10^{-12}	2.170×10^{-12}	2.260×10^{-12}	2.350×10^{-12}	2.450×10^{-12}
1, 3/2 → 5, 5/2	1.530×10^{-12}	1.380×10^{-12}	1.380×10^{-12}	1.440×10^{-12}	1.510×10^{-12}	1.570×10^{-12}	1.640×10^{-12}
1, 7/2 → 5, 5/2	3.050×10^{-12}	2.760×10^{-12}	2.760×10^{-12}	2.890×10^{-12}	3.010×10^{-12}	3.140×10^{-12}	3.270×10^{-12}
1, 5/2 → 5, 5/2	2.290×10^{-12}	2.070×10^{-12}	2.070×10^{-12}	2.170×10^{-12}	2.260×10^{-12}	2.350×10^{-12}	2.450×10^{-12}
1, 3/2 → 5, 7/2	1.530×10^{-12}	1.380×10^{-12}	1.380×10^{-12}	1.440×10^{-12}	1.510×10^{-12}	1.570×10^{-12}	1.640×10^{-12}
1, 7/2 → 5, 7/2	3.050×10^{-12}	2.760×10^{-12}	2.760×10^{-12}	2.890×10^{-12}	3.010×10^{-12}	3.140×10^{-12}	3.270×10^{-12}
1, 5/2 → 5, 7/2	2.290×10^{-12}	2.070×10^{-12}	2.070×10^{-12}	2.170×10^{-12}	2.260×10^{-12}	2.350×10^{-12}	2.450×10^{-12}
1, 3/2 → 5, 13/2	1.530×10^{-12}	1.380×10^{-12}	1.380×10^{-12}	1.440×10^{-12}	1.510×10^{-12}	1.570×10^{-12}	1.640×10^{-12}
1, 7/2 → 5, 13/2	3.050×10^{-12}	2.760×10^{-12}	2.760×10^{-12}	2.890×10^{-12}	3.010×10^{-12}	3.140×10^{-12}	3.270×10^{-12}
1, 5/2 → 5, 13/2	2.290×10^{-12}	2.070×10^{-12}	2.070×10^{-12}	2.170×10^{-12}	2.260×10^{-12}	2.350×10^{-12}	2.450×10^{-12}
1, 3/2 → 5, 9/2	1.530×10^{-12}	1.380×10^{-12}	1.380×10^{-12}	1.440×10^{-12}	1.510×10^{-12}	1.570×10^{-12}	1.640×10^{-12}
1, 7/2 → 5, 9/2	3.050×10^{-12}	2.760×10^{-12}	2.760×10^{-12}	2.890×10^{-12}	3.010×10^{-12}	3.140×10^{-12}	3.270×10^{-12}
1, 5/2 → 5, 9/2	2.290×10^{-12}	2.070×10^{-12}	2.070×10^{-12}	2.170×10^{-12}	2.260×10^{-12}	2.350×10^{-12}	2.450×10^{-12}
1, 3/2 → 5, 11/2	1.530×10^{-12}	1.380×10^{-12}	1.380×10^{-12}	1.440×10^{-12}	1.510×10^{-12}	1.570×10^{-12}	1.640×10^{-12}
1, 7/2 → 5, 11/2	3.050×10^{-12}	2.760×10^{-12}	2.760×10^{-12}	2.890×10^{-12}	3.010×10^{-12}	3.140×10^{-12}	3.270×10^{-12}
1, 5/2 → 5, 11/2	2.290×10^{-12}	2.070×10^{-12}	2.070×10^{-12}	2.170×10^{-12}	2.260×10^{-12}	2.350×10^{-12}	2.450×10^{-12}
2, 1/2 → 5, 15/2	5.410×10^{-13}	6.600×10^{-13}	8.340×10^{-13}	9.750×10^{-13}	1.050×10^{-12}	1.130×10^{-12}	1.210×10^{-12}
2, 9/2 → 5, 15/2	2.700×10^{-12}	3.300×10^{-12}	4.170×10^{-12}	4.870×10^{-12}	5.270×10^{-12}	5.650×10^{-12}	6.030×10^{-12}
2, 3/2 → 5, 15/2	1.080×10^{-12}	1.320×10^{-12}	1.670×10^{-12}	1.950×10^{-12}	2.110×10^{-12}	2.260×10^{-12}	2.410×10^{-12}
2, 5/2 → 5, 15/2	1.620×10^{-12}	1.980×10^{-12}	2.500×10^{-12}	2.920×10^{-12}	3.160×10^{-12}	3.390×10^{-12}	3.620×10^{-12}
2, 7/2 → 5, 15/2	2.160×10^{-12}	2.640×10^{-12}	3.340×10^{-12}	3.900×10^{-12}	4.220×10^{-12}	4.520×10^{-12}	4.830×10^{-12}
2, 1/2 → 5, 5/2	5.410×10^{-13}	6.600×10^{-13}	8.340×10^{-13}	9.750×10^{-13}	1.050×10^{-12}	1.130×10^{-12}	1.210×10^{-12}
2, 9/2 → 5, 5/2	2.700×10^{-12}	3.300×10^{-12}	4.170×10^{-12}	4.870×10^{-12}	5.270×10^{-12}	5.650×10^{-12}	6.030×10^{-12}
2, 3/2 → 5, 5/2	1.080×10^{-12}	1.320×10^{-12}	1.670×10^{-12}	1.950×10^{-12}	2.110×10^{-12}	2.260×10^{-12}	2.410×10^{-12}
2, 5/2 → 5, 5/2	1.620×10^{-12}	1.980×10^{-12}	2.500×10^{-12}	2.920×10^{-12}	3.160×10^{-12}	3.390×10^{-12}	3.620×10^{-12}
2, 7/2 → 5, 5/2	2.160×10^{-12}	2.640×10^{-12}	3.340×10^{-12}	3.900×10^{-12}	4.220×10^{-12}	4.520×10^{-12}	4.830×10^{-12}
2, 1/2 → 5, 7/2	5.410×10^{-13}	6.600×10^{-13}	8.340×10^{-13}	9.750×10^{-13}	1.050×10^{-12}	1.130×10^{-12}	1.210×10^{-12}
2, 9/2 → 5, 7/2	2.700×10^{-12}	3.300×10^{-12}	4.170×10^{-12}	4.870×10^{-12}	5.270×10^{-12}	5.650×10^{-12}	6.030×10^{-12}
2, 3/2 → 5, 7/2	1.080×10^{-12}	1.320×10^{-12}	1.670×10^{-12}	1.950×10^{-12}	2.110×10^{-12}	2.260×10^{-12}	2.410×10^{-12}
2, 5/2 → 5, 7/2	1.620×10^{-12}	1.980×10^{-12}	2.500×10^{-12}	2.920×10^{-12}	3.160×10^{-12}	3.390×10^{-12}	3.620×10^{-12}
2, 7/2 → 5, 7/2	2.160×10^{-12}	2.640×10^{-12}	3.340×10^{-12}	3.900×10^{-12}	4.220×10^{-12}	4.520×10^{-12}	4.830×10^{-12}
2, 1/2 → 5, 13/2	5.410×10^{-13}	6.600×10^{-13}	8.340×10^{-13}	9.750×10^{-13}	1.050×10^{-12}	1.130×10^{-12}	1.210×10^{-12}
2, 9/2 → 5, 13/2	2.700×10^{-12}	3.300×10^{-12}	4.170×10^{-12}	4.870×10^{-12}	5.270×10^{-12}	5.650×10^{-12}	6.030×10^{-12}
2, 3/2 → 5, 13/2	1.080×10^{-12}	1.320×10^{-12}	1.670×10^{-12}	1.950×10^{-12}	2.110×10^{-12}	2.260×10^{-12}	2.410×10^{-12}
2, 5/2 → 5, 13/2	1.620×10^{-12}	1.980×10^{-12}	2.500×10^{-12}	2.920×10^{-12}	3.160×10^{-12}	3.390×10^{-12}	3.620×10^{-12}
2, 7/2 → 5, 13/2	2.160×10^{-12}	2.640×10^{-12}	3.340×10^{-12}	3.900×10^{-12}	4.220×10^{-12}	4.520×10^{-12}	4.830×10^{-12}

Table A.4: continued.

Quantum Numbers			T				
J, $F \rightarrow J^{'}$,$F^{'}$	2 K	5 K	10 K	20 K	30 K	40 K	50 K
2, 1/2 → 5, 9/2	5.410×10^{-13}	6.600×10^{-13}	8.340×10^{-13}	9.750×10^{-13}	1.050×10^{-12}	1.130×10^{-12}	1.210×10^{-12}
2, 9/2 → 5, 9/2	2.700×10^{-12}	3.300×10^{-12}	4.170×10^{-12}	4.870×10^{-12}	5.270×10^{-12}	5.650×10^{-12}	6.030×10^{-12}
2, 3/2 → 5, 9/2	1.080×10^{-12}	1.320×10^{-12}	1.670×10^{-12}	1.950×10^{-12}	2.110×10^{-12}	2.260×10^{-12}	2.410×10^{-12}
2, 5/2 → 5, 9/2	1.620×10^{-12}	1.980×10^{-12}	2.500×10^{-12}	2.920×10^{-12}	3.160×10^{-12}	3.390×10^{-12}	3.620×10^{-12}
2, 7/2 → 5, 9/2	2.160×10^{-12}	2.640×10^{-12}	3.340×10^{-12}	3.900×10^{-12}	4.220×10^{-12}	4.520×10^{-12}	4.830×10^{-12}
2, 1/2 → 5, 11/2	5.410×10^{-13}	6.600×10^{-13}	8.340×10^{-13}	9.750×10^{-13}	1.050×10^{-12}	1.130×10^{-12}	1.210×10^{-12}
2, 9/2 → 5, 11/2	2.700×10^{-12}	3.300×10^{-12}	4.170×10^{-12}	4.870×10^{-12}	5.270×10^{-12}	5.650×10^{-12}	6.030×10^{-12}
2, 3/2 → 5, 11/2	1.080×10^{-12}	1.320×10^{-12}	1.670×10^{-12}	1.950×10^{-12}	2.110×10^{-12}	2.260×10^{-12}	2.410×10^{-12}
2, 5/2 → 5, 11/2	1.620×10^{-12}	1.980×10^{-12}	2.500×10^{-12}	2.920×10^{-12}	3.160×10^{-12}	3.390×10^{-12}	3.620×10^{-12}
2, 7/2 → 5, 11/2	2.160×10^{-12}	2.640×10^{-12}	3.340×10^{-12}	3.900×10^{-12}	4.220×10^{-12}	4.520×10^{-12}	4.830×10^{-12}
3, 11/2 → 5, 15/2	2.360×10^{-11}	2.210×10^{-11}	2.180×10^{-11}	2.090×10^{-11}	2.020×10^{-11}	1.960×10^{-11}	1.910×10^{-11}
3, 1/2 → 5, 15/2	3.940×10^{-12}	3.680×10^{-12}	3.630×10^{-12}	3.490×10^{-12}	3.360×10^{-12}	3.260×10^{-12}	3.190×10^{-12}
3, 3/2 → 5, 15/2	7.880×10^{-12}	7.360×10^{-12}	7.250×10^{-12}	6.980×10^{-12}	6.720×10^{-12}	6.520×10^{-12}	6.380×10^{-12}
3, 5/2 → 5, 15/2	1.180×10^{-11}	1.100×10^{-11}	1.090×10^{-11}	1.050×10^{-11}	1.010×10^{-11}	9.780×10^{-12}	9.570×10^{-12}
3, 9/2 → 5, 15/2	1.970×10^{-11}	1.840×10^{-11}	1.810×10^{-11}	1.740×10^{-11}	1.680×10^{-11}	1.630×10^{-11}	1.600×10^{-11}
3, 7/2 → 5, 15/2	1.580×10^{-11}	1.470×10^{-11}	1.450×10^{-11}	1.400×10^{-11}	1.340×10^{-11}	1.300×10^{-11}	1.280×10^{-11}
3, 11/2 → 5, 5/2	2.360×10^{-11}	2.210×10^{-11}	2.180×10^{-11}	2.090×10^{-11}	2.020×10^{-11}	1.960×10^{-11}	1.910×10^{-11}
3, 1/2 → 5, 5/2	3.940×10^{-12}	3.680×10^{-12}	3.630×10^{-12}	3.490×10^{-12}	3.360×10^{-12}	3.260×10^{-12}	3.190×10^{-12}
3, 3/2 → 5, 5/2	7.880×10^{-12}	7.360×10^{-12}	7.250×10^{-12}	6.980×10^{-12}	6.720×10^{-12}	6.520×10^{-12}	6.380×10^{-12}
3, 5/2 → 5, 5/2	1.180×10^{-11}	1.100×10^{-11}	1.090×10^{-11}	1.050×10^{-11}	1.010×10^{-11}	9.780×10^{-12}	9.570×10^{-12}
3, 9/2 → 5, 5/2	1.970×10^{-11}	1.840×10^{-11}	1.810×10^{-11}	1.740×10^{-11}	1.680×10^{-11}	1.630×10^{-11}	1.600×10^{-11}
3, 7/2 → 5, 5/2	1.580×10^{-11}	1.470×10^{-11}	1.450×10^{-11}	1.400×10^{-11}	1.340×10^{-11}	1.300×10^{-11}	1.280×10^{-11}
3, 11/2 → 5, 7/2	2.360×10^{-11}	2.210×10^{-11}	2.180×10^{-11}	2.090×10^{-11}	2.020×10^{-11}	1.960×10^{-11}	1.910×10^{-11}
3, 1/2 → 5, 7/2	3.940×10^{-12}	3.680×10^{-12}	3.630×10^{-12}	3.490×10^{-12}	3.360×10^{-12}	3.260×10^{-12}	3.190×10^{-12}
3, 3/2 → 5, 7/2	7.880×10^{-12}	7.360×10^{-12}	7.250×10^{-12}	6.980×10^{-12}	6.720×10^{-12}	6.520×10^{-12}	6.380×10^{-12}
3, 5/2 → 5, 7/2	1.180×10^{-11}	1.100×10^{-11}	1.090×10^{-11}	1.050×10^{-11}	1.010×10^{-11}	9.780×10^{-12}	9.570×10^{-12}
3, 9/2 → 5, 7/2	1.970×10^{-11}	1.840×10^{-11}	1.810×10^{-11}	1.740×10^{-11}	1.680×10^{-11}	1.630×10^{-11}	1.600×10^{-11}
3, 7/2 → 5, 7/2	1.580×10^{-11}	1.470×10^{-11}	1.450×10^{-11}	1.400×10^{-11}	1.340×10^{-11}	1.300×10^{-11}	1.280×10^{-11}
3, 11/2 → 5, 13/2	2.360×10^{-11}	2.210×10^{-11}	2.180×10^{-11}	2.090×10^{-11}	2.020×10^{-11}	1.960×10^{-11}	1.910×10^{-11}
3, 1/2 → 5, 13/2	3.940×10^{-12}	3.680×10^{-12}	3.630×10^{-12}	3.490×10^{-12}	3.360×10^{-12}	3.260×10^{-12}	3.190×10^{-12}
3, 3/2 → 5, 13/2	7.880×10^{-12}	7.360×10^{-12}	7.250×10^{-12}	6.980×10^{-12}	6.720×10^{-12}	6.520×10^{-12}	6.380×10^{-12}
3, 5/2 → 5, 13/2	1.180×10^{-11}	1.100×10^{-11}	1.090×10^{-11}	1.050×10^{-11}	1.010×10^{-11}	9.780×10^{-12}	9.570×10^{-12}
3, 9/2 → 5, 13/2	1.970×10^{-11}	1.840×10^{-11}	1.810×10^{-11}	1.740×10^{-11}	1.680×10^{-11}	1.630×10^{-11}	1.600×10^{-11}
3, 7/2 → 5, 13/2	1.580×10^{-11}	1.470×10^{-11}	1.450×10^{-11}	1.400×10^{-11}	1.340×10^{-11}	1.300×10^{-11}	1.280×10^{-11}
3, 11/2 → 5, 9/2	2.360×10^{-11}	2.210×10^{-11}	2.180×10^{-11}	2.090×10^{-11}	2.020×10^{-11}	1.960×10^{-11}	1.910×10^{-11}
3, 1/2 → 5, 9/2	3.940×10^{-12}	3.680×10^{-12}	3.630×10^{-12}	3.490×10^{-12}	3.360×10^{-12}	3.260×10^{-12}	3.190×10^{-12}
3, 3/2 → 5, 9/2	7.880×10^{-12}	7.360×10^{-12}	7.250×10^{-12}	6.980×10^{-12}	6.720×10^{-12}	6.520×10^{-12}	6.380×10^{-12}

Table A.4: continued.

Quantum Numbers	T						
J, $F \rightarrow J^{'}$,$F^{'}$	2 K	5 K	10 K	20 K	30 K	40 K	50 K
3, 5/2 → 5, 9/2	1.180×10^{-11}	1.100×10^{-11}	1.090×10^{-11}	1.050×10^{-11}	1.010×10^{-11}	9.780×10^{-12}	9.570×10^{-12}
3, 9/2 → 5, 9/2	1.970×10^{-11}	1.840×10^{-11}	1.810×10^{-11}	1.740×10^{-11}	1.680×10^{-11}	1.630×10^{-11}	1.600×10^{-11}
3, 7/2 → 5, 9/2	1.580×10^{-11}	1.470×10^{-11}	1.450×10^{-11}	1.400×10^{-11}	1.340×10^{-11}	1.300×10^{-11}	1.280×10^{-11}
3, 11/2 → 5, 11/2	2.360×10^{-11}	2.210×10^{-11}	2.180×10^{-11}	2.090×10^{-11}	2.020×10^{-11}	1.960×10^{-11}	1.910×10^{-11}
3, 1/2 → 5, 11/2	3.940×10^{-12}	3.680×10^{-12}	3.630×10^{-12}	3.490×10^{-12}	3.360×10^{-12}	3.260×10^{-12}	3.190×10^{-12}
3, 3/2 → 5, 11/2	7.880×10^{-12}	7.360×10^{-12}	7.250×10^{-12}	6.980×10^{-12}	6.720×10^{-12}	6.520×10^{-12}	6.380×10^{-12}
3, 5/2 → 5, 11/2	1.180×10^{-11}	1.100×10^{-11}	1.090×10^{-11}	1.050×10^{-11}	1.010×10^{-11}	9.780×10^{-12}	9.570×10^{-12}
3, 9/2 → 5, 11/2	1.970×10^{-11}	1.840×10^{-11}	1.810×10^{-11}	1.740×10^{-11}	1.680×10^{-11}	1.630×10^{-11}	1.600×10^{-11}
3, 7/2 → 5, 11/2	1.580×10^{-11}	1.470×10^{-11}	1.450×10^{-11}	1.400×10^{-11}	1.340×10^{-11}	1.300×10^{-11}	1.280×10^{-11}
4, 13/2 → 5, 15/2	6.120×10^{-12}	1.260×10^{-11}	1.700×10^{-11}	1.820×10^{-11}	1.810×10^{-11}	1.800×10^{-11}	1.800×10^{-11}
4, 3/2 → 5, 15/2	1.750×10^{-12}	3.590×10^{-12}	4.850×10^{-12}	5.210×10^{-12}	5.170×10^{-12}	5.140×10^{-12}	5.130×10^{-12}
4, 5/2 → 5, 15/2	2.620×10^{-12}	5.390×10^{-12}	7.280×10^{-12}	7.820×10^{-12}	7.760×10^{-12}	7.700×10^{-12}	7.700×10^{-12}
4, 11/2 → 5, 15/2	5.240×10^{-12}	1.080×10^{-11}	1.460×10^{-11}	1.560×10^{-11}	1.550×10^{-11}	1.540×10^{-11}	1.540×10^{-11}
4, 7/2 → 5, 15/2	3.490×10^{-12}	7.180×10^{-12}	9.710×10^{-12}	1.040×10^{-11}	1.030×10^{-11}	1.030×10^{-11}	1.030×10^{-11}
4, 9/2 → 5, 15/2	4.370×10^{-12}	8.980×10^{-12}	1.210×10^{-11}	1.300×10^{-11}	1.290×10^{-11}	1.280×10^{-11}	1.280×10^{-11}
4, 13/2 → 5, 5/2	6.120×10^{-12}	1.260×10^{-11}	1.700×10^{-11}	1.820×10^{-11}	1.810×10^{-11}	1.800×10^{-11}	1.800×10^{-11}
4, 3/2 → 5, 5/2	1.750×10^{-12}	3.590×10^{-12}	4.850×10^{-12}	5.210×10^{-12}	5.170×10^{-12}	5.140×10^{-12}	5.130×10^{-12}
4, 5/2 → 5, 5/2	2.620×10^{-12}	5.390×10^{-12}	7.280×10^{-12}	7.820×10^{-12}	7.760×10^{-12}	7.700×10^{-12}	7.700×10^{-12}
4, 11/2 → 5, 5/2	5.240×10^{-12}	1.080×10^{-11}	1.460×10^{-11}	1.560×10^{-11}	1.550×10^{-11}	1.540×10^{-11}	1.540×10^{-11}
4, 7/2 → 5, 5/2	3.490×10^{-12}	7.180×10^{-12}	9.710×10^{-12}	1.040×10^{-11}	1.030×10^{-11}	1.030×10^{-11}	1.030×10^{-11}
4, 9/2 → 5, 5/2	4.370×10^{-12}	8.980×10^{-12}	1.210×10^{-11}	1.300×10^{-11}	1.290×10^{-11}	1.280×10^{-11}	1.280×10^{-11}
4, 13/2 → 5, 7/2	6.120×10^{-12}	1.260×10^{-11}	1.700×10^{-11}	1.820×10^{-11}	1.810×10^{-11}	1.800×10^{-11}	1.800×10^{-11}
4, 3/2 → 5, 7/2	1.750×10^{-12}	3.590×10^{-12}	4.850×10^{-12}	5.210×10^{-12}	5.170×10^{-12}	5.140×10^{-12}	5.130×10^{-12}
4, 5/2 → 5, 7/2	2.620×10^{-12}	5.390×10^{-12}	7.280×10^{-12}	7.820×10^{-12}	7.760×10^{-12}	7.700×10^{-12}	7.700×10^{-12}
4, 11/2 → 5, 7/2	5.240×10^{-12}	1.080×10^{-11}	1.460×10^{-11}	1.560×10^{-11}	1.550×10^{-11}	1.540×10^{-11}	1.540×10^{-11}
4, 7/2 → 5, 7/2	3.490×10^{-12}	7.180×10^{-12}	9.710×10^{-12}	1.040×10^{-11}	1.030×10^{-11}	1.030×10^{-11}	1.030×10^{-11}
4, 9/2 → 5, 7/2	4.370×10^{-12}	8.980×10^{-12}	1.210×10^{-11}	1.300×10^{-11}	1.290×10^{-11}	1.280×10^{-11}	1.280×10^{-11}
4, 13/2 → 5, 13/2	6.120×10^{-12}	1.260×10^{-11}	1.700×10^{-11}	1.820×10^{-11}	1.810×10^{-11}	1.800×10^{-11}	1.800×10^{-11}
4, 3/2 → 5, 13/2	1.750×10^{-12}	3.590×10^{-12}	4.850×10^{-12}	5.210×10^{-12}	5.170×10^{-12}	5.140×10^{-12}	5.130×10^{-12}
4, 5/2 → 5, 13/2	2.620×10^{-12}	5.390×10^{-12}	7.280×10^{-12}	7.820×10^{-12}	7.760×10^{-12}	7.700×10^{-12}	7.700×10^{-12}
4, 11/2 → 5, 13/2	5.240×10^{-12}	1.080×10^{-11}	1.460×10^{-11}	1.560×10^{-11}	1.550×10^{-11}	1.540×10^{-11}	1.540×10^{-11}
4, 7/2 → 5, 13/2	3.490×10^{-12}	7.180×10^{-12}	9.710×10^{-12}	1.040×10^{-11}	1.030×10^{-11}	1.030×10^{-11}	1.030×10^{-11}
4, 9/2 → 5, 13/2	4.370×10^{-12}	8.980×10^{-12}	1.210×10^{-11}	1.300×10^{-11}	1.290×10^{-11}	1.280×10^{-11}	1.280×10^{-11}
4, 13/2 → 5, 9/2	6.120×10^{-12}	1.260×10^{-11}	1.700×10^{-11}	1.820×10^{-11}	1.810×10^{-11}	1.800×10^{-11}	1.800×10^{-11}
4, 3/2 → 5, 9/2	1.750×10^{-12}	3.590×10^{-12}	4.850×10^{-12}	5.210×10^{-12}	5.170×10^{-12}	5.140×10^{-12}	5.130×10^{-12}
4, 5/2 → 5, 9/2	2.620×10^{-12}	5.390×10^{-12}	7.280×10^{-12}	7.820×10^{-12}	7.760×10^{-12}	7.700×10^{-12}	7.700×10^{-12}
4, 11/2 → 5, 9/2	5.240×10^{-12}	1.080×10^{-11}	1.460×10^{-11}	1.560×10^{-11}	1.550×10^{-11}	1.540×10^{-11}	1.540×10^{-11}

Table A.4: continued.

Quantum Numbers			T				
J, $F \rightarrow J^{'}$,$F^{'}$	2 K	5 K	10 K	20 K	30 K	40 K	50 K
4, 7/2 → 5, 9/2	3.490×10^{-12}	7.180×10^{-12}	9.710×10^{-12}	1.040×10^{-11}	1.030×10^{-11}	1.030×10^{-11}	1.030×10^{-11}
4, 9/2 → 5, 9/2	4.370×10^{-12}	8.980×10^{-12}	1.210×10^{-11}	1.300×10^{-11}	1.290×10^{-11}	1.280×10^{-11}	1.280×10^{-11}
4, 13/2 → 5, 11/2	6.120×10^{-12}	1.260×10^{-11}	1.700×10^{-11}	1.820×10^{-11}	1.810×10^{-11}	1.800×10^{-11}	1.800×10^{-11}
4, 3/2 → 5, 11/2	1.750×10^{-12}	3.590×10^{-12}	4.850×10^{-12}	5.210×10^{-12}	5.170×10^{-12}	5.140×10^{-12}	5.130×10^{-12}
4, 5/2 → 5, 11/2	2.620×10^{-12}	5.390×10^{-12}	7.280×10^{-12}	7.820×10^{-12}	7.760×10^{-12}	7.700×10^{-12}	7.700×10^{-12}
4, 11/2 → 5, 11/2	5.240×10^{-12}	1.080×10^{-11}	1.460×10^{-11}	1.560×10^{-11}	1.550×10^{-11}	1.540×10^{-11}	1.540×10^{-11}
4, 7/2 → 5, 11/2	3.490×10^{-12}	7.180×10^{-12}	9.710×10^{-12}	1.040×10^{-11}	1.030×10^{-11}	1.030×10^{-11}	1.030×10^{-11}
4, 9/2 → 5, 11/2	4.370×10^{-12}	8.980×10^{-12}	1.210×10^{-11}	1.300×10^{-11}	1.290×10^{-11}	1.280×10^{-11}	1.280×10^{-11}
0, 5/2 → 6, 17/2	5.350×10^{-13}	4.960×10^{-13}	5.020×10^{-13}	5.520×10^{-13}	6.150×10^{-13}	6.870×10^{-13}	7.650×10^{-13}
0, 5/2 → 6, 7/2	5.350×10^{-13}	4.960×10^{-13}	5.020×10^{-13}	5.520×10^{-13}	6.150×10^{-13}	6.870×10^{-13}	7.650×10^{-13}
0, 5/2 → 6, 15/2	5.350×10^{-13}	4.960×10^{-13}	5.020×10^{-13}	5.520×10^{-13}	6.150×10^{-13}	6.870×10^{-13}	7.650×10^{-13}
0, 5/2 → 6, 9/2	5.350×10^{-13}	4.960×10^{-13}	5.020×10^{-13}	5.520×10^{-13}	6.150×10^{-13}	6.870×10^{-13}	7.650×10^{-13}
0, 5/2 → 6, 11/2	5.350×10^{-13}	4.960×10^{-13}	5.020×10^{-13}	5.520×10^{-13}	6.150×10^{-13}	6.870×10^{-13}	7.650×10^{-13}
0, 5/2 → 6, 13/2	5.350×10^{-13}	4.960×10^{-13}	5.020×10^{-13}	5.520×10^{-13}	6.150×10^{-13}	6.870×10^{-13}	7.650×10^{-13}
1, 3/2 → 6, 17/2	4.770×10^{-13}	4.600×10^{-13}	4.960×10^{-13}	5.730×10^{-13}	6.500×10^{-13}	7.360×10^{-13}	8.310×10^{-13}
1, 7/2 → 6, 17/2	9.540×10^{-13}	9.200×10^{-13}	9.920×10^{-13}	1.150×10^{-12}	1.300×10^{-12}	1.470×10^{-12}	1.660×10^{-12}
1, 5/2 → 6, 17/2	7.150×10^{-13}	6.900×10^{-13}	7.440×10^{-13}	8.600×10^{-13}	9.750×10^{-13}	1.100×10^{-12}	1.250×10^{-12}
1, 3/2 → 6, 7/2	4.770×10^{-13}	4.600×10^{-13}	4.960×10^{-13}	5.730×10^{-13}	6.500×10^{-13}	7.360×10^{-13}	8.310×10^{-13}
1, 7/2 → 6, 7/2	9.540×10^{-13}	9.200×10^{-13}	9.920×10^{-13}	1.150×10^{-12}	1.300×10^{-12}	1.470×10^{-12}	1.660×10^{-12}
1, 5/2 → 6, 7/2	7.150×10^{-13}	6.900×10^{-13}	7.440×10^{-13}	8.600×10^{-13}	9.750×10^{-13}	1.100×10^{-12}	1.250×10^{-12}
1, 3/2 → 6, 15/2	4.770×10^{-13}	4.600×10^{-13}	4.960×10^{-13}	5.730×10^{-13}	6.500×10^{-13}	7.360×10^{-13}	8.310×10^{-13}
1, 7/2 → 6, 15/2	9.540×10^{-13}	9.200×10^{-13}	9.920×10^{-13}	1.150×10^{-12}	1.300×10^{-12}	1.470×10^{-12}	1.660×10^{-12}
1, 5/2 → 6, 15/2	7.150×10^{-13}	6.900×10^{-13}	7.440×10^{-13}	8.600×10^{-13}	9.750×10^{-13}	1.100×10^{-12}	1.250×10^{-12}
1, 3/2 → 6, 9/2	4.770×10^{-13}	4.600×10^{-13}	4.960×10^{-13}	5.730×10^{-13}	6.500×10^{-13}	7.360×10^{-13}	8.310×10^{-13}
1, 7/2 → 6, 9/2	9.540×10^{-13}	9.200×10^{-13}	9.920×10^{-13}	1.150×10^{-12}	1.300×10^{-12}	1.470×10^{-12}	1.660×10^{-12}
1, 5/2 → 6, 9/2	7.150×10^{-13}	6.900×10^{-13}	7.440×10^{-13}	8.600×10^{-13}	9.750×10^{-13}	1.100×10^{-12}	1.250×10^{-12}
1, 3/2 → 6, 11/2	4.770×10^{-13}	4.600×10^{-13}	4.960×10^{-13}	5.730×10^{-13}	6.500×10^{-13}	7.360×10^{-13}	8.310×10^{-13}
1, 7/2 → 6, 11/2	9.540×10^{-13}	9.200×10^{-13}	9.920×10^{-13}	1.150×10^{-12}	1.300×10^{-12}	1.470×10^{-12}	1.660×10^{-12}
1, 5/2 → 6, 11/2	7.150×10^{-13}	6.900×10^{-13}	7.440×10^{-13}	8.600×10^{-13}	9.750×10^{-13}	1.100×10^{-12}	1.250×10^{-12}
1, 3/2 → 6, 13/2	4.770×10^{-13}	4.600×10^{-13}	4.960×10^{-13}	5.730×10^{-13}	6.500×10^{-13}	7.360×10^{-13}	8.310×10^{-13}
1, 7/2 → 6, 13/2	9.540×10^{-13}	9.200×10^{-13}	9.920×10^{-13}	1.150×10^{-12}	1.300×10^{-12}	1.470×10^{-12}	1.660×10^{-12}
1, 5/2 → 6, 13/2	7.150×10^{-13}	6.900×10^{-13}	7.440×10^{-13}	8.600×10^{-13}	9.750×10^{-13}	1.100×10^{-12}	1.250×10^{-12}
2, 1/2 → 6, 17/2	6.590×10^{-13}	6.100×10^{-13}	5.950×10^{-13}	5.950×10^{-13}	6.040×10^{-13}	6.170×10^{-13}	6.320×10^{-13}
2, 9/2 → 6, 17/2	3.290×10^{-12}	3.050×10^{-12}	2.970×10^{-12}	2.970×10^{-12}	3.020×10^{-12}	3.080×10^{-12}	3.160×10^{-12}
2, 3/2 → 6, 17/2	1.320×10^{-12}	1.220×10^{-12}	1.190×10^{-12}	1.190×10^{-12}	1.210×10^{-12}	1.230×10^{-12}	1.260×10^{-12}
2, 5/2 → 6, 17/2	1.980×10^{-12}	1.830×10^{-12}	1.780×10^{-12}	1.780×10^{-12}	1.810×10^{-12}	1.850×10^{-12}	1.900×10^{-12}
2, 7/2 → 6, 17/2	2.640×10^{-12}	2.440×10^{-12}	2.380×10^{-12}	2.380×10^{-12}	2.410×10^{-12}	2.470×10^{-12}	2.530×10^{-12}

Table A.4: continued.

Quantum Numbers	T						
J, $F \rightarrow J^{'}$,$F^{'}$	2 K	5 K	10 K	20 K	30 K	40 K	50 K
2, 1/2 → 6, 7/2	6.590×10^{-13}	6.100×10^{-13}	5.950×10^{-13}	5.950×10^{-13}	6.040×10^{-13}	6.170×10^{-13}	6.320×10^{-13}
2, 9/2 → 6, 7/2	3.290×10^{-12}	3.050×10^{-12}	2.970×10^{-12}	2.970×10^{-12}	3.020×10^{-12}	3.080×10^{-12}	3.160×10^{-12}
2, 3/2 → 6, 7/2	1.320×10^{-12}	1.220×10^{-12}	1.190×10^{-12}	1.190×10^{-12}	1.210×10^{-12}	1.230×10^{-12}	1.260×10^{-12}
2, 5/2 → 6, 7/2	1.980×10^{-12}	1.830×10^{-12}	1.780×10^{-12}	1.780×10^{-12}	1.810×10^{-12}	1.850×10^{-12}	1.900×10^{-12}
2, 7/2 → 6, 7/2	2.640×10^{-12}	2.440×10^{-12}	2.380×10^{-12}	2.380×10^{-12}	2.410×10^{-12}	2.470×10^{-12}	2.530×10^{-12}
2, 1/2 → 6, 15/2	6.590×10^{-13}	6.100×10^{-13}	5.950×10^{-13}	5.950×10^{-13}	6.040×10^{-13}	6.170×10^{-13}	6.320×10^{-13}
2, 9/2 → 6, 15/2	3.290×10^{-12}	3.050×10^{-12}	2.970×10^{-12}	2.970×10^{-12}	3.020×10^{-12}	3.080×10^{-12}	3.160×10^{-12}
2, 3/2 → 6, 15/2	1.320×10^{-12}	1.220×10^{-12}	1.190×10^{-12}	1.190×10^{-12}	1.210×10^{-12}	1.230×10^{-12}	1.260×10^{-12}
2, 5/2 → 6, 15/2	1.980×10^{-12}	1.830×10^{-12}	1.780×10^{-12}	1.780×10^{-12}	1.810×10^{-12}	1.850×10^{-12}	1.900×10^{-12}
2, 7/2 → 6, 15/2	2.640×10^{-12}	2.440×10^{-12}	2.380×10^{-12}	2.380×10^{-12}	2.410×10^{-12}	2.470×10^{-12}	2.530×10^{-12}
2, 1/2 → 6, 9/2	6.590×10^{-13}	6.100×10^{-13}	5.950×10^{-13}	5.950×10^{-13}	6.040×10^{-13}	6.170×10^{-13}	6.320×10^{-13}
2, 9/2 → 6, 9/2	3.290×10^{-12}	3.050×10^{-12}	2.970×10^{-12}	2.970×10^{-12}	3.020×10^{-12}	3.080×10^{-12}	3.160×10^{-12}
2, 3/2 → 6, 9/2	1.320×10^{-12}	1.220×10^{-12}	1.190×10^{-12}	1.190×10^{-12}	1.210×10^{-12}	1.230×10^{-12}	1.260×10^{-12}
2, 5/2 → 6, 9/2	1.980×10^{-12}	1.830×10^{-12}	1.780×10^{-12}	1.780×10^{-12}	1.810×10^{-12}	1.850×10^{-12}	1.900×10^{-12}
2, 7/2 → 6, 9/2	2.640×10^{-12}	2.440×10^{-12}	2.380×10^{-12}	2.380×10^{-12}	2.410×10^{-12}	2.470×10^{-12}	2.530×10^{-12}
2, 1/2 → 6, 11/2	6.590×10^{-13}	6.100×10^{-13}	5.950×10^{-13}	5.950×10^{-13}	6.040×10^{-13}	6.170×10^{-13}	6.320×10^{-13}
2, 9/2 → 6, 11/2	3.290×10^{-12}	3.050×10^{-12}	2.970×10^{-12}	2.970×10^{-12}	3.020×10^{-12}	3.080×10^{-12}	3.160×10^{-12}
2, 3/2 → 6, 11/2	1.320×10^{-12}	1.220×10^{-12}	1.190×10^{-12}	1.190×10^{-12}	1.210×10^{-12}	1.230×10^{-12}	1.260×10^{-12}
2, 5/2 → 6, 11/2	1.980×10^{-12}	1.830×10^{-12}	1.780×10^{-12}	1.780×10^{-12}	1.810×10^{-12}	1.850×10^{-12}	1.900×10^{-12}
2, 7/2 → 6, 11/2	2.640×10^{-12}	2.440×10^{-12}	2.380×10^{-12}	2.380×10^{-12}	2.410×10^{-12}	2.470×10^{-12}	2.530×10^{-12}
2, 1/2 → 6, 13/2	6.590×10^{-13}	6.100×10^{-13}	5.950×10^{-13}	5.950×10^{-13}	6.040×10^{-13}	6.170×10^{-13}	6.320×10^{-13}
2, 9/2 → 6, 13/2	3.290×10^{-12}	3.050×10^{-12}	2.970×10^{-12}	2.970×10^{-12}	3.020×10^{-12}	3.080×10^{-12}	3.160×10^{-12}
2, 3/2 → 6, 13/2	1.320×10^{-12}	1.220×10^{-12}	1.190×10^{-12}	1.190×10^{-12}	1.210×10^{-12}	1.230×10^{-12}	1.260×10^{-12}
2, 5/2 → 6, 13/2	1.980×10^{-12}	1.830×10^{-12}	1.780×10^{-12}	1.780×10^{-12}	1.810×10^{-12}	1.850×10^{-12}	1.900×10^{-12}
2, 7/2 → 6, 13/2	2.640×10^{-12}	2.440×10^{-12}	2.380×10^{-12}	2.380×10^{-12}	2.410×10^{-12}	2.470×10^{-12}	2.530×10^{-12}
3, 11/2 → 6, 17/2	4.130×10^{-12}	4.180×10^{-12}	4.770×10^{-12}	5.420×10^{-12}	5.780×10^{-12}	6.100×10^{-12}	6.420×10^{-12}
3, 1/2 → 6, 17/2	6.880×10^{-13}	6.960×10^{-13}	7.950×10^{-13}	9.040×10^{-13}	9.630×10^{-13}	1.020×10^{-12}	1.070×10^{-12}
3, 3/2 → 6, 17/2	1.380×10^{-12}	1.390×10^{-12}	1.590×10^{-12}	1.810×10^{-12}	1.930×10^{-12}	2.030×10^{-12}	2.140×10^{-12}
3, 5/2 → 6, 17/2	2.060×10^{-12}	2.090×10^{-12}	2.380×10^{-12}	2.710×10^{-12}	2.890×10^{-12}	3.050×10^{-12}	3.210×10^{-12}
3, 9/2 → 6, 17/2	3.440×10^{-12}	3.480×10^{-12}	3.970×10^{-12}	4.520×10^{-12}	4.820×10^{-12}	5.080×10^{-12}	5.350×10^{-12}
3, 7/2 → 6, 17/2	2.750×10^{-12}	2.780×10^{-12}	3.180×10^{-12}	3.620×10^{-12}	3.850×10^{-12}	4.060×10^{-12}	4.280×10^{-12}
3, 11/2 → 6, 7/2	4.130×10^{-12}	4.180×10^{-12}	4.770×10^{-12}	5.420×10^{-12}	5.780×10^{-12}	6.100×10^{-12}	6.420×10^{-12}
3, 1/2 → 6, 7/2	6.880×10^{-13}	6.960×10^{-13}	7.950×10^{-13}	9.040×10^{-13}	9.630×10^{-13}	1.020×10^{-12}	1.070×10^{-12}
3, 3/2 → 6, 7/2	1.380×10^{-12}	1.390×10^{-12}	1.590×10^{-12}	1.810×10^{-12}	1.930×10^{-12}	2.030×10^{-12}	2.140×10^{-12}
3, 5/2 → 6, 7/2	2.060×10^{-12}	2.090×10^{-12}	2.380×10^{-12}	2.710×10^{-12}	2.890×10^{-12}	3.050×10^{-12}	3.210×10^{-12}
3, 9/2 → 6, 7/2	3.440×10^{-12}	3.480×10^{-12}	3.970×10^{-12}	4.520×10^{-12}	4.820×10^{-12}	5.080×10^{-12}	5.350×10^{-12}
3, 7/2 → 6, 7/2	2.750×10^{-12}	2.780×10^{-12}	3.180×10^{-12}	3.620×10^{-12}	3.850×10^{-12}	4.060×10^{-12}	4.280×10^{-12}

Table A.4: continued.

Quantum Numbers	T						
J, $F \rightarrow J^{'}$,$F^{'}$	2 K	5 K	10 K	20 K	30 K	40 K	50 K
3, 11/2 → 6, 15/2	4.130×10^{-12}	4.180×10^{-12}	4.770×10^{-12}	5.420×10^{-12}	5.780×10^{-12}	6.100×10^{-12}	6.420×10^{-12}
3, 1/2 → 6, 15/2	6.880×10^{-13}	6.960×10^{-13}	7.950×10^{-13}	9.040×10^{-13}	9.630×10^{-13}	1.020×10^{-12}	1.070×10^{-12}
3, 3/2 → 6, 15/2	1.380×10^{-12}	1.390×10^{-12}	1.590×10^{-12}	1.810×10^{-12}	1.930×10^{-12}	2.030×10^{-12}	2.140×10^{-12}
3, 5/2 → 6, 15/2	2.060×10^{-12}	2.090×10^{-12}	2.380×10^{-12}	2.710×10^{-12}	2.890×10^{-12}	3.050×10^{-12}	3.210×10^{-12}
3, 9/2 → 6, 15/2	3.440×10^{-12}	3.480×10^{-12}	3.970×10^{-12}	4.520×10^{-12}	4.820×10^{-12}	5.080×10^{-12}	5.350×10^{-12}
3, 7/2 → 6, 15/2	2.750×10^{-12}	2.780×10^{-12}	3.180×10^{-12}	3.620×10^{-12}	3.850×10^{-12}	4.060×10^{-12}	4.280×10^{-12}
3, 11/2 → 6, 9/2	4.130×10^{-12}	4.180×10^{-12}	4.770×10^{-12}	5.420×10^{-12}	5.780×10^{-12}	6.100×10^{-12}	6.420×10^{-12}
3, 1/2 → 6, 9/2	6.880×10^{-13}	6.960×10^{-13}	7.950×10^{-13}	9.040×10^{-13}	9.630×10^{-13}	1.020×10^{-12}	1.070×10^{-12}
3, 3/2 → 6, 9/2	1.380×10^{-12}	1.390×10^{-12}	1.590×10^{-12}	1.810×10^{-12}	1.930×10^{-12}	2.030×10^{-12}	2.140×10^{-12}
3, 5/2 → 6, 9/2	2.060×10^{-12}	2.090×10^{-12}	2.380×10^{-12}	2.710×10^{-12}	2.890×10^{-12}	3.050×10^{-12}	3.210×10^{-12}
3, 9/2 → 6, 9/2	3.440×10^{-12}	3.480×10^{-12}	3.970×10^{-12}	4.520×10^{-12}	4.820×10^{-12}	5.080×10^{-12}	5.350×10^{-12}
3, 7/2 → 6, 9/2	2.750×10^{-12}	2.780×10^{-12}	3.180×10^{-12}	3.620×10^{-12}	3.850×10^{-12}	4.060×10^{-12}	4.280×10^{-12}
3, 11/2 → 6, 11/2	4.130×10^{-12}	4.180×10^{-12}	4.770×10^{-12}	5.420×10^{-12}	5.780×10^{-12}	6.100×10^{-12}	6.420×10^{-12}
3, 1/2 → 6, 11/2	6.880×10^{-13}	6.960×10^{-13}	7.950×10^{-13}	9.040×10^{-13}	9.630×10^{-13}	1.020×10^{-12}	1.070×10^{-12}
3, 3/2 → 6, 11/2	1.380×10^{-12}	1.390×10^{-12}	1.590×10^{-12}	1.810×10^{-12}	1.930×10^{-12}	2.030×10^{-12}	2.140×10^{-12}
3, 5/2 → 6, 11/2	2.060×10^{-12}	2.090×10^{-12}	2.380×10^{-12}	2.710×10^{-12}	2.890×10^{-12}	3.050×10^{-12}	3.210×10^{-12}
3, 9/2 → 6, 11/2	3.440×10^{-12}	3.480×10^{-12}	3.970×10^{-12}	4.520×10^{-12}	4.820×10^{-12}	5.080×10^{-12}	5.350×10^{-12}
3, 7/2 → 6, 11/2	2.750×10^{-12}	2.780×10^{-12}	3.180×10^{-12}	3.620×10^{-12}	3.850×10^{-12}	4.060×10^{-12}	4.280×10^{-12}
3, 11/2 → 6, 13/2	4.130×10^{-12}	4.180×10^{-12}	4.770×10^{-12}	5.420×10^{-12}	5.780×10^{-12}	6.100×10^{-12}	6.420×10^{-12}
3, 1/2 → 6, 13/2	6.880×10^{-13}	6.960×10^{-13}	7.950×10^{-13}	9.040×10^{-13}	9.630×10^{-13}	1.020×10^{-12}	1.070×10^{-12}
3, 3/2 → 6, 13/2	1.380×10^{-12}	1.390×10^{-12}	1.590×10^{-12}	1.810×10^{-12}	1.930×10^{-12}	2.030×10^{-12}	2.140×10^{-12}
3, 5/2 → 6, 13/2	2.060×10^{-12}	2.090×10^{-12}	2.380×10^{-12}	2.710×10^{-12}	2.890×10^{-12}	3.050×10^{-12}	3.210×10^{-12}
3, 9/2 → 6, 13/2	3.440×10^{-12}	3.480×10^{-12}	3.970×10^{-12}	4.520×10^{-12}	4.820×10^{-12}	5.080×10^{-12}	5.350×10^{-12}
3, 7/2 → 6, 13/2	2.750×10^{-12}	2.780×10^{-12}	3.180×10^{-12}	3.620×10^{-12}	3.850×10^{-12}	4.060×10^{-12}	4.280×10^{-12}
4, 13/2 → 6, 17/2	2.270×10^{-11}	2.230×10^{-11}	2.220×10^{-11}	2.110×10^{-11}	2.020×10^{-11}	1.940×10^{-11}	1.890×10^{-11}
4, 3/2 → 6, 17/2	6.470×10^{-12}	6.370×10^{-12}	6.330×10^{-12}	6.040×10^{-12}	5.760×10^{-12}	5.550×10^{-12}	5.390×10^{-12}
4, 5/2 → 6, 17/2	9.710×10^{-12}	9.550×10^{-12}	9.500×10^{-12}	9.060×10^{-12}	8.640×10^{-12}	8.320×10^{-12}	8.090×10^{-12}
4, 11/2 → 6, 17/2	1.940×10^{-11}	1.910×10^{-11}	1.900×10^{-11}	1.810×10^{-11}	1.730×10^{-11}	1.660×10^{-11}	1.620×10^{-11}
4, 7/2 → 6, 17/2	1.290×10^{-11}	1.270×10^{-11}	1.270×10^{-11}	1.210×10^{-11}	1.150×10^{-11}	1.110×10^{-11}	1.080×10^{-11}
4, 9/2 → 6, 17/2	1.620×10^{-11}	1.590×10^{-11}	1.580×10^{-11}	1.510×10^{-11}	1.440×10^{-11}	1.390×10^{-11}	1.350×10^{-11}
4, 13/2 → 6, 7/2	2.270×10^{-11}	2.230×10^{-11}	2.220×10^{-11}	2.110×10^{-11}	2.020×10^{-11}	1.940×10^{-11}	1.890×10^{-11}
4, 3/2 → 6, 7/2	6.470×10^{-12}	6.370×10^{-12}	6.330×10^{-12}	6.040×10^{-12}	5.760×10^{-12}	5.550×10^{-12}	5.390×10^{-12}
4, 5/2 → 6, 7/2	9.710×10^{-12}	9.550×10^{-12}	9.500×10^{-12}	9.060×10^{-12}	8.640×10^{-12}	8.320×10^{-12}	8.090×10^{-12}
4, 11/2 → 6, 7/2	1.940×10^{-11}	1.910×10^{-11}	1.900×10^{-11}	1.810×10^{-11}	1.730×10^{-11}	1.660×10^{-11}	1.620×10^{-11}
4, 7/2 → 6, 7/2	1.290×10^{-11}	1.270×10^{-11}	1.270×10^{-11}	1.210×10^{-11}	1.150×10^{-11}	1.110×10^{-11}	1.080×10^{-11}
4, 9/2 → 6, 7/2	1.620×10^{-11}	1.590×10^{-11}	1.580×10^{-11}	1.510×10^{-11}	1.440×10^{-11}	1.390×10^{-11}	1.350×10^{-11}
4, 13/2 → 6, 15/2	2.270×10^{-11}	2.230×10^{-11}	2.220×10^{-11}	2.110×10^{-11}	2.020×10^{-11}	1.940×10^{-11}	1.890×10^{-11}

Table A.4: continued.

Quantum Numbers	T						
J, $F \rightarrow J^{'}$,$F^{'}$	2 K	5 K	10 K	20 K	30 K	40 K	50 K
4, 3/2 → 6, 15/2	6.470×10^{-12}	6.370×10^{-12}	6.330×10^{-12}	6.040×10^{-12}	5.760×10^{-12}	5.550×10^{-12}	5.390×10^{-12}
4, 5/2 → 6, 15/2	9.710×10^{-12}	9.550×10^{-12}	9.500×10^{-12}	9.060×10^{-12}	8.640×10^{-12}	8.320×10^{-12}	8.090×10^{-12}
4, 11/2 → 6, 15/2	1.940×10^{-11}	1.910×10^{-11}	1.900×10^{-11}	1.810×10^{-11}	1.730×10^{-11}	1.660×10^{-11}	1.620×10^{-11}
4, 7/2 → 6, 15/2	1.290×10^{-11}	1.270×10^{-11}	1.270×10^{-11}	1.210×10^{-11}	1.150×10^{-11}	1.110×10^{-11}	1.080×10^{-11}
4, 9/2 → 6, 15/2	1.620×10^{-11}	1.590×10^{-11}	1.580×10^{-11}	1.510×10^{-11}	1.440×10^{-11}	1.390×10^{-11}	1.350×10^{-11}
4, 13/2 → 6, 9/2	2.270×10^{-11}	2.230×10^{-11}	2.220×10^{-11}	2.110×10^{-11}	2.020×10^{-11}	1.940×10^{-11}	1.890×10^{-11}
4, 3/2 → 6, 9/2	6.470×10^{-12}	6.370×10^{-12}	6.330×10^{-12}	6.040×10^{-12}	5.760×10^{-12}	5.550×10^{-12}	5.390×10^{-12}
4, 5/2 → 6, 9/2	9.710×10^{-12}	9.550×10^{-12}	9.500×10^{-12}	9.060×10^{-12}	8.640×10^{-12}	8.320×10^{-12}	8.090×10^{-12}
4, 11/2 → 6, 9/2	1.940×10^{-11}	1.910×10^{-11}	1.900×10^{-11}	1.810×10^{-11}	1.730×10^{-11}	1.660×10^{-11}	1.620×10^{-11}
4, 7/2 → 6, 9/2	1.290×10^{-11}	1.270×10^{-11}	1.270×10^{-11}	1.210×10^{-11}	1.150×10^{-11}	1.110×10^{-11}	1.080×10^{-11}
4, 9/2 → 6, 9/2	1.620×10^{-11}	1.590×10^{-11}	1.580×10^{-11}	1.510×10^{-11}	1.440×10^{-11}	1.390×10^{-11}	1.350×10^{-11}
4, 13/2 → 6, 11/2	2.270×10^{-11}	2.230×10^{-11}	2.220×10^{-11}	2.110×10^{-11}	2.020×10^{-11}	1.940×10^{-11}	1.890×10^{-11}
4, 3/2 → 6, 11/2	6.470×10^{-12}	6.370×10^{-12}	6.330×10^{-12}	6.040×10^{-12}	5.760×10^{-12}	5.550×10^{-12}	5.390×10^{-12}
4, 5/2 → 6, 11/2	9.710×10^{-12}	9.550×10^{-12}	9.500×10^{-12}	9.060×10^{-12}	8.640×10^{-12}	8.320×10^{-12}	8.090×10^{-12}
4, 11/2 → 6, 11/2	1.940×10^{-11}	1.910×10^{-11}	1.900×10^{-11}	1.810×10^{-11}	1.730×10^{-11}	1.660×10^{-11}	1.620×10^{-11}
4, 7/2 → 6, 11/2	1.290×10^{-11}	1.270×10^{-11}	1.270×10^{-11}	1.210×10^{-11}	1.150×10^{-11}	1.110×10^{-11}	1.080×10^{-11}
4, 9/2 → 6, 11/2	1.620×10^{-11}	1.590×10^{-11}	1.580×10^{-11}	1.510×10^{-11}	1.440×10^{-11}	1.390×10^{-11}	1.350×10^{-11}
4, 13/2 → 6, 13/2	2.270×10^{-11}	2.230×10^{-11}	2.220×10^{-11}	2.110×10^{-11}	2.020×10^{-11}	1.940×10^{-11}	1.890×10^{-11}
4, 3/2 → 6, 13/2	6.470×10^{-12}	6.370×10^{-12}	6.330×10^{-12}	6.040×10^{-12}	5.760×10^{-12}	5.550×10^{-12}	5.390×10^{-12}
4, 5/2 → 6, 13/2	9.710×10^{-12}	9.550×10^{-12}	9.500×10^{-12}	9.060×10^{-12}	8.640×10^{-12}	8.320×10^{-12}	8.090×10^{-12}
4, 11/2 → 6, 13/2	1.940×10^{-11}	1.910×10^{-11}	1.900×10^{-11}	1.810×10^{-11}	1.730×10^{-11}	1.660×10^{-11}	1.620×10^{-11}
4, 7/2 → 6, 13/2	1.290×10^{-11}	1.270×10^{-11}	1.270×10^{-11}	1.210×10^{-11}	1.150×10^{-11}	1.110×10^{-11}	1.080×10^{-11}
4, 9/2 → 6, 13/2	1.620×10^{-11}	1.590×10^{-11}	1.580×10^{-11}	1.510×10^{-11}	1.440×10^{-11}	1.390×10^{-11}	1.350×10^{-11}
5, 15/2 → 6, 17/2	6.590×10^{-12}	9.620×10^{-12}	1.410×10^{-11}	1.670×10^{-11}	1.710×10^{-11}	1.720×10^{-11}	1.730×10^{-11}
5, 5/2 → 6, 17/2	2.470×10^{-12}	3.610×10^{-12}	5.270×10^{-12}	6.260×10^{-12}	6.420×10^{-12}	6.450×10^{-12}	6.480×10^{-12}
5, 7/2 → 6, 17/2	3.290×10^{-12}	4.810×10^{-12}	7.030×10^{-12}	8.350×10^{-12}	8.560×10^{-12}	8.600×10^{-12}	8.640×10^{-12}
5, 13/2 → 6, 17/2	5.760×10^{-12}	8.420×10^{-12}	1.230×10^{-11}	1.460×10^{-11}	1.500×10^{-11}	1.510×10^{-11}	1.510×10^{-11}
5, 9/2 → 6, 17/2	4.120×10^{-12}	6.010×10^{-12}	8.790×10^{-12}	1.040×10^{-11}	1.070×10^{-11}	1.080×10^{-11}	1.080×10^{-11}
5, 11/2 → 6, 17/2	4.940×10^{-12}	7.220×10^{-12}	1.050×10^{-11}	1.250×10^{-11}	1.280×10^{-11}	1.290×10^{-11}	1.300×10^{-11}
5, 15/2 → 6, 7/2	6.590×10^{-12}	9.620×10^{-12}	1.410×10^{-11}	1.670×10^{-11}	1.710×10^{-11}	1.720×10^{-11}	1.730×10^{-11}
5, 5/2 → 6, 7/2	2.470×10^{-12}	3.610×10^{-12}	5.270×10^{-12}	6.260×10^{-12}	6.420×10^{-12}	6.450×10^{-12}	6.480×10^{-12}
5, 7/2 → 6, 7/2	3.290×10^{-12}	4.810×10^{-12}	7.030×10^{-12}	8.350×10^{-12}	8.560×10^{-12}	8.600×10^{-12}	8.640×10^{-12}
5, 13/2 → 6, 7/2	5.760×10^{-12}	8.420×10^{-12}	1.230×10^{-11}	1.460×10^{-11}	1.500×10^{-11}	1.510×10^{-11}	1.510×10^{-11}
5, 9/2 → 6, 7/2	4.120×10^{-12}	6.010×10^{-12}	8.790×10^{-12}	1.040×10^{-11}	1.070×10^{-11}	1.080×10^{-11}	1.080×10^{-11}
5, 11/2 → 6, 7/2	4.940×10^{-12}	7.220×10^{-12}	1.050×10^{-11}	1.250×10^{-11}	1.280×10^{-11}	1.290×10^{-11}	1.300×10^{-11}
5, 15/2 → 6, 15/2	6.590×10^{-12}	9.620×10^{-12}	1.410×10^{-11}	1.670×10^{-11}	1.710×10^{-11}	1.720×10^{-11}	1.730×10^{-11}
5, 5/2 → 6, 15/2	2.470×10^{-12}	3.610×10^{-12}	5.270×10^{-12}	6.260×10^{-12}	6.420×10^{-12}	6.450×10^{-12}	6.480×10^{-12}

Table A.4: continued.

Quantum Numbers	T						
J, $F \rightarrow J^{'}$,$F^{'}$	2 K	5 K	10 K	20 K	30 K	40 K	50 K
5, 7/2 → 6, 15/2	3.290×10^{-12}	4.810×10^{-12}	7.030×10^{-12}	8.350×10^{-12}	8.560×10^{-12}	8.600×10^{-12}	8.640×10^{-12}
5, 13/2 → 6, 15/2	5.760×10^{-12}	8.420×10^{-12}	1.230×10^{-11}	1.460×10^{-11}	1.500×10^{-11}	1.510×10^{-11}	1.510×10^{-11}
5, 9/2 → 6, 15/2	4.120×10^{-12}	6.010×10^{-12}	8.790×10^{-12}	1.040×10^{-11}	1.070×10^{-11}	1.080×10^{-11}	1.080×10^{-11}
5, 11/2 → 6, 15/2	4.940×10^{-12}	7.220×10^{-12}	1.050×10^{-11}	1.250×10^{-11}	1.280×10^{-11}	1.290×10^{-11}	1.300×10^{-11}
5, 15/2 → 6, 9/2	6.590×10^{-12}	9.620×10^{-12}	1.410×10^{-11}	1.670×10^{-11}	1.710×10^{-11}	1.720×10^{-11}	1.730×10^{-11}
5, 5/2 → 6, 9/2	2.470×10^{-12}	3.610×10^{-12}	5.270×10^{-12}	6.260×10^{-12}	6.420×10^{-12}	6.450×10^{-12}	6.480×10^{-12}
5, 7/2 → 6, 9/2	3.290×10^{-12}	4.810×10^{-12}	7.030×10^{-12}	8.350×10^{-12}	8.560×10^{-12}	8.600×10^{-12}	8.640×10^{-12}
5, 13/2 → 6, 9/2	5.760×10^{-12}	8.420×10^{-12}	1.230×10^{-11}	1.460×10^{-11}	1.500×10^{-11}	1.510×10^{-11}	1.510×10^{-11}
5, 9/2 → 6, 9/2	4.120×10^{-12}	6.010×10^{-12}	8.790×10^{-12}	1.040×10^{-11}	1.070×10^{-11}	1.080×10^{-11}	1.080×10^{-11}
5, 11/2 → 6, 9/2	4.940×10^{-12}	7.220×10^{-12}	1.050×10^{-11}	1.250×10^{-11}	1.280×10^{-11}	1.290×10^{-11}	1.300×10^{-11}
5, 15/2 → 6, 11/2	6.590×10^{-12}	9.620×10^{-12}	1.410×10^{-11}	1.670×10^{-11}	1.710×10^{-11}	1.720×10^{-11}	1.730×10^{-11}
5, 5/2 → 6, 11/2	2.470×10^{-12}	3.610×10^{-12}	5.270×10^{-12}	6.260×10^{-12}	6.420×10^{-12}	6.450×10^{-12}	6.480×10^{-12}
5, 7/2 → 6, 11/2	3.290×10^{-12}	4.810×10^{-12}	7.030×10^{-12}	8.350×10^{-12}	8.560×10^{-12}	8.600×10^{-12}	8.640×10^{-12}
5, 13/2 → 6, 11/2	5.760×10^{-12}	8.420×10^{-12}	1.230×10^{-11}	1.460×10^{-11}	1.500×10^{-11}	1.510×10^{-11}	1.510×10^{-11}
5, 9/2 → 6, 11/2	4.120×10^{-12}	6.010×10^{-12}	8.790×10^{-12}	1.040×10^{-11}	1.070×10^{-11}	1.080×10^{-11}	1.080×10^{-11}
5, 11/2 → 6, 11/2	4.940×10^{-12}	7.220×10^{-12}	1.050×10^{-11}	1.250×10^{-11}	1.280×10^{-11}	1.290×10^{-11}	1.300×10^{-11}
5, 15/2 → 6, 13/2	6.590×10^{-12}	9.620×10^{-12}	1.410×10^{-11}	1.670×10^{-11}	1.710×10^{-11}	1.720×10^{-11}	1.730×10^{-11}
5, 5/2 → 6, 13/2	2.470×10^{-12}	3.610×10^{-12}	5.270×10^{-12}	6.260×10^{-12}	6.420×10^{-12}	6.450×10^{-12}	6.480×10^{-12}
5, 7/2 → 6, 13/2	3.290×10^{-12}	4.810×10^{-12}	7.030×10^{-12}	8.350×10^{-12}	8.560×10^{-12}	8.600×10^{-12}	8.640×10^{-12}
5, 13/2 → 6, 13/2	5.760×10^{-12}	8.420×10^{-12}	1.230×10^{-11}	1.460×10^{-11}	1.500×10^{-11}	1.510×10^{-11}	1.510×10^{-11}
5, 9/2 → 6, 13/2	4.120×10^{-12}	6.010×10^{-12}	8.790×10^{-12}	1.040×10^{-11}	1.070×10^{-11}	1.080×10^{-11}	1.080×10^{-11}
5, 11/2 → 6, 13/2	4.940×10^{-12}	7.220×10^{-12}	1.050×10^{-11}	1.250×10^{-11}	1.280×10^{-11}	1.290×10^{-11}	1.300×10^{-11}
0, 5/2 → 7, 19/2	2.330×10^{-13}	2.270×10^{-13}	2.370×10^{-13}	2.700×10^{-13}	3.150×10^{-13}	3.700×10^{-13}	4.360×10^{-13}
0, 5/2 → 7, 9/2	2.330×10^{-13}	2.270×10^{-13}	2.370×10^{-13}	2.700×10^{-13}	3.150×10^{-13}	3.700×10^{-13}	4.360×10^{-13}
0, 5/2 → 7, 17/2	2.330×10^{-13}	2.270×10^{-13}	2.370×10^{-13}	2.700×10^{-13}	3.150×10^{-13}	3.700×10^{-13}	4.360×10^{-13}
0, 5/2 → 7, 11/2	2.330×10^{-13}	2.270×10^{-13}	2.370×10^{-13}	2.700×10^{-13}	3.150×10^{-13}	3.700×10^{-13}	4.360×10^{-13}
0, 5/2 → 7, 15/2	2.330×10^{-13}	2.270×10^{-13}	2.370×10^{-13}	2.700×10^{-13}	3.150×10^{-13}	3.700×10^{-13}	4.360×10^{-13}
0, 5/2 → 7, 13/2	2.330×10^{-13}	2.270×10^{-13}	2.370×10^{-13}	2.700×10^{-13}	3.150×10^{-13}	3.700×10^{-13}	4.360×10^{-13}
1, 3/2 → 7, 19/2	2.530×10^{-13}	2.400×10^{-13}	2.390×10^{-13}	2.540×10^{-13}	2.770×10^{-13}	3.050×10^{-13}	3.360×10^{-13}
1, 7/2 → 7, 19/2	5.060×10^{-13}	4.790×10^{-13}	4.790×10^{-13}	5.080×10^{-13}	5.540×10^{-13}	6.100×10^{-13}	6.720×10^{-13}
1, 5/2 → 7, 19/2	3.800×10^{-13}	3.590×10^{-13}	3.590×10^{-13}	3.810×10^{-13}	4.160×10^{-13}	4.570×10^{-13}	5.040×10^{-13}
1, 3/2 → 7, 9/2	2.530×10^{-13}	2.400×10^{-13}	2.390×10^{-13}	2.540×10^{-13}	2.770×10^{-13}	3.050×10^{-13}	3.360×10^{-13}
1, 7/2 → 7, 9/2	5.060×10^{-13}	4.790×10^{-13}	4.790×10^{-13}	5.080×10^{-13}	5.540×10^{-13}	6.100×10^{-13}	6.720×10^{-13}
1, 5/2 → 7, 9/2	3.800×10^{-13}	3.590×10^{-13}	3.590×10^{-13}	3.810×10^{-13}	4.160×10^{-13}	4.570×10^{-13}	5.040×10^{-13}
1, 3/2 → 7, 17/2	2.530×10^{-13}	2.400×10^{-13}	2.390×10^{-13}	2.540×10^{-13}	2.770×10^{-13}	3.050×10^{-13}	3.360×10^{-13}
1, 7/2 → 7, 17/2	5.060×10^{-13}	4.790×10^{-13}	4.790×10^{-13}	5.080×10^{-13}	5.540×10^{-13}	6.100×10^{-13}	6.720×10^{-13}
1, 5/2 → 7, 17/2	3.800×10^{-13}	3.590×10^{-13}	3.590×10^{-13}	3.810×10^{-13}	4.160×10^{-13}	4.570×10^{-13}	5.040×10^{-13}

Table A.4: continued.

Quantum Numbers	T						
J, $F \rightarrow J^{'}$,$F^{'}$	2 K	5 K	10 K	20 K	30 K	40 K	50 K
1, 3/2 → 7, 11/2	2.530×10^{-13}	2.400×10^{-13}	2.390×10^{-13}	2.540×10^{-13}	2.770×10^{-13}	3.050×10^{-13}	3.360×10^{-13}
1, 7/2 → 7, 11/2	5.060×10^{-13}	4.790×10^{-13}	4.790×10^{-13}	5.080×10^{-13}	5.540×10^{-13}	6.100×10^{-13}	6.720×10^{-13}
1, 5/2 → 7, 11/2	3.800×10^{-13}	3.590×10^{-13}	3.590×10^{-13}	3.810×10^{-13}	4.160×10^{-13}	4.570×10^{-13}	5.040×10^{-13}
1, 3/2 → 7, 15/2	2.530×10^{-13}	2.400×10^{-13}	2.390×10^{-13}	2.540×10^{-13}	2.770×10^{-13}	3.050×10^{-13}	3.360×10^{-13}
1, 7/2 → 7, 15/2	5.060×10^{-13}	4.790×10^{-13}	4.790×10^{-13}	5.080×10^{-13}	5.540×10^{-13}	6.100×10^{-13}	6.720×10^{-13}
1, 5/2 → 7, 15/2	3.800×10^{-13}	3.590×10^{-13}	3.590×10^{-13}	3.810×10^{-13}	4.160×10^{-13}	4.570×10^{-13}	5.040×10^{-13}
1, 3/2 → 7, 13/2	2.530×10^{-13}	2.400×10^{-13}	2.390×10^{-13}	2.540×10^{-13}	2.770×10^{-13}	3.050×10^{-13}	3.360×10^{-13}
1, 7/2 → 7, 13/2	5.060×10^{-13}	4.790×10^{-13}	4.790×10^{-13}	5.080×10^{-13}	5.540×10^{-13}	6.100×10^{-13}	6.720×10^{-13}
1, 5/2 → 7, 13/2	3.800×10^{-13}	3.590×10^{-13}	3.590×10^{-13}	3.810×10^{-13}	4.160×10^{-13}	4.570×10^{-13}	5.040×10^{-13}
2, 1/2 → 7, 19/2	2.420×10^{-13}	2.330×10^{-13}	2.400×10^{-13}	2.640×10^{-13}	2.910×10^{-13}	3.200×10^{-13}	3.530×10^{-13}
2, 9/2 → 7, 19/2	1.210×10^{-12}	1.160×10^{-12}	1.200×10^{-12}	1.320×10^{-12}	1.450×10^{-12}	1.600×10^{-12}	1.770×10^{-12}
2, 3/2 → 7, 19/2	4.830×10^{-13}	4.650×10^{-13}	4.810×10^{-13}	5.280×10^{-13}	5.810×10^{-13}	6.410×10^{-13}	7.060×10^{-13}
2, 5/2 → 7, 19/2	7.250×10^{-13}	6.980×10^{-13}	7.210×10^{-13}	7.930×10^{-13}	8.720×10^{-13}	9.610×10^{-13}	1.060×10^{-12}
2, 7/2 → 7, 19/2	9.660×10^{-13}	9.310×10^{-13}	9.610×10^{-13}	1.060×10^{-12}	1.160×10^{-12}	1.280×10^{-12}	1.410×10^{-12}
2, 1/2 → 7, 9/2	2.420×10^{-13}	2.330×10^{-13}	2.400×10^{-13}	2.640×10^{-13}	2.910×10^{-13}	3.200×10^{-13}	3.530×10^{-13}
2, 9/2 → 7, 9/2	1.210×10^{-12}	1.160×10^{-12}	1.200×10^{-12}	1.320×10^{-12}	1.450×10^{-12}	1.600×10^{-12}	1.770×10^{-12}
2, 3/2 → 7, 9/2	4.830×10^{-13}	4.650×10^{-13}	4.810×10^{-13}	5.280×10^{-13}	5.810×10^{-13}	6.410×10^{-13}	7.060×10^{-13}
2, 5/2 → 7, 9/2	7.250×10^{-13}	6.980×10^{-13}	7.210×10^{-13}	7.930×10^{-13}	8.720×10^{-13}	9.610×10^{-13}	1.060×10^{-12}
2, 7/2 → 7, 9/2	9.660×10^{-13}	9.310×10^{-13}	9.610×10^{-13}	1.060×10^{-12}	1.160×10^{-12}	1.280×10^{-12}	1.410×10^{-12}
2, 1/2 → 7, 17/2	2.420×10^{-13}	2.330×10^{-13}	2.400×10^{-13}	2.640×10^{-13}	2.910×10^{-13}	3.200×10^{-13}	3.530×10^{-13}
2, 9/2 → 7, 17/2	1.210×10^{-12}	1.160×10^{-12}	1.200×10^{-12}	1.320×10^{-12}	1.450×10^{-12}	1.600×10^{-12}	1.770×10^{-12}
2, 3/2 → 7, 17/2	4.830×10^{-13}	4.650×10^{-13}	4.810×10^{-13}	5.280×10^{-13}	5.810×10^{-13}	6.410×10^{-13}	7.060×10^{-13}
2, 5/2 → 7, 17/2	7.250×10^{-13}	6.980×10^{-13}	7.210×10^{-13}	7.930×10^{-13}	8.720×10^{-13}	9.610×10^{-13}	1.060×10^{-12}
2, 7/2 → 7, 17/2	9.660×10^{-13}	9.310×10^{-13}	9.610×10^{-13}	1.060×10^{-12}	1.160×10^{-12}	1.280×10^{-12}	1.410×10^{-12}
2, 1/2 → 7, 11/2	2.420×10^{-13}	2.330×10^{-13}	2.400×10^{-13}	2.640×10^{-13}	2.910×10^{-13}	3.200×10^{-13}	3.530×10^{-13}
2, 9/2 → 7, 11/2	1.210×10^{-12}	1.160×10^{-12}	1.200×10^{-12}	1.320×10^{-12}	1.450×10^{-12}	1.600×10^{-12}	1.770×10^{-12}
2, 3/2 → 7, 11/2	4.830×10^{-13}	4.650×10^{-13}	4.810×10^{-13}	5.280×10^{-13}	5.810×10^{-13}	6.410×10^{-13}	7.060×10^{-13}
2, 5/2 → 7, 11/2	7.250×10^{-13}	6.980×10^{-13}	7.210×10^{-13}	7.930×10^{-13}	8.720×10^{-13}	9.610×10^{-13}	1.060×10^{-12}
2, 7/2 → 7, 11/2	9.660×10^{-13}	9.310×10^{-13}	9.610×10^{-13}	1.060×10^{-12}	1.160×10^{-12}	1.280×10^{-12}	1.410×10^{-12}
2, 1/2 → 7, 15/2	2.420×10^{-13}	2.330×10^{-13}	2.400×10^{-13}	2.640×10^{-13}	2.910×10^{-13}	3.200×10^{-13}	3.530×10^{-13}
2, 9/2 → 7, 15/2	1.210×10^{-12}	1.160×10^{-12}	1.200×10^{-12}	1.320×10^{-12}	1.450×10^{-12}	1.600×10^{-12}	1.770×10^{-12}
2, 3/2 → 7, 15/2	4.830×10^{-13}	4.650×10^{-13}	4.810×10^{-13}	5.280×10^{-13}	5.810×10^{-13}	6.410×10^{-13}	7.060×10^{-13}
2, 5/2 → 7, 15/2	7.250×10^{-13}	6.980×10^{-13}	7.210×10^{-13}	7.930×10^{-13}	8.720×10^{-13}	9.610×10^{-13}	1.060×10^{-12}
2, 7/2 → 7, 15/2	9.660×10^{-13}	9.310×10^{-13}	9.610×10^{-13}	1.060×10^{-12}	1.160×10^{-12}	1.280×10^{-12}	1.410×10^{-12}
2, 1/2 → 7, 13/2	2.420×10^{-13}	2.330×10^{-13}	2.400×10^{-13}	2.640×10^{-13}	2.910×10^{-13}	3.200×10^{-13}	3.530×10^{-13}
2, 9/2 → 7, 13/2	1.210×10^{-12}	1.160×10^{-12}	1.200×10^{-12}	1.320×10^{-12}	1.450×10^{-12}	1.600×10^{-12}	1.770×10^{-12}
2, 3/2 → 7, 13/2	4.830×10^{-13}	4.650×10^{-13}	4.810×10^{-13}	5.280×10^{-13}	5.810×10^{-13}	6.410×10^{-13}	7.060×10^{-13}

Table A.4: continued.

Quantum Numbers	T						
J, $F \rightarrow J^{'}$,$F^{'}$	2 K	5 K	10 K	20 K	30 K	40 K	50 K
2, 5/2 → 7, 13/2	7.250×10^{-13}	6.980×10^{-13}	7.210×10^{-13}	7.930×10^{-13}	8.720×10^{-13}	9.610×10^{-13}	1.060×10^{-12}
2, 7/2 → 7, 13/2	9.660×10^{-13}	9.310×10^{-13}	9.610×10^{-13}	1.060×10^{-12}	1.160×10^{-12}	1.280×10^{-12}	1.410×10^{-12}
3, 11/2 → 7, 19/2	3.460×10^{-12}	3.300×10^{-12}	3.250×10^{-12}	3.190×10^{-12}	3.180×10^{-12}	3.210×10^{-12}	3.240×10^{-12}
3, 1/2 → 7, 19/2	5.760×10^{-13}	5.500×10^{-13}	5.410×10^{-13}	5.320×10^{-13}	5.300×10^{-13}	5.340×10^{-13}	5.400×10^{-13}
3, 3/2 → 7, 19/2	1.150×10^{-12}	1.100×10^{-12}	1.080×10^{-12}	1.060×10^{-12}	1.060×10^{-12}	1.070×10^{-12}	1.080×10^{-12}
3, 5/2 → 7, 19/2	1.730×10^{-12}	1.650×10^{-12}	1.620×10^{-12}	1.600×10^{-12}	1.590×10^{-12}	1.600×10^{-12}	1.620×10^{-12}
3, 9/2 → 7, 19/2	2.880×10^{-12}	2.750×10^{-12}	2.710×10^{-12}	2.660×10^{-12}	2.650×10^{-12}	2.670×10^{-12}	2.700×10^{-12}
3, 7/2 → 7, 19/2	2.300×10^{-12}	2.200×10^{-12}	2.170×10^{-12}	2.130×10^{-12}	2.120×10^{-12}	2.140×10^{-12}	2.160×10^{-12}
3, 11/2 → 7, 9/2	3.460×10^{-12}	3.300×10^{-12}	3.250×10^{-12}	3.190×10^{-12}	3.180×10^{-12}	3.210×10^{-12}	3.240×10^{-12}
3, 1/2 → 7, 9/2	5.760×10^{-13}	5.500×10^{-13}	5.410×10^{-13}	5.320×10^{-13}	5.300×10^{-13}	5.340×10^{-13}	5.400×10^{-13}
3, 3/2 → 7, 9/2	1.150×10^{-12}	1.100×10^{-12}	1.080×10^{-12}	1.060×10^{-12}	1.060×10^{-12}	1.070×10^{-12}	1.080×10^{-12}
3, 5/2 → 7, 9/2	1.730×10^{-12}	1.650×10^{-12}	1.620×10^{-12}	1.600×10^{-12}	1.590×10^{-12}	1.600×10^{-12}	1.620×10^{-12}
3, 9/2 → 7, 9/2	2.880×10^{-12}	2.750×10^{-12}	2.710×10^{-12}	2.660×10^{-12}	2.650×10^{-12}	2.670×10^{-12}	2.700×10^{-12}
3, 7/2 → 7, 9/2	2.300×10^{-12}	2.200×10^{-12}	2.170×10^{-12}	2.130×10^{-12}	2.120×10^{-12}	2.140×10^{-12}	2.160×10^{-12}
3, 11/2 → 7, 17/2	3.460×10^{-12}	3.300×10^{-12}	3.250×10^{-12}	3.190×10^{-12}	3.180×10^{-12}	3.210×10^{-12}	3.240×10^{-12}
3, 1/2 → 7, 17/2	5.760×10^{-13}	5.500×10^{-13}	5.410×10^{-13}	5.320×10^{-13}	5.300×10^{-13}	5.340×10^{-13}	5.400×10^{-13}
3, 3/2 → 7, 17/2	1.150×10^{-12}	1.100×10^{-12}	1.080×10^{-12}	1.060×10^{-12}	1.060×10^{-12}	1.070×10^{-12}	1.080×10^{-12}
3, 5/2 → 7, 17/2	1.730×10^{-12}	1.650×10^{-12}	1.620×10^{-12}	1.600×10^{-12}	1.590×10^{-12}	1.600×10^{-12}	1.620×10^{-12}
3, 9/2 → 7, 17/2	2.880×10^{-12}	2.750×10^{-12}	2.710×10^{-12}	2.660×10^{-12}	2.650×10^{-12}	2.670×10^{-12}	2.700×10^{-12}
3, 7/2 → 7, 17/2	2.300×10^{-12}	2.200×10^{-12}	2.170×10^{-12}	2.130×10^{-12}	2.120×10^{-12}	2.140×10^{-12}	2.160×10^{-12}
3, 11/2 → 7, 11/2	3.460×10^{-12}	3.300×10^{-12}	3.250×10^{-12}	3.190×10^{-12}	3.180×10^{-12}	3.210×10^{-12}	3.240×10^{-12}
3, 1/2 → 7, 11/2	5.760×10^{-13}	5.500×10^{-13}	5.410×10^{-13}	5.320×10^{-13}	5.300×10^{-13}	5.340×10^{-13}	5.400×10^{-13}
3, 3/2 → 7, 11/2	1.150×10^{-12}	1.100×10^{-12}	1.080×10^{-12}	1.060×10^{-12}	1.060×10^{-12}	1.070×10^{-12}	1.080×10^{-12}
3, 5/2 → 7, 11/2	1.730×10^{-12}	1.650×10^{-12}	1.620×10^{-12}	1.600×10^{-12}	1.590×10^{-12}	1.600×10^{-12}	1.620×10^{-12}
3, 9/2 → 7, 11/2	2.880×10^{-12}	2.750×10^{-12}	2.710×10^{-12}	2.660×10^{-12}	2.650×10^{-12}	2.670×10^{-12}	2.700×10^{-12}
3, 7/2 → 7, 11/2	2.300×10^{-12}	2.200×10^{-12}	2.170×10^{-12}	2.130×10^{-12}	2.120×10^{-12}	2.140×10^{-12}	2.160×10^{-12}
3, 11/2 → 7, 15/2	3.460×10^{-12}	3.300×10^{-12}	3.250×10^{-12}	3.190×10^{-12}	3.180×10^{-12}	3.210×10^{-12}	3.240×10^{-12}
3, 1/2 → 7, 15/2	5.760×10^{-13}	5.500×10^{-13}	5.410×10^{-13}	5.320×10^{-13}	5.300×10^{-13}	5.340×10^{-13}	5.400×10^{-13}
3, 3/2 → 7, 15/2	1.150×10^{-12}	1.100×10^{-12}	1.080×10^{-12}	1.060×10^{-12}	1.060×10^{-12}	1.070×10^{-12}	1.080×10^{-12}
3, 5/2 → 7, 15/2	1.730×10^{-12}	1.650×10^{-12}	1.620×10^{-12}	1.600×10^{-12}	1.590×10^{-12}	1.600×10^{-12}	1.620×10^{-12}
3, 9/2 → 7, 15/2	2.880×10^{-12}	2.750×10^{-12}	2.710×10^{-12}	2.660×10^{-12}	2.650×10^{-12}	2.670×10^{-12}	2.700×10^{-12}
3, 7/2 → 7, 15/2	2.300×10^{-12}	2.200×10^{-12}	2.170×10^{-12}	2.130×10^{-12}	2.120×10^{-12}	2.140×10^{-12}	2.160×10^{-12}
3, 11/2 → 7, 13/2	3.460×10^{-12}	3.300×10^{-12}	3.250×10^{-12}	3.190×10^{-12}	3.180×10^{-12}	3.210×10^{-12}	3.240×10^{-12}
3, 1/2 → 7, 13/2	5.760×10^{-13}	5.500×10^{-13}	5.410×10^{-13}	5.320×10^{-13}	5.300×10^{-13}	5.340×10^{-13}	5.400×10^{-13}
3, 3/2 → 7, 13/2	1.150×10^{-12}	1.100×10^{-12}	1.080×10^{-12}	1.060×10^{-12}	1.060×10^{-12}	1.070×10^{-12}	1.080×10^{-12}
3, 5/2 → 7, 13/2	1.730×10^{-12}	1.650×10^{-12}	1.620×10^{-12}	1.600×10^{-12}	1.590×10^{-12}	1.600×10^{-12}	1.620×10^{-12}
3, 9/2 → 7, 13/2	2.880×10^{-12}	2.750×10^{-12}	2.710×10^{-12}	2.660×10^{-12}	2.650×10^{-12}	2.670×10^{-12}	2.700×10^{-12}

Table A.4: continued.

Quantum Numbers	T						
J, $F \rightarrow J^{'}$,$F^{'}$	2 K	5 K	10 K	20 K	30 K	40 K	50 K
3, 7/2 → 7, 13/2	2.300×10^{-12}	2.200×10^{-12}	2.170×10^{-12}	2.130×10^{-12}	2.120×10^{-12}	2.140×10^{-12}	2.160×10^{-12}
4, 13/2 → 7, 19/2	5.420×10^{-12}	5.330×10^{-12}	5.670×10^{-12}	6.180×10^{-12}	6.490×10^{-12}	6.760×10^{-12}	7.030×10^{-12}
4, 3/2 → 7, 19/2	1.550×10^{-12}	1.520×10^{-12}	1.620×10^{-12}	1.770×10^{-12}	1.850×10^{-12}	1.930×10^{-12}	2.010×10^{-12}
4, 5/2 → 7, 19/2	2.320×10^{-12}	2.290×10^{-12}	2.430×10^{-12}	2.650×10^{-12}	2.780×10^{-12}	2.900×10^{-12}	3.010×10^{-12}
4, 11/2 → 7, 19/2	4.650×10^{-12}	4.570×10^{-12}	4.860×10^{-12}	5.300×10^{-12}	5.560×10^{-12}	5.800×10^{-12}	6.020×10^{-12}
4, 7/2 → 7, 19/2	3.100×10^{-12}	3.050×10^{-12}	3.240×10^{-12}	3.530×10^{-12}	3.710×10^{-12}	3.870×10^{-12}	4.020×10^{-12}
4, 9/2 → 7, 19/2	3.870×10^{-12}	3.810×10^{-12}	4.050×10^{-12}	4.410×10^{-12}	4.640×10^{-12}	4.830×10^{-12}	5.020×10^{-12}
4, 13/2 → 7, 9/2	5.420×10^{-12}	5.330×10^{-12}	5.670×10^{-12}	6.180×10^{-12}	6.490×10^{-12}	6.760×10^{-12}	7.030×10^{-12}
4, 3/2 → 7, 9/2	1.550×10^{-12}	1.520×10^{-12}	1.620×10^{-12}	1.770×10^{-12}	1.850×10^{-12}	1.930×10^{-12}	2.010×10^{-12}
4, 5/2 → 7, 9/2	2.320×10^{-12}	2.290×10^{-12}	2.430×10^{-12}	2.650×10^{-12}	2.780×10^{-12}	2.900×10^{-12}	3.010×10^{-12}
4, 11/2 → 7, 9/2	4.650×10^{-12}	4.570×10^{-12}	4.860×10^{-12}	5.300×10^{-12}	5.560×10^{-12}	5.800×10^{-12}	6.020×10^{-12}
4, 7/2 → 7, 9/2	3.100×10^{-12}	3.050×10^{-12}	3.240×10^{-12}	3.530×10^{-12}	3.710×10^{-12}	3.870×10^{-12}	4.020×10^{-12}
4, 9/2 → 7, 9/2	3.870×10^{-12}	3.810×10^{-12}	4.050×10^{-12}	4.410×10^{-12}	4.640×10^{-12}	4.830×10^{-12}	5.020×10^{-12}
4, 13/2 → 7, 17/2	5.420×10^{-12}	5.330×10^{-12}	5.670×10^{-12}	6.180×10^{-12}	6.490×10^{-12}	6.760×10^{-12}	7.030×10^{-12}
4, 3/2 → 7, 17/2	1.550×10^{-12}	1.520×10^{-12}	1.620×10^{-12}	1.770×10^{-12}	1.850×10^{-12}	1.930×10^{-12}	2.010×10^{-12}
4, 5/2 → 7, 17/2	2.320×10^{-12}	2.290×10^{-12}	2.430×10^{-12}	2.650×10^{-12}	2.780×10^{-12}	2.900×10^{-12}	3.010×10^{-12}
4, 11/2 → 7, 17/2	4.650×10^{-12}	4.570×10^{-12}	4.860×10^{-12}	5.300×10^{-12}	5.560×10^{-12}	5.800×10^{-12}	6.020×10^{-12}
4, 7/2 → 7, 17/2	3.100×10^{-12}	3.050×10^{-12}	3.240×10^{-12}	3.530×10^{-12}	3.710×10^{-12}	3.870×10^{-12}	4.020×10^{-12}
4, 9/2 → 7, 17/2	3.870×10^{-12}	3.810×10^{-12}	4.050×10^{-12}	4.410×10^{-12}	4.640×10^{-12}	4.830×10^{-12}	5.020×10^{-12}
4, 13/2 → 7, 11/2	5.420×10^{-12}	5.330×10^{-12}	5.670×10^{-12}	6.180×10^{-12}	6.490×10^{-12}	6.760×10^{-12}	7.030×10^{-12}
4, 3/2 → 7, 11/2	1.550×10^{-12}	1.520×10^{-12}	1.620×10^{-12}	1.770×10^{-12}	1.850×10^{-12}	1.930×10^{-12}	2.010×10^{-12}
4, 5/2 → 7, 11/2	2.320×10^{-12}	2.290×10^{-12}	2.430×10^{-12}	2.650×10^{-12}	2.780×10^{-12}	2.900×10^{-12}	3.010×10^{-12}
4, 11/2 → 7, 11/2	4.650×10^{-12}	4.570×10^{-12}	4.860×10^{-12}	5.300×10^{-12}	5.560×10^{-12}	5.800×10^{-12}	6.020×10^{-12}
4, 7/2 → 7, 11/2	3.100×10^{-12}	3.050×10^{-12}	3.240×10^{-12}	3.530×10^{-12}	3.710×10^{-12}	3.870×10^{-12}	4.020×10^{-12}
4, 9/2 → 7, 11/2	3.870×10^{-12}	3.810×10^{-12}	4.050×10^{-12}	4.410×10^{-12}	4.640×10^{-12}	4.830×10^{-12}	5.020×10^{-12}
4, 13/2 → 7, 15/2	5.420×10^{-12}	5.330×10^{-12}	5.670×10^{-12}	6.180×10^{-12}	6.490×10^{-12}	6.760×10^{-12}	7.030×10^{-12}
4, 3/2 → 7, 15/2	1.550×10^{-12}	1.520×10^{-12}	1.620×10^{-12}	1.770×10^{-12}	1.850×10^{-12}	1.930×10^{-12}	2.010×10^{-12}
4, 5/2 → 7, 15/2	2.320×10^{-12}	2.290×10^{-12}	2.430×10^{-12}	2.650×10^{-12}	2.780×10^{-12}	2.900×10^{-12}	3.010×10^{-12}
4, 11/2 → 7, 15/2	4.650×10^{-12}	4.570×10^{-12}	4.860×10^{-12}	5.300×10^{-12}	5.560×10^{-12}	5.800×10^{-12}	6.020×10^{-12}
4, 7/2 → 7, 15/2	3.100×10^{-12}	3.050×10^{-12}	3.240×10^{-12}	3.530×10^{-12}	3.710×10^{-12}	3.870×10^{-12}	4.020×10^{-12}
4, 9/2 → 7, 15/2	3.870×10^{-12}	3.810×10^{-12}	4.050×10^{-12}	4.410×10^{-12}	4.640×10^{-12}	4.830×10^{-12}	5.020×10^{-12}
4, 13/2 → 7, 13/2	5.420×10^{-12}	5.330×10^{-12}	5.670×10^{-12}	6.180×10^{-12}	6.490×10^{-12}	6.760×10^{-12}	7.030×10^{-12}
4, 3/2 → 7, 13/2	1.550×10^{-12}	1.520×10^{-12}	1.620×10^{-12}	1.770×10^{-12}	1.850×10^{-12}	1.930×10^{-12}	2.010×10^{-12}
4, 5/2 → 7, 13/2	2.320×10^{-12}	2.290×10^{-12}	2.430×10^{-12}	2.650×10^{-12}	2.780×10^{-12}	2.900×10^{-12}	3.010×10^{-12}
4, 11/2 → 7, 13/2	4.650×10^{-12}	4.570×10^{-12}	4.860×10^{-12}	5.300×10^{-12}	5.560×10^{-12}	5.800×10^{-12}	6.020×10^{-12}
4, 7/2 → 7, 13/2	3.100×10^{-12}	3.050×10^{-12}	3.240×10^{-12}	3.530×10^{-12}	3.710×10^{-12}	3.870×10^{-12}	4.020×10^{-12}
4, 9/2 → 7, 13/2	3.870×10^{-12}	3.810×10^{-12}	4.050×10^{-12}	4.410×10^{-12}	4.640×10^{-12}	4.830×10^{-12}	5.020×10^{-12}

Table A.4: continued.

Quantum Numbers	T						
J, $F \rightarrow J^{'}$,$F^{'}$	2 K	5 K	10 K	20 K	30 K	40 K	50 K
5, 15/2 → 7, 19/2	2.090×10^{-11}	2.130×10^{-11}	2.180×10^{-11}	2.100×10^{-11}	2.000×10^{-11}	1.930×10^{-11}	1.870×10^{-11}
5, 5/2 → 7, 19/2	7.830×10^{-12}	7.980×10^{-12}	8.170×10^{-12}	7.870×10^{-12}	7.520×10^{-12}	7.230×10^{-12}	7.010×10^{-12}
5, 7/2 → 7, 19/2	1.040×10^{-11}	1.060×10^{-11}	1.090×10^{-11}	1.050×10^{-11}	1.000×10^{-11}	9.640×10^{-12}	9.350×10^{-12}
5, 13/2 → 7, 19/2	1.830×10^{-11}	1.860×10^{-11}	1.910×10^{-11}	1.840×10^{-11}	1.750×10^{-11}	1.690×10^{-11}	1.640×10^{-11}
5, 9/2 → 7, 19/2	1.310×10^{-11}	1.330×10^{-11}	1.360×10^{-11}	1.310×10^{-11}	1.250×10^{-11}	1.200×10^{-11}	1.170×10^{-11}
5, 11/2 → 7, 19/2	1.570×10^{-11}	1.600×10^{-11}	1.630×10^{-11}	1.570×10^{-11}	1.500×10^{-11}	1.450×10^{-11}	1.400×10^{-11}
5, 15/2 → 7, 9/2	2.090×10^{-11}	2.130×10^{-11}	2.180×10^{-11}	2.100×10^{-11}	2.000×10^{-11}	1.930×10^{-11}	1.870×10^{-11}
5, 5/2 → 7, 9/2	7.830×10^{-12}	7.980×10^{-12}	8.170×10^{-12}	7.870×10^{-12}	7.520×10^{-12}	7.230×10^{-12}	7.010×10^{-12}
5, 7/2 → 7, 9/2	1.040×10^{-11}	1.060×10^{-11}	1.090×10^{-11}	1.050×10^{-11}	1.000×10^{-11}	9.640×10^{-12}	9.350×10^{-12}
5, 13/2 → 7, 9/2	1.830×10^{-11}	1.860×10^{-11}	1.910×10^{-11}	1.840×10^{-11}	1.750×10^{-11}	1.690×10^{-11}	1.640×10^{-11}
5, 9/2 → 7, 9/2	1.310×10^{-11}	1.330×10^{-11}	1.360×10^{-11}	1.310×10^{-11}	1.250×10^{-11}	1.200×10^{-11}	1.170×10^{-11}
5, 11/2 → 7, 9/2	1.570×10^{-11}	1.600×10^{-11}	1.630×10^{-11}	1.570×10^{-11}	1.500×10^{-11}	1.450×10^{-11}	1.400×10^{-11}
5, 15/2 → 7, 17/2	2.090×10^{-11}	2.130×10^{-11}	2.180×10^{-11}	2.100×10^{-11}	2.000×10^{-11}	1.930×10^{-11}	1.870×10^{-11}
5, 5/2 → 7, 17/2	7.830×10^{-12}	7.980×10^{-12}	8.170×10^{-12}	7.870×10^{-12}	7.520×10^{-12}	7.230×10^{-12}	7.010×10^{-12}
5, 7/2 → 7, 17/2	1.040×10^{-11}	1.060×10^{-11}	1.090×10^{-11}	1.050×10^{-11}	1.000×10^{-11}	9.640×10^{-12}	9.350×10^{-12}
5, 13/2 → 7, 17/2	1.830×10^{-11}	1.860×10^{-11}	1.910×10^{-11}	1.840×10^{-11}	1.750×10^{-11}	1.690×10^{-11}	1.640×10^{-11}
5, 9/2 → 7, 17/2	1.310×10^{-11}	1.330×10^{-11}	1.360×10^{-11}	1.310×10^{-11}	1.250×10^{-11}	1.200×10^{-11}	1.170×10^{-11}
5, 11/2 → 7, 17/2	1.570×10^{-11}	1.600×10^{-11}	1.630×10^{-11}	1.570×10^{-11}	1.500×10^{-11}	1.450×10^{-11}	1.400×10^{-11}
5, 15/2 → 7, 11/2	2.090×10^{-11}	2.130×10^{-11}	2.180×10^{-11}	2.100×10^{-11}	2.000×10^{-11}	1.930×10^{-11}	1.870×10^{-11}
5, 5/2 → 7, 11/2	7.830×10^{-12}	7.980×10^{-12}	8.170×10^{-12}	7.870×10^{-12}	7.520×10^{-12}	7.230×10^{-12}	7.010×10^{-12}
5, 7/2 → 7, 11/2	1.040×10^{-11}	1.060×10^{-11}	1.090×10^{-11}	1.050×10^{-11}	1.000×10^{-11}	9.640×10^{-12}	9.350×10^{-12}
5, 13/2 → 7, 11/2	1.830×10^{-11}	1.860×10^{-11}	1.910×10^{-11}	1.840×10^{-11}	1.750×10^{-11}	1.690×10^{-11}	1.640×10^{-11}
5, 9/2 → 7, 11/2	1.310×10^{-11}	1.330×10^{-11}	1.360×10^{-11}	1.310×10^{-11}	1.250×10^{-11}	1.200×10^{-11}	1.170×10^{-11}
5, 11/2 → 7, 11/2	1.570×10^{-11}	1.600×10^{-11}	1.630×10^{-11}	1.570×10^{-11}	1.500×10^{-11}	1.450×10^{-11}	1.400×10^{-11}
5, 15/2 → 7, 15/2	2.090×10^{-11}	2.130×10^{-11}	2.180×10^{-11}	2.100×10^{-11}	2.000×10^{-11}	1.930×10^{-11}	1.870×10^{-11}
5, 5/2 → 7, 15/2	7.830×10^{-12}	7.980×10^{-12}	8.170×10^{-12}	7.870×10^{-12}	7.520×10^{-12}	7.230×10^{-12}	7.010×10^{-12}
5, 7/2 → 7, 15/2	1.040×10^{-11}	1.060×10^{-11}	1.090×10^{-11}	1.050×10^{-11}	1.000×10^{-11}	9.640×10^{-12}	9.350×10^{-12}
5, 13/2 → 7, 15/2	1.830×10^{-11}	1.860×10^{-11}	1.910×10^{-11}	1.840×10^{-11}	1.750×10^{-11}	1.690×10^{-11}	1.640×10^{-11}
5, 9/2 → 7, 15/2	1.310×10^{-11}	1.330×10^{-11}	1.360×10^{-11}	1.310×10^{-11}	1.250×10^{-11}	1.200×10^{-11}	1.170×10^{-11}
5, 11/2 → 7, 15/2	1.570×10^{-11}	1.600×10^{-11}	1.630×10^{-11}	1.570×10^{-11}	1.500×10^{-11}	1.450×10^{-11}	1.400×10^{-11}
5, 15/2 → 7, 13/2	2.090×10^{-11}	2.130×10^{-11}	2.180×10^{-11}	2.100×10^{-11}	2.000×10^{-11}	1.930×10^{-11}	1.870×10^{-11}
5, 5/2 → 7, 13/2	7.830×10^{-12}	7.980×10^{-12}	8.170×10^{-12}	7.870×10^{-12}	7.520×10^{-12}	7.230×10^{-12}	7.010×10^{-12}
5, 7/2 → 7, 13/2	1.040×10^{-11}	1.060×10^{-11}	1.090×10^{-11}	1.050×10^{-11}	1.000×10^{-11}	9.640×10^{-12}	9.350×10^{-12}
5, 13/2 → 7, 13/2	1.830×10^{-11}	1.860×10^{-11}	1.910×10^{-11}	1.840×10^{-11}	1.750×10^{-11}	1.690×10^{-11}	1.640×10^{-11}
5, 9/2 → 7, 13/2	1.310×10^{-11}	1.330×10^{-11}	1.360×10^{-11}	1.310×10^{-11}	1.250×10^{-11}	1.200×10^{-11}	1.170×10^{-11}
5, 11/2 → 7, 13/2	1.570×10^{-11}	1.600×10^{-11}	1.630×10^{-11}	1.570×10^{-11}	1.500×10^{-11}	1.450×10^{-11}	1.400×10^{-11}
6, 17/2 → 7, 19/2	8.840×10^{-12}	1.030×10^{-11}	1.340×10^{-11}	1.610×10^{-11}	1.680×10^{-11}	1.710×10^{-11}	1.720×10^{-11}

Table A.4: continued.

Quantum Numbers	T						
J, $F \rightarrow J^{'}$,$F^{'}$	2 K	5 K	10 K	20 K	30 K	40 K	50 K
6, 7/2 → 7, 19/2	3.930×10^{-12}	4.570×10^{-12}	5.960×10^{-12}	7.170×10^{-12}	7.480×10^{-12}	7.580×10^{-12}	7.630×10^{-12}
6, 15/2 → 7, 19/2	7.860×10^{-12}	9.140×10^{-12}	1.190×10^{-11}	1.430×10^{-11}	1.500×10^{-11}	1.520×10^{-11}	1.530×10^{-11}
6, 9/2 → 7, 19/2	4.910×10^{-12}	5.720×10^{-12}	7.440×10^{-12}	8.960×10^{-12}	9.350×10^{-12}	9.480×10^{-12}	9.540×10^{-12}
6, 11/2 → 7, 19/2	5.900×10^{-12}	6.860×10^{-12}	8.930×10^{-12}	1.080×10^{-11}	1.120×10^{-11}	1.140×10^{-11}	1.140×10^{-11}
6, 13/2 → 7, 19/2	6.880×10^{-12}	8.000×10^{-12}	1.040×10^{-11}	1.250×10^{-11}	1.310×10^{-11}	1.330×10^{-11}	1.340×10^{-11}
6, 17/2 → 7, 9/2	8.840×10^{-12}	1.030×10^{-11}	1.340×10^{-11}	1.610×10^{-11}	1.680×10^{-11}	1.710×10^{-11}	1.720×10^{-11}
6, 7/2 → 7, 9/2	3.930×10^{-12}	4.570×10^{-12}	5.960×10^{-12}	7.170×10^{-12}	7.480×10^{-12}	7.580×10^{-12}	7.630×10^{-12}
6, 15/2 → 7, 9/2	7.860×10^{-12}	9.140×10^{-12}	1.190×10^{-11}	1.430×10^{-11}	1.500×10^{-11}	1.520×10^{-11}	1.530×10^{-11}
6, 9/2 → 7, 9/2	4.910×10^{-12}	5.720×10^{-12}	7.440×10^{-12}	8.960×10^{-12}	9.350×10^{-12}	9.480×10^{-12}	9.540×10^{-12}
6, 11/2 → 7, 9/2	5.900×10^{-12}	6.860×10^{-12}	8.930×10^{-12}	1.080×10^{-11}	1.120×10^{-11}	1.140×10^{-11}	1.140×10^{-11}
6, 13/2 → 7, 9/2	6.880×10^{-12}	8.000×10^{-12}	1.040×10^{-11}	1.250×10^{-11}	1.310×10^{-11}	1.330×10^{-11}	1.340×10^{-11}
6, 17/2 → 7, 17/2	8.840×10^{-12}	1.030×10^{-11}	1.340×10^{-11}	1.610×10^{-11}	1.680×10^{-11}	1.710×10^{-11}	1.720×10^{-11}
6, 7/2 → 7, 17/2	3.930×10^{-12}	4.570×10^{-12}	5.960×10^{-12}	7.170×10^{-12}	7.480×10^{-12}	7.580×10^{-12}	7.630×10^{-12}
6, 15/2 → 7, 17/2	7.860×10^{-12}	9.140×10^{-12}	1.190×10^{-11}	1.430×10^{-11}	1.500×10^{-11}	1.520×10^{-11}	1.530×10^{-11}
6, 9/2 → 7, 17/2	4.910×10^{-12}	5.720×10^{-12}	7.440×10^{-12}	8.960×10^{-12}	9.350×10^{-12}	9.480×10^{-12}	9.540×10^{-12}
6, 11/2 → 7, 17/2	5.900×10^{-12}	6.860×10^{-12}	8.930×10^{-12}	1.080×10^{-11}	1.120×10^{-11}	1.140×10^{-11}	1.140×10^{-11}
6, 13/2 → 7, 17/2	6.880×10^{-12}	8.000×10^{-12}	1.040×10^{-11}	1.250×10^{-11}	1.310×10^{-11}	1.330×10^{-11}	1.340×10^{-11}
6, 17/2 → 7, 11/2	8.840×10^{-12}	1.030×10^{-11}	1.340×10^{-11}	1.610×10^{-11}	1.680×10^{-11}	1.710×10^{-11}	1.720×10^{-11}
6, 7/2 → 7, 11/2	3.930×10^{-12}	4.570×10^{-12}	5.960×10^{-12}	7.170×10^{-12}	7.480×10^{-12}	7.580×10^{-12}	7.630×10^{-12}
6, 15/2 → 7, 11/2	7.860×10^{-12}	9.140×10^{-12}	1.190×10^{-11}	1.430×10^{-11}	1.500×10^{-11}	1.520×10^{-11}	1.530×10^{-11}
6, 9/2 → 7, 11/2	4.910×10^{-12}	5.720×10^{-12}	7.440×10^{-12}	8.960×10^{-12}	9.350×10^{-12}	9.480×10^{-12}	9.540×10^{-12}
6, 11/2 → 7, 11/2	5.900×10^{-12}	6.860×10^{-12}	8.930×10^{-12}	1.080×10^{-11}	1.120×10^{-11}	1.140×10^{-11}	1.140×10^{-11}
6, 13/2 → 7, 11/2	6.880×10^{-12}	8.000×10^{-12}	1.040×10^{-11}	1.250×10^{-11}	1.310×10^{-11}	1.330×10^{-11}	1.340×10^{-11}
6, 17/2 → 7, 15/2	8.840×10^{-12}	1.030×10^{-11}	1.340×10^{-11}	1.610×10^{-11}	1.680×10^{-11}	1.710×10^{-11}	1.720×10^{-11}
6, 7/2 → 7, 15/2	3.930×10^{-12}	4.570×10^{-12}	5.960×10^{-12}	7.170×10^{-12}	7.480×10^{-12}	7.580×10^{-12}	7.630×10^{-12}
6, 15/2 → 7, 15/2	7.860×10^{-12}	9.140×10^{-12}	1.190×10^{-11}	1.430×10^{-11}	1.500×10^{-11}	1.520×10^{-11}	1.530×10^{-11}
6, 9/2 → 7, 15/2	4.910×10^{-12}	5.720×10^{-12}	7.440×10^{-12}	8.960×10^{-12}	9.350×10^{-12}	9.480×10^{-12}	9.540×10^{-12}
6, 11/2 → 7, 15/2	5.900×10^{-12}	6.860×10^{-12}	8.930×10^{-12}	1.080×10^{-11}	1.120×10^{-11}	1.140×10^{-11}	1.140×10^{-11}
6, 13/2 → 7, 15/2	6.880×10^{-12}	8.000×10^{-12}	1.040×10^{-11}	1.250×10^{-11}	1.310×10^{-11}	1.330×10^{-11}	1.340×10^{-11}
6, 17/2 → 7, 13/2	8.840×10^{-12}	1.030×10^{-11}	1.340×10^{-11}	1.610×10^{-11}	1.680×10^{-11}	1.710×10^{-11}	1.720×10^{-11}
6, 7/2 → 7, 13/2	3.930×10^{-12}	4.570×10^{-12}	5.960×10^{-12}	7.170×10^{-12}	7.480×10^{-12}	7.580×10^{-12}	7.630×10^{-12}
6, 15/2 → 7, 13/2	7.860×10^{-12}	9.140×10^{-12}	1.190×10^{-11}	1.430×10^{-11}	1.500×10^{-11}	1.520×10^{-11}	1.530×10^{-11}
6, 9/2 → 7, 13/2	4.910×10^{-12}	5.720×10^{-12}	7.440×10^{-12}	8.960×10^{-12}	9.350×10^{-12}	9.480×10^{-12}	9.540×10^{-12}
6, 11/2 → 7, 13/2	5.900×10^{-12}	6.860×10^{-12}	8.930×10^{-12}	1.080×10^{-11}	1.120×10^{-11}	1.140×10^{-11}	1.140×10^{-11}
6, 13/2 → 7, 13/2	6.880×10^{-12}	8.000×10^{-12}	1.040×10^{-11}	1.250×10^{-11}	1.310×10^{-11}	1.330×10^{-11}	1.340×10^{-11}
0, 5/2 → 8, 21/2	9.920×10^{-14}	9.680×10^{-14}	9.950×10^{-14}	1.100×10^{-13}	1.260×10^{-13}	1.470×10^{-13}	1.720×10^{-13}
0, 5/2 → 8, 19/2	9.920×10^{-14}	9.680×10^{-14}	9.950×10^{-14}	1.100×10^{-13}	1.260×10^{-13}	1.470×10^{-13}	1.720×10^{-13}

Table A.4: continued.

Quantum Numbers			T				
J, $F \rightarrow J^{'}$,$F^{'}$	2 K	5 K	10 K	20 K	30 K	40 K	50 K
0, 5/2 → 8, 11/2	9.920×10^{-14}	9.680×10^{-14}	9.950×10^{-14}	1.100×10^{-13}	1.260×10^{-13}	1.470×10^{-13}	1.720×10^{-13}
0, 5/2 → 8, 13/2	9.920×10^{-14}	9.680×10^{-14}	9.950×10^{-14}	1.100×10^{-13}	1.260×10^{-13}	1.470×10^{-13}	1.720×10^{-13}
0, 5/2 → 8, 17/2	9.920×10^{-14}	9.680×10^{-14}	9.950×10^{-14}	1.100×10^{-13}	1.260×10^{-13}	1.470×10^{-13}	1.720×10^{-13}
1, 3/2 → 8, 21/2	1.200×10^{-13}	1.180×10^{-13}	1.220×10^{-13}	1.340×10^{-13}	1.520×10^{-13}	1.750×10^{-13}	2.020×10^{-13}
1, 7/2 → 8, 21/2	2.410×10^{-13}	2.370×10^{-13}	2.440×10^{-13}	2.690×10^{-13}	3.050×10^{-13}	3.500×10^{-13}	4.040×10^{-13}
1, 5/2 → 8, 21/2	1.810×10^{-13}	1.770×10^{-13}	1.830×10^{-13}	2.020×10^{-13}	2.280×10^{-13}	2.630×10^{-13}	3.030×10^{-13}
1, 3/2 → 8, 19/2	1.200×10^{-13}	1.180×10^{-13}	1.220×10^{-13}	1.340×10^{-13}	1.520×10^{-13}	1.750×10^{-13}	2.020×10^{-13}
1, 7/2 → 8, 19/2	2.410×10^{-13}	2.370×10^{-13}	2.440×10^{-13}	2.690×10^{-13}	3.050×10^{-13}	3.500×10^{-13}	4.040×10^{-13}
1, 5/2 → 8, 19/2	1.810×10^{-13}	1.770×10^{-13}	1.830×10^{-13}	2.020×10^{-13}	2.280×10^{-13}	2.630×10^{-13}	3.030×10^{-13}
1, 3/2 → 8, 11/2	1.200×10^{-13}	1.180×10^{-13}	1.220×10^{-13}	1.340×10^{-13}	1.520×10^{-13}	1.750×10^{-13}	2.020×10^{-13}
1, 7/2 → 8, 11/2	2.410×10^{-13}	2.370×10^{-13}	2.440×10^{-13}	2.690×10^{-13}	3.050×10^{-13}	3.500×10^{-13}	4.040×10^{-13}
1, 5/2 → 8, 11/2	1.810×10^{-13}	1.770×10^{-13}	1.830×10^{-13}	2.020×10^{-13}	2.280×10^{-13}	2.630×10^{-13}	3.030×10^{-13}
1, 3/2 → 8, 13/2	1.200×10^{-13}	1.180×10^{-13}	1.220×10^{-13}	1.340×10^{-13}	1.520×10^{-13}	1.750×10^{-13}	2.020×10^{-13}
1, 7/2 → 8, 13/2	2.410×10^{-13}	2.370×10^{-13}	2.440×10^{-13}	2.690×10^{-13}	3.050×10^{-13}	3.500×10^{-13}	4.040×10^{-13}
1, 5/2 → 8, 13/2	1.810×10^{-13}	1.770×10^{-13}	1.830×10^{-13}	2.020×10^{-13}	2.280×10^{-13}	2.630×10^{-13}	3.030×10^{-13}
1, 3/2 → 8, 17/2	1.200×10^{-13}	1.180×10^{-13}	1.220×10^{-13}	1.340×10^{-13}	1.520×10^{-13}	1.750×10^{-13}	2.020×10^{-13}
1, 7/2 → 8, 17/2	2.410×10^{-13}	2.370×10^{-13}	2.440×10^{-13}	2.690×10^{-13}	3.050×10^{-13}	3.500×10^{-13}	4.040×10^{-13}
1, 5/2 → 8, 17/2	1.810×10^{-13}	1.770×10^{-13}	1.830×10^{-13}	2.020×10^{-13}	2.280×10^{-13}	2.630×10^{-13}	3.030×10^{-13}
2, 1/2 → 8, 21/2	1.130×10^{-13}	1.080×10^{-13}	1.080×10^{-13}	1.120×10^{-13}	1.180×10^{-13}	1.270×10^{-13}	1.370×10^{-13}
2, 9/2 → 8, 21/2	5.640×10^{-13}	5.420×10^{-13}	5.410×10^{-13}	5.580×10^{-13}	5.920×10^{-13}	6.360×10^{-13}	6.870×10^{-13}
2, 3/2 → 8, 21/2	2.260×10^{-13}	2.170×10^{-13}	2.170×10^{-13}	2.230×10^{-13}	2.370×10^{-13}	2.550×10^{-13}	2.750×10^{-13}
2, 5/2 → 8, 21/2	3.380×10^{-13}	3.250×10^{-13}	3.250×10^{-13}	3.350×10^{-13}	3.550×10^{-13}	3.820×10^{-13}	4.120×10^{-13}
2, 7/2 → 8, 21/2	4.510×10^{-13}	4.340×10^{-13}	4.330×10^{-13}	4.470×10^{-13}	4.740×10^{-13}	5.090×10^{-13}	5.500×10^{-13}
2, 1/2 → 8, 19/2	1.130×10^{-13}	1.080×10^{-13}	1.080×10^{-13}	1.120×10^{-13}	1.180×10^{-13}	1.270×10^{-13}	1.370×10^{-13}
2, 9/2 → 8, 19/2	5.640×10^{-13}	5.420×10^{-13}	5.410×10^{-13}	5.580×10^{-13}	5.920×10^{-13}	6.360×10^{-13}	6.870×10^{-13}
2, 3/2 → 8, 19/2	2.260×10^{-13}	2.170×10^{-13}	2.170×10^{-13}	2.230×10^{-13}	2.370×10^{-13}	2.550×10^{-13}	2.750×10^{-13}
2, 5/2 → 8, 19/2	3.380×10^{-13}	3.250×10^{-13}	3.250×10^{-13}	3.350×10^{-13}	3.550×10^{-13}	3.820×10^{-13}	4.120×10^{-13}
2, 7/2 → 8, 19/2	4.510×10^{-13}	4.340×10^{-13}	4.330×10^{-13}	4.470×10^{-13}	4.740×10^{-13}	5.090×10^{-13}	5.500×10^{-13}
2, 1/2 → 8, 11/2	1.130×10^{-13}	1.080×10^{-13}	1.080×10^{-13}	1.120×10^{-13}	1.180×10^{-13}	1.270×10^{-13}	1.370×10^{-13}
2, 9/2 → 8, 11/2	5.640×10^{-13}	5.420×10^{-13}	5.410×10^{-13}	5.580×10^{-13}	5.920×10^{-13}	6.360×10^{-13}	6.870×10^{-13}
2, 3/2 → 8, 11/2	2.260×10^{-13}	2.170×10^{-13}	2.170×10^{-13}	2.230×10^{-13}	2.370×10^{-13}	2.550×10^{-13}	2.750×10^{-13}
2, 5/2 → 8, 11/2	3.380×10^{-13}	3.250×10^{-13}	3.250×10^{-13}	3.350×10^{-13}	3.550×10^{-13}	3.820×10^{-13}	4.120×10^{-13}
2, 7/2 → 8, 11/2	4.510×10^{-13}	4.340×10^{-13}	4.330×10^{-13}	4.470×10^{-13}	4.740×10^{-13}	5.090×10^{-13}	5.500×10^{-13}
2, 1/2 → 8, 13/2	1.130×10^{-13}	1.080×10^{-13}	1.080×10^{-13}	1.120×10^{-13}	1.180×10^{-13}	1.270×10^{-13}	1.370×10^{-13}
2, 9/2 → 8, 13/2	5.640×10^{-13}	5.420×10^{-13}	5.410×10^{-13}	5.580×10^{-13}	5.920×10^{-13}	6.360×10^{-13}	6.870×10^{-13}
2, 3/2 → 8, 13/2	2.260×10^{-13}	2.170×10^{-13}	2.170×10^{-13}	2.230×10^{-13}	2.370×10^{-13}	2.550×10^{-13}	2.750×10^{-13}
2, 5/2 → 8, 13/2	3.380×10^{-13}	3.250×10^{-13}	3.250×10^{-13}	3.350×10^{-13}	3.550×10^{-13}	3.820×10^{-13}	4.120×10^{-13}

Table A.4: continued.

Quantum Numbers	T						
J, $F \rightarrow J^{'}$,$F^{'}$	2 K	5 K	10 K	20 K	30 K	40 K	50 K
2, 7/2 → 8, 13/2	4.510×10^{-13}	4.340×10^{-13}	4.330×10^{-13}	4.470×10^{-13}	4.740×10^{-13}	5.090×10^{-13}	5.500×10^{-13}
2, 1/2 → 8, 17/2	1.130×10^{-13}	1.080×10^{-13}	1.080×10^{-13}	1.120×10^{-13}	1.180×10^{-13}	1.270×10^{-13}	1.370×10^{-13}
2, 9/2 → 8, 17/2	5.640×10^{-13}	5.420×10^{-13}	5.410×10^{-13}	5.580×10^{-13}	5.920×10^{-13}	6.360×10^{-13}	6.870×10^{-13}
2, 3/2 → 8, 17/2	2.260×10^{-13}	2.170×10^{-13}	2.170×10^{-13}	2.230×10^{-13}	2.370×10^{-13}	2.550×10^{-13}	2.750×10^{-13}
2, 5/2 → 8, 17/2	3.380×10^{-13}	3.250×10^{-13}	3.250×10^{-13}	3.350×10^{-13}	3.550×10^{-13}	3.820×10^{-13}	4.120×10^{-13}
2, 7/2 → 8, 17/2	4.510×10^{-13}	4.340×10^{-13}	4.330×10^{-13}	4.470×10^{-13}	4.740×10^{-13}	5.090×10^{-13}	5.500×10^{-13}
3, 11/2 → 8, 21/2	1.520×10^{-12}	1.480×10^{-12}	1.510×10^{-12}	1.590×10^{-12}	1.700×10^{-12}	1.840×10^{-12}	1.980×10^{-12}
3, 1/2 → 8, 21/2	2.540×10^{-13}	2.470×10^{-13}	2.510×10^{-13}	2.650×10^{-13}	2.840×10^{-13}	3.060×10^{-13}	3.300×10^{-13}
3, 3/2 → 8, 21/2	5.080×10^{-13}	4.940×10^{-13}	5.020×10^{-13}	5.300×10^{-13}	5.680×10^{-13}	6.120×10^{-13}	6.610×10^{-13}
3, 5/2 → 8, 21/2	7.620×10^{-13}	7.420×10^{-13}	7.530×10^{-13}	7.950×10^{-13}	8.510×10^{-13}	9.180×10^{-13}	9.910×10^{-13}
3, 9/2 → 8, 21/2	1.270×10^{-12}	1.240×10^{-12}	1.250×10^{-12}	1.320×10^{-12}	1.420×10^{-12}	1.530×10^{-12}	1.650×10^{-12}
3, 7/2 → 8, 21/2	1.020×10^{-12}	9.890×10^{-13}	1.000×10^{-12}	1.060×10^{-12}	1.140×10^{-12}	1.220×10^{-12}	1.320×10^{-12}
3, 11/2 → 8, 19/2	1.520×10^{-12}	1.480×10^{-12}	1.510×10^{-12}	1.590×10^{-12}	1.700×10^{-12}	1.840×10^{-12}	1.980×10^{-12}
3, 1/2 → 8, 19/2	2.540×10^{-13}	2.470×10^{-13}	2.510×10^{-13}	2.650×10^{-13}	2.840×10^{-13}	3.060×10^{-13}	3.300×10^{-13}
3, 3/2 → 8, 19/2	5.080×10^{-13}	4.940×10^{-13}	5.020×10^{-13}	5.300×10^{-13}	5.680×10^{-13}	6.120×10^{-13}	6.610×10^{-13}
3, 5/2 → 8, 19/2	7.620×10^{-13}	7.420×10^{-13}	7.530×10^{-13}	7.950×10^{-13}	8.510×10^{-13}	9.180×10^{-13}	9.910×10^{-13}
3, 9/2 → 8, 19/2	1.270×10^{-12}	1.240×10^{-12}	1.250×10^{-12}	1.320×10^{-12}	1.420×10^{-12}	1.530×10^{-12}	1.650×10^{-12}
3, 7/2 → 8, 19/2	1.020×10^{-12}	9.890×10^{-13}	1.000×10^{-12}	1.060×10^{-12}	1.140×10^{-12}	1.220×10^{-12}	1.320×10^{-12}
3, 11/2 → 8, 11/2	1.520×10^{-12}	1.480×10^{-12}	1.510×10^{-12}	1.590×10^{-12}	1.700×10^{-12}	1.840×10^{-12}	1.980×10^{-12}
3, 1/2 → 8, 11/2	2.540×10^{-13}	2.470×10^{-13}	2.510×10^{-13}	2.650×10^{-13}	2.840×10^{-13}	3.060×10^{-13}	3.300×10^{-13}
3, 3/2 → 8, 11/2	5.080×10^{-13}	4.940×10^{-13}	5.020×10^{-13}	5.300×10^{-13}	5.680×10^{-13}	6.120×10^{-13}	6.610×10^{-13}
3, 5/2 → 8, 11/2	7.620×10^{-13}	7.420×10^{-13}	7.530×10^{-13}	7.950×10^{-13}	8.510×10^{-13}	9.180×10^{-13}	9.910×10^{-13}
3, 9/2 → 8, 11/2	1.270×10^{-12}	1.240×10^{-12}	1.250×10^{-12}	1.320×10^{-12}	1.420×10^{-12}	1.530×10^{-12}	1.650×10^{-12}
3, 7/2 → 8, 11/2	1.020×10^{-12}	9.890×10^{-13}	1.000×10^{-12}	1.060×10^{-12}	1.140×10^{-12}	1.220×10^{-12}	1.320×10^{-12}
3, 11/2 → 8, 13/2	1.520×10^{-12}	1.480×10^{-12}	1.510×10^{-12}	1.590×10^{-12}	1.700×10^{-12}	1.840×10^{-12}	1.980×10^{-12}
3, 1/2 → 8, 13/2	2.540×10^{-13}	2.470×10^{-13}	2.510×10^{-13}	2.650×10^{-13}	2.840×10^{-13}	3.060×10^{-13}	3.300×10^{-13}
3, 3/2 → 8, 13/2	5.080×10^{-13}	4.940×10^{-13}	5.020×10^{-13}	5.300×10^{-13}	5.680×10^{-13}	6.120×10^{-13}	6.610×10^{-13}
3, 5/2 → 8, 13/2	7.620×10^{-13}	7.420×10^{-13}	7.530×10^{-13}	7.950×10^{-13}	8.510×10^{-13}	9.180×10^{-13}	9.910×10^{-13}
3, 9/2 → 8, 13/2	1.270×10^{-12}	1.240×10^{-12}	1.250×10^{-12}	1.320×10^{-12}	1.420×10^{-12}	1.530×10^{-12}	1.650×10^{-12}
3, 7/2 → 8, 13/2	1.020×10^{-12}	9.890×10^{-13}	1.000×10^{-12}	1.060×10^{-12}	1.140×10^{-12}	1.220×10^{-12}	1.320×10^{-12}
3, 11/2 → 8, 17/2	1.520×10^{-12}	1.480×10^{-12}	1.510×10^{-12}	1.590×10^{-12}	1.700×10^{-12}	1.840×10^{-12}	1.980×10^{-12}
3, 1/2 → 8, 17/2	2.540×10^{-13}	2.470×10^{-13}	2.510×10^{-13}	2.650×10^{-13}	2.840×10^{-13}	3.060×10^{-13}	3.300×10^{-13}
3, 3/2 → 8, 17/2	5.080×10^{-13}	4.940×10^{-13}	5.020×10^{-13}	5.300×10^{-13}	5.680×10^{-13}	6.120×10^{-13}	6.610×10^{-13}
3, 5/2 → 8, 17/2	7.620×10^{-13}	7.420×10^{-13}	7.530×10^{-13}	7.950×10^{-13}	8.510×10^{-13}	9.180×10^{-13}	9.910×10^{-13}
3, 9/2 → 8, 17/2	1.270×10^{-12}	1.240×10^{-12}	1.250×10^{-12}	1.320×10^{-12}	1.420×10^{-12}	1.530×10^{-12}	1.650×10^{-12}
3, 7/2 → 8, 17/2	1.020×10^{-12}	9.890×10^{-13}	1.000×10^{-12}	1.060×10^{-12}	1.140×10^{-12}	1.220×10^{-12}	1.320×10^{-12}
4, 13/2 → 8, 21/2	3.540×10^{-12}	3.460×10^{-12}	3.460×10^{-12}	3.390×10^{-12}	3.340×10^{-12}	3.330×10^{-12}	3.330×10^{-12}

Table A.4: continued.

Quantum Numbers	T						
J, $F \rightarrow J^{'}$,$F^{'}$	2 K	5 K	10 K	20 K	30 K	40 K	50 K
4, 3/2 → 8, 21/2	1.010×10^{-12}	9.900×10^{-13}	9.900×10^{-13}	9.690×10^{-13}	9.560×10^{-13}	9.510×10^{-13}	9.530×10^{-13}
4, 5/2 → 8, 21/2	1.520×10^{-12}	1.480×10^{-12}	1.480×10^{-12}	1.450×10^{-12}	1.430×10^{-12}	1.430×10^{-12}	1.430×10^{-12}
4, 11/2 → 8, 21/2	3.030×10^{-12}	2.970×10^{-12}	2.970×10^{-12}	2.910×10^{-12}	2.870×10^{-12}	2.850×10^{-12}	2.860×10^{-12}
4, 7/2 → 8, 21/2	2.020×10^{-12}	1.980×10^{-12}	1.980×10^{-12}	1.940×10^{-12}	1.910×10^{-12}	1.900×10^{-12}	1.910×10^{-12}
4, 9/2 → 8, 21/2	2.530×10^{-12}	2.470×10^{-12}	2.470×10^{-12}	2.420×10^{-12}	2.390×10^{-12}	2.380×10^{-12}	2.380×10^{-12}
4, 13/2 → 8, 19/2	3.540×10^{-12}	3.460×10^{-12}	3.460×10^{-12}	3.390×10^{-12}	3.340×10^{-12}	3.330×10^{-12}	3.330×10^{-12}
4, 3/2 → 8, 19/2	1.010×10^{-12}	9.900×10^{-13}	9.900×10^{-13}	9.690×10^{-13}	9.560×10^{-13}	9.510×10^{-13}	9.530×10^{-13}
4, 5/2 → 8, 19/2	1.520×10^{-12}	1.480×10^{-12}	1.480×10^{-12}	1.450×10^{-12}	1.430×10^{-12}	1.430×10^{-12}	1.430×10^{-12}
4, 11/2 → 8, 19/2	3.030×10^{-12}	2.970×10^{-12}	2.970×10^{-12}	2.910×10^{-12}	2.870×10^{-12}	2.850×10^{-12}	2.860×10^{-12}
4, 7/2 → 8, 19/2	2.020×10^{-12}	1.980×10^{-12}	1.980×10^{-12}	1.940×10^{-12}	1.910×10^{-12}	1.900×10^{-12}	1.910×10^{-12}
4, 9/2 → 8, 19/2	2.530×10^{-12}	2.470×10^{-12}	2.470×10^{-12}	2.420×10^{-12}	2.390×10^{-12}	2.380×10^{-12}	2.380×10^{-12}
4, 13/2 → 8, 11/2	3.540×10^{-12}	3.460×10^{-12}	3.460×10^{-12}	3.390×10^{-12}	3.340×10^{-12}	3.330×10^{-12}	3.330×10^{-12}
4, 3/2 → 8, 11/2	1.010×10^{-12}	9.900×10^{-13}	9.900×10^{-13}	9.690×10^{-13}	9.560×10^{-13}	9.510×10^{-13}	9.530×10^{-13}
4, 5/2 → 8, 11/2	1.520×10^{-12}	1.480×10^{-12}	1.480×10^{-12}	1.450×10^{-12}	1.430×10^{-12}	1.430×10^{-12}	1.430×10^{-12}
4, 11/2 → 8, 11/2	3.030×10^{-12}	2.970×10^{-12}	2.970×10^{-12}	2.910×10^{-12}	2.870×10^{-12}	2.850×10^{-12}	2.860×10^{-12}
4, 7/2 → 8, 11/2	2.020×10^{-12}	1.980×10^{-12}	1.980×10^{-12}	1.940×10^{-12}	1.910×10^{-12}	1.900×10^{-12}	1.910×10^{-12}
4, 9/2 → 8, 11/2	2.530×10^{-12}	2.470×10^{-12}	2.470×10^{-12}	2.420×10^{-12}	2.390×10^{-12}	2.380×10^{-12}	2.380×10^{-12}
4, 13/2 → 8, 13/2	3.540×10^{-12}	3.460×10^{-12}	3.460×10^{-12}	3.390×10^{-12}	3.340×10^{-12}	3.330×10^{-12}	3.330×10^{-12}
4, 3/2 → 8, 13/2	1.010×10^{-12}	9.900×10^{-13}	9.900×10^{-13}	9.690×10^{-13}	9.560×10^{-13}	9.510×10^{-13}	9.530×10^{-13}
4, 5/2 → 8, 13/2	1.520×10^{-12}	1.480×10^{-12}	1.480×10^{-12}	1.450×10^{-12}	1.430×10^{-12}	1.430×10^{-12}	1.430×10^{-12}
4, 11/2 → 8, 13/2	3.030×10^{-12}	2.970×10^{-12}	2.970×10^{-12}	2.910×10^{-12}	2.870×10^{-12}	2.850×10^{-12}	2.860×10^{-12}
4, 7/2 → 8, 13/2	2.020×10^{-12}	1.980×10^{-12}	1.980×10^{-12}	1.940×10^{-12}	1.910×10^{-12}	1.900×10^{-12}	1.910×10^{-12}
4, 9/2 → 8, 13/2	2.530×10^{-12}	2.470×10^{-12}	2.470×10^{-12}	2.420×10^{-12}	2.390×10^{-12}	2.380×10^{-12}	2.380×10^{-12}
4, 13/2 → 8, 17/2	3.540×10^{-12}	3.460×10^{-12}	3.460×10^{-12}	3.390×10^{-12}	3.340×10^{-12}	3.330×10^{-12}	3.330×10^{-12}
4, 3/2 → 8, 17/2	1.010×10^{-12}	9.900×10^{-13}	9.900×10^{-13}	9.690×10^{-13}	9.560×10^{-13}	9.510×10^{-13}	9.530×10^{-13}
4, 5/2 → 8, 17/2	1.520×10^{-12}	1.480×10^{-12}	1.480×10^{-12}	1.450×10^{-12}	1.430×10^{-12}	1.430×10^{-12}	1.430×10^{-12}
4, 11/2 → 8, 17/2	3.030×10^{-12}	2.970×10^{-12}	2.970×10^{-12}	2.910×10^{-12}	2.870×10^{-12}	2.850×10^{-12}	2.860×10^{-12}
4, 7/2 → 8, 17/2	2.020×10^{-12}	1.980×10^{-12}	1.980×10^{-12}	1.940×10^{-12}	1.910×10^{-12}	1.900×10^{-12}	1.910×10^{-12}
4, 9/2 → 8, 17/2	2.530×10^{-12}	2.470×10^{-12}	2.470×10^{-12}	2.420×10^{-12}	2.390×10^{-12}	2.380×10^{-12}	2.380×10^{-12}
5, 15/2 → 8, 21/2	6.540×10^{-12}	6.500×10^{-12}	6.700×10^{-12}	7.020×10^{-12}	7.240×10^{-12}	7.450×10^{-12}	7.660×10^{-12}
5, 5/2 → 8, 21/2	2.450×10^{-12}	2.440×10^{-12}	2.510×10^{-12}	2.630×10^{-12}	2.720×10^{-12}	2.790×10^{-12}	2.870×10^{-12}
5, 7/2 → 8, 21/2	3.270×10^{-12}	3.250×10^{-12}	3.350×10^{-12}	3.510×10^{-12}	3.620×10^{-12}	3.730×10^{-12}	3.830×10^{-12}
5, 13/2 → 8, 21/2	5.720×10^{-12}	5.690×10^{-12}	5.860×10^{-12}	6.140×10^{-12}	6.340×10^{-12}	6.520×10^{-12}	6.710×10^{-12}
5, 9/2 → 8, 21/2	4.090×10^{-12}	4.060×10^{-12}	4.190×10^{-12}	4.390×10^{-12}	4.530×10^{-12}	4.660×10^{-12}	4.790×10^{-12}
5, 11/2 → 8, 21/2	4.910×10^{-12}	4.870×10^{-12}	5.030×10^{-12}	5.260×10^{-12}	5.430×10^{-12}	5.590×10^{-12}	5.750×10^{-12}
5, 15/2 → 8, 19/2	6.540×10^{-12}	6.500×10^{-12}	6.700×10^{-12}	7.020×10^{-12}	7.240×10^{-12}	7.450×10^{-12}	7.660×10^{-12}
5, 5/2 → 8, 19/2	2.450×10^{-12}	2.440×10^{-12}	2.510×10^{-12}	2.630×10^{-12}	2.720×10^{-12}	2.790×10^{-12}	2.870×10^{-12}

Table A.4: continued.

Quantum Numbers	T						
J, $F \rightarrow J^{'}$,$F^{'}$	2 K	5 K	10 K	20 K	30 K	40 K	50 K
5, 7/2 → 8, 19/2	3.270×10^{-12}	3.250×10^{-12}	3.350×10^{-12}	3.510×10^{-12}	3.620×10^{-12}	3.730×10^{-12}	3.830×10^{-12}
5, 13/2 → 8, 19/2	5.720×10^{-12}	5.690×10^{-12}	5.860×10^{-12}	6.140×10^{-12}	6.340×10^{-12}	6.520×10^{-12}	6.710×10^{-12}
5, 9/2 → 8, 19/2	4.090×10^{-12}	4.060×10^{-12}	4.190×10^{-12}	4.390×10^{-12}	4.530×10^{-12}	4.660×10^{-12}	4.790×10^{-12}
5, 11/2 → 8, 19/2	4.910×10^{-12}	4.870×10^{-12}	5.030×10^{-12}	5.260×10^{-12}	5.430×10^{-12}	5.590×10^{-12}	5.750×10^{-12}
5, 15/2 → 8, 11/2	6.540×10^{-12}	6.500×10^{-12}	6.700×10^{-12}	7.020×10^{-12}	7.240×10^{-12}	7.450×10^{-12}	7.660×10^{-12}
5, 5/2 → 8, 11/2	2.450×10^{-12}	2.440×10^{-12}	2.510×10^{-12}	2.630×10^{-12}	2.720×10^{-12}	2.790×10^{-12}	2.870×10^{-12}
5, 7/2 → 8, 11/2	3.270×10^{-12}	3.250×10^{-12}	3.350×10^{-12}	3.510×10^{-12}	3.620×10^{-12}	3.730×10^{-12}	3.830×10^{-12}
5, 13/2 → 8, 11/2	5.720×10^{-12}	5.690×10^{-12}	5.860×10^{-12}	6.140×10^{-12}	6.340×10^{-12}	6.520×10^{-12}	6.710×10^{-12}
5, 9/2 → 8, 11/2	4.090×10^{-12}	4.060×10^{-12}	4.190×10^{-12}	4.390×10^{-12}	4.530×10^{-12}	4.660×10^{-12}	4.790×10^{-12}
5, 11/2 → 8, 11/2	4.910×10^{-12}	4.870×10^{-12}	5.030×10^{-12}	5.260×10^{-12}	5.430×10^{-12}	5.590×10^{-12}	5.750×10^{-12}
5, 15/2 → 8, 13/2	6.540×10^{-12}	6.500×10^{-12}	6.700×10^{-12}	7.020×10^{-12}	7.240×10^{-12}	7.450×10^{-12}	7.660×10^{-12}
5, 5/2 → 8, 13/2	2.450×10^{-12}	2.440×10^{-12}	2.510×10^{-12}	2.630×10^{-12}	2.720×10^{-12}	2.790×10^{-12}	2.870×10^{-12}
5, 7/2 → 8, 13/2	3.270×10^{-12}	3.250×10^{-12}	3.350×10^{-12}	3.510×10^{-12}	3.620×10^{-12}	3.730×10^{-12}	3.830×10^{-12}
5, 13/2 → 8, 13/2	5.720×10^{-12}	5.690×10^{-12}	5.860×10^{-12}	6.140×10^{-12}	6.340×10^{-12}	6.520×10^{-12}	6.710×10^{-12}
5, 9/2 → 8, 13/2	4.090×10^{-12}	4.060×10^{-12}	4.190×10^{-12}	4.390×10^{-12}	4.530×10^{-12}	4.660×10^{-12}	4.790×10^{-12}
5, 11/2 → 8, 13/2	4.910×10^{-12}	4.870×10^{-12}	5.030×10^{-12}	5.260×10^{-12}	5.430×10^{-12}	5.590×10^{-12}	5.750×10^{-12}
5, 15/2 → 8, 17/2	6.540×10^{-12}	6.500×10^{-12}	6.700×10^{-12}	7.020×10^{-12}	7.240×10^{-12}	7.450×10^{-12}	7.660×10^{-12}
5, 5/2 → 8, 17/2	2.450×10^{-12}	2.440×10^{-12}	2.510×10^{-12}	2.630×10^{-12}	2.720×10^{-12}	2.790×10^{-12}	2.870×10^{-12}
5, 7/2 → 8, 17/2	3.270×10^{-12}	3.250×10^{-12}	3.350×10^{-12}	3.510×10^{-12}	3.620×10^{-12}	3.730×10^{-12}	3.830×10^{-12}
5, 13/2 → 8, 17/2	5.720×10^{-12}	5.690×10^{-12}	5.860×10^{-12}	6.140×10^{-12}	6.340×10^{-12}	6.520×10^{-12}	6.710×10^{-12}
5, 9/2 → 8, 17/2	4.090×10^{-12}	4.060×10^{-12}	4.190×10^{-12}	4.390×10^{-12}	4.530×10^{-12}	4.660×10^{-12}	4.790×10^{-12}
5, 11/2 → 8, 17/2	4.910×10^{-12}	4.870×10^{-12}	5.030×10^{-12}	5.260×10^{-12}	5.430×10^{-12}	5.590×10^{-12}	5.750×10^{-12}
6, 17/2 → 8, 21/2	1.910×10^{-11}	1.990×10^{-11}	2.090×10^{-11}	2.050×10^{-11}	1.960×10^{-11}	1.890×10^{-11}	1.830×10^{-11}
6, 7/2 → 8, 21/2	8.470×10^{-12}	8.830×10^{-12}	9.280×10^{-12}	9.100×10^{-12}	8.720×10^{-12}	8.390×10^{-12}	8.130×10^{-12}
6, 15/2 → 8, 21/2	1.690×10^{-11}	1.770×10^{-11}	1.860×10^{-11}	1.820×10^{-11}	1.740×10^{-11}	1.680×10^{-11}	1.630×10^{-11}
6, 9/2 → 8, 21/2	1.060×10^{-11}	1.100×10^{-11}	1.160×10^{-11}	1.140×10^{-11}	1.090×10^{-11}	1.050×10^{-11}	1.020×10^{-11}
6, 11/2 → 8, 21/2	1.270×10^{-11}	1.320×10^{-11}	1.390×10^{-11}	1.360×10^{-11}	1.310×10^{-11}	1.260×10^{-11}	1.220×10^{-11}
6, 13/2 → 8, 21/2	1.480×10^{-11}	1.540×10^{-11}	1.620×10^{-11}	1.590×10^{-11}	1.530×10^{-11}	1.470×10^{-11}	1.420×10^{-11}
6, 17/2 → 8, 19/2	1.910×10^{-11}	1.990×10^{-11}	2.090×10^{-11}	2.050×10^{-11}	1.960×10^{-11}	1.890×10^{-11}	1.830×10^{-11}
6, 7/2 → 8, 19/2	8.470×10^{-12}	8.830×10^{-12}	9.280×10^{-12}	9.100×10^{-12}	8.720×10^{-12}	8.390×10^{-12}	8.130×10^{-12}
6, 15/2 → 8, 19/2	1.690×10^{-11}	1.770×10^{-11}	1.860×10^{-11}	1.820×10^{-11}	1.740×10^{-11}	1.680×10^{-11}	1.630×10^{-11}
6, 9/2 → 8, 19/2	1.060×10^{-11}	1.100×10^{-11}	1.160×10^{-11}	1.140×10^{-11}	1.090×10^{-11}	1.050×10^{-11}	1.020×10^{-11}
6, 11/2 → 8, 19/2	1.270×10^{-11}	1.320×10^{-11}	1.390×10^{-11}	1.360×10^{-11}	1.310×10^{-11}	1.260×10^{-11}	1.220×10^{-11}
6, 13/2 → 8, 19/2	1.480×10^{-11}	1.540×10^{-11}	1.620×10^{-11}	1.590×10^{-11}	1.530×10^{-11}	1.470×10^{-11}	1.420×10^{-11}
6, 17/2 → 8, 11/2	1.910×10^{-11}	1.990×10^{-11}	2.090×10^{-11}	2.050×10^{-11}	1.960×10^{-11}	1.890×10^{-11}	1.830×10^{-11}
6, 7/2 → 8, 11/2	8.470×10^{-12}	8.830×10^{-12}	9.280×10^{-12}	9.100×10^{-12}	8.720×10^{-12}	8.390×10^{-12}	8.130×10^{-12}
6, 15/2 → 8, 11/2	1.690×10^{-11}	1.770×10^{-11}	1.860×10^{-11}	1.820×10^{-11}	1.740×10^{-11}	1.680×10^{-11}	1.630×10^{-11}

Table A.4: continued.

Quantum Numbers	T						
J, $F \rightarrow J^{'}$,$F^{'}$	2 K	5 K	10 K	20 K	30 K	40 K	50 K
6, 9/2 → 8, 11/2	1.060×10^{-11}	1.100×10^{-11}	1.160×10^{-11}	1.140×10^{-11}	1.090×10^{-11}	1.050×10^{-11}	1.020×10^{-11}
6, 11/2 → 8, 11/2	1.270×10^{-11}	1.320×10^{-11}	1.390×10^{-11}	1.360×10^{-11}	1.310×10^{-11}	1.260×10^{-11}	1.220×10^{-11}
6, 13/2 → 8, 11/2	1.480×10^{-11}	1.540×10^{-11}	1.620×10^{-11}	1.590×10^{-11}	1.530×10^{-11}	1.470×10^{-11}	1.420×10^{-11}
6, 17/2 → 8, 13/2	1.910×10^{-11}	1.990×10^{-11}	2.090×10^{-11}	2.050×10^{-11}	1.960×10^{-11}	1.890×10^{-11}	1.830×10^{-11}
6, 7/2 → 8, 13/2	8.470×10^{-12}	8.830×10^{-12}	9.280×10^{-12}	9.100×10^{-12}	8.720×10^{-12}	8.390×10^{-12}	8.130×10^{-12}
6, 15/2 → 8, 13/2	1.690×10^{-11}	1.770×10^{-11}	1.860×10^{-11}	1.820×10^{-11}	1.740×10^{-11}	1.680×10^{-11}	1.630×10^{-11}
6, 9/2 → 8, 13/2	1.060×10^{-11}	1.100×10^{-11}	1.160×10^{-11}	1.140×10^{-11}	1.090×10^{-11}	1.050×10^{-11}	1.020×10^{-11}
6, 11/2 → 8, 13/2	1.270×10^{-11}	1.320×10^{-11}	1.390×10^{-11}	1.360×10^{-11}	1.310×10^{-11}	1.260×10^{-11}	1.220×10^{-11}
6, 13/2 → 8, 13/2	1.480×10^{-11}	1.540×10^{-11}	1.620×10^{-11}	1.590×10^{-11}	1.530×10^{-11}	1.470×10^{-11}	1.420×10^{-11}
6, 17/2 → 8, 17/2	1.910×10^{-11}	1.990×10^{-11}	2.090×10^{-11}	2.050×10^{-11}	1.960×10^{-11}	1.890×10^{-11}	1.830×10^{-11}
6, 7/2 → 8, 17/2	8.470×10^{-12}	8.830×10^{-12}	9.280×10^{-12}	9.100×10^{-12}	8.720×10^{-12}	8.390×10^{-12}	8.130×10^{-12}
6, 15/2 → 8, 17/2	1.690×10^{-11}	1.770×10^{-11}	1.860×10^{-11}	1.820×10^{-11}	1.740×10^{-11}	1.680×10^{-11}	1.630×10^{-11}
6, 9/2 → 8, 17/2	1.060×10^{-11}	1.100×10^{-11}	1.160×10^{-11}	1.140×10^{-11}	1.090×10^{-11}	1.050×10^{-11}	1.020×10^{-11}
6, 11/2 → 8, 17/2	1.270×10^{-11}	1.320×10^{-11}	1.390×10^{-11}	1.360×10^{-11}	1.310×10^{-11}	1.260×10^{-11}	1.220×10^{-11}
6, 13/2 → 8, 17/2	1.480×10^{-11}	1.540×10^{-11}	1.620×10^{-11}	1.590×10^{-11}	1.530×10^{-11}	1.470×10^{-11}	1.420×10^{-11}
7, 19/2 → 8, 21/2	1.070×10^{-11}	1.190×10^{-11}	1.400×10^{-11}	1.630×10^{-11}	1.700×10^{-11}	1.720×10^{-11}	1.730×10^{-11}
7, 9/2 → 8, 21/2	5.370×10^{-12}	5.950×10^{-12}	7.020×10^{-12}	8.130×10^{-12}	8.480×10^{-12}	8.600×10^{-12}	8.650×10^{-12}
7, 17/2 → 8, 21/2	9.670×10^{-12}	1.070×10^{-11}	1.260×10^{-11}	1.460×10^{-11}	1.530×10^{-11}	1.550×10^{-11}	1.560×10^{-11}
7, 11/2 → 8, 21/2	6.450×10^{-12}	7.140×10^{-12}	8.420×10^{-12}	9.760×10^{-12}	1.020×10^{-11}	1.030×10^{-11}	1.040×10^{-11}
7, 15/2 → 8, 21/2	8.600×10^{-12}	9.520×10^{-12}	1.120×10^{-11}	1.300×10^{-11}	1.360×10^{-11}	1.380×10^{-11}	1.380×10^{-11}
7, 13/2 → 8, 21/2	7.520×10^{-12}	8.330×10^{-12}	9.820×10^{-12}	1.140×10^{-11}	1.190×10^{-11}	1.200×10^{-11}	1.210×10^{-11}
7, 19/2 → 8, 19/2	1.070×10^{-11}	1.190×10^{-11}	1.400×10^{-11}	1.630×10^{-11}	1.700×10^{-11}	1.720×10^{-11}	1.730×10^{-11}
7, 9/2 → 8, 19/2	5.370×10^{-12}	5.950×10^{-12}	7.020×10^{-12}	8.130×10^{-12}	8.480×10^{-12}	8.600×10^{-12}	8.650×10^{-12}
7, 17/2 → 8, 19/2	9.670×10^{-12}	1.070×10^{-11}	1.260×10^{-11}	1.460×10^{-11}	1.530×10^{-11}	1.550×10^{-11}	1.560×10^{-11}
7, 11/2 → 8, 19/2	6.450×10^{-12}	7.140×10^{-12}	8.420×10^{-12}	9.760×10^{-12}	1.020×10^{-11}	1.030×10^{-11}	1.040×10^{-11}
7, 15/2 → 8, 19/2	8.600×10^{-12}	9.520×10^{-12}	1.120×10^{-11}	1.300×10^{-11}	1.360×10^{-11}	1.380×10^{-11}	1.380×10^{-11}
7, 13/2 → 8, 19/2	7.520×10^{-12}	8.330×10^{-12}	9.820×10^{-12}	1.140×10^{-11}	1.190×10^{-11}	1.200×10^{-11}	1.210×10^{-11}
7, 19/2 → 8, 11/2	1.070×10^{-11}	1.190×10^{-11}	1.400×10^{-11}	1.630×10^{-11}	1.700×10^{-11}	1.720×10^{-11}	1.730×10^{-11}
7, 9/2 → 8, 11/2	5.370×10^{-12}	5.950×10^{-12}	7.020×10^{-12}	8.130×10^{-12}	8.480×10^{-12}	8.600×10^{-12}	8.650×10^{-12}
7, 17/2 → 8, 11/2	9.670×10^{-12}	1.070×10^{-11}	1.260×10^{-11}	1.460×10^{-11}	1.530×10^{-11}	1.550×10^{-11}	1.560×10^{-11}
7, 11/2 → 8, 11/2	6.450×10^{-12}	7.140×10^{-12}	8.420×10^{-12}	9.760×10^{-12}	1.020×10^{-11}	1.030×10^{-11}	1.040×10^{-11}
7, 15/2 → 8, 11/2	8.600×10^{-12}	9.520×10^{-12}	1.120×10^{-11}	1.300×10^{-11}	1.360×10^{-11}	1.380×10^{-11}	1.380×10^{-11}
7, 13/2 → 8, 11/2	7.520×10^{-12}	8.330×10^{-12}	9.820×10^{-12}	1.140×10^{-11}	1.190×10^{-11}	1.200×10^{-11}	1.210×10^{-11}
7, 19/2 → 8, 13/2	1.070×10^{-11}	1.190×10^{-11}	1.400×10^{-11}	1.630×10^{-11}	1.700×10^{-11}	1.720×10^{-11}	1.730×10^{-11}
7, 9/2 → 8, 13/2	5.370×10^{-12}	5.950×10^{-12}	7.020×10^{-12}	8.130×10^{-12}	8.480×10^{-12}	8.600×10^{-12}	8.650×10^{-12}
7, 17/2 → 8, 13/2	9.670×10^{-12}	1.070×10^{-11}	1.260×10^{-11}	1.460×10^{-11}	1.530×10^{-11}	1.550×10^{-11}	1.560×10^{-11}
7, 11/2 → 8, 13/2	6.450×10^{-12}	7.140×10^{-12}	8.420×10^{-12}	9.760×10^{-12}	1.020×10^{-11}	1.030×10^{-11}	1.040×10^{-11}

Table A.4: continued.

Quantum Numbers	T						
J, $F \rightarrow J^{'}$,$F^{'}$	2 K	5 K	10 K	20 K	30 K	40 K	50 K
7, 15/2 → 8, 13/2	8.600×10^{-12}	9.520×10^{-12}	1.120×10^{-11}	1.300×10^{-11}	1.360×10^{-11}	1.380×10^{-11}	1.380×10^{-11}
7, 13/2 → 8, 13/2	7.520×10^{-12}	8.330×10^{-12}	9.820×10^{-12}	1.140×10^{-11}	1.190×10^{-11}	1.200×10^{-11}	1.210×10^{-11}
7, 19/2 → 8, 17/2	1.070×10^{-11}	1.190×10^{-11}	1.400×10^{-11}	1.630×10^{-11}	1.700×10^{-11}	1.720×10^{-11}	1.730×10^{-11}
7, 9/2 → 8, 17/2	5.370×10^{-12}	5.950×10^{-12}	7.020×10^{-12}	8.130×10^{-12}	8.480×10^{-12}	8.600×10^{-12}	8.650×10^{-12}
7, 17/2 → 8, 17/2	9.670×10^{-12}	1.070×10^{-11}	1.260×10^{-11}	1.460×10^{-11}	1.530×10^{-11}	1.550×10^{-11}	1.560×10^{-11}
7, 11/2 → 8, 17/2	6.450×10^{-12}	7.140×10^{-12}	8.420×10^{-12}	9.760×10^{-12}	1.020×10^{-11}	1.030×10^{-11}	1.040×10^{-11}
7, 15/2 → 8, 17/2	8.600×10^{-12}	9.520×10^{-12}	1.120×10^{-11}	1.300×10^{-11}	1.360×10^{-11}	1.380×10^{-11}	1.380×10^{-11}
7, 13/2 → 8, 17/2	7.520×10^{-12}	8.330×10^{-12}	9.820×10^{-12}	1.140×10^{-11}	1.190×10^{-11}	1.200×10^{-11}	1.210×10^{-11}

B

Millimetre and sub-millimetre spectroscopy of doubly deuterated acetaldehyde (CHD_2CHO) and first detection towards IRAS 16293-2422

In this Section of the Appendix, I present additional material complementary to the content presented in Chapter 3. This includes the fits of modelled CHD_2CHO spectra to the PILS observations as well as a list of all of the detected CHD_2CHO transitions towards the protostellar system IRAS 16293 - 2422.

B.1 Detected CHD_2CHO transitions

In this section, we present the fits of these transitions assuming a rotational temperature of 125 K over the PILS ALMA Band 7 spectrum in Figure B.1. Moreover, we present Table B.1, which lists the transitions of CHD_2CHO detected in the PILS ALMA Band 7 frequency range.

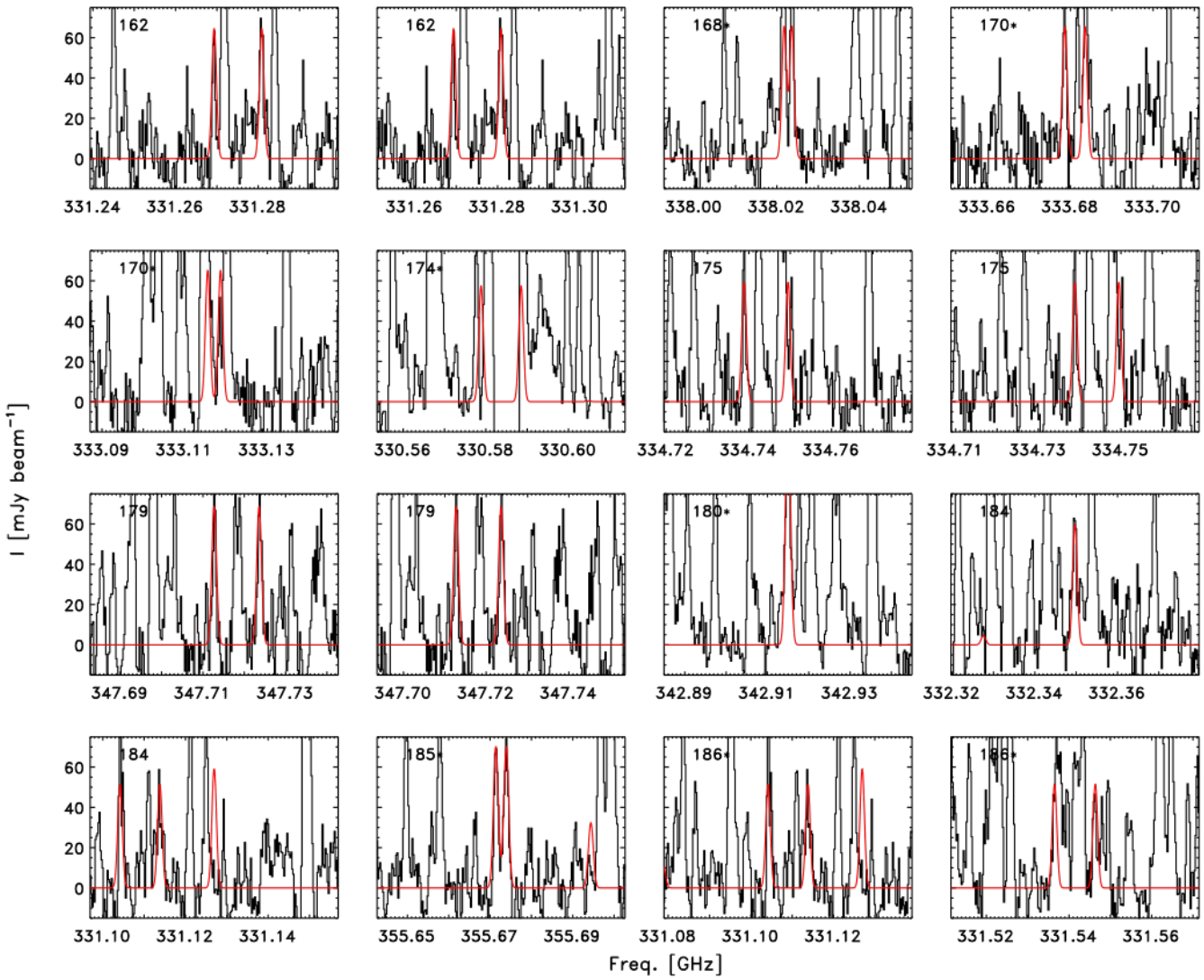

Figure B.1: 68 transitions of CHD_2CHO predicted to be the brightest, assuming a rotational temperature of 125 K. The red line indicates the predicted line intensities obtained by fitting the lines with the synthetic spectra, thereby constraining the column density. In each panel, the numbers on the upper left corner indicate the excitation temperature T_{ex} of the fitted transitions. An asterisk next to this number indicates situations where two lines from Table B.1 with similar values for E_u fall within 10 MHz of each other and are shown together in one panel.

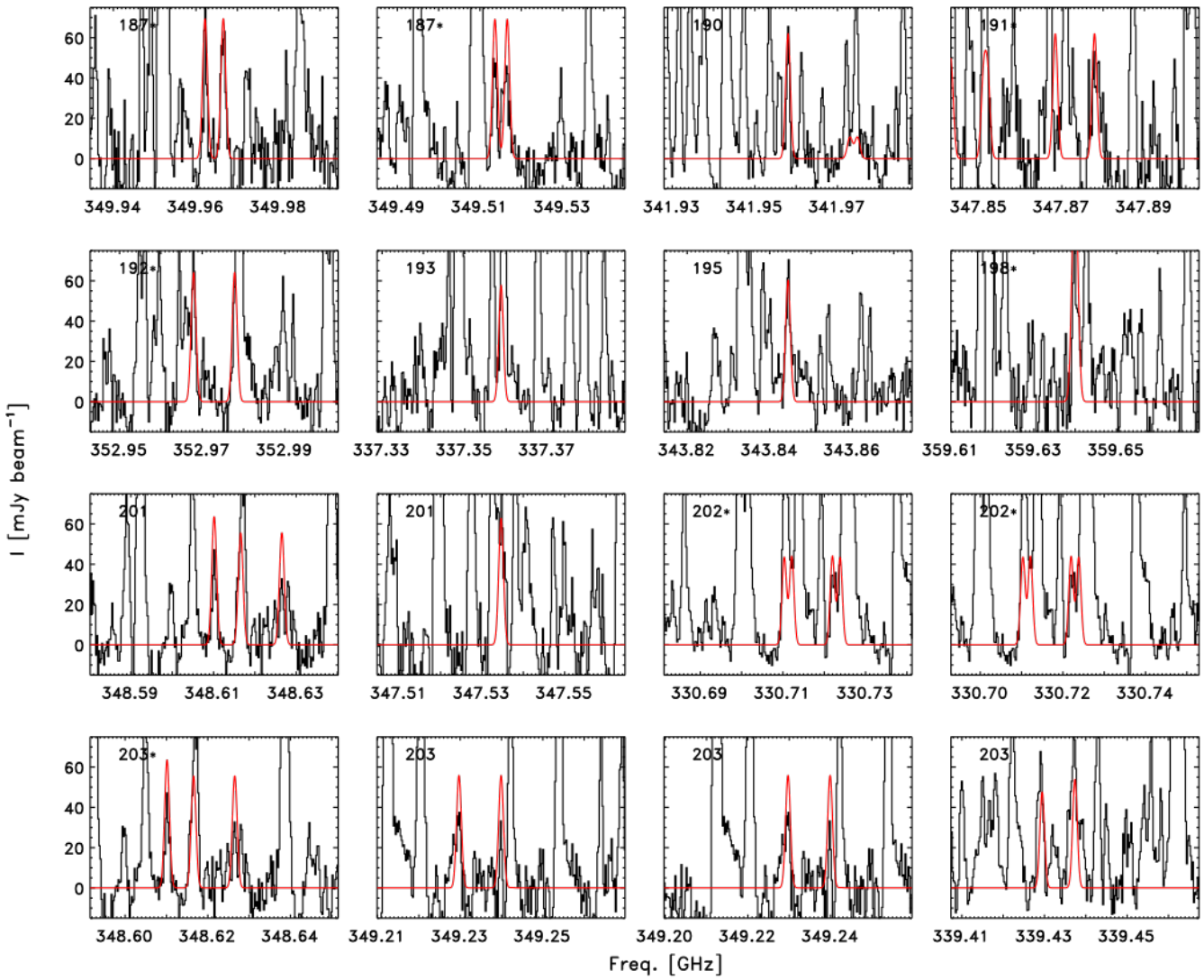

Figure B.1: continued.

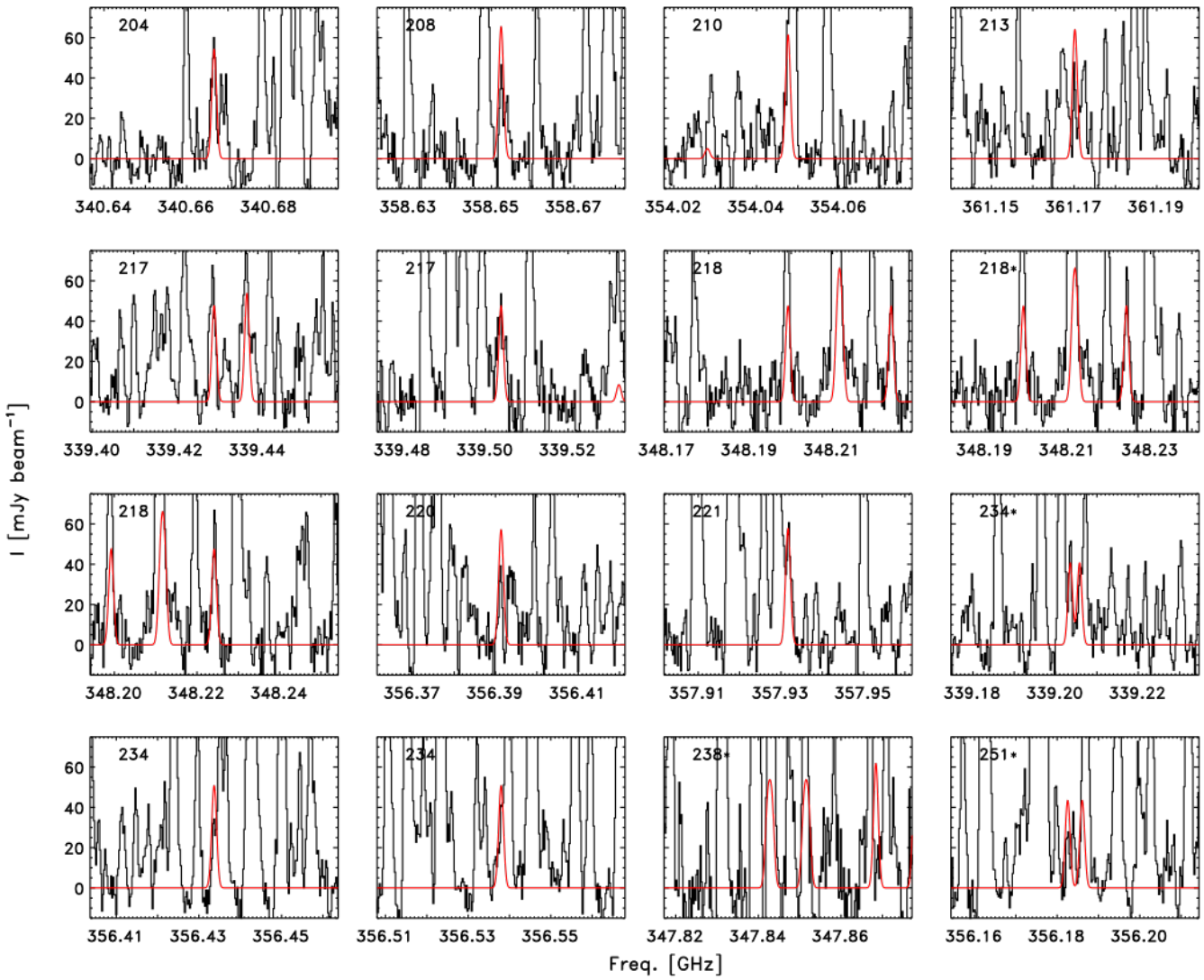

Figure B.1: continued.

Table B.1: Detected CHD_2CHO transitions towards IRAS 16293-2422.

Transition $J'_{K'_a,K'_c,v'} \rightarrow J_{K_a,K_c,v}$	Frequency MHz	E_{up} K	Transition $J'_{K'_a,K'_c,v'} \rightarrow J_{K_a,K_c,v}$	Frequency MHz	E_{up} K
$19_{3,17,0} \rightarrow 18_{3,16,0}$	330578.85	174	$20_{1,19,1} \rightarrow 19_{1,18,1}$	347712.71	179
$19_{3,17,1} \rightarrow 18_{3,16,1}$	330588.53	174	$20_{1,19,0} \rightarrow 19_{1,18,0}$	347723.60	179
$19_{5,14,0} \rightarrow 18_{5,13,0}$	330710.33	202	$20_{6,14,1} \rightarrow 19_{6,13,1}$	347843.28	238
$19_{5,15,0} \rightarrow 18_{5,14,0}$	330712.14	202	$20_{6,15,0} \rightarrow 19_{6,14,0}$	347851.04	238
$19_{5,14,1} \rightarrow 18_{5,13,1}$	330721.99	202	$20_{3,18,0} \rightarrow 19_{3,17,0}$	347868.44	191
$19_{5,15,1} \rightarrow 18_{5,14,1}$	330723.84	202	$20_{3,18,1} \rightarrow 19_{3,17,1}$	347877.93	191
$19_{4,16,0} \rightarrow 18_{4,15,0}$	331104.17	186	$20_{5,16,0} \rightarrow 19_{5,15,0}$	348199.22	218
$19_{4,16,1} \rightarrow 18_{4,15,1}$	331113.81	186	$20_{5,15,0} \rightarrow 19_{5,14,0}$*	348211.24	218
$20_{1,20,2} \rightarrow 19_{1,19,2}$	331126.94	184	$20_{5,16,1} \rightarrow 19_{5,15,1}$*	348212.14	218
$19_{1,18,1} \rightarrow 18_{1,17,1}$	331269.34	162	$20_{5,15,1} \rightarrow 19_{5,14,1}$	348224.15	218
$19_{1,18,0} \rightarrow 18_{1,17,0}$	331280.85	162	$21_{0,21,2} \rightarrow 20_{0,20,2}$	348610.15	201
$19_{4,15,0} \rightarrow 18_{4,14,0}$	331536.50	186	$20_{4,17,0} \rightarrow 19_{4,16,0}$	348616.55	203
$19_{4,15,1} \rightarrow 18_{4,14,1}$	331546.36	186	$20_{4,17,1} \rightarrow 19_{4,16,1}$	348626.53	203
$20_{0,20,2} \rightarrow 19_{0,19,2}$	332349.70	184	$20_{4,16,0} \rightarrow 19_{4,15,0}$	349229.71	203
$20_{1,20,1} \rightarrow 19_{1,19,1}$	333115.59	170	$20_{4,16,1} \rightarrow 19_{4,15,1}$	349239.90	203
$20_{1,20,0} \rightarrow 19_{1,19,0}$	333118.70	170	$21_{1,21,1} \rightarrow 20_{1,20,1}$	349513.62	187
$20_{0,20,1} \rightarrow 19_{0,19,1}$	333678.65	170	$21_{1,21,0} \rightarrow 20_{1,20,0}$	349516.59	187
$20_{0,20,0} \rightarrow 19_{0,19,0}$	333683.53	170	$21_{0,21,1} \rightarrow 20_{0,20,1}$	349962.17	187
$19_{2,17,1} \rightarrow 18_{2,16,1}$	338021.76	168	$21_{0,21,0} \rightarrow 20_{0,20,0}$	349966.60	187
$19_{2,17,0} \rightarrow 18_{2,16,0}$	338023.63	168	$20_{3,17,0} \rightarrow 19_{3,16,0}$	352967.92	192
$20_{5,16,2} \rightarrow 19_{5,15,2}$	339203.56	234	$20_{3,17,1} \rightarrow 19_{3,16,1}$	352977.86	192
$20_{5,15,2} \rightarrow 19_{5,14,2}$	339205.81	234	$21_{2,20,2} \rightarrow 20_{2,19,2}$	354047.62	210
$20_{2,19,1} \rightarrow 19_{2,18,1}$*	342914.69	180	$20_{2,18,1} \rightarrow 19_{2,17,1}$	355671.41	185
$20_{2,19,0} \rightarrow 19_{2,18,0}$*	342915.25	180	$20_{2,18,0} \rightarrow 19_{2,17,0}$	355673.91	185
$19_{3,16,0} \rightarrow 18_{3,15,0}$	334738.86	175	$21_{5,17,2} \rightarrow 20_{5,16,2}$	356182.55	251
$19_{3,16,1} \rightarrow 18_{3,15,1}$	334749.47	175	$21_{5,16,2} \rightarrow 20_{5,15,2}$	356186.06	251
$20_{2,19,2} \rightarrow 19_{2,18,2}$	337358.80	193	$21_{3,19,2} \rightarrow 20_{3,18,2}$	356391.35	220
$20_{4,17,2} \rightarrow 19_{4,16,2}$	339429.44	217	$21_{4,18,2} \rightarrow 20_{4,17,2}$	356433.69	234
$20_{3,18,2} \rightarrow 19_{3,17,2}$	339437.37	203	$21_{4,17,2} \rightarrow 20_{4,16,2}$	356537.97	234
$20_{4,16,2} \rightarrow 19_{4,15,2}$	339503.77	217	$21_{3,18,2} \rightarrow 20_{3,17,2}$	357931.72	221
$20_{3,17,2} \rightarrow 19_{3,16,2}$	340666.65	204	$21_{1,20,2} \rightarrow 20_{1,19,2}$	358652.34	208
$20_{1,19,2} \rightarrow 19_{1,18,2}$	341958.03	190	$21_{2,20,1} \rightarrow 20_{2,19,1}$*	359639.51	198
$20_{2,18,2} \rightarrow 19_{2,17,2}$	343844.42	195	$21_{2,20,0} \rightarrow 20_{2,19,0}$*	359640.38	198
$21_{1,21,2} \rightarrow 20_{1,20,2}$	347534.63	201	$21_{2,19,2} \rightarrow 20_{2,18,2}$	361170.20	213

Transitions with predicted intensities above 40 mJy beam^{-1} km s^{-1} shown in Fig. B.1 with the fitted column density and excitation temperature described in Sect. 3.3. The frequencies appear in MHz and the upper energies in K. * Transitions separated by less than 1 km s^{-1} (the FWHM of lines towards IRAS16293B) that consequently appear blended in Fig. B.1.

C

High sensitivity and spectral resolution molecular line observations towards the L1544 pre-stellar core: challenges to current models

In this Section of the Appendix, I present additional material to complement the results shown in Chapter 4. This includes the combined main and rare isotopologue fits as well as the optically thick line model results that were not included in the main text.

C.1 CS + $C^{34}S$ Modelling

In an attempt to improve the fit and parameter constraints presented in Section 4.4.2, we construct a new model which fits the CS and $C^{34}S$ (2 - 1) observed lines simultaneously. The idea behind this combined modelling is to have the same amount of variables explored with the MCMC with more observational constraints coming from two observed spectral lines instead of one. This model assumes that the main and rarer isotopologue share the same abundance profile, and the rarer isotopologue profile is scaled down by the $^{32}S/^{34}S = 22$ ratio (Wilson & Rood 1994). Thus, we have the same variables as for the CS and $C^{34}S$ separated models: a_{in}, a_{out}, r, f_v and v_{turb}. We test this combined modelling for both the "non-extended" and the "extended" models.

The combined "non-extended" model results for CS and $C^{34}S$ can be found in Figures C.2 and C.3, respectively. The best model fit parameters are presented in Table C.1, and the corner plot is shown in Figure C.1. The CS (2 - 1) modelled transition does not fit the observations. The model predicts an enhanced self-absorption, seen as a more pronounced dip w.r.t. the observations, and an enhanced peak asymmetry. The $C^{34}S$ (2 - 1) modelled transition reproduces the line worse compared to the stand-alone $C^{34}S$ model in Section 4.4.1. The best model parameters show values that are in between the values found for the CS and $C^{34}S$ alone fits with a tendency to be closer to the $C^{34}S$ parameters. The combined "non-extended" model mainly fits $C^{34}S$, and thus, the modelled parameters reflect the physical and chemical conditions in the inner part of the core.

In view of the combined "non-extended" model failing to reproduce the CS line and the results reflecting the inner part of the core, we proceed to test the combined "extended" model. The combined "extended" model results for CS and $C^{34}S$ can be found in Figures C.5 and C.6, respectively. The best model parameters are presented in Table C.2, and the corner plot is shown in Figure C.4. In this case, the fit for the CS (2 - 1) line improves w.r.t. the combined "non-extended" model (Figure C.2). On the other hand, this model fails to reproduce the $C^{34}S$(2 - 1) line profile. The best model parameter values are also in between the alone CS and $C^{34}S$ models, but in this case, inclined to the alone CS parameters. The combined "extended" model is fitting primarily the CS transition, with the parameters tracing the outer parts of the core.

From these results, we confirm that $C^{34}S$(2 - 1) traces the inner core and that CS (2 - 1) traces an outer region of the core.

Table C.1: CS + $C^{34}S$ (2 - 1) best "non-extended" model parameters

a_{in}	$1.45^{+12.84}_{-1.32} \times 10^{-12}$
a_{out}	$4.70^{+3.13}_{-0.73} \times 10^{-8}$
r (au)	4518^{+768}_{-725}
f_v	$1.21^{+0.09}_{-0.05}$
v_{turb} (km/s)	$0.059^{+0.090}_{-0.011}$

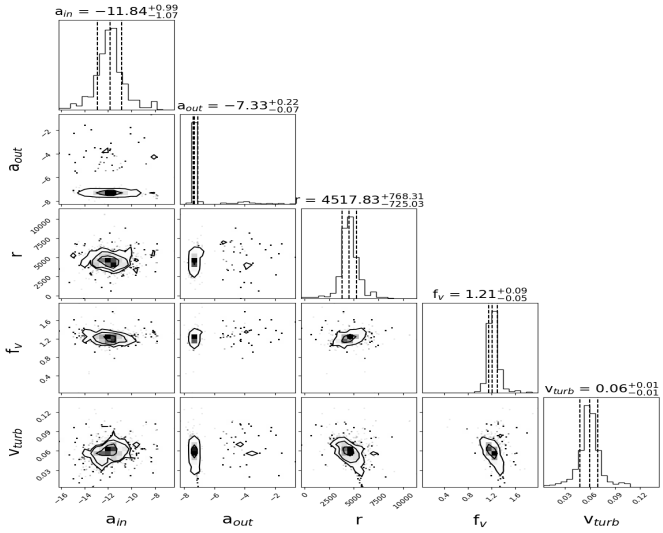

Figure C.1: Corner plot for the CS + $C^{34}S$ "non-extended" model.

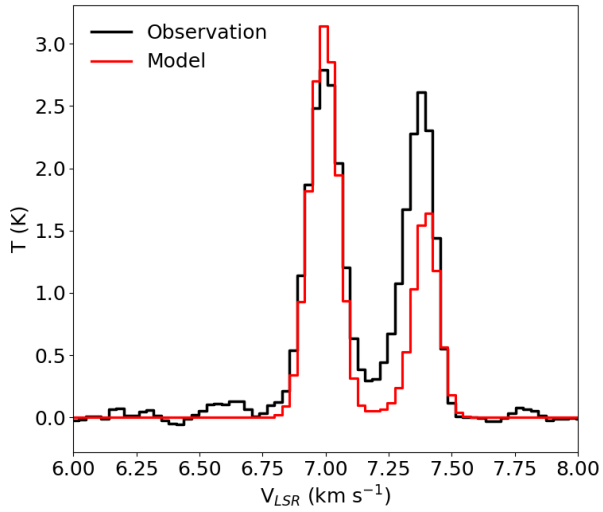

Figure C.2: CS (2-1) observations towards the L1544 dust peak in black and modelling results in red.

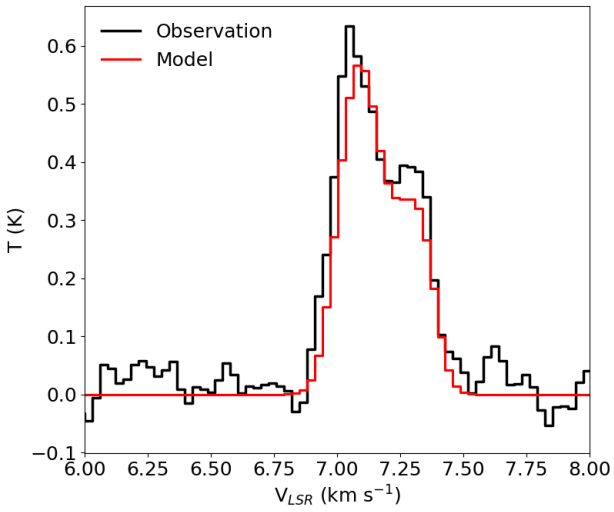

Figure C.3: $C^{34}S$ (2-1) observations towards the L1544 dust peak in black and modelling results in red.

Table C.2: CS + $C^{34}S$ (2 - 1) best "extended" model parameters

a_{in}	$7.64^{+46.43}_{-6.34} \times 10^{-13}$
a_{out}	$5.69^{+19.78}_{-0.68} \times 10^{-9}$
r (au)	3738^{+1570}_{-236}
f_v	$0.51^{+0.67}_{-0.04}$
v_{turb} (km/s)	$0.112^{+0.004}_{-0.028}$

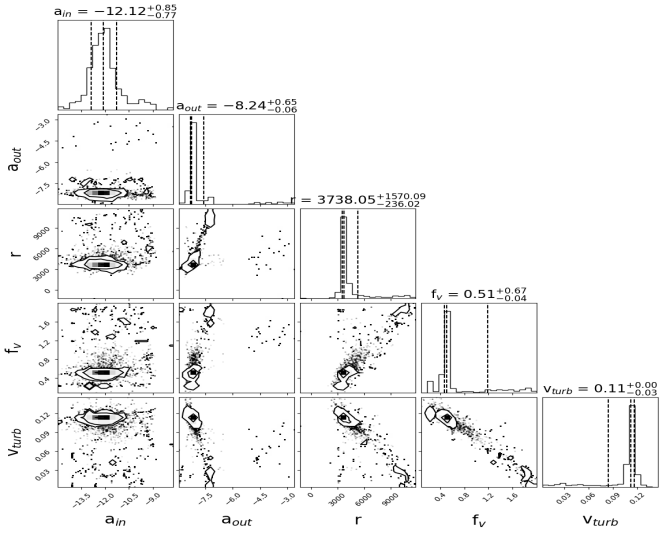

Figure C.4: Corner plot for the CS + $C^{34}S$ "extended" model.

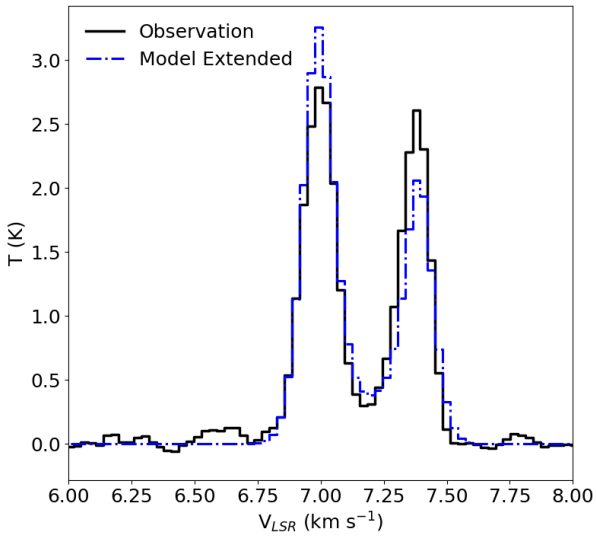

Figure C.5: CS (2-1) observations towards the L1544 dust peak in black and modelling results in a dash-dotted blue line.

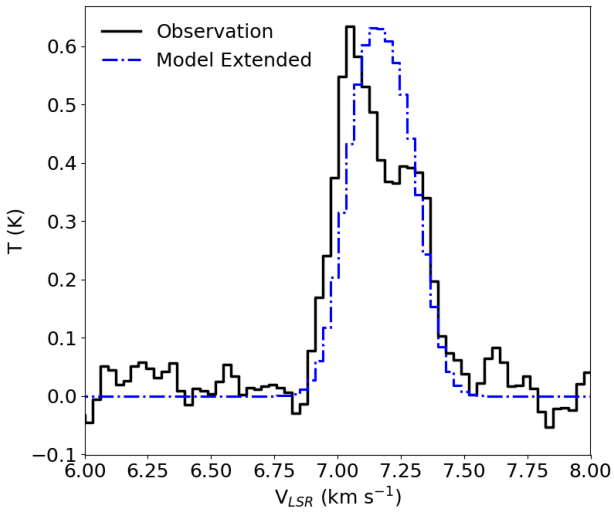

Figure C.6: $C^{34}S$ (2-1) observations towards the L1544 dust peak in black and modelling results in a dash-dotted blue line.

C.2 SO + ^{34}SO Modelling

With the same aim as for CS + C^{34}S, we construct a new model to fit SO and ^{34}SO (2,3 - 1,2) simultaneously. As for CS + C^{34}S (Section C.1) the model for SO and ^{34}SO assumes that the main and rarer isotopologue share the same abundance profile but the rarer isotopologue profile to be scaled down by the ^{32}S/^{34}S = 22 ratio (Wilson & Rood 1994). As the SO fit the observations with the "non-extended" model, we try the SO + ^{34}SO combined fit with the "non-extended model.

The fit results can be found in Figures C.8 and C.9. The best model parameters are presented in Table C.3 and the corner plot in Figure C.7. The combined model fits SO and ^{34}SO similarly as the respective single models do (Figures 4.23 and 4.8, respectively). The model parameters lie between the values for the single SO and ^{34}SO models, leaning towards the SO alone fit values.

Table C.3: SO + ^{34}SO (2,3 - 1,2) combined "non-extended" model parameters.

a_{in}	$6.11^{+100.03}_{-5.46} \times 10^{-13}$
a_{out}	$1.70^{+0.60}_{-0.41} \times 10^{-8}$
r (au)	5627^{+414}_{-1150}
$v_{scaling}$	$1.16^{+0.29}_{-0.27}$
v_{turb} (km/s)	$0.095^{+0.015}_{-0.029}$

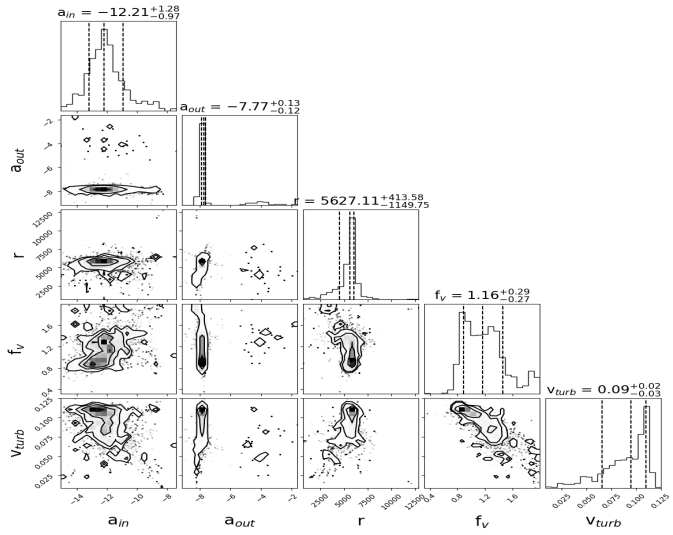

Figure C.7: Corner plot of the parameters used for the SO + ^{34}SO "non-extended" model.

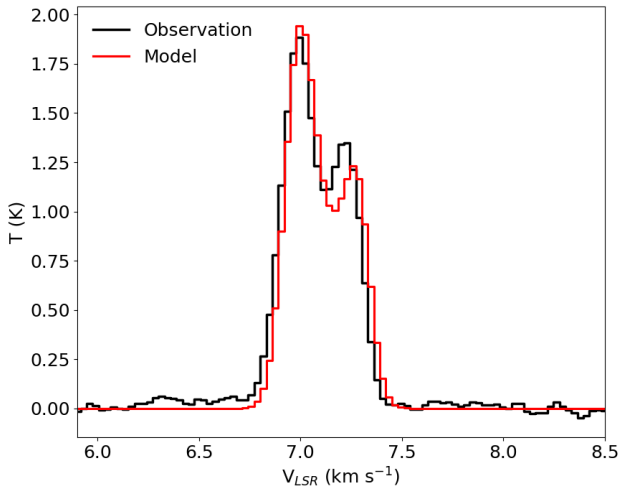

Figure C.8: SO (2,3 - 1,2) observations towards the L1544 dust peak in black and combined modelling results in red.

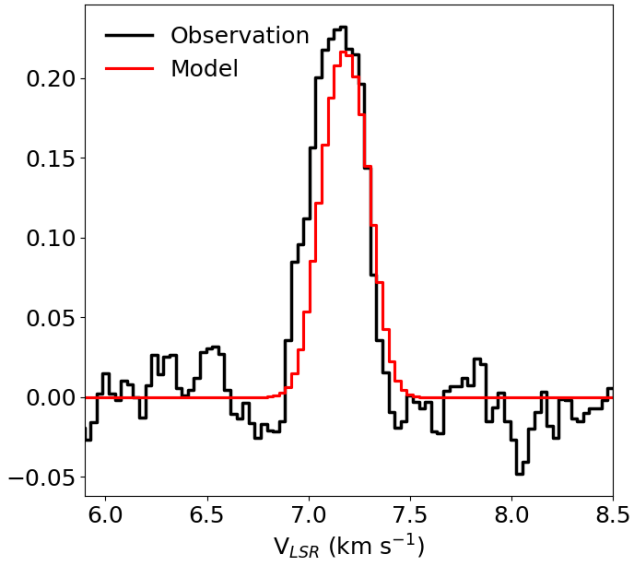

Figure C.9: ^{34}SO (2,3 - 1,2) observations towards the L1544 dust peak in black and combined modelling results in red.

C.3 HCO$^+$

The HCO$^+$ (1 - 0) line shows a pronounced self-absorption dip that reaches the spectral baseline as well as an asymmetric relative component intensity (third-column, first-row panel in Figure 4.1). Moreover, there is the presence of a blue excess feature on the lowest velocity area of the line ($\sim$ 6.9 km/s). With the LOC RT model utilized here, we reproduce the HCO$^+$ (1-0) fit performed by Redaelli et al. (2022) using the RT code MOLLIE (Keto & Field 2005). This is shown in Section C.3.1 in the Appendix.

In this Section, we test the LOC + MCMC methodology to fit the HCO$^+$ observations. As previous works pointed out the need for an external layer (Redaelli et al. 2019, 2022), we modelled HCO$^+$ with the "extended" model described in Section 4.3.2 with some adjustments. The velocity and n_{H_2}, instead to the value at 0.32 pc on the Keto et al. (2015) model, were fixed to -0.05 km/s and 27 cm^{-3}, respectively (Redaelli et al. 2022). The abundance of HCO$^+$ in the external layer is kept constant with the value of the abundance profile (Sipilä et al. 2015) at 0.32 pc, as done in Redaelli et al. (2022).

This approach reproduces the HCO$^+$ (1 - 0) fairly well, except for the separation between the two peaks, which is overestimated by the model (Figure C.10). The parameters are presented in Table C.4. The variables histograms in the corner plot (Figure C.11) deviate from the expected Gaussian profiles and are not well constrained.

In view of these results, and thinking the blue excess feature could be interfering with the modelling of the main line components, we perform an additional test where we remove the blue excess feature from the spectrum. The blue excess feature was removed by fitting two Gaussian profiles in the main blue and red components of the HCO$^+$ line and subtracting the rest with the CLASS software. We then test our "extended" model with this new spectrum with the blue excess feature removed and present the results in Figure C.12. The model fit does not improve from the original observation fit presented in Figure C.10. The parameters (Table C.5) are the same within errors compared to the original observation parameters in Table C.4. The corner plot (Figure C.13) also looks similar. Removing the blue excess feature does not improve the fit.

Table C.4: HCO$^+$ (1 - 0) "extended" model parameters.

a_{in}	$2.73^{+103.68}_{-2.45} \times 10^{-13}$
a_{out}	$2.35^{+5.56}_{-0.20} \times 10^{-10}$
r (au)	1554^{+2381}_{-641}
f_v	$1.62^{+0.14}_{-0.14}$
v_{turb} (km/s)	$0.107^{+0.013}_{-0.004}$

Table C.5: HCO$^+$ (1 - 0) without blue excess "extended" model parameters.

a_{in}	$4.58^{+1074.37}_{-4.43} \times 10^{-13}$
a_{out}	$2.79^{+7.58}_{-1.09} \times 10^{-10}$
r (au)	3044^{+3998}_{-1928}
f_v	$1.82^{+0.14}_{-0.26}$
v_{turb} (km/s)	$0.117^{+0.005}_{-0.260}$

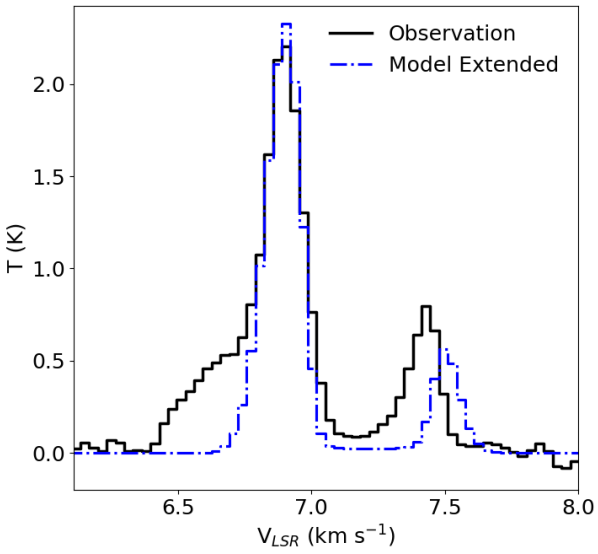

Figure C.10: HCO^+ (1 - 0) observations towards the L1544 dust peak in black and "extended" modelling results in dash-dotted blue.

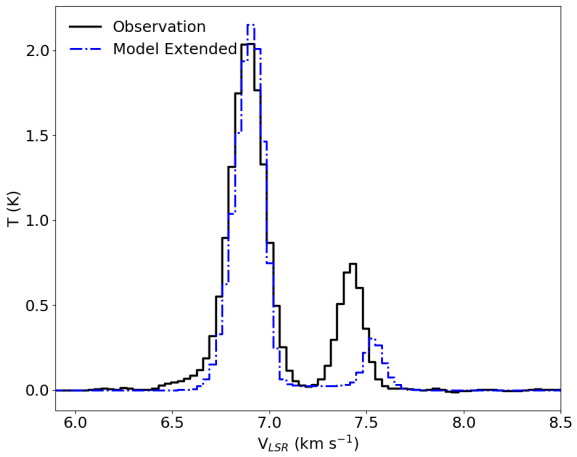

Figure C.12: HCO^+ (1 - 0) observations towards the L1544 dust peak without the blue extended feature in black and "extended" modelling results in dash-dotted blue.

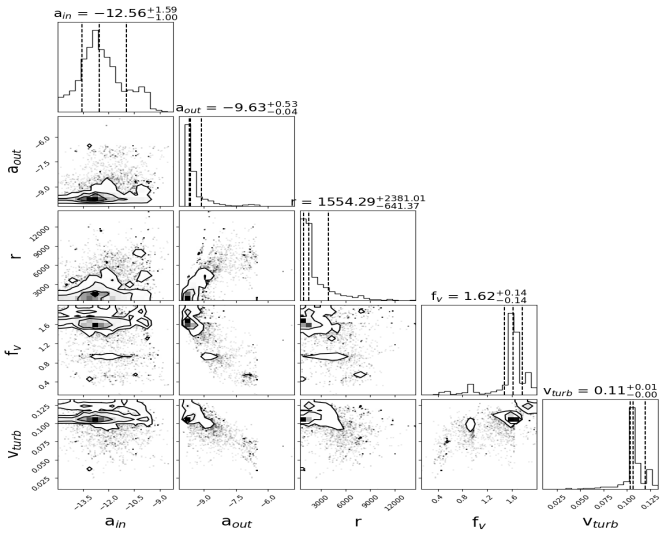

Figure C.11: Corner plot for the results displayed in Figure C.10.

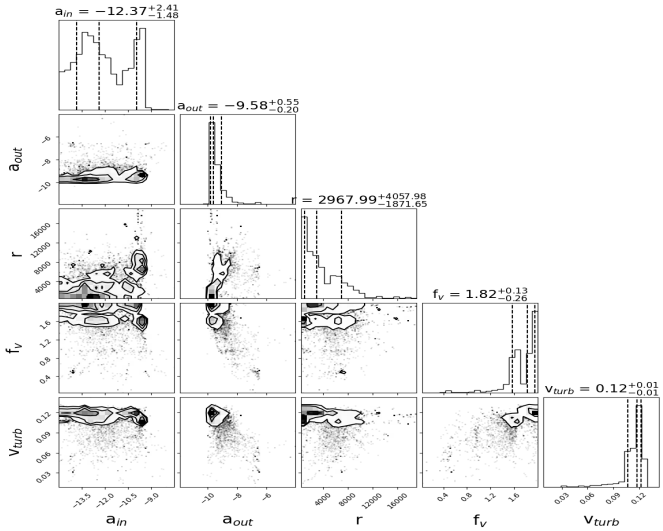

Figure C.13: Corner plot for the results displayed in Figure C.12.

In addition, we also tested fitting HCO^+ and $HC^{17}O^+$ together. This test does not add new information than the one found for the single HCO^+ and $H^{17}CO^+$ model fits. This test can be found in Section C.3.2 in the Appendix.

C.3.1 HCO^+ Redaelli et al. 2022 reproduction.

This line was successfully reproduced using the HCO^+ abundance profile from the pyRate chemical model described in Sipilä et al. (2015) in Redaelli et al. (2022). When using the same modelling approach as (Redaelli et al. 2022), we can reproduce their results (right panel in Figure 7, Redaelli et al. (2022)). See Figure C.14. The model intensity increase of ∼14% in our model.

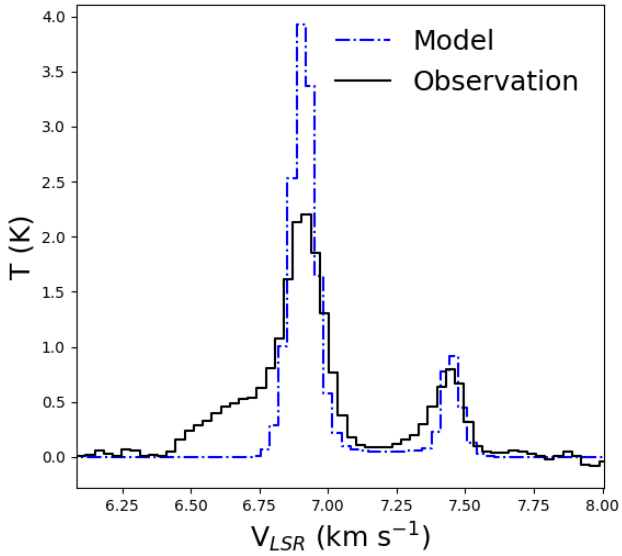

Figure C.14: The model using the approach on Redaelli et al. (2022) is shown in a dash-dotted blue line. Observations towards the L1544 dust peak are shown in black.

C.3.2 HCO^+ + $HC^{17}O^+$ modelling

The combined HCO^+ + $HC^{17}O^+$ (1 - 0) fit has been constructed similarly as the CS + $C^{34}S$ and the SO + ^{34}SO pair fits. The abundance profile used is the same as the one described in Section C.3 for HCO^+ and it is scaled down by $[^{16}O/^{17}O] = 2044$ (Penzias 1981; Wilson & Rood 1994) for $HC^{17}O^+$. As for the HCO^+ alone fit, we only test the "extended" fit.

The HCO^+ + $HC^{17}O^+$ "extended" model fits are shown on Figures C.16 and C.17. The best model parameters are presented in Table C.6, and the corner plot is shown in Figure C.15. The HCO^+ modelled spectrum does not reproduce the observed relative intensity of the blue and red components but reproduces the blue and red peak separation. The $HC^{17}O^+$ modelled spectrum does not fit the observed line intensity nor its profile. The HCO^+ + $HC^{17}O^+$ combine fit does not improve the constraints on the fractional abundance profile compared to the separate HCO^+ and $HC^{17}O^+$ fits.

Table C.6: HCO^+ + $HC^{17}O^+$ (1 - 0) best "extended" model parameters.

a_{in}	$7.94^{+370.50}_{-7.69} \times 10^{-13}$
a_{out}	$3.18^{+45.01}_{-1.36} \times 10^{-9}$
r (au)	5444^{+6943}_{-4632}
$v_{scaling}$	$1.08^{+0.41}_{-0.17}$
v_{turb} (km/s)	$0.081^{+0.022}_{-0.031}$

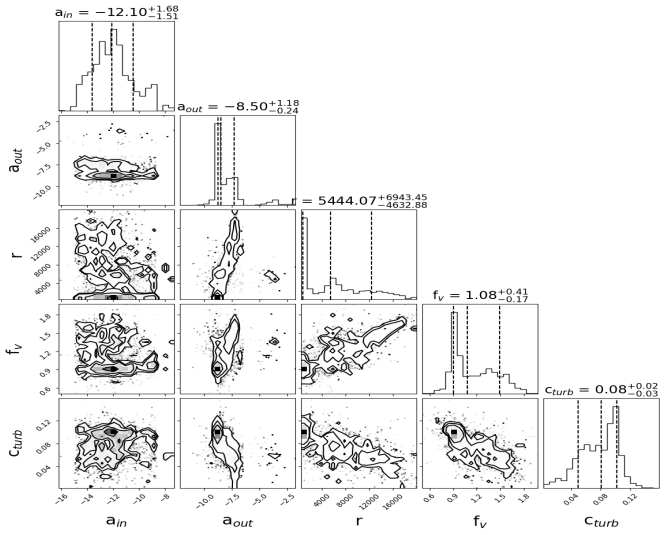

Figure C.15: Corner plot of the parameters used for the HCO^+ + $HC^{17}O^+$ "extended" model.

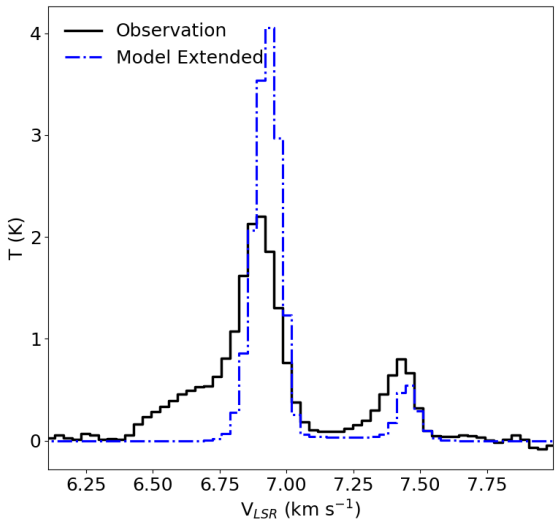

Figure C.16: HCO$^+$ (1 - 0) observations towards the L1544 dust peak in black and combined modelling results in a dash-dotted blue line.

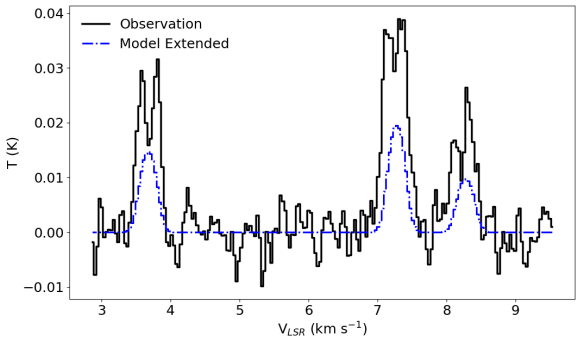

Figure C.17: HC^{17}O$^+$ (1 - 0) observations towards the L1544 dust peak in black and combined modelling results in a dash-dotted blue line.

Additionally, we tested the combined "extended" without the blue excess feature removed model. The HCO$^+$ and HC^{17}O$^+$ modelled spectra are shown in Figures C.19 and C.20, respectively. The best model parameters are presented in Table C.7, and the corner plot is shown in Figure C.18. The HCO$^+$ modelled spectrum does not improve w.r.t. the one shown in Figure C.16. The HC^{17}O$^+$ modelled spectrum does not improve from the one shown in Figure C.17. The combined HCO$^+$ and HC^{17}O$^+$ fit with the HCO$^+$ blue excess feature removed does not result in a better constrain of the fractional abundance profile w.r.t. the combined HCO$^+$ + HC^{17}O$^+$ nor the fit of HCO$^+$ alone. Further work is needed to understand the behaviour of the LOC + MCMC approach when modelling the HCO$^+$ transition.

Table C.7: HCO^+ + $HC^{17}O^+$ (1 - 0) best "extended" without the blue excess feature model parameters.

a_{in}	$6.44^{+301.88}_{-6.09} \times 10^{-13}$
a_{out}	$1.73^{+7.41}_{-1.34} \times 10^{-9}$
r (au)	6635^{+3303}_{-2650}
$v_{scaling}$	$1.49^{+0.14}_{-0.42}$
v_{turb} (km/s)	$0.081^{+0.020}_{-0.019}$

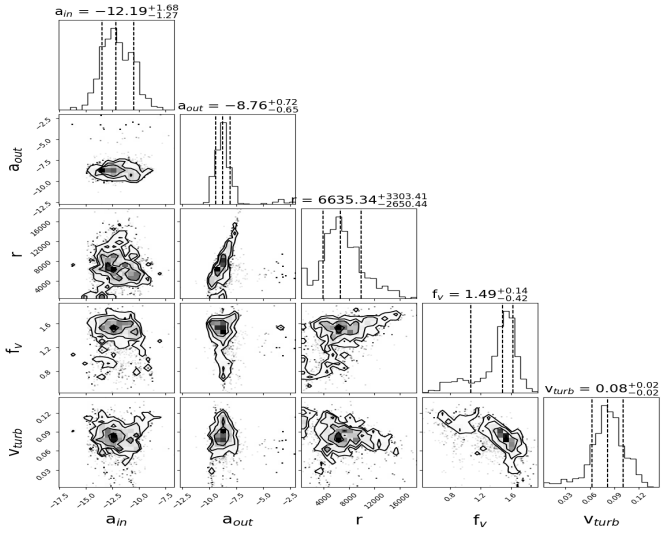

Figure C.18: Corner plot of the parameters used for the HCO^+ + $HC^{17}O^+$ "extended" without the blue excess feature model.

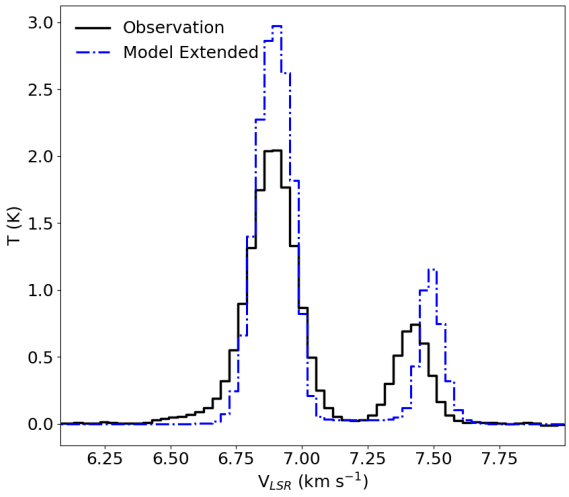

Figure C.19: HCO^+ (1 - 0) observations towards the L1544 dust peak in black and combined modelling results in a dash-dotted blue line.

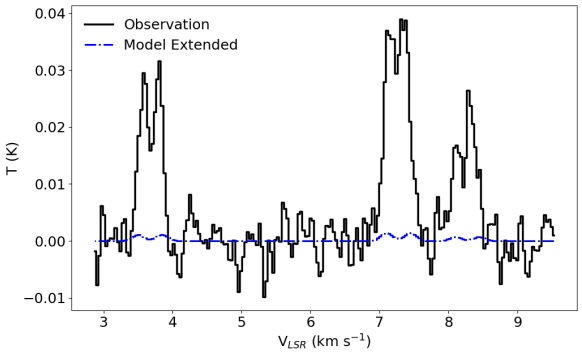

Figure C.20: $HC^{17}O^+$ (1 - 0) observations towards the L1544 dust peak in black and combined modelling results in a dash-dotted blue line.

C.4 H_2CO

The H_2CO ($2_{1,2}$ - $1_{1,1}$) transition presents a self-absorption dip that reaches the baseline (fourth-column, first-row panel in Figure 4.1). Moreover, the blue component is brighter than the red component. The asymmetry of the blue and red peaks indicates H_2CO traces contracting gas. The results for the "non-extended" modelling are presented in a solid red line in Figure C.21. The best model parameters are presented in Table C.8. The corner plot presents for all of the parameters, except for a_{in}, two peaks indicating two mostly-equal best possible solutions (Figure C.21).

In view of these results, we test the "extended" model. The constant H_2CO abundance profile in the external layer is fixed to the value 3.7×10^{-9} as found for diffuse clouds (Snow & McCall 2006). The "extended" model under-reproduces the line intensity (blue dash-dotted line in Figure C.21). This model is not an improvement w.r.t. the "non-extended" model results. The best model parameters are presented in Table C.9. The a_{out} value ($1.02^{+1.32}_{-0.53} \times 10^{-9}$) is lower than for the fixed a_{ext} value of 3.7×10^{-9}. Nevertheless, we don't expect the H_2CO abundance to be higher on an external layer, which should resemble a diffuse cloud. The corner plot for the extended model (Figure C.23) shows single-peaked histograms.

Table C.8: H_2CO ($2_{1,2}$ - $1_{1,1}$) best "non-extended" model parameters

a_{in}	$5.26^{+37.30}_{-4.43} \times 10^{-13}$
a_{out}	$1.30^{+0.62}_{-1.27} \times 10^{-8}$
r (au)	7684^{+1274}_{-5336}
f_v	$0.89^{+1.05}_{-0.35}$
v_{turb} (km/s)	$0.107^{+0.018}_{-0.056}$

Table C.9: H_2CO ($2_{1,2}$ - $1_{1,1}$) best "extended" model parameters

a_{in}	$3.68^{+19.87}_{-3.37} \times 10^{-13}$
a_{out}	$1.02^{+1.32}_{-0.53} \times 10^{-9}$
r (au)	4427^{+1438}_{-1141}
f_v	$1.57^{+0.09}_{-0.19}$
v_{turb} (km/s)	$0.062^{+0.013}_{-0.018}$

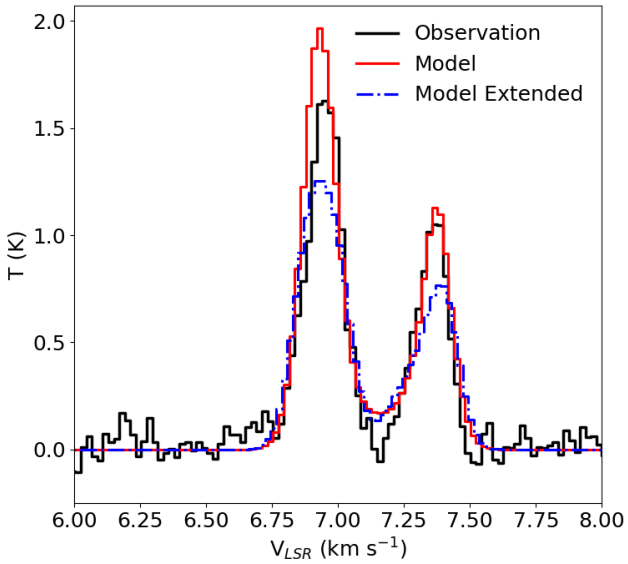

Figure C.21: H_2CO ($2_{1,2}$ - $1_{1,1}$) observations towards the L1544 dust peak are plotted in black, the "non-extended" modelling result is plotted in a solid red line, and the "extended" modelling result is plotted with a dash-dotted blue line.

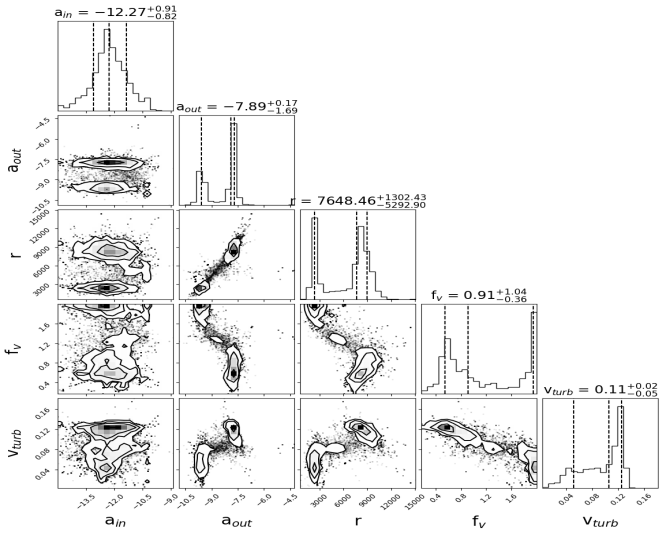

Figure C.22: Corner plot for the "non-extended" results displayed in Figure C.21.

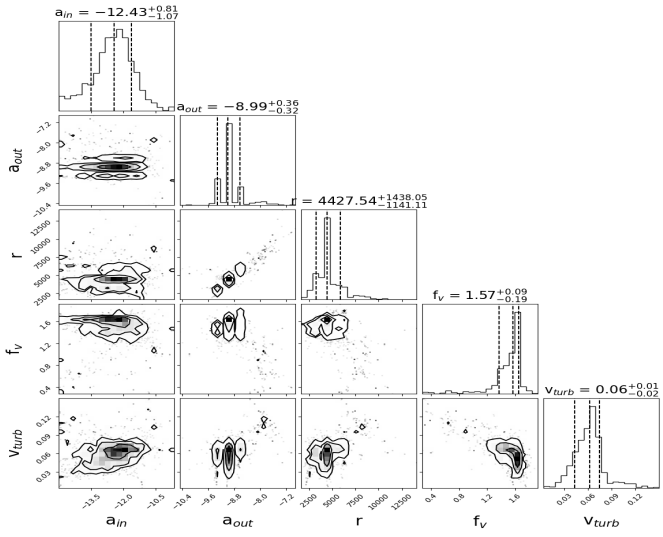

Figure C.23: Corner plot for the "extended" results displayed in Figure C.21.

C.5 c-C_3H_2

The c-C_3H_2 ($2_{1,2}$ - $1_{0,1}$) transition also presents a self-absorption feature but not as pronounced as for CS, HCO^+ and H_2CO (fourth-column, second-row in Figure 4.1). The blue and red peaks show similar intensities, hinting at this transition arising from a static layer (as seen for CS in Section 4.4.2).

The results of the "non-extended" model are shown with a solid red line in Figure C.24. The model fails to reproduce the relative intensity of the two observed c-C_3H_2 peaks. The parameters are presented in Table C.10. The histograms in the corner plot (Figure C.25), as seen for other optically think lines presented in this Section, deviate from a Gaussian shape.

We also tested the "extended" model to see if this would improve the fit w.r.t. the "non-extended" model. We set the c-C_3H_2 constant abundance value in the external layer to 6.4×10^{-10}, as seen in diffuse clouds (Snow & McCall 2006). In this case, the model reproduces better the relative intensity of the two line peaks (blue dash-dotted line in Figure C.24). The parameters are presented in Table C.11. The histograms for r and f_v are two-peaked (Figure C.26). All of the histograms deviate from a Gaussian shape.

The c-C_3H_2 ($2_{1,2}$ - $1_{0,1}$) transition is not constrained with the LOC + MCMC modelling approach.

Table C.10: c-C_3H_2 ($2_{1,2}$ - $1_{0,1}$) best "non-extended" model parameters

a_{in}	$2.72^{+58.66}_{-2.66} \times 10^{-13}$
a_{out}	$4.67^{+1.54}_{-0.10} \times 10^{-10}$
r (au)	1905^{+1331}_{-155}
f_v	$1.68^{+0.01}_{-0.15}$
v_{turb} (km/s)	$0.038^{+0.030}_{-0.005}$

Table C.11: c-C_3H_2 ($2_{1,2}$ - $1_{0,1}$) best "extended" model parameters

a_{in}	$3.07^{+464.67}_{-3.06} \times 10^{-13}$
a_{out}	$1.51^{+0.10}_{-0.13} \times 10^{-9}$
r (au)	1462^{+1675}_{-556}
f_v	$0.92^{+0.21}_{-0.18}$
v_{turb} (km/s)	$0.103^{+0.006}_{-0.017}$

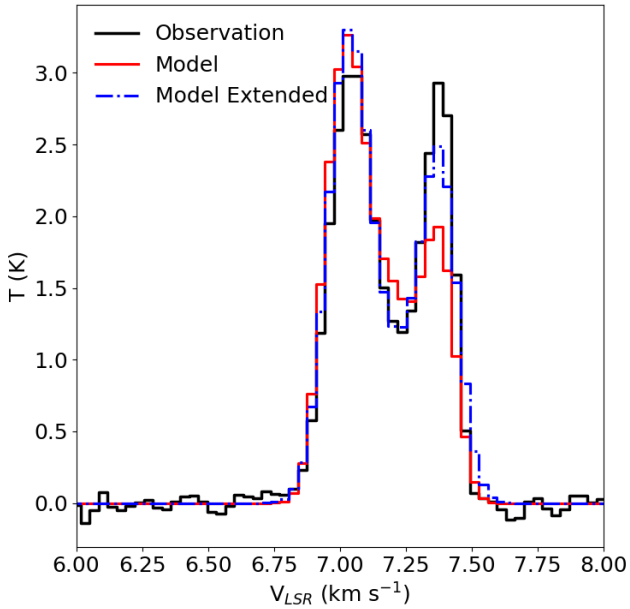

Figure C.24: The results of the c-C_3H_2 ($2_{1,2}$ - $1_{0,1}$) "non-extended" model are plotted with a solid red line, the "extended" model results are plotted with a blue dash-dotted line, and the observations towards the L1544 dust peak are plotted in black.

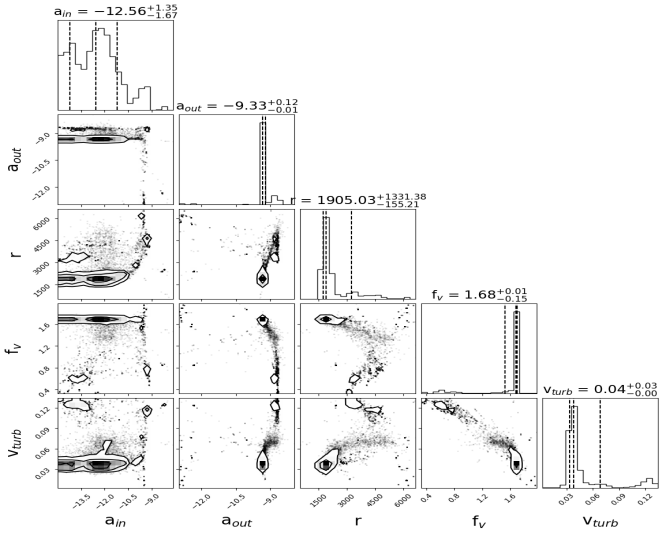

Figure C.25: Corner plot for the "non-extended" model results displayed in Figure C.24.

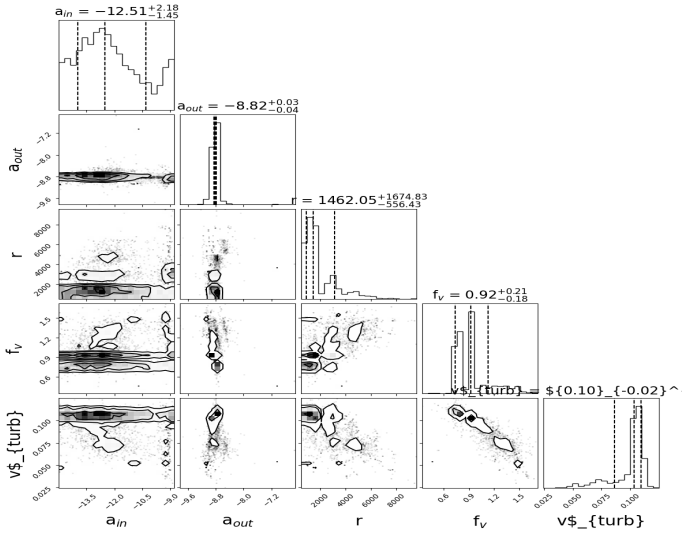

Figure C.26: Corner plot for the "extended" model results displayed in Figure C.24.

Bibliography

Adams, F. C. 2010, Annual Review of Astron. and Astrophysis., 48, 47

Alexander, M. H. 1985, Chem. Phys., 92, 337

Altwegg, K., Balsiger, H., & Fuselier, S. A. 2019, Annual Review of Astron. and Astrophysis., 57, 113

Ambrose, H. E., Shirley, Y. L., & Scibelli, S. 2021, Monthly Notices of the RAS, 501, 347

André, P., Di Francesco, J., Ward-Thompson, D., et al. 2014, in Protostars and Planets VI, ed. H. Beuther, R. S. Klessen, C. P. Dullemond, & T. Henning, 27

Bauder, A. & Günthard, H. H. 1976, J. Mol. Spectrosc., 60, 290

Bisschop, S. E., Jørgensen, J. K., Bourke, T. L., Bottinelli, S., & van Dishoeck, E. F. 2008, A&A, 488, 959

Bizzocchi, L., Caselli, P., Leonardo, E., & Dore, L. 2013, A&A, 555, A109

Bizzocchi, L., Lattanzi, V., Laas, J., et al. 2017, A&A, 602, A34

Bogey, M., Demuynck, C., & Destombes, J. L. 1981, Chemical Physics Letters, 81, 256

Bogey, M., Demuynck, C., & Destombes, J. L. 1986, Chemical Physics Letters, 125, 383

Bonnor, W. B. 1956, Monthly Notices of the RAS, 116, 351

Brünken, S., Müller, H. S. P., Lewen, F., & Winnewisser, G. 2003, Physical Chemistry Chemical Physics (Incorporating Faraday Transactions), 5, 1515

Bunker, P. & Jensen, P. 2018, Fundamentals of Molecular Symmetry, Chemical Physics (CRC Press LLC)

Burkhard, D. G. & Dennison, D. M. 1951, Phys. Rev., 84, 408

Butner, H. M., Charnley, S. B., Ceccarelli, C., et al. 2007, Astrophysical Journal, Letters, 659, L137

Calcutt, H., Jørgensen, J. K., Müller, H. S. P., et al. 2018, A&A, 616, A90

Cami, J., Bernard-Salas, J., Peeters, E., & Malek, S. E. 2010, Science, 329, 1180

Caselli, P., Bizzocchi, L., Keto, E., et al. 2017, A&A, 603, L1

Caselli, P. & Ceccarelli, C. 2012, A&A, 20, 56

Caselli, P., Keto, E., Bergin, E., et al. 2012, ApJ, 759, L37

Caselli, P., Myers, P., & Thaddeus, P. 1995, Astrophys.J.Lett., 455, L77

Caselli, P., Pineda, J., Zhao, B., et al. 2019, ApJ, 874, 89

Caselli, P., Pineda, J. E., Sipilä, O., et al. 2022, Astrophysical Journal, 929, 13

Caselli, P., Walmsley, C., Tafalla, M., Dore, L., & Myers, P. 1999, ApJ, 523, L165

Caselli, P., Walmsley, C., Zucconi, A., et al. 2002a, ApJ, 565, 331

Caselli, P., Walmsley, C. M., Zucconi, A., et al. 2002b, Astrophysical Journal, 565, 344

Ceccarelli, C., Caselli, P., Bockelée-Morvan, D., et al. 2014, in Protostars and Planets VI, ed. H. Beuther, R. S. Klessen, C. P. Dullemond, & T. Henning, 859–882

Chacón-Tanarro, A., Caselli, P., Bizzocchi, L., et al. 2019, A&A, 622, A141

Cheung, A. C., Rank, D. M., Townes, C. H., Thornton, D. D., & Welch, W. J. 1968, Physical Review Letters, 21, 1701

Cheung, A. C., Rank, D. M., Townes, C. H., Thornton, D. D., & Welch, W. J. 1969, Nature, 221, 626

Ciolek, G. E. & Basu, S. 2000, Astrophysical Journal, 529, 925

Clark, W. W. & De Lucia, F. C. 1976, Journal of Molecular Spectroscopy, 60, 332

Corey, G. C. & McCourt, F. R. 1983, J. Phys. Chem, 87, 2723

Coudert, L. H. & Hougen, J. T. 1988, J. Mol. Spectrosc., 130, 86

Coudert, L. H. & López, J. C. 2006, J. Mol. Spectrosc., 239, 135

Coudert, L. H., Margulès, L., Huet, T. R., et al. 2012, A&A, 543, A46

Coudert, L. H., Margulès, L., Vastel, C., et al. 2019, A&A, 624, A70

Coudert, L. H., Motiyenko, R. A., Margulès, L., & Kwabia Tchana, F. 2021, J. Mol. Spectrosc., 381, 111515

Coudert, L. H., Zemouli, M., Motiyenko, R. A., Margulès, L., & Klee, S. 2014, J. Chem. Phys., 140, 064307

Coutens, A., Ligterink, N. F. W., Loison, J. C., et al. 2019, A&A, 623, L13

Cox, A. P., Hughes, K. H., & MacDonald, J. N. 2003, Mol. Phys., 101, 569

Crapsi, A., Caselli, P., Malcolm, C., & Tafalla, M. 2007, A&A, 470, 221

Crapsi, A., Caselli, P., Walmsley, C. M., et al. 2005, Astrophysical Journal, 619, 379

Dagdigian, P. J. 2022, Monthly Notices of the RAS, 514, 2214

Dalgarno, A. & Lepp, S. 1984, Astrophysical Journal, Letters, 287, L47

Daniel, F., Faure, A., Pagani, L., et al. 2016, A&A, 592, A45

De Lucia, F. C., Herbst, E., Anderson, T., & Helminger, P. 1989, J. Mol. Spectrosc., 134, 395

Dore, L., Cazzoli, G., & Caselli, P. 2001a, A&A, 368, 721

Dore, L., Puzzarini, C., & Cazzoli, G. 2001b, Canadian Journal of Physics, 79, 359

Douglas, A. E. & Herzberg, G. 1941, Astrophysical Journal, 94, 381

Draine, B. T. 2011, Physics of the Interstellar and Intergalactic Medium

Drozdovskaya, M. N., Coudert, L. H., Margulès, L., et al. 2022, A&A, 659, A69

Drozdovskaya, M. N., Schroeder I, I. R. H. G., Rubin, M., et al. 2021, Monthly Notices of the RAS, 500, 4901

Ebert, R. 1955, Zeitschrift fuer Astrophysik, 37, 217

Elkeurti, M., Coudert, L. H., Medvedev, I. R., et al. 2010, J. Mol. Spectrosc., 263, 145

Endres, C. P., Schlemmer, S., Schilke, P., Stutzki, J., & Müller, H. S. P. 2016, Journal of Molecular Spectroscopy, 327, 95

Faure, A. & Lique, F. 2012, Monthly Notices of the RAS, 425, 740

Fayolle, E. C., Öberg, K. I., Jørgensen, J. K., et al. 2017, Nature Astronomy, 1, 703

Fedoseev, G., Qasim, D., Chuang, K.-J., et al. 2022, Astrophysical Journal, 924, 110

Ferrer Asensio, J., Spezzano, S., Caselli, P., et al. 2022, A&A, 667, A119

Foreman-Mackey, D., Hogg, D. W., Lang, D., & Goodman, J. 2013, Publications of the Astronomical Society of the Pacific, 125, 306–312

Franz, F. A. & Franz, J. R. 1966, Physical Review, 148, 82

Frisch, M. J., Trucks, G. W., Schlegel, H. B., et al. 2016, Gaussian 16 Revision B.01, gaussian Inc. Wallingford CT

Galli, D. & Palla, F. 1998, A&A, 335, 403

Galli, D., Walmsley, M., & Gonçalves, J. 2002, A&A, 394, 275

Galli, P. A. B., Loinard, L., Bouy, H., et al. 2019, A&A, 630, A137

Giers, K., Spezzano, S., Alves, F., et al. 2022, A&A, 664, A119

Gilmore, W., Morris, M., Johnson, D. R., et al. 1976, Astrophysical Journal, 204, 43

Gordy, W. & Cook, R. 1970, Microwave Molecular Spectra, Chemical applications of spectroscopy (Interscience Pub.)

Guélin, M., Cernicharo, J., & Linke, R. 1982, ApJ, 263, L89

Hacar, A., Clark, S., Heitsch, F., et al. 2022, Initial Conditions for Star Formation: A Physical Description of the Filamentary ISM

Hasegawa, T. I., Herbst, E., & Leung, C. M. 1992, Astrophysical Journal, Supplement, 82, 167

Hecht, K. T. & Dennison, D. M. 1957a, J. Chem. Phys., 26, 31

Hecht, K. T. & Dennison, D. M. 1957b, J. Chem. Phys., 26, 48

Hershbach, D. R. 1959, J. Chem. Phys., 31, 91

Hidaka, H., Watanabe, M., Kouchi, A., & Watanabe, N. 2009, Astrophysical Journal, 702, 291

Hollenbach, D. & Salpeter, E. E. 1971, Astrophysical Journal, 163, 155

Hougen, J. T. 1985, J. Mol. Spectrosc., 114, 395

Iijima, T. & Tsuchiya, S. 1972, J. Mol. Spectrosc., 44, 88

Ilyushin, V. V., Müller, H. S. P., Jørgensen, J. K., et al. 2022, A&A, 658, A127

Ilyushin, V. V., Zakharenko, O., Lewen, F., et al. 2020, Canadian Journal of Physics, 98, 530

Ivash, E. V. & Dennison, D. M. 1953, J. Chem. Phys., 21, 1804

Jensen, S. S., Jørgensen, J. K., Kristensen, L. E., et al. 2021, A&A, 650, A172

Jensen, S. S., Jørgensen, J. K., Kristensen, L. E., et al. 2019, A&A, 631, A25

Jensen, S. S., Spezzano, S., Caselli, P., Grassi, T., & Haugbølle, T. 2023, A&A, 675, A34

Jiménez-Serra, I., Vasyunin, A. I., Caselli, P., et al. 2016, Astrophysical Journal, Letters, 830, L6

Jin, M. & Garrod, R. T. 2020, ApJS, 249, 26

Jørgensen, J. K., Bourke, T. L., Nguyen Luong, Q., & Takakuwa, S. 2011, A&A, 534, A100

Jørgensen, J. K., Favre, C., Bisschop, S. E., et al. 2012, Astrophysical Journal, Letters, 757, L4

Jørgensen, J. K., Müller, H. S. P., Calcutt, H., et al. 2018, A&A, 620, A170

Jørgensen, J. K., Schöier, F. L., & van Dishoeck, E. F. 2005, A&A, 435, 177

Jørgensen, J. K., van der Wiel, M. H. D., Coutens, A., et al. 2016, A&A, 595, A117

Juvela, M. 2020, A&A, 644, A151

Kahane, C., Frerking, M. A., Langer, W. D., Encrenas, P., & Lucas, R. 1984, A&A, 137, 211

Keto, E. & Caselli, P. 2008, ApJ, 683, 238

Keto, E. & Caselli, P. 2010, Monthly Notices of the RAS, 402, 1625

Keto, E., Caselli, P., & Rawlings, J. 2015, MNRAS, 446, 3713

Keto, E. & Field, G. 2005, Astrophysical Journal, 635, 1151

Keto, E., Rawlings, J., & Caselli, P. 2014, MNRAS, 440, 2616

Keto, E. & Rybicki, G. 2010, ApJ, 716, 1315

Kilb, R. W., Lin, C. C., & Wilson Jr., E. B. 1957, J. Chem. Phys., 26, 1695

Kleiner, I. 2010, Journal of Molecular Spectroscopy, 260, 1

Kleiner, I. & Hougen, J. T. 2020, Journal of Molecular Spectroscopy, 368, 111255

Knude, J. & Hog, E. 1998, A&A, 338, 897

Koehler, J. S. & Dennison, D. M. 1940, J. Mol. Spectrosc., 57, 1006

Lattanzi, V., Bizzocchi, L., Vasyunin, A. I., et al. 2020, A&A, 633, A118

Lees, R. M. & Baker, J. G. 1968, J. Chem. Phys., 48, 5299

Lin, Y., Spezzano, S., Sipilä, O., Vasyunin, A., & Caselli, P. 2022, A&A, 665, A131

Linsky, J. L. 2003, Space Science Reviews, 106, 49

Lique, F., Daniel, F., Pagani, L., & Feautrier, N. 2015, MNRAS, 446, 1245

Loinard, L., Torres, R. M., Mioduszewski, A. J., & Rodríguez, L. F. 2008, Astrophysical Journal, Letters, 675, L29

Lombardi, M., Lada, C. J., & Alves, J. 2008, A&A, 489, 143

Mangum, J. G. & Shirley, Y. L. 2015, Publications of the ASP, 127, 266

Manigand, S., Calcutt, H., Jørgensen, J. K., et al. 2019, A&A, 623, A69

Manigand, S., Jørgensen, J. K., Calcutt, H., et al. 2020, A&A, 635, A48

Margulès, L., Coudert, L. H., Møllendal, H., et al. 2009, J. Mol. Spectrosc., 254, 55

Maureira, M. J., Gong, M., Pineda, J. E., et al. 2022, Astrophysical Journal, Letters, 941, L23

McKellar, A. 1940, Publications of the ASP, 52, 187

Mullins, A. M., Loughnane, R. M., Redman, M. P., et al. 2016, Monthly Notices of the RAS, 459, 2882

Mundy, L. G., Wootten, A., Wilking, B. A., Blake, G. A., & Sargent, A. I. 1992, Astrophysical Journal, 385, 306

Myers, P. C., Mardones, D., Tafalla, M., Williams, J. P., & Wilner, D. J. 1996, Astrophys. J. Lett., 465, L133

Nagaoka, A., Watanabe, N., & Kouchi, A. 2005, Astrophysical Journal, Letters, 624, L29

Nagaoka, A., Watanabe, N., & Kouchi, A. 2007, Journal of Physical Chemistry A, 111, 3016

Naraoka, H., Takano, Y., Dworkin, J. P., et al. 2023, Science, 379, abn9033

Ndao, M., Kwabia Tchana, F., Coudert, L. H., et al. 2015, J. Mol. Spectrosc., 326, 136

Pagani, L., Salez, M., & Wannier, P. G. 1992, A&A, 258, 479

Palmeirim, P., André, P., Kirk, J., et al. 2013, A&A, 550, A38

Parise, B., Castets, A., Herbst, E., et al. 2004, A&A, 416, 159

Parise, B., Ceccarelli, C., Tielens, A. G. G. M., et al. 2002, A&A, 393, L49

Pearson, J. C., Yu, S., & Drouin, B. J. 2012, J. Mol. Spectrosc., 280, 119

Penzias, A. 1981, ApJ, 249, 518

Persson, M. V., Jørgensen, J. K., Müller, H. S. P., et al. 2018, A&A, 610, A54

Pety, J. 2005, in SF2A-2005: Semaine de l'Astrophysique Francaise, ed. F. Casoli, T. Contini, J. M. Hameury, & L. Pagani, 721

Pickett, H. M., Poynter, R. L., Cohen, E. A., et al. 1998, 60, 883

Pineda, J. E., Arzoumanian, D., Andre, P., et al. 2023, in Astronomical Society of the Pacific Conference Series, Vol. 534, Protostars and Planets VII, ed. S. Inutsuka, Y. Aikawa, T. Muto, K. Tomida, & M. Tamura, 233

Redaelli, E., Bizzocchi, L., Caselli, P., et al. 2018, A&A, 617, A7

Redaelli, E., Bizzocchi, L., Caselli, P., et al. 2019, A&A, 629, A15

Redaelli, E., Chacón-Tanarro, A., Caselli, P., et al. 2022, Astrophysical Journal, 941, 168

Redaelli, E., Sipilä, O., Padovani, M., et al. 2021, A&A, 656, A109

Richard, C., Jørgensen, J. K., Margulès, L., et al. 2021, A&A, 651, A120

Ruffle, D. P., Hartquist, T. W., Caselli, P., & Williams, D. A. 1999, Monthly Notices of the RAS, 306, 691

Rybicki, G. & Hummer, D. 1991, A&A, 245, 171

Scibelli, S. & Shirley, Y. 2020, Astrophysical Journal, 891, 73

Shu, F. H. 1977, Astrophysical Journal, 214, 488

Sipilä, O. & Caselli, P. 2018, A&A, 615, A15

Sipilä, O., Caselli, P., & Harju, J. 2015, A&A, 578, A55

Sipilä, O., Caselli, P., Redaelli, E., Juvela, M., & Bizzocchi, L. 2019, MNRAS, 487, 1269

Sipilä, O., Caselli, P., Redaelli, E., & Spezzano, S. 2022 Submitted, A&A

Snow, T. P. & McCall, B. J. 2006, Annual Review of Astron. and Astrophysis., 44, 367

Sohn, J., Lee, C. W., Park, Y.-S., et al. 2007, ApJ, 664, 928

Spezzano, S., Brünken, S., Schilke, P., et al. 2013, Astrophysical Journal, Letters, 769, L19

Spezzano, S., Caselli, P., Bizzocchi, L., Giuliano, B. M., & Lattanzi, V. 2017, A&A, 606, A82

Spezzano, S., Sipilä, O., Caselli, P., et al. 2022, A&A, 661, A111

Stahler, S. W. & Palla, F. 2004, The Formation of Stars

Swade, D. A. 1989, Astrophysical Journal, 345, 828

Tafalla, M., Mardones, D., Myers, P., et al. 1998, ApJ, 504, 900

Taquet, V., Ceccarelli, C., & Kahane, C. 2012, A&A, 538, A42

Taquet, V., Charnley, S. B., & Sipilä, O. 2014, Astrophysical Journal, 791, 1

Taquet, V., Peters, P. S., Kahane, C., et al. 2013, A&A, 550, A127

Tiemann, E. 1974, Journal of Physical and Chemical Reference Data, 3, 259

Tinti, F., Bizzocchi, L., Degli Esposti, C., & Dore, L. 2007, Astrophysical Journal, Letters, 669, L113

Turner, B. E. 1990, Astrophysical Journal, Letters, 362, L29

Turner, P. H. & Cox, A. P. 1976, Chemical Physics Letters, 42, 84

Turner, P. H. & Cox, A. P. 1978, J. Chem. Soc. Faraday Trans. 2, 74, 533

Turner, P. H., Cox, A. P., & Hardy, J. A. 1981, J. Chem. Soc., Faraday Trans. 2, 77, 1217

van der Tak, F. F. S., Caselli, P., & Ceccarelli, C. 2005, A&A, 439, 195

van Gelder, M. L., Jaspers, J., Nazari, P., et al. 2022, A&A, 667, A136

Vastel, C., Ceccarelli, C., Lefloch, B., & Bachiller, R. 2014, ApJL, 795, L2

Vazart, F., Ceccarelli, C., Balucani, N., Bianchi, E., & Skouteris, D. 2020, Monthly Notices of the RAS, 499, 5547

Ward-Thompson, D., Motte, F., & Andre, P. 1999, MNRAS, 305, 143

Watson, J. K. G. 1967, J. Chem. Phys., 46, 1935

Watson, J. K. G. 1968a, J. Chem. Phys., 48, 181

Watson, J. K. G. 1968b, J. Chem. Phys., 48, 4517

Williams, J., Rohrbacher, A., Seong, J., et al. 1999, J. Chem. Phys., 111, 997

Wilson, T. & Rood, R. 1994, ARA&A, 32, 191

Wirström, E. S., Geppert, W. D., Hjalmarson, Å., et al. 2011, A&A, 533, A24

Xu, L.-H., Lees, R. M., Zakharenko, O., et al. 2021, Journal of Molecular Spectroscopy, 378, 111473

Yamamoto, S. 2016, Introduction to Astrochemistry: Chemical Evolution from Interstellar Clouds to Star and Planet Formation, Astronomy and Astrophysics Library (Springer Japan)

Yang, B., Stancil, P. C., Balakrishnan, N., & Forrey, R. C. 2010, Astrophysical Journal, 718, 1062

Yazidi, O., Ben Abdallah, D., & Lique, F. 2014, Monthly Notices of the RAS, 441, 664

Zaleski, D. P., Duan, C., Carvajal, M., Kleiner, I., & Prozument, K. 2017, J. Mol. Spectrosc., 342, 17

Acknowledgements

I have always known that the last words I want to utter on this Earth are those of gratitude. The placement of this section at the end of this manuscript is then, rather fitting. The text below can be then interpreted as my "last words" preceding the imminent culmination of a scientific and personal era.

First and foremost, I want to thank my parents. Since I was a kid, I have had the extreme privilege of being exposed to the wonders of the world from a safe and caring place. It is from the combination of this environment and my innate curiosity that my fascination for the world was born and nourished.

I want to thank Paola Caselli, who introduced me to the field of astrochemistry and believed in my potential. I want to thank Felipe de Oliveira Alves, the first person who made me imagine a future in this career. I want to thank Silvia Spezzano, the person I have learned the most from during this stage of my education. She has shaped, through patience and kindness, the scientist that I am today. I also want to acknowledge the different generations of the CAS group with whom I had the honour of working. Thank you for supporting me, listening to me, and creating one of the most enriching and safe environments I have encountered to date.

Last but not least, I am grateful to my friends, my greatest supporters, who have given me the strength to navigate the challenges of this stage of my life.